Extragalactic and Cosmological Tests of Gravity Theories with Additional Scalar or Vector Fields

by

Martin Feix

Submitted for the degree of Doctor of Philosophy in Astrophysics

4th March 2011

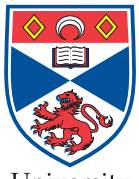

University of St Andrews

Declaration

I, Martin Feix, hereby certify that this thesis, which is approximately 30,000 words in length, has been written by me, that it is the record of work carried out by me and that it has not been submitted in any previous application for a higher degree.

Date Signature of candidate

I was admitted as a research student in September 2007 and as a candidate for the degree of PhD in September 2007; the higher study for which this is a record was carried out in the University of St Andrews between 2007 and 2011.

Date Signature of candidate

I hereby certify that the candidate has fulfilled the conditions of the Resolution and Regulations appropriate for the degree of PhD in the University of St Andrews and that the candidate is qualified to submit this thesis in application for that degree.

Date Signature of supervisor

Copyright Agreement

In submitting this thesis to the University of St Andrews we understand that we are giving permission for it to be made available for use in accordance with the regulations of the University Library for the time being in force, subject to any copyright vested in the work not being affected thereby. We also understand that the title and the abstract will be published, and that a copy of the work may be made and supplied to any bona fide library or research worker, that my thesis will be electronically accessible for personal or research use unless exempt by award of an embargo as requested below, and that the library has the right to migrate my thesis into new electronic forms as required to ensure continued access to the thesis. We have obtained any third-party copyright permissions that may be required in order to allow such access and migration, or have requested the appropriate embargo below.

The following is an agreed request by candidate and supervisor regarding the electronic publication of this thesis: Access to printed copy and electronic publication of the thesis through the University of St Andrews.

Date Signature of candidate

Date Signature of supervisor

Abstract

Despite the many successes of the current standard model of cosmology on the largest physical scales, it relies on two phenomenologically motivated constituents, cold dark matter and dark energy, which account for approximately 95% of the energy-matter content of the universe. From a more fundamental point of view, however, the introduction of a dark energy (DE) component is theoretically challenging and extremely fine-tuned, despite the many proposals for its dynamics. On the other hand, the concept of cold dark matter (CDM) also suffers from several issues such as the lack of direct experimental detection, the question of its cosmological abundance and problems related to the formation of structure on small scales. A perhaps more natural solution might be that the gravitational interaction genuinely differs from that of general relativity, which expresses itself as either one or even both of the above dark components. Here we consider different possibilities on how to constrain hypothetical modifications to the gravitational sector, focusing on the subset of tensor-vector-scalar (TeVeS) theory as an alternative to CDM on galactic scales and a particular class of chameleon models which aim at explaining the coincidences of DE. Developing an analytic model for nonspherical lenses, we begin our analysis with testing TeVeS against observations of multiple-image systems. We then approach the role of low-density objects such as cosmic filaments in this framework and discuss potentially observable signatures. Along these lines, we also consider the possibility of massive neutrinos in TeVeS theory and outline a general approach for constraining this hypothesis with the help of cluster lenses. This approach is then demonstrated using the cluster lens A2390 with its remarkable straight arc. Presenting a general framework to explore the nonlinear clustering of density perturbations in coupled scalar field models, we then consider a particular chameleon model and highlight the possibility of measurable effects on intermediate scales, i.e. those relevant for galaxy clusters. Finally, we discuss the prospects of applying similar methods in the context of TeVeS and present an ansatz which allows to cast the linear perturbation equations into a more convenient form.

Acknowledgements

There are several people who deserve enormous credit for their encouragement, persistent support and stimulating discussions: Cosimo Fedeli, Garry Angus, Benoit Famaey, Matthias Bartelmann and Massimo Meneghetti.

Furthermore, I owe a huge debt to my parents and family for having made all of this possible in the first place and for supporting me through everything.

Other people who have either been of some scientific help or contributed to my personal amusement are: Flo, Jochen, Philipp, Emerson, Jan, David, Lee, Marina, Paul, Matthias, Paula, and many, many more.

Finally, I thank my supervisor HongSheng Zhao, our systems administrator Ian and other members of staff at St. Andrews University, especially Ian Bonnell and Keith Horne.

List of publications

This thesis is based on the following papers:

Is gravitational lensing by intercluster filaments always negligible?
Feix M., Xu D., Shan H., Famaey B., Limousin M., Zhao H. S., Taylor A., 2008, ApJ, 682, 711
[arXiv e-print 0710.4935]

An analytic model for non-spherical lenses in covariant MOdified Newtonian Dynamics
Shan H. Y., Feix M., Famaey B., Zhao H. S., 2008, MNRAS, 387, 1303
[arXiv e-print 0804.2668]

Structure formation by fifth force: Power spectrum from N-body simulations
Zhao H. S., Macciò A. V., Li B., Hoekstra H., Feix M., 2010, ApJL, 712, L179
[arXiv e-print 0910.3207]

Substructure lensing in galaxy clusters as a constraint on low-mass sterile neutrinos in tensor-vector-scalar theory: The straight arc of Abell 2390
Feix M., Zhao H. S., Fedeli C., Pestaña J. L. G., Hoekstra H., 2010, Phys. Rev. D 82, 124003
[arXiv e-print 1008.1963]

Revisiting metric perturbations in tensor-vector-scalar theory
Feix M., 2011, in preparation

Contents

List of Figures

List of Tables

Chapter 1

Introduction

1.1 The standard model of cosmology

Current observations of the universe at large scales indicate that it is to good approximation isotropic and - following the Copernican principle - homogeneous. Within the commonly accepted framework of general relativity (GR), this remarkably allowed cosmologists to develop suitable theoretical models of the universe as a whole and to constrain possible scenarios regarding its origin and evolution as well as to pinpoint its energy budget. With the advent of observational evidence supporting a spatially flat spacetime geometry, it was inferred that the universe's energy density must be close to a critical value ρ_{crit}. Naively, one expects this density to be made out of known matter described by the standard model of particle physics (SMPP), in which case it should be dominated by the contribution of baryonic material. However, current cosmological constraints do not agree with this picture. For instance, Big Bang nucleosynthesis (BBN), which provides a theoretical description for the creation of light elements in the first three minutes after the Big Bang, gives strict limits on the amount of ordinary matter in the universe [1] and suggests that baryons contribute less than 5% to the found value of ρ_{crit}. The fully isotropic and homogeneous universe is, of course, an idealization. In reality, the universe exhibits a plethora of structures, ranging from large-scale filaments and cosmic voids down to stars, galaxies and clusters thereof. It is now widely believed that these originally formed from tiny quantum fluctuations in the very early universe. According to the current picture, these fluctuations originated from a scalar field, the so-called inflaton, which is also responsible for a rapid phase of cosmological expansion very shortly after the Big Bang. Once inflation sets in, the vacuum fluctuations quickly lose causal contact and effectively become classical, fixing the initial conditions for the growth of perturba-

tions driven by gravitational attraction. Since inflation ensures that all of the observable universe emerged from a small causally connected region, it provides a suitable explanation for the found isotropy and homogeneity on the largest scales today. Furthermore, the inflationary scenario predicts a spatially flat spacetime geometry in accordance with the current observational evidence for a critical energy density. The theoretical study of perturbations and their evolution has made it possible to make firm statistical predictions which can be tested with the help of astronomical data. Up to today, all of these tests consistently agree with the view that baryonic material accounts for only a fraction of the universe's present energy density, with a contribution of around $4 - 5\%$. Therefore, if one assumes GR and the theory of inflation to be correct, the remaining $95 - 96\%$ must be constituted by something that is not part of the SMPP.

Indeed, the problem of missing matter is not entirely new. Already in the early 30s, an analysis of the Coma cluster [2] pointed out that the mass inferred from the cluster's luminosity distribution is not able to account for the system's gravitational potential, and it was postulated that this discrepancy might be due to the presence of dark matter (DM) in the cluster, i.e. a hypothetical form of matter which does not couple to light and thus is invisible to direct observations. This assumption has been further strengthened by the first analysis of rotation curves of spiral galaxies [3, 4], followed by many more studies in the general context of dynamical investigations as well as gravitational lensing (see, e.g., Refs. [5–7] for recent reviews), and the currently shared view is that this DM component is essentially collisionless [8], i.e. cold dark matter (CDM). However, observations of the cosmic microwave background (CMB) and the ratio of CDM to baryons measured by the combination of weak lensing and x-ray analysis in galaxy clusters revealed that this mysterious component alone is not able to fully account for the missing 95% of the critical density. As it turned out, one had to add yet another ingredient to the cosmic inventory which is commonly denoted as the cosmological constant or more generally dark energy (DE) and - unlike any other known matter field - characterized by a strong negative pressure. The introduction of such a quantity became necessary to explain a further observed property of the current universe, its accelerated expansion. Although the fact that the present universe is undergoing a phase of expansion was already discovered by Edwin Hubble at the beginning of the twentieth century, the first convincing evidence for an accelerated expansion came from observations on supernovae Ia [9]. Sharing a common scale (in the form of the Chandrasekhar mass limit), these objects are believed to form standard candles, i.e. objects with known luminosities, which allows one to use them as cosmological distance indicators and thus as probes of the universe's expansion history. Other

evidence for DE comes from the observed peaks in the CMB anisotropy spectrum, the imprint of baryonic acoustic oscillations in the matter power spectrum [10], the relative speeds of galaxies in the local group [11], weak gravitational lensing [12] or the late-time integrated Sachs-Wolfe effect [13] which describes the energy gain of CMB photons traveling through the time-dependent gravitational potentials generated by large-scale structure such as galaxy clusters.

Putting everything together, the present view is that the total energy density of today's universe is dominated by DE, followed by CDM and ordinary baryonic matter with fractional contributions of $20-25\%$ and around $4-5\%$, respectively. Combined with the framework of GR and inflation, these constituents form the pillars of what is now known as the ΛCDM model, the standard model of cosmology. Over the recent years, the ΛCDM model has been remarkably successful in forming a coherent picture on the largest physical scales and provides suitable explanations for the observations on supernovae [14], large-scale structure [15, 16], weak lensing [17] and the CMB [18, 19]. Despite its achievements as a phenomenological description of the universe, however, the ΛCDM model is not free of problems and as we shall discuss below, it seems intriguing that these difficulties are related to the concepts of DE and CDM.

Cold dark matter At present, the generally accepted view is that CDM is primarily made out of nonbaryonic particles. Among the most common proposals, one finds so-called weakly interacting massive particles (WIMPs), axions or sterile neutrinos (cf. Sec. 3.4.1). None of these are actually part of the SMPP, but can arise within certain extensions to it. Assuming that CDM particles were thermally produced in the very early universe, WIMPs provide a quite natural choice for DM: Considering particle interaction rates and taking the expansion of the universe into account, it has been found that the abundance of a particle is directly related to its typical cross section [20]. The higher the cross section is, the lower its abundance in the universe will be and vice versa. If a nonrelativistic particle interacts with typical weak-scale cross sections, however, its relative abundance to ordinary matter turns out to be just of the right order, i.e. one obtains a DM contribution which is in good accordance with current observational evidence. This is called the "WIMP Miracle". For instance, many supersymmetric models naturally give rise to stable and heavy WIMPs in the form of neutralinos [1], with a lightest neutralino around a mass of roughly $10-10^4$GeV providing an excellent candidate to comprise the universe's CDM. Until now, however, none of the above particles has been directly detected in any of the experiments conducted so far [21] and

[1] Having the same quantum numbers, the supersymmetric partners of Z boson, photon and the neutral Higgs boson can mix, forming four eigenstates of the mass operator which are commonly denoted as neutralinos.

it should be emphasized that their existence still remains theoretical speculation. Furthermore, even if such CDM candidates were found, one would still be left with the problem that producing the right amount of CDM is likely to require severe fine-tuning of the model parameters - even in the case of WIMPs [22]. On the other hand, the concept of CDM also suffers from several issues related to the formation of structure on small scales. For instance, cosmological simulations predict that there should be a substantially larger number of satellite galaxies orbiting around galaxies like the Milky Way than actually observed [23–25]. A common explanation is that there may exist feedback processes such as supernovae which extinguish the star formation of such small galaxies. However, no fully convincing mechanism for this kind of scenario has been proposed so far. Another consequence of the CDM paradigm is the prediction of cuspy density profiles in galaxies, which appears to contradict the observed cored distribution of dwarf galaxies [26, 27]. Similar evidence against such central cusps is also seen in the rotation curves of spiral galaxies [28] where the CDM density does not increase towards the center. Possible remedies to this problem such as feedback from active galactic nuclei or supernova winds, which are principally capable of reducing the CDM density at the center of galaxies, have been found to be insufficient [29].

Dark energy Even more mysterious than assuming the presence of DM particles is the necessity for DE which appears to constitute most of the total energy-matter content of the present universe. To be consistent with current observations supporting accelerated expansion, DE must come with a pressure which is approximately equal to its energy density, but with the opposite sign. In this case, the effects of DE could be explained by simply allowing for a cosmological constant term in the gravitational field equations, the same constant originally proposed (and later discarded) by Einstein to enforce a static universe. To explain where this constant comes from, however, poses a great challenge to physics [30, 31]. From a quantum theoretical point of view, it should be identified as the energy density of the vacuum. Following the standard methods of quantum field theory [32, 33], one may obtain a rough estimate for its order of magnitude by considering the vacuum energy of a free scalar field. Introducing natural units where Planck's constant $\hbar$ and the speed of light c are set to unity, i.e. $\hbar = c = 1$, this leads to

$$\langle \rho_{\mathrm{vac}} \rangle \sim \frac{1}{2} \int_0^\infty \frac{d^3k}{(2\pi)^3} \sqrt{k^2 + m^2} \tag{1.1}$$

if one takes the contribution of all the modes into account. Since the integral in Eq. (1.1) is ultraviolet divergent, one might expect that such high-energy modes do not contribute within a

more fundamental theory and introduce a cut-off to the integral. A natural choice would be the Planck scale where quantum effects are believed to become important. Using this assumption, one finds an estimate for ρ_{vac} which is approximately by a factor 10^{120} larger than the actual observed value. Obviously, there is a cancellation effect needed which should lead to the desired value. Certain supersymmetric theories even require a cosmological constant that is exactly zero, which further complicates things. This is the cosmological constant problem, the worst problem of fine-tuning in physics. Another related fine-tuning issue is the so-called cosmic coincidence problem which simply concerns the question why the energy contributions of DE and matter (mostly CDM) have become comparable just recently. This is disturbing in view of the fact that the size of the universe at the creation of the CMB, where DE was completely negligible, has roughly grown by a factor of 10^3 until the present and that after an additional increase by a factor of around 10, everything except DE will be negligible. Looked at this way, the transition between these two regimes appears almost instantaneous and one would like to understand why this is the case. Furthermore, it is curious that the effects of DE and DM in various systems seem to be tuned to a common scale [34], hence requiring a coincidence in both dark sectors which appears unlikely given their current interpretation.

A perhaps more natural solution might be that the description of gravitational interaction genuinely differs from GR, which expresses itself as either one or even both of the above dark components. Having only been accurately tested in the very strong gravity regime, i.e. the solar system, there is no guarantee that GR will hold everywhere in the universe. This has motivated different modifications to the gravity sector, either by directly changing the underlying principles of spacetime geometry or by introducing new fields and nonstandard couplings. Typical examples are $f(R)$ gravity [35], conformal Weyl gravity or scalar-tensor theories, but there exist many more [34, 36–40]. While some of these modifications are explicitly constructed to provide a phenomenological description of observational findings, others emerge from theoretical considerations in the context of high energy physics. For example, there exist attempts to reconcile gravitation with quantum theory by introducing corrections to the conventional gravitational interaction. Other approaches involve strong couplings between spacetime curvature and scalar fields like the Higgs field in order to provide an explanation for DE, or introduce unconventional vector fields to create the effects of CDM on astrophysical scales. Finally, certain formulations in the context of string theory propose that extra-dimensions could have gravitational effects on the visible universe, meaning that DE and DM are not necessarily needed for a unified theory of cosmology.

Ultimately, a modified theory of gravity must be able to consistently explain observations before one may consider it as a serious competitor to the ΛCDM model. In the following, we shall discuss certain aspects of these theories such as their generic properties and possible approaches to test and constrain them on extragalactic and cosmological scales, restricting ourselves to a subset of modified gravity theories which have recently gained interest within the scientific community. After a general review of GR and cosmology, we will introduce these modifications in Sec. 2.

1.2 Structure and contents of the thesis

The thesis is structured as follows:

- In Sec. 2, we will briefly review the basics of general relativity and cosmology, followed by a discussion of selected possible extensions.
- The contents of Sec. 3 are concerned with the study of gravitational lensing in tensor-vector-scalar gravity. Starting with a test of multiple-image lens systems, we discuss the role of low-density objects such as filaments and finally consider the possibility of constraining massive neutrino matter with galaxy cluster lenses.
- In Sec. 4, we shall investigate the nonlinear regime of structure formation in the context of coupled scalar field models. This is followed by an analysis of metric perturbations in tensor-vector-scalar gravity, aiming at how to principally approach such problems in this case.
- Finally, we summarize in Sec. 5.

Chapter 2

Gravitation and cosmology

As the dynamics of the universe at large scales is governed by gravity, we will begin with a brief introduction to GR and its cosmological application. We will also discuss more speculative extensions to this framework, focusing on their motivations and basic structure. Throughout this thesis, we will mostly follow the conventions of Ref. [41]. In particular, we will assume a positive metric signature $(-,+,+,+)$ and units where the speed of light equals unity, i.e. $c = 1$. While greek indices run from 0 to 3, latin ones run from 1 to 3.

2.1 General relativistic description of the universe

2.1.1 Basic equations

In GR, gravitation is described in terms of spacetime geometry. The geometry is determined by the matter content while the matter's movement is in turn governed by the geometry. More mathematically, this interplay can be expressed in terms of field equations which read

$$R_{\mu\nu} - \frac{1}{2}Rg_{\mu\nu} = 8\pi G T_{\mu\nu}, \tag{2.1}$$

where G is Newton's constant, $R_{\mu\nu}$ is the Ricci tensor and $T_{\mu\nu}$ denotes the energy-momentum tensor. Here R is defined as the contraction of $R_{\mu\nu}$, i.e. $R \equiv g^{\mu\nu}R_{\mu\nu}$, and $R_{\mu\nu}$ is constructed from the metric field $g_{\mu\nu}$ according to (e.g., see Ref. [42])

$$R_{\mu\nu} \equiv \Gamma^{\alpha}_{\mu\nu,\alpha} - \Gamma^{\alpha}_{\mu\alpha,\nu} + \Gamma^{\alpha}_{\alpha\lambda}\Gamma^{\lambda}_{\mu\nu} - \Gamma^{\alpha}_{\mu\lambda}\Gamma^{\lambda}_{\alpha\nu}, \tag{2.2}$$

where Γ is associated with the Levi-Civita connection of the metric (the Γ's are then also called the Christoffel symbols),

$$\Gamma^{\alpha}_{\beta\gamma} \equiv \frac{1}{2} g^{\alpha\lambda} \left(g_{\lambda\beta,\gamma} + g_{\lambda\gamma,\beta} - g_{\beta\gamma,\lambda} \right). \tag{2.3}$$

The above quantities describe the geometry of spacetime in the combination defined as the Einstein tensor $G_{\mu\nu}$,

$$G_{\mu\nu} \equiv R_{\mu\nu} - \frac{1}{2} R g_{\mu\nu}, \tag{2.4}$$

while $T_{\mu\nu}$ contains the information of the matter configuration. In four dimensions, there are 16 field equations, but since in Einsteinian gravity $g_{\mu\nu}$ and $T_{\mu\nu}$ are symmetric, i.e. $g_{\mu\nu} = g_{\nu\mu}$, the number of independent equations is reduced to ten. In general, this set of highly nonlinear equations is practically impossible to solve. However, there exist remarkable exceptions in cases of abundant symmetries. In such situations, the number of independent degrees of freedom can be substantially reduced, resulting in a system of equations simple enough to be analytically trackable. The first such example was found by Schwarzschild in 1915 and describes the vacuum outside a spherically symmetric matter distribution.

The field equations in Eq. (2.1) can be derived from the action principle and a suitable starting point is given by the Einstein-Hilbert action which reads

$$S_g = \int d^4x \sqrt{-g} \left[\frac{R}{16\pi G} + \mathcal{L}_m \left(g_{\mu\nu}, \Upsilon^B \right) \right], \tag{2.5}$$

where g is the determinant of the covariant metric $g_{\mu\nu}$. The Lagrangian density $\mathcal{L}_m$ depends on the metric and some collection of matter fields Υ^B, perhaps also on their first derivatives. The form of Eq. (2.1) is obtained through minimization of Eq. (2.5): Variation of the gravitational part with respect to the dynamical variable $g^{\mu\nu}$ yields the previously defined Einstein tensor $G_{\mu\nu}$. To satisfy the structural form of the field equations, one notes that the energy-momentum tensor has to be defined as the variation

$$T_{\mu\nu} \equiv -\frac{2}{\sqrt{-g}} \frac{\delta(\sqrt{-g}\mathcal{L}_m)}{\delta g^{\mu\nu}}. \tag{2.6}$$

As we shall see further below, the action principle offers the most convenient way of introducing possible modifications to the gravitational sector [1]. In particular, this approach will automatically include necessary conservation laws through the action's symmetry properties (see Noether's first and second theorems).

[1] Note that such modifications do not necessarily involve changing the geometric part of the action, but may be achieved by introducing coupling terms between the metric and additional (new) fields.

Finally, let us briefly comment on how Newtonian dynamics emerges from the framework of GR. In the limit of weak fields and quasistatic configurations [2], the metric may be decomposed as

$$g_{\mu\nu} = \eta_{\mu\nu} + h_{\mu\nu}, \tag{2.7}$$

where $\eta_{\mu\nu}$ denotes the Minkowski metric and $h_{\mu\nu}$ is "small" in the sense that its components are much smaller than unity and higher order terms are negligible. The equation of motion for test particles is determined by the underlying spacetime geometry and given by the geodesic equation,

$$\frac{d^2x^\mu}{d\lambda^2} = -\Gamma^\mu_{\nu\kappa}\frac{dx^\nu}{d\lambda}\frac{dx^\kappa}{d\lambda}, \tag{2.8}$$

where λ is some suitable affine parameter characterizing the trajectory of the particles. Using the decomposition in Eq. (2.7), the geodesic equation then approximately takes the form (for details, see again Ref. [42])

$$\frac{d^2x^i}{dt^2} = -\Gamma^i_{00}, \tag{2.9}$$

with

$$\Gamma^i_{00} = -\frac{1}{2}\frac{\partial h_{00}}{\partial x^i} \equiv \frac{\partial \Phi}{\partial x^i} \tag{2.10}$$

and

$$\Delta\Phi = 4\pi G\rho, \tag{2.11}$$

which directly follows from the field equations in Eq. (2.1). Clearly, the above describes the equation of motion for a Newtonian system and we identify Φ as the corresponding Newtonian potential. However, it is important to note that - unlike the Newtonian case - the resulting trajectories are not a consequence of forces acting upon massive particles, but rather follow from (free) propagation in a curved spacetime.

2.1.2 Friedmann-Robertson-Walker cosmology

Another example of a highly symmetric gravitational system is provided by the universe as a whole. Cosmological observations indicate that the universe on large physical scales is homogeneous and isotropic [3]. The most general metric under these conditions is the Friedmann-

[2] Here we explicitly assume that there exists a global inertial coordinate system of $\eta_{\mu\nu}$ such that $T_{\mu\nu}$ has only a time-time component and that derivatives with respect to time can safely be neglected.

[3] If a spacetime is isotropic at every point (the cosmological principle), it is also homogeneous.

Robertson-Walker (FRW) metric whose line element is given by

$$ds^2 = -dt^2 + a^2(t)\left[d\chi^2 + f_K^2(\chi)d\omega^2\right], \tag{2.12}$$

where we have introduced a set of polar coordinates (χ, θ, φ) with

$$d\omega^2 = d\theta^2 + \sin^2\theta d\varphi^2, \tag{2.13}$$

the scale factor a and a radial function $f_K(\chi)$. The choice of the function $f_K(\chi)$ is restricted by the requirement of homogeneity. It can be shown that $f_K(\chi)$ is either linear, trigonometric or hyperbolic in χ, which corresponds to a flat, closed or open universe respectively,

$$f_K(\chi) = \begin{cases} K^{-1/2}\sin\left(K^{1/2}\chi\right) & (K > 0) \\ \chi & (K = 0) \\ |K|^{-1/2}\sinh\left(|K|^{1/2}\chi\right) & (K < 0) \end{cases}. \tag{2.14}$$

Here K is a constant parameterizing the curvature of spatial hypersurfaces and both $f_K(\chi)$ and $|K|^{-1/2}$ have the dimension of length. There is cosmological evidence that the curvature of the universe is negligibly small. Would there be a not too small curvature, it should recently have become detectable as its contribution to the expansion of the universe would have started to dominate over that of matter. A universe with $K = 0$ is also what one expects from the simplest models of inflation. Therefore, we will mostly concentrate on flat cosmologies for which the line element takes the particularly simple form

$$ds^2 = a^2(\tau)\left[-d\tau^2 + \delta_{ij}dx^i dx^j\right], \tag{2.15}$$

where we have used Cartesian coordinates x_i and introduced the conformal time τ which is related to the coordinate time t via $dt = a(\tau)d\tau$. Obviously, such a metric is also conformally flat, i.e. a Weyl transformation of the Minkowski metric $\eta_{\mu\nu}$.

The isotropy of the universe implies that it consists of matter which can be described as a perfect fluid. In this case, the energy-momentum tensor is written as

$$T_{\mu\nu} = \rho u_\mu u_\nu + P(g_{\mu\nu} + u_\mu u_\nu), \tag{2.16}$$

where ρ and P are the fluid's energy density and pressure, respectively, and u_μ denotes the four-velocity. Evaluating Eq. (2.16) in comoving coordinates, one finds

$$T^\mu_\nu = diag(-\rho, P, P, P). \tag{2.17}$$

Furthermore, homogeneity dictates that both ρ and P are functions of time only. Their relation is called the equation of state (EoS),

$$w \equiv \frac{P}{\rho}, \tag{2.18}$$

and the quantity w is called the EoS parameter which is generally a function of time. Recalling from statistical mechanics that for relativistic matter (radiation) $w = 1/3$, we see that this is consistent with the theoretical result of a traceless energy-momentum tensor for the Maxwell field. In case of nonrelativistic matter (dust), the pressure may approximately be neglected and one has $w = 0$. For any matter at hand, the energy-momentum tensor is conserved [4], meaning that

$$\nabla^\mu T_{\mu\nu} = 0, \tag{2.19}$$

The $\nu = 0$ component of the above leads to the continuity equation which determines the evolution of the matter density in an expanding universe,

$$\dot{\rho} + 3\frac{\dot{a}}{a}(1 + w)\rho = 0, \tag{2.20}$$

where an overdot denotes the derivative with respect to conformal time. Assuming a constant EoS parameter, the solution of Eq. (2.20) is

$$\rho \propto a^{-3(1+w)}. \tag{2.21}$$

In the case of dust, the energy density decreases inverse proportionally to the comoving volume as the universe expands. The energy density of radiation dilutes faster, $\rho \propto a^{-4}$, where the additional factor of a^{-1} can be explained with the loss of photon energy due to the stretching of wavelength.

To find an evolution equation for the scale factor, one has to return to Eq. (2.1). Considering

[4]Note that this does not generally correspond to the conservation of energy and momentum, but emerges from the invariance under general coordinate transformations. The fundamental problem is that vectorial quantities like energy-momentum cannot be parallelly transported to another spacetime point in a unique way.

the equation's time-time component, we arrive at the Friedmann equation,

$$H^2 = \frac{8\pi G}{3}\rho - \frac{K}{a^2}, \tag{2.22}$$

where the physical Hubble parameter is defined as $H = \dot{a}/a^2$. Again, note that there appears an additional factor of a in the denominator because we are taking the derivative with respect to conformal time. The spatial components of Eq. (2.1) do not yield any additional information. Assuming that the matter properties are given in terms of w, there remain two unknowns, ρ and a, which may be determined from Eqs. (2.20) and (2.22). On the other hand, given a measured expansion history of the universe, this also allows one to reconstruct the matter content.

Parameterization To clarify the discussion of cosmological models, it is convenient to introduce both dimensional and dimensionless parameters. In what follows, the subscript "0" will be used to denote the values of different quantities as measured today. We begin with defining the current value of the physical Hubble parameter as

$$H_0 \equiv 100h\,\mathrm{km\,s^{-1}\,Mpc^{-1}}, \tag{2.23}$$

where h is a dimensionless constant and H_0 is called the Hubble constant. Current cosmological observations indicate that $h \approx 0.7$. Next, we define the critical density

$$\rho_{\mathrm{crit}} \equiv \frac{3H^2}{8\pi G} \tag{2.24}$$

and expressing the energy density in terms of ρ_{crit} leads to the dimensionless density parameter

$$\Omega \equiv \frac{\rho}{\rho_{\mathrm{crit}}}. \tag{2.25}$$

For multiple matter fluids, we have $\rho = \sum_i \rho_i$ and Eq. (2.22) takes the form

$$1 + \frac{K}{a^2H^2} = \sum_i \Omega_i = \Omega_{\mathrm{tot}}. \tag{2.26}$$

From Eq. (2.26), one may also understand the notion of a critical density: If the total energy density equals ρ_{crit}, the universe is flat. Whereas the total density is smaller than ρ_{crit} for open universes, it is larger in closed ones. Apart from the possibility of more exotic matter fluids, a realistic universe will consist of both relativistic (e.g., photon radiation or massless neutrinos)

and nonrelativistic (e.g., baryonic matter) density components. Defining the curvature parameter, $\Omega_K \equiv -K/H_0^2$, and allowing for a cosmological constant (which may be described in terms of a matter fluid with $w = -1$), we may recast Eq. (2.22) into

$$E^2(a) = \Omega_{r0}a^{-4} + \Omega_{m0}a^{-3} + \Omega_{\Lambda 0} + \Omega_K a^{-2}, \tag{2.27}$$

where the scale factor has been normalized such that $a_0 = 1$ and $E^2(a) \equiv H^2/H_0^2$. Instead of using the scale factor a, the above equations may also be written in terms of the cosmological redshift z which is defined as the relative increase of photon wavelength between a and $a_0 = 1$, thus yielding the relation $z = -1 + 1/a$.

From the density scaling of individual components in Eq. (2.27), it becomes evident that relativistic matter must have been the most significant contributor at an early stage of the universe, i.e. $\Omega_r \gg \Omega_m$. Nowadays, radiation has cooled down, causing other components such as Ω_m or Ω_Λ to take over. With the help of cosmological observations, it is possible to put constraints on the above parameters and there is now vast evidence supporting that the known matter fields account for only less than 5% of Ω_{tot} in the present universe. For instance, one may infer the radiation contribution as $\Omega_{r0} \approx 4.7 \times 10^{-5}$ from the CMB temperature which is well described by a thermal black body spectrum at around $T = 2.7$K. On the other hand, one may also estimate the baryonic content of the universe, either from direct astrophysical measurements or using the predicted primordial abundance of light elements produced at big bang nucleosynthesis (BBN) which took place during the first minutes of the universe. Although there appears some discrepancy between these approaches, both imply $\Omega_b \leq 0.05$, which is also consistent with recent observations of CMB anisotropies [18]. If the framework of GR indeed holds true, then the missing energy density has to be described by something which is not rooted within the standard model of particle physics. The ΛCDM model provides the most simplistic example of consistently explaining observational data by incorporating such unknown physics in a phenomenological way.

Cosmological distances Given a curved spacetime geometry, distance measures are no longer unique and need to be defined according to idealizations or measurement prescriptions. The comoving distance D_C is defined as the distance on the spatial hypersurface at $t = \text{const}$ between the world lines of a source and an observer moving with the mean cosmic flow. Therefore, one has the relation $dD_C = d\chi$ (see Eq. (2.12) above) and because light rays propagate according to $ds = 0$,

integration yields the result

$$D_C\left[a(z_1), a(z_2)\right] = \int_{a(z_2)}^{a(z_1)} \frac{da}{\dot{a}} = \frac{1}{H_0} \int_{a(z_2)}^{a(z_1)} \frac{da}{a^2 E(a)}. \tag{2.28}$$

Using $da = -a^2 dz$, we can alternatively express Eq. (2.28) in terms of redshift z

$$D_C(z_1, z_2) = \frac{1}{H_0} \int_{z_1}^{z_2} \frac{dz'}{E(z')}, \tag{2.29}$$

where $E(z)$ is given by Eq. (2.27),

$$E(z) = \left[\Omega_{r0}(1+z)^4 + \Omega_{m0}(1+z)^3 + \Omega_{\Lambda 0} + \Omega_K(1+z)^2\right]^{1/2}. \tag{2.30}$$

In preparation for Sec. 3, we also introduce the angular diameter distance D_A. It is defined in accordance with the relation in Euclidean space between the area δA and the solid angle $\delta\omega$ of an object, $\delta\omega D_{A,E}^2 = \delta A$. As the solid angle of spheres of constant radial coordinate χ is scaled by $f_K(\chi)$ in Eq. (2.12), one must have

$$\frac{\delta A}{4\pi a^2(z_2) f_K^2\left[D_C(z_1, z_2)\right]} = \frac{\delta\omega}{4\pi}. \tag{2.31}$$

From the above, it follows that

$$D_A(z_1, z_2) = a(z_2) f_K(D_C(z_1, z_2)) = \frac{1}{1+z_2} f_K\left[D_C(z_1, z_2)\right]. \tag{2.32}$$

The angular diameter distance shows that cosmological distances are not necessarily monotonic. Assuming a universe filled with pressureless matter only, for example, $D_A(0, z)$ has a maximum at $z = 5/4$ and gently decreases for larger values of z, which is a consequence of spacetime curvature.

2.2 Tensor-vector-scalar theory

In the following sections, we will discuss possible modifications to the gravitational sector which are motivated by observational findings or more fundamental theoretical ideas. To begin with, we give an introduction to Bekenstein's tensor-vector-scalar theory [43] which has originally been constructed to explain empirical relations in galaxies.

2.2.1 Modified Newtonian dynamics

Without resorting to CDM, the modified Newtonian dynamics paradigm (MOND) aims at solving the missing mass problem on a nonrelativistic level by postulating an acceleration-dependent change of Newton's law which is characterized by a scale a_0 [44–47]:

$$\tilde{\mu}\left(\frac{|\mathbf{a}|}{a_0}\right)\mathbf{a} = -\boldsymbol{\nabla}\Phi_N + \mathbf{S}. \tag{2.33}$$

Here, Φ_N denotes the common Newtonian potential of a matter source and $\mathbf{S}$ is a solenoidal vector field determined by the condition that $\mathbf{a}$ can be expressed as the gradient of a scalar potential. The function $\tilde{\mu}$, controlling the modification of Newton's law, has the following asymptotic behavior:

$$\begin{aligned} \tilde{\mu}(x) &\sim x \qquad x \ll 1, \\ \tilde{\mu}(x) &\sim 1 \qquad x \gg 1. \end{aligned} \tag{2.34}$$

For nonspherical geometries, one typically has $\mathbf{S} \neq \mathbf{0}$ and finding the solution of Eq. (2.33) usually requires the use of a numerical solver [48–50]. The law given by Eq. (2.33) has been constructed to agree with the fact that the rotation curves of spiral galaxies become flat outside their central parts. In such regions, the Newtonian potential caused by a galaxy of mass M is approximately spherical ($\mathbf{S} \approx \mathbf{0}$) and we have

$$|\boldsymbol{\nabla}\Phi_N| \approx GMr^{-2}. \tag{2.35}$$

Now let us consider the situation in which $|\boldsymbol{\nabla}\Phi_N| \ll a_0$ such that the first expression in Eq. (2.34) is satisfied. Introducing the centripetal acceleration v_c^2/r with circular velocity v_c, we arrive at

$$\frac{v_c^2}{r} = \frac{\sqrt{GMa_0}}{r}, \tag{2.36}$$

and thus

$$v_c^4 = GMa_0. \tag{2.37}$$

Assuming a constant mass-to-luminosity ratio in a specified spectral band, the luminosity in that band should therefore scale as v_c^4, i.e.

$$L \propto v_c^4. \tag{2.38}$$

The above relation corresponds to the well-known Tully-Fisher law [53] which is shown in the right panel of Fig. 2.1 for the Ursa Major spirals in the near-infrared (K′ band) [52]. Analyzing

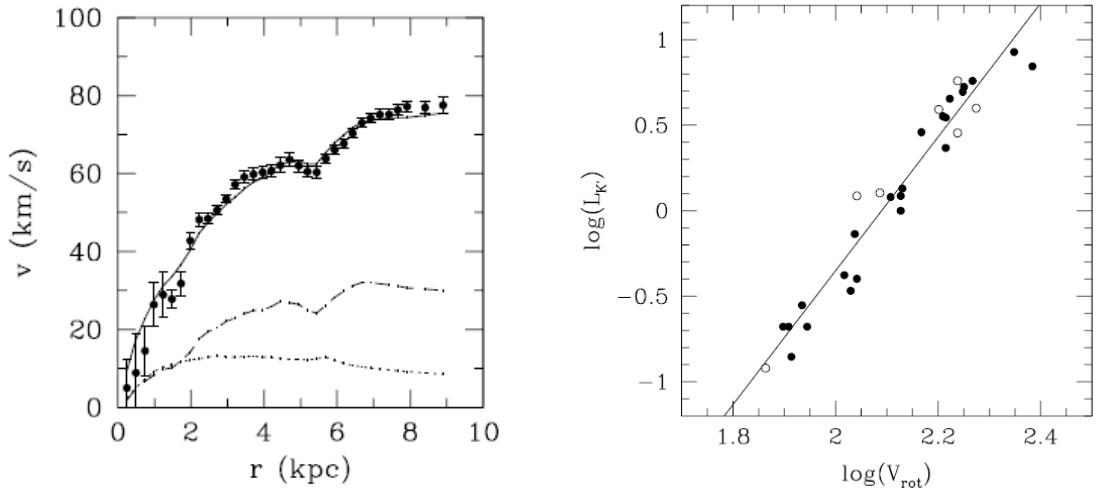

Figure 2.1: *Left*: The points show the observed 21cm line rotation curve of the low surface brightness galaxy NGC 1560 (the figure is taken from Ref. [51]). The dotted and dashed lines are the Newtonian rotation curves of the visible and gaseous components of the disk and the solid line is the MOND rotation curve with $a_0 = 1.2{\times}10^{-10}\mathrm{m\,s^{-2}}$. The only free parameter is the mass-to-light ratio of the visible component. *Right*: The near-infrared (K′ band) Tully-Fisher relation of Ursa Major spirals (the figure is taken from Ref. [52]). The rotation velocity is the asymptotically constant value in units of km $\mathrm{s^{-1}}$ and the luminosity is given in $10^{10}L_\odot$. The unshaded points are galaxies with disturbed kinematics. The line is a least-square fit to the data and has a slope of 3.9 ± 0.2.

observational data, Milgrom estimated an acceleration scale of $a_0 \approx 1.2 \times 10^{-10}\mathrm{m\,s^{-2}}$. For example, using this value for a_0 and choosing the so-called standard form of the interpolating function $\tilde{\mu}(x)$,

$$\tilde{\mu}(x) = \frac{x}{\sqrt{1+x^2}}, \tag{2.39}$$

it is possible to fit the observed rotation curve of the galaxy NGC 1560 as shown in the left panel of Fig. 2.1. Since accelerations in the solar system are strong compared to a_0, Eq. (2.33) will turn into the classical Newtonian law there.

The MOND paradigm still appears suitable to explain the observed "conspiracy" between the distribution of baryons and the gravitational field in spiral galaxies [54–57]. It is striking that such a simple prescription leads to extremely successful predictions for galaxies ranging over five decades in mass (see Refs. [58, 59] for reviews), including our own Milky Way [60–62], dwarf spheroidals [63–65], x-ray dim elliptical galaxies [66, 67], and tidal dwarf galaxies [68–70]. In addition to the Tully-Fisher law [71, 72], MOND successfully reproduces empirical galaxy scaling relations such as the Faber-Jackson relation [73, 74] and, more recently, the central surface brightness predicted by dark halos [75–77]. In the view of MOND, these empirical laws emerge as a consequence of dynamics in the low acceleration regime.

While the framework of MONDian dynamics appears to work extremely well on galactic scales, the situation in galaxy groups and clusters is quite different: Several studies of such systems [78–80] have shown that an additional nonluminous matter component is required to explain observations, even after taking into account the gravitational boost induced by the MOND formula. In galaxy clusters, for example, this discrepancy is about a factor of two at very large radii, meaning that there should be as much dark matter (mainly in the central parts) as observed baryons. Assuming that MOND is a viable description for such gravitating systems, this result has led to the question of what the needed matter component should be. It is obvious that any possible form of exotic CDM is disfavored as it would cause the original idea of Eq. (2.33) to become redundant. Possible remedies range from undiscovered baryonic material such as cold molecular gas clouds to the hypothesis of massive neutrinos accounting for the missing mass [81]. We shall address this issue further when considering the situation of gravitational lens systems in Sec. 3.

A further problem arises from the fact that the original MOND formulation does not specify cosmology or the nature of gravitational light deflection. Recent developments in the theory of gravity, however, have been able to embed MONDian dynamics into fully Lorentz-covariant theories by means of a dynamical four-vector field [43, 82–85]. Although still lacking a derivation from fundamental principles underpinning the MOND paradigm, these theories allow for new predictions regarding cosmology and structure formation [86–89] as well as gravitational lensing [50, 90–94]. As it turns out, another appealing feature of such modifications is also that they might be able to simultaneously explain the observed effects of DE [40, 95–100], but we do not consider this possibility in this thesis. In the next section, we will introduce the first proposed relativistic theory of MOND, Bekenstein's tensor-vector-scalar theory (TeVeS), and discuss some of its properties in more detail.

2.2.2 Fundamentals of TeVeS

In this section, we shall briefly review the basics of TeVeS. In particular, we will focus on its implications for quasistatic systems and cosmology and see how the theory is related to MOND. Finally, we also comment on more general constructions whose primary motivation goes beyond the interpretation of astrophysical observations.

2.2.2 A Fields and action

TeVeS [43] is a bimetric theory of gravity and based on three dynamical fields: an Einstein metric $\tilde{g}_{\mu\nu}$, a time-like vector field A_μ such that

$$\tilde{g}^{\mu\nu}A_\mu A_\nu = -1, \tag{2.40}$$

and a scalar field ϕ. Furthermore, there is a second metric $g_{\mu\nu}$ which is needed for gravity-matter coupling only and obtained from the non-conformal relation

$$g_{\mu\nu} = e^{-2\phi}\tilde{g}_{\mu\nu} - 2A_\mu A_\nu \sinh(2\phi). \tag{2.41}$$

The frames delineated by the metric fields $\tilde{g}_{\mu\nu}$ and $g_{\mu\nu}$ will be called *Einstein frame* and *matter frame*, respectively. The geometric part of the action is exactly the same as in GR:

$$S_g = \frac{1}{16\pi G}\int \tilde{g}^{\mu\nu}\tilde{R}_{\mu\nu}\sqrt{-\tilde{g}}d^4x, \tag{2.42}$$

where $\tilde{R}_{\mu\nu}$ is the Ricci tensor of $\tilde{g}_{\mu\nu}$ and $\tilde{g}$ the determinant of $\tilde{g}_{\mu\nu}$. Note that the TeVeS constant G must not be mistaken for the Newtonian gravitational constant G_N (see Sec. 2.2.2 B). The vector field's action S_v reads as follows:

$$S_v = -\frac{1}{32\pi G}\int \left[K_B F^{\mu\nu}F_{\mu\nu} - \lambda(A_\mu A^\mu + 1)\right]\sqrt{-\tilde{g}}d^4x, \tag{2.43}$$

with $F_{\mu\nu} = \tilde{\nabla}_\mu A_\nu - \tilde{\nabla}_\nu A_\mu$ and indices being raised and lowered with respect to $\tilde{g}_{\mu\nu}$, i.e. $A^\mu = \tilde{g}^{\mu\nu}A_\nu$. Here the constant K_B describes the coupling of the vector field to gravity and λ is a Lagrangian multiplier enforcing the normalization condition given by Eq. (2.40). Equation (2.43) corresponds to the classical Maxwell action, the field A_μ now having an effective mass. The action S_s of the scalar field ϕ involves an additional nondynamical scalar field σ_B, and takes the form

$$S_s = -\frac{1}{2}\int \left[\sigma_B^2 h^{\mu\nu}\tilde{\nabla}_\mu\phi\tilde{\nabla}_\nu\phi + \frac{G\sigma_B^4}{2l_B^2}F\left(k_B G\sigma_B^2\right)\right]\sqrt{-\tilde{g}}d^4x, \tag{2.44}$$

where $h^{\mu\nu} = \tilde{g}^{\mu\nu} - A^\mu A^\nu$ and F is an initially arbitrary function. Furthermore, there appear two new constants, k_B and l_B, where k_B is dimensionless and l_B corresponds to a length scale. As there is no kinetic term for σ_B, it is related to the invariant $h^{\mu\nu}\tilde{\nabla}_\mu\phi\tilde{\nabla}_\nu\phi$ and could in principle be eliminated from the action. This follows from the fact that the field equation obtained from variation of Eq.

(2.44) with respect to σ_B just corresponds to an algebraic relation between σ_B and derivatives of the field ϕ. From this point of view, the introduction of σ_B may simply be regarded as an auxiliary construction which allows one to write the scalar field action in a clearly arranged form. To get a better insight into the structure of the scalar field action, we follow the approach of Ref. [101] by introducing $\mu \equiv 8\pi G\sigma_B^2$ and

$$V(\mu) \equiv \frac{\mu^2}{16\pi l_B^2} F = \frac{4\pi G^2 \sigma_B^4}{l_B^2} F\left(k_B G\sigma_B^2\right), \tag{2.45}$$

where we absorb the constant k_B into the definition of $V(\mu)$. Using the above allows one may rewrite Eq. (2.44) as

$$S_s = -\frac{1}{16\pi G}\int \left[\mu h^{\mu\nu}\tilde{\nabla}_\mu\phi\tilde{\nabla}_\nu\phi + V(\mu)\right]\sqrt{-\tilde{g}}d^4x. \tag{2.46}$$

From Eq. (2.46), one identifies both a kinetic-like and a potential-like term and the action now resembles other popular scalar field constructions like, for example, k-essence models [102] which are based on noncanonical kinetic terms for the scalar field. In the following, however, we shall stick to the form of the scalar field action in Eq. (2.44). Note that whether TeVeS recovers the dynamics of MOND in the nonrelativistic limit depends on the actual choice of the potential V or equivalently F. In the next section, we will discuss this issue in more detail.

Finally, matter is required to obey the weak equivalence principle, and thus the matter action is given by

$$S_m = \int \mathcal{L}_m\left(g, \Upsilon^B, \nabla\Upsilon^B\right)\sqrt{-g}d^4x, \tag{2.47}$$

where Υ^B is a generic collection of matter fields. Note that world lines are by construction geodesics of the metric $g_{\mu\nu}$ rather than $\tilde{g}_{\mu\nu}$. As usual, the corresponding equations of motion can be derived by varying the total action $S = S_g + S_v + S_s + S_m$ with respect to the basic fields (see, e.g., Refs. [43, 101]). As already pointed out in Ref. [43], a requirement for obtaining Newton's law in the nonrelativistic high acceleration regime ($a \gg a_0$) is that k_B, $K_B \ll 1$ (also see Ref. [43] for a discussion on lower bounds of k). Therefore, TeVeS is kept close to GR in a sense that it will recover well-known features of GR, but there will be modifications induced by the other fields. Albeit not a unique extension, TeVeS is the most popular "MONDian representative" so far, and a variety of its aspects have been extensively studied in the literature (see Ref. [103] for a review). Although the original formulation of TeVeS suffers from several problems, e.g. in

the strong gravity regime [104, 105] or - at least for certain models - in the cosmological domain [89, 106], it still provides a viable description of relativistic MOND on extragalactic scales.

2.2.2 B The free function, quasistatic systems and relation to MOND

Following the lines of Ref. [43], the "equation of motion" for σ_B suggests the introduction of a new function $\mu_B(y)$ [5] which is implicitly given by

$$-\mu_B F(\mu_B) - \frac{1}{2}\mu_B^2 F'(\mu_B) = -\frac{1}{2}\left(\mu_B^2 F\right)' = k_B l_B^2 h^{\mu\nu}\tilde{\nabla}_\mu\phi\tilde{\nabla}_\nu\phi \equiv y, \tag{2.48}$$

with

$$k_B G\sigma_B^2 = \mu_B\left(k_B l_B^2 h^{\mu\nu}\tilde{\nabla}_\mu\phi\tilde{\nabla}_\nu\phi\right) = \mu_B(y). \tag{2.49}$$

Here the prime denotes the derivative with respect to μ_B, i.e. $F' \equiv dF/d\mu_B$. Whether or not TeVeS recovers the dynamics of MOND in the nonrelativistic limit depends on the assumed form of the function F which determines the properties of μ_B. Originally, Bekenstein made the choice

$$F = \frac{3}{8}\frac{\mu_B(4 + 2\mu_B - 4\mu_B^2 + \mu_B^3) + 2\log(1-\mu_B)^2}{\mu_B^2}, \tag{2.50}$$

which leads to

$$y = \frac{3}{4}\frac{\mu_B^2(\mu_B - 2)^2}{1-\mu_B}. \tag{2.51}$$

The function $y(\mu_B)$ is illustrated in Fig. 2.2. What are the essential features of this function? First of all, we note that quasistatic systems and cosmological situations will be characterized by $y > 0$ and $y < 0$, respectively. This directly follows from the definition of y in Eq. (2.48) and our sign convention for the metric. Next we need to specify the physically relevant branches of $y(\mu_B)$ if we require the function to be single-valued, thus avoiding the problem of ambiguity in the theory. Let us begin by considering the situation of quasistatic systems ($y > 0$). The denominator in Eq. (2.51) ensures that $y \to \infty$ when μ_B approaches unity, which, as will become clear shortly, is responsible for TeVeS to have a Newtonian limit. In Eq. (2.51), this behavior is realized by a simple pole at $\mu_B = 1$, but one may also construct different expressions for F (and thus y) which lead to a singularity of higher order at this point. Likewise, the behavior for small values of y, i.e. $y \approx 3\mu_B^2$ for $0 < y \ll 1$, forces the MONDian limit to be contained in the theory. For $y > 0$, we therefore choose the branch covering the range $0 < \mu_B < 1$ as the physical one. Considering cosmological

[5] Note that we could also use the previously defined field μ which is related to $\mu_B(y)$ through $\mu_B(y) = (k/8\pi)\mu$. In the following, however, we shall stick to the original notation of Ref. [43].

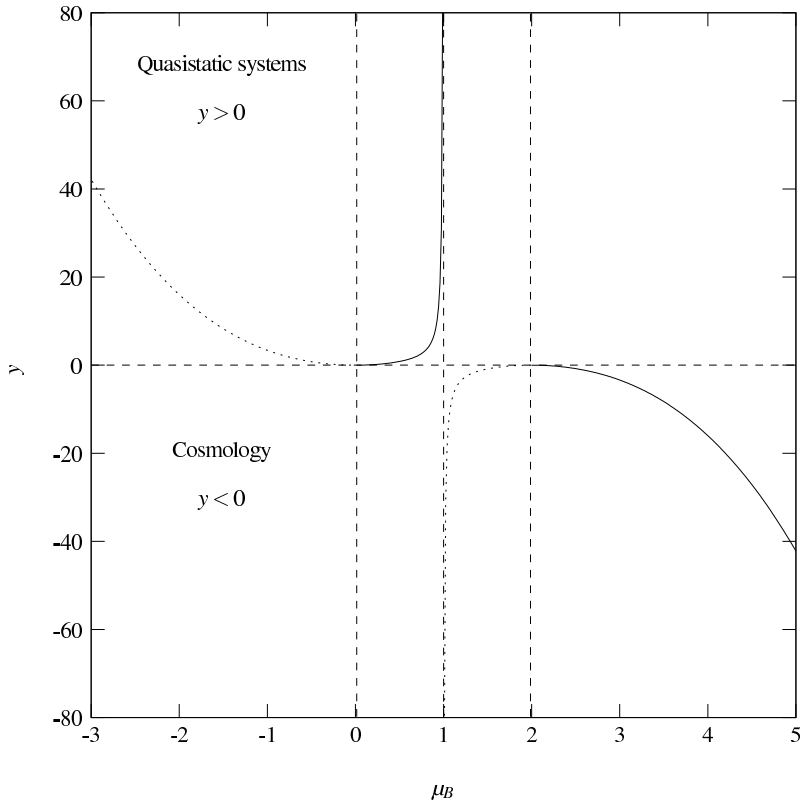

Figure 2.2: Illustration of the free function $y(\mu_B)$ given by Eq. (2.51): Shown are the regimes for quasistatic systems ($y > 0$) and cosmology ($y < 0$). Our choice of the physical branches of $y(\mu_B)$ is denoted by solid lines, branches without any physical relevance by dotted lines.

situations ($y < 0$), we have to make a similar choice. As can be seen from Fig. 2.2, one branch ranges from $\mu_B = 1$ to the extremum at $\mu_B = 2$ while the other one ranges from the extremum to infinity. It can be shown that the energy density contributed by the cosmological scalar field depends on the slope of a particularly chosen branch [43]. For the monotonically increasing branch ($1 < \mu_B < 2$), this contribution will be strictly negative whereas it will be strictly positive for the monotonically decreasing one ($2 < \mu_B < \infty$). In accordance with previous work, we shall exclude such negative contributions to the energy density and thus define the decreasing branch as the physical one (see Sec. 2.2.2 C). This is also the reason for the factor $(\mu_B - 2)^2$ in Eq. (2.51) which ensures the existence of a monotonically decreasing branch covering the whole range $y \in [0, -\infty)$. Note, however, that a negative energy contribution of the scalar field does not necessarily violate the requirement of a positive overall energy density [43] and could provide an interesting scenario for future studies.

To obtain the theory's nonrelativistic limit, one may apply the usual approximations for weak fields and quasistatic systems. In this case, one has $y > 0$, and therefore $0 < \mu_B < 1$ in accordance

with our assumptions. Using that also $F < 0$ for the given range, the resulting metric $g_{\mu\nu}$ turns out to be identical to the metric obtained in GR if the nonrelativistic gravitational potential Φ (cf. Sec. 2.1.1) is replaced by

$$\Phi = \Xi\Phi_N + \phi \equiv \Phi_{\text{tot}}, \tag{2.52}$$

where

$$\Xi = e^{-2\phi_C}\,(1 + K_B/2)^{-1}\,. \tag{2.53}$$

The quantity ϕ_C is the cosmological value of the scalar field ϕ at the time the system in question breaks away from the cosmological expansion and Φ_N is the Newtonian potential generated by the matter density ρ [6]. In this approximation, it is consistent to assume that A_μ is pointing into the direction of the timelike Killing vector associated with the static spacetime. Then we have

$$h^{\mu\nu}\tilde{\nabla}_\mu\phi\tilde{\nabla}_\nu\phi \to (\boldsymbol{\nabla}\phi)^2 \equiv \|\boldsymbol{\nabla}\phi\|_2^2 \tag{2.54}$$

and the equation of the scalar field reduces to

$$\boldsymbol{\nabla}\cdot\left(\mu_B\left(k_B l_B^2(\boldsymbol{\nabla}\phi)^2\right)\boldsymbol{\nabla}\phi\right) = k_B G\rho. \tag{2.55}$$

As has been shown in Ref. [43], Eqs. (2.52) and (2.55) correspond to the MOND paradigm: If $\mu_B \to 1$ (corresponding to $|\boldsymbol{\nabla}\phi| \to \infty$), the theory reaches its (exact) Newtonian limit, and the measured gravitational constant G_N is given by

$$G_N = \left(\frac{e^{-2\phi_C}}{1 + K_B/2} + \frac{k_B}{4\pi}\right)G. \tag{2.56}$$

Similarly, the theory reaches its MONDian limit as $\mu_B \to 0$ and the acceleration constant a_0 can be defined in terms of the TeVeS parameters,

$$a_0 \equiv e^{2\phi_C}\frac{\sqrt{3k_B}}{4\pi l_B}(1 + K_B/2). \tag{2.57}$$

As can be seen from above, a_0 depends on ϕ_C and may therefore, in principal, change with time. For viable cosmological models (see Sect. 2.2.2 C), however, such changes are expected to be basically imperceptible [107]. Moreover, we will see that it is also viable to assume $|\phi_C| \ll 1$ and together with k_B, $K_B \ll 1$ this yields $G \approx G_N$. Thus we will assume that $G = G_N$ and $\Xi = 1$

[6] Note that for $\phi_C \neq 0$, $g_{\mu\nu}$ does not asymptotically correspond to a Minkowski metric. As already remarked in Ref. [43], however, this is easily remedied by an appropriate rescaling of coordinates.

throughout this thesis when working within the quasistatic approximation.

As is obvious from the above, the TeVeS function μ_B plays a similar role as the MOND interpolating function $\tilde{\mu}$ from Sec. 2.2.1 and the resulting dynamics is characterized by its asymptotic behavior. More generally, it turns out that one needs only the requirement $y \propto \mu_B^2$ for $y \ll 1$ to guarantee a MONDian limit in TeVeS because the proportionality constant may always be absorbed into the definition of a_0 [50]. Unlike $\tilde{\mu}$, however, the function μ_B does not depend on the gradient of the nonrelativistic potential, but on $\boldsymbol{\nabla}\phi$. This means that there is generally no direct correspondence between the two except for symmetric configurations which require the aforementioned gradients to be parallel (cf. Sec. 3.4). For an appropriate choice of μ_B, such configurations further allow one to express the total nonrelativistic potential in particularly simple form. To see this, we follow the lines of Ref. [92] and redefine μ_B and y in terms of two new functions, μ_s and δ_ϕ, according to

$$\frac{\mu_s}{1-\mu_s} \equiv \frac{4\pi}{k_B}\left(1-\frac{K_B}{2}\right)^{-1}\mu_B \tag{2.58}$$

and

$$\delta_\phi^2 \equiv \left(\frac{4\pi}{k_B}\left(1-\frac{K_B}{2}\right)\right)^2 \frac{y}{b_s}, \tag{2.59}$$

where b_s is defined as the value of y/μ_B^2 in the limit $y \to 0$. Using Eq. (2.51), we have $b_s = 3$ and a bit of algebra reveals the relation

$$\delta_\phi^2 = \frac{\mu_s^2}{(1-\mu_s)^2}\frac{\left(1-\frac{k_B}{8\pi}\left(1-\frac{K_B}{2}\right)\frac{\mu_s}{1-\mu_s}\right)^2}{\left(1-\frac{k_B}{4\pi}\left(1-\frac{K_B}{2}\right)\frac{\mu_s}{1-\mu_s}\right)}. \tag{2.60}$$

Since k_B and K_B are much smaller than unity, we take the limit k_B, $K_B \to 0$ and obtain

$$\delta_\phi^2 = \frac{\mu_s^2}{(1-\mu_s)^2}, \quad \mu_s^2 = \frac{\delta_\phi^2}{(1+\delta_\phi)^2}. \tag{2.61}$$

Note that this implicitly defines a new μ_B which will be close to the one given in Eq. (2.51). Next, we substitute μ_B for μ_s in Eq. (2.55). Restricting ourselves to spherically or cylindrically symmetric systems, it then follows from Gauss' theorem that

$$\boldsymbol{\nabla}\phi = \frac{1-\mu_s}{\mu_s}\boldsymbol{\nabla}\Phi_N. \tag{2.62}$$

Using Eq. (2.54) together with the definition of a_0 in Eq. (2.59), we also find

$$\delta_\phi^2 = \frac{(\boldsymbol{\nabla}\phi)^2}{a_0^2}. \tag{2.63}$$

Combining the above relations, one finally arrives at

$$|\boldsymbol{\nabla}\phi| = \sqrt{a_0|\boldsymbol{\nabla}\Phi_N|}, \tag{2.64}$$

which allows one to express the gradient of the total nonrelativistic potential in terms of $\boldsymbol{\nabla}\Phi_N$. As we shall see, the choice of Eq. (2.61) and the corresponding resulting relations will be extremely useful for analytic studies of the quasistatic limit in TeVeS (cf. Sec. 3).

2.2.2 C Modified FRW cosmology

Similar to the case of GR, it is possible to derive a cosmological model in TeVeS. Imposing the usual assumptions of an isotropic and homogeneous spacetime, both $g_{\mu\nu}$ and $\tilde{g}_{\mu\nu}$ are given by FRW metrics with scale factors a and $b = ae^{\phi}$, respectively. For a flat universe ($K = 0$), the analog of the Friedmann equation then reads [43, 101]

$$3\frac{\dot{b}^2}{b^2} = 8\pi G a^2 e^{-4\phi}\left(\rho_\phi + \rho\right) \tag{2.65}$$

while the equation governing the evolution of the density ρ remains the same as in GR (see Sec. 2.1.2). Here the overdot denotes the derivative with respect to the conformal time coordinate in the matter frame and ρ_ϕ is the energy density of the scalar field,

$$\rho_\phi = \frac{\mu_B e^{2\phi}}{4k_B^2 l_B^2 G}\left(\mu_B F - 2y\right). \tag{2.66}$$

For cosmological models in TeVeS, we have the condition $y < 0$. Requiring that the function μ_B is single-valued, one is free to choose between two possible potential branches given the form of F in Eq. (2.50). One branch ranges from $\mu_B = 1$ to the extremum at $\mu_B = 2$ while the other one ranges from the extremum to infinity. In accordance with previous work, we define the latter possibility as the physical one.

To find solutions for the evolution of the scale factors a and b, one additionally needs to consider the equation of motion for the scalar field ϕ (see Sec. 4.3) which leads to a closed system of equations. For Eq. (2.50) and more general classes of the potential, it has been shown

that the cosmological scalar field evolves slowly in time and that its absolute value is much less than unity throughout cosmological history [43, 96]. Therefore, its contribution to the Hubble expansion is negligibly small, with a ratio of $\mathcal{O}(k)$ compared to the contribution of other matter fields. Setting $\rho_\phi = 0$ and using that $|\phi| \ll 1$ at the background level, the Hubble parameter in the matter frame takes the form of Eq. (2.22) with $K = 0$ and the background evolution in TeVeS becomes structurally identical with that of a standard ΛCDM model [7]. While this approximation will suffice in many cases, a more detailed treatment of the cosmological background will become necessary when dealing with the growth of TeVeS metric perturbations in Sec. 4.3.

2.2.3 Aether-type theories and beyond

Despite its explicit bimetric construction, TeVeS may be written in pure tensor-vector form [108] and provides a particular example for an Aether-type theory [82] whose action involves a four-vector field A_α and is of the general form

$$S = \int d^4x \sqrt{-g}\left[\frac{R}{16\pi G} + \mathcal{L}(g, A)\right] + S_m, \tag{2.67}$$

where $\mathcal{L}$ is constructed to be generally covariant and local while S_m couples only to the metric and not to A_α. If we require the Lagrangian to depend on covariant derivatives of A_α only and the field A_α to be both timelike and of unit norm, the theory may be written in the form

$$\mathcal{L}(g, A^\alpha) = M^2\mathcal{F}(\mathcal{K}) + \lambda(A^\alpha A_\alpha + 1), \tag{2.68}$$

where

$$\begin{aligned} \mathcal{K} &= M^{-2}\mathcal{K}^{\alpha\beta}{}_{\gamma\sigma}\nabla_\alpha A^\gamma \nabla_\beta A^\sigma, \\ \mathcal{K}^{\alpha\beta}{}_{\gamma\sigma} &= c_1 g^{\alpha\beta} g_{\gamma\sigma} + c_2 \delta^\alpha_\gamma \delta^\beta_\sigma + c_3 \delta^\alpha_\sigma \delta^\beta_\gamma \end{aligned} \tag{2.69}$$

and the c_i are dimensionless constants. Here M is a constant with the dimension of mass (in natural units) and λ is a Lagrange multiplier, enforcing the unit-timelike condition for A_α. Given the form in Eqs. (2.68) and (2.69), the Aether action includes all generally covariant terms with two derivatives (without total divergences). The particular form of $\mathcal{F}(\mathcal{K})$ is principally unconstrained and one may also construct more complicated expressions for $\mathcal{K}$ than specified in Eq. (2.69),

[7] Note that this "identity" does not apply to the matter content of the universe since we assume that there is no CDM in TeVeS. In Sec. 3, we shall address this issue and its implications in more detail and comment on viable cosmological models in such a framework.

including higher-order terms of the field A_α and its derivatives. Indeed, the framework of TeVeS does correspond to a theory with such an extended $\mathcal{K}$. Therefore, Aether theory can be regarded as generalized formulation of the Einstein-Aether framework [109].

A basic feature of these theories is the violation of local Lorentz invariance (and thus also gauge invariance) which is a consequence of the Aether field's non-vanishing expectation value. In other words, the Aether field dynamically selects a preferred frame at each point of spacetime which is given in terms of a distinct spacetime foliation defined by A_α. Traditionally, formulations of this type have been designed as possible effective field theories and are used as phenomenological probes of Lorentz-violating effects in quantum gravity. In the context of more fundamental theories like, for instance, string theory or M-theory, such effects are expected to generically occur via spontaneous symmetry breaking at some early stage of the universe (see, e.g., Refs. [110, 111]). Nevertheless, it is still unknown whether constructions of this type exist as quantum field theories or whether they can be derived from first principles using field theoretical methods. Employing different approaches like classical tests of gravitation in the strong field limit [112, 113] or the analysis of cosmological observations, one ultimately hopes to detect intrinsic signatures pointing towards the existence of Lorentz-violation or to falsify this class of theories. In any case, this will likely help to constrain theoretical gravity models in the high-energy sector. Note that this gives phenomenological models like TeVeS, which has been designed from empirical evidence only, a more fundamental motivation and encourages one to explore such frameworks in more detail. Of course, effective descriptions like Eq. (2.67) are not the most general models one can think of and there exist many others like, for instance, generalized TeVeS [85], scalar-Aether inflation models [114] or the generalized dark fluid theory [115, 116].

2.3 Dynamical dark energy models

Assuming that CDM exists and accounts for the missing matter content in the universe, one still has to face the problem of what is driving the accelerated expansion of the universe. In this section, we shall present a selection of phenomenological DE models which involve a scalar field and promote DE to a dynamical quantity with generally time-dependent EoS.

2.3.1 Quintessence

The effects of dynamical DE on the background expansion are fully described by its generally time-dependent EoS. If DE does not correspond to the cosmological constant, i.e. $w_{\rm de} \neq -1$, its

interpretation as vacuum energy becomes unviable and one has to think of something else. Current observational constraints give $-1.34 < w_{\rm de} < -0.79$ (assuming $w = \text{const}$) and $dw_{\rm de}/dz = 1.0^{+1.0}_{-0.8}$ for a possible variation (assuming a simple parametrization) [117]. More recently, it was possible to improve these limits by combining different distance indicators [118], giving $w_{\rm de} = -0.96 \pm 0.08$ or $w_{\rm de} = -0.87 \pm 0.1$ (depending on the data set of supernova observations) for DE with constant EoS. Although a cosmological constant provides a good fit to the available data, it still allows one to have more general models for DE, including the so-called phantom DE models with $w_{\rm de} < -1$.

The most popular candidate for dynamical DE is a light scalar field [119, 120] which is generically called quintessence. Its action takes the form of a minimally coupled, self-interacting scalar field with canonical kinetic term,

$$S_\phi = -\int d^4x\,\sqrt{-g}\left[\frac{1}{2}g^{\mu\nu}\nabla_\mu\phi\nabla_\nu\phi + V(\phi)\right], \tag{2.70}$$

which yields its contribution to the cosmological energy density and pressure as

$$\rho_\phi = \frac{1}{2a^2}\dot{\phi}^2 + V(\phi) \tag{2.71}$$

and

$$P_\phi = \frac{1}{2a^2}\dot{\phi}^2 - V(\phi), \tag{2.72}$$

respectively. Under slow-rolling conditions, i.e. conditions where the kinetic term is much smaller than the potential energy, i.e. $V(\phi) \gg a^{-2}\dot{\phi}^2/2$ the scalar field's EoS turns negative with $w_\phi \approx -1$, thus mimicking the behavior of a cosmological constant. Again, quintessence should be regarded as effective phenomenological description of physics rooted within more fundamental theoretical frameworks. For example, the occurrence of such scalar fields is commonly predicted in supersymmetric field theories and string theory.

Quintessence models may be classified in terms of the assumed potential shape. In accordance with today's observations, the scalar field must be situated in a sufficiently flat region of its potential for the slow roll condition to apply. Further constraints on viable potentials can be obtained if one requires the field to exhibit a so-called tracking behavior, implying the existence of an attractor solution which is reached for a wide range of different initial conditions and thus avoiding fine-tuning issues. During tracking, the evolution of the scalar's energy density will be determined by the evolution of the background fluid, i.e. $w_\phi = w_\phi(w_B)$, where w_B denotes the

EoS of the background fluid. For exponential potentials $V(\phi) \sim e^{\lambda\phi}$ which naturally appear in high-energy physics, however, it has been found that this tracking is exact, meaning $w_\phi = w_B$. Therefore, exponential models are either fine-tuned or their impact on the cosmological expansion is indistinguishable from the background, suggesting that $w_{\rm de} = 0$. This has motivated a variety of different plausible scenarios for such scalar fields, ranging from potential modifications as in power-law models or Planck-scale quintessence [121] to more complicated constructions such as general k-essence (phantom DE models) [99] or extended quintessence [122]. Finally, note these dynamical DE models will generally exhibit clustering properties (similar to ordinary matter fluids) which will have an impact on the formation of structure. Independent of the background evolution, this offers additional ways of constraining the viability of such DE proposals (cf. Sec. 4.2).

2.3.2 Chameleon fields

In the last section, we have discussed quintessence models as a possible candidate for DE. In order to explain the cosmological expansion of the universe, these scalar fields must currently have a mass [8] on the order of the Hubble expansion H_0 (in Heaviside units), thus leading to the situation of an essentially massless scalar on solar system scales. From the high-energy physics point of view, however, it is commonly expected that such scalar fields should also couple to matter, leading to an additional force acting on matter particles. In this case, however, experimental tests of the equivalence principle [112] would constrain this coupling to be unnaturally small due to the field's low effective mass. An interesting approach to avoid this problem is given in terms of the chameleon mechanism [123, 124] where one allows the self-interacting scalar field ϕ to also have a strong coupling to matter. The key input here is that the dynamics of ϕ is no longer governed by its potential $V(\phi)$, but instead by an effective potential which takes the general form

$$V_{\rm eff} = V(\phi) - C(\phi)\mathcal{L}_m, \tag{2.73}$$

where $C(\phi)$ denotes the coupling to matter and $V(\phi)$ is typically assumed to be of runaway form, i.e. a monotonically decreasing function satisfying $V \to \infty$ for $\phi \to 0$ and $V \to 0$ for $\phi \to \infty$, which is generically predicted for non-perturbative potentials in string theory. Assuming a species

[8] The presence of a self-interaction potential for the scalar field allows to introduce the notion of an effective mass in analogy to the mass term appearing in the action of the relativistic Klein-Gordon field.

of nonrelativistic matter particles with density ρ_m, Eq. (2.73) may approximately be written as

$$V_{\rm eff} = V(\phi) + C(\phi)\rho_m. \tag{2.74}$$

If $C(\phi)$ is chosen to be of exponential form (cf. Sec. 2.3.1), i.e. a monotonically increasing function of ϕ, $V_{\rm eff}$ exhibits a minimum $\phi_{\rm min}$ and an effective mass $m_{\rm eff}$, usually defined by the Taylor expansion around the minimum,

$$V_\phi \approx V(\phi_{\rm min}) + \frac{m_{\rm eff}}{2}(\phi - \phi_{\rm min})^2, \tag{2.75}$$

which are determined by the local matter density. For the given construction, it turns out that $\phi_{\rm min}$ and $m_{\rm eff}$ are then decreasing and increasing functions of ρ_m, respectively, meaning that if the matter density is low (cosmological situations), $m_{\rm eff}$ becomes small and the scalar field may act as dynamical DE. On the other hand, if ρ_m is very large (e.g., in the solar system), so is $m_{\rm eff}$ and the scalar force is significantly suppressed, thus being able to evade experimental detection. Therefore, models of this kind are called chameleon fields. Also note that such coupled scalar field models are mathematically equivalent to the framework of $f(R)$ gravity, which can be shown by performing an appropriate conformal transformation to the Jordan frame [9].

To completely evade the constraints from solar system tests of gravity, one may also consider models where the scalar field only couples to CDM particles. This idea has recently gained a lot of interest because the physics of CDM are unknown and such a coupling could alleviate the coincidence problem of DE [125, 126]. Typically, these coupled scalar field models yield a background evolution which is virtually indistinguishable from a standard ΛCDM cosmology and one has to look out for other potentially observable discriminators. An interesting approach into this direction is to consider the nonlinear clustering of density perturbations in this context. In Sec. 4.2, we shall investigate the impact of such scalars on the matter power spectrum and discuss the prospects of observing characteristic signatures, choosing the particular coupled scalar field model of Ref. [127]

[9] Given a scalar-tensor theory and using an appropriate conformal transformation of the metric tensor, it is possible to express the Lagrangian in the *Einstein frame*, in which the Ricci scalar enters in the form of the usual Einstein-Hilbert action, or in the *Jordan frame* where the Ricci scalar is multiplied by the scalar field or a function thereof. For the models we consider here, the non-minimal coupling to matter vanishes in the Jordan frame and the Lagrangian takes the form of a particular (nonlinear) $f(R)$ gravity theory.

Chapter 3

Gravitational lensing in relativistic formulations of MOND

With the advent of fully relativistic theories for the MOND paradigm, it has become possible to extend the analysis of such modifications beyond the field of galactic dynamics. It is clear that any theory trying to get along without CDM ultimately needs to face observations and a powerful tool to challenge these models is gravitational lensing. Adopting the framework of TeVeS, we will begin with a brief introduction to its basics, discuss relevant details on the cosmological background and present several applications thereafter.

3.1 Gravitational lensing in a nutshell

3.1.1 Light deflection in slightly curved spacetime

For any metric theory, the propagation of light rays is generally determined by the null geodesics of the metric $g_{\mu\nu}$ (assuming that this is the metric matter fields couple to), i.e

$$g_{\mu\nu}\frac{dx^\mu}{d\lambda}\frac{dx^\nu}{d\lambda} = 0, \tag{3.1}$$

where λ is some suitable affine parameter for the light ray. In general, finding solutions for Eq. (3.1) is a very complicated problem. However, in the limit of weak fields and quasi-static systems, i.e. if the metric potential given by Eq. (2.52) and the peculiar velocity v of the lens are small ($\Phi,\ v \ll 1$), one can presume a locally flat spacetime which is only disturbed close to inhomogeneities acting as gravitational lenses; these conditions are typically well satisfied for galaxies

and galaxy clusters. In this case, the line element approximately takes the form [1]

$$ds^2 = -(1+2\Phi)dt^2 + (1-2\Phi)\delta_{ij}dx^i dx^j. \tag{3.2}$$

Since light rays obey Eq. (3.1), we have $ds = 0$, which allows one to express the refractive index n, i.e. the ratio between the speed of light in the vacuum and that in the gravitational field as ($\Phi \ll 1$)

$$n = \sqrt{\frac{1-2\Phi}{1+2\Phi}} \approx 1 - 2\Phi. \tag{3.3}$$

Note that the gravitational potential is attractive, i.e. $\Phi \leq 0$, leading to $n \geq 1$ and therefore to a slower light propagation in the gravitational field than in the vacuum. Next, we consider the light travel time between two points A and B which is given by the expression

$$\Delta t_{AB} = \int_A^B n[\mathbf{x}(l)]dl, \tag{3.4}$$

where $\mathbf{x}(l)$ denotes the light path. According to Fermat's principle, light rays traverse the path between two points which takes the least time. Therefore, we need to find the light path which minimizes Eq. (3.4). Clearly, this is a standard variational problem which leads to the well-known Euler-Lagrange equations. Introducing the curve parameter λ and defining $\dot{x}^i \equiv dx^i/d\lambda$, we have

$$dl = \sqrt{\delta_{ij}\dot{x}^i\dot{x}^j}d\lambda \equiv |\dot{\mathbf{x}}|\, d\lambda \tag{3.5}$$

the variational problem can be written as

$$\delta \int_{\lambda_A}^{\lambda_B} L\left(\mathbf{x}, \dot{\mathbf{x}}, \lambda\right) d\lambda \equiv \delta \int_{\lambda_A}^{\lambda_B} n[\mathbf{x}(\lambda)]\, |\dot{\mathbf{x}}|\, d\lambda = 0. \tag{3.6}$$

From the corresponding Euler-Lagrange equations,

$$\frac{d}{d\lambda}\frac{\partial L}{\partial \dot{x}^i} - \frac{\partial L}{\partial x^i} = 0, \tag{3.7}$$

[1] Note that a more rigorous treatment should consider perturbations around a FRW spacetime in which the potentials in the time-time and space-space components of the metric tensor are not necessarily the same. In TeVeS, for instance, such a difference may be induced by both anisotropic stress of the matter fluid and the growth of vector perturbations. We shall further comment on this at a later point in the thesis.

it then immediately follows that

$$\frac{d}{d\lambda}\left(n\frac{\dot{\mathbf{x}}}{|\dot{\mathbf{x}}|}\right) - |\dot{\mathbf{x}}|\,\boldsymbol{\nabla} n = 0. \tag{3.8}$$

Evidently, $\dot{\mathbf{x}}$ is a tangent vector to the light path, which we can assume to be normalized by a suitable choice for the curve parameter λ. We thus set $|\dot{\mathbf{x}}| = 1$ and write $\mathbf{e} \equiv \dot{\mathbf{x}}$ for the unit tangent vector to the light path. Then Eq. (3.8) takes the form

$$n\dot{\mathbf{e}} = \boldsymbol{\nabla} n - (\mathbf{e}\cdot\boldsymbol{\nabla} n)\,\mathbf{e}. \tag{3.9}$$

As the second term on the right-hand side of Eq. (3.9) is the derivative along the light path, the whole right-hand side corresponds to $\boldsymbol{\nabla}_\perp n$, the gradient of n perpendicular to the direction of light propagation, and we finally arrive at

$$\dot{\mathbf{e}} = \frac{1}{n}\boldsymbol{\nabla}_\perp n = \boldsymbol{\nabla}_\perp \log n \approx -2\boldsymbol{\nabla}_\perp \Phi, \tag{3.10}$$

where we have again used that $\Phi \ll 1$. The deflection angle can now be obtained by integrating $-\dot{\mathbf{e}}$ along the light path, i.e.

$$\hat{\boldsymbol{\alpha}} = 2\int_{\lambda_A}^{\lambda_B} \boldsymbol{\nabla}_\perp \Phi\, d\lambda. \tag{3.11}$$

Given our present assumptions, the deflection of light rays will typically be very small. In this case, we may apply Born's approximation and integrate along the unperturbed light path. Identifying Φ with the Newtonian potential Φ_N and assuming that the unperturbed light rays propagate along the z-axis, the total deflection angle in GR finally reads

$$\hat{\boldsymbol{\alpha}}_{\mathrm{GR}} = 2\int_{-\infty}^{\infty} \boldsymbol{\nabla}_\perp \Phi\, dz. \tag{3.12}$$

Because all of the above is based on the metric approach in Eq. (3.2), our results may directly be transferred to the framework of TeVeS. Using Eq. (2.52), the deflection angle of a light ray in TeVeS under the given assumptions can therefore be expressed as [2]

$$\hat{\boldsymbol{\alpha}} = 2\int_{-\infty}^{\infty} \boldsymbol{\nabla}_\perp \Phi_{\mathrm{tot}}\, dl = \hat{\boldsymbol{\alpha}}_{\mathrm{GR}} + 2\int_{-\infty}^{\infty} \boldsymbol{\nabla}_\perp \phi\, dl, \tag{3.13}$$

[2] As previously mentioned in Sec. 2.2.2 B, we assume that $\Xi = 1$ and $G = G_N$ in the context of quasi-static systems.

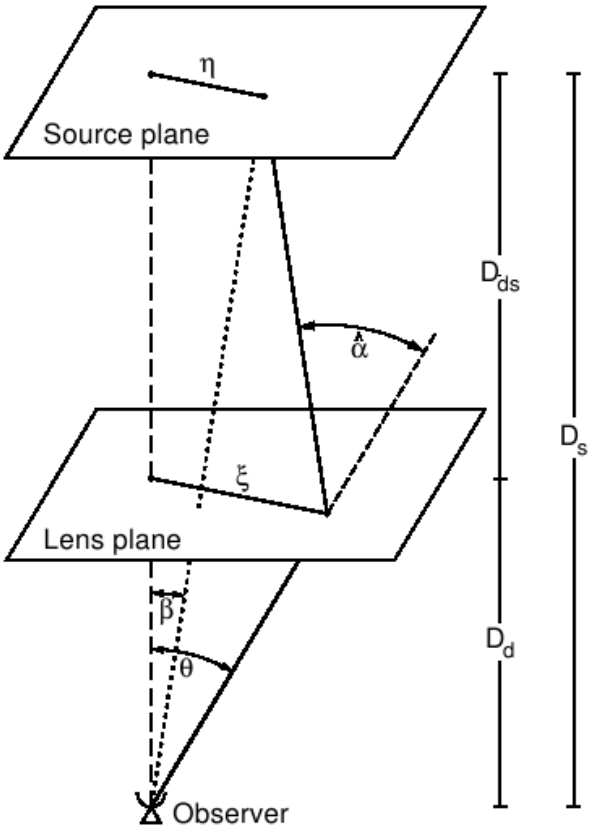

Figure 3.1: Illustration of a gravitational lens system. The distances between source and observer, lens and observer, and lens and source are D_s, D_d, and D_{ds}, respectively (the figure is taken from Ref. [128]).

In addition to the deflection angle caused by the Newtonian potential Φ_N, there is a contribution arising from the scalar field ϕ. Compared to the distances between lens and source and observer and source, however, we may still assume that most of the bending occurs within a small range around the lens [43, 50]. Assuming that the nonrelativistic metric potential Φ_{tot} is known from solving the corresponding field equations, one can therefore directly proceed to calculate the usual lensing quantities, fully adopting the standard GR formalism which is briefly reviewed in the following section.

3.1.2 Lensing formalism

The effects of gravitational lensing can mathematically be described as a mapping in a two-dimensional space. Given the assumptions introduced in the last section, Fig. 3.1 shows a typical gravitational lens system. As one may directly read off the figure, the mapping of light rays from

the source to the lens plane takes the form [128, 129]

$$\boldsymbol{\eta} = \frac{D_s}{D_d}\boldsymbol{\xi} - D_{ds}\hat{\boldsymbol{\alpha}}(\boldsymbol{\xi}), \tag{3.14}$$

where $\boldsymbol{\xi}$ denotes the two-dimensional position vector in the lens plane, $\boldsymbol{\eta}$ is the two-dimensional position vector in the source plane and D_s, D_d, and D_{ds} are the (angular diameter) distances between source and observer, lens and observer, and lens and source, respectively. Introducing angular coordinates by $\boldsymbol{\beta} \equiv \boldsymbol{\eta}/D_s$ and $\boldsymbol{\theta} \equiv \boldsymbol{\xi}/D_d$, Eq. (3.14) may be rewritten in terms of dimensionless quantities,

$$\boldsymbol{\beta} = \boldsymbol{\theta} - \frac{D_{ds}}{D_s}\hat{\boldsymbol{\alpha}}(D_d\boldsymbol{\theta}) = \boldsymbol{\theta} - \boldsymbol{\alpha}(\boldsymbol{\theta}), \tag{3.15}$$

where we have used the definition of the scaled deflection angle $\boldsymbol{\alpha} \equiv D_{ds}\hat{\boldsymbol{\alpha}}/D_s$. The relation in Eq. (3.15) is called the lens equation and determines the angular position $\boldsymbol{\theta}$ of the image for a given source position $\boldsymbol{\beta}$. If there is more than one solution for a fixed value of $\boldsymbol{\beta}$, the lens produces multiple images. Furthermore, it is convenient to introduce the deflection potential $\Psi(\boldsymbol{\theta})$:

$$\Psi(\boldsymbol{\theta}) = 2\frac{D_{ds}}{D_s D_d}\int \Phi_{\mathrm{tot}}(D_d\boldsymbol{\theta}, z)dz, \tag{3.16}$$

where we have chosen coordinates such that unperturbed light rays propagate parallel to the z axis. Since light rays are deflected differentially, shapes of images and sources will differ from each other. If a source is much smaller than the angular scale on which the lens properties change, the lens mapping can locally be linearized. Thus, the distortion of an image can be described by the Jacobian matrix

$$\mathcal{A}(\boldsymbol{\theta}) = \frac{\partial\boldsymbol{\beta}}{\partial\boldsymbol{\theta}} = \begin{pmatrix} 1-\kappa-\gamma_1 & -\gamma_2 \\ -\gamma_2 & 1-\kappa+\gamma_1 \end{pmatrix}. \tag{3.17}$$

The convergence κ is directly related to the deflection potential Ψ through

$$\kappa = \frac{1}{2}\Delta_{\boldsymbol{\theta}}\Psi = \frac{1}{2}\left(\frac{\partial^2\Psi}{\partial\theta_1^2} + \frac{\partial^2\Psi}{\partial\theta_2^2}\right) \tag{3.18}$$

and the shear components γ_1 and γ_2 are given by

$$\gamma_1 = \frac{1}{2}\left(\frac{\partial^2\Psi}{\partial\theta_1^2} - \frac{\partial^2\Psi}{\partial\theta_2^2}\right), \quad \gamma_2 = \frac{\partial^2\Psi}{\partial\theta_1\partial\theta_2}, \quad \gamma = \sqrt{\gamma_1^2+\gamma_2^2}. \tag{3.19}$$

As there is no absorption or emission of photons in gravitational lensing, Liouville's theorem implies that lensing conserves surface brightness, i.e. if $I^{(s)}(\boldsymbol{\beta})$ is the surface brightness distribution

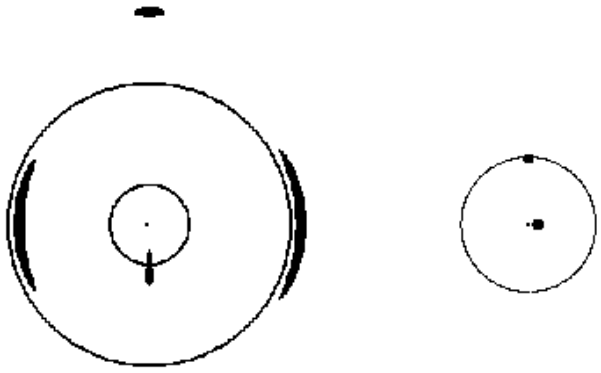

Figure 3.2: Imaging of an extended source by a non-singular circularly symmetric lens (the figure is taken from Ref. [128]): Closed curves in the lens plane (*left*) are denoted as *critical curves*, those in the source plane (*right*) as *caustics*. Because of their image properties, the outer and inner critical curves are called *tangential* and *radial*, respectively.

in the source plane, the observed surface brightness distribution in the lens plane is

$$I(\boldsymbol{\theta}) = I^{(s)}\left(\boldsymbol{\beta}(\boldsymbol{\theta})\right). \tag{3.20}$$

The fluxes observed from image and unlensed source can be calculated by integrating over the corresponding brightness distributions and their ratio is defined as the magnification which is given as the inverse of the Jacobi determinant,

$$\det \mathcal{A} = (1-\kappa-\gamma)(1-\kappa+\gamma). \tag{3.21}$$

While the convergence causes an isotropic focusing of light bundles, the shear, acting anisotropically within the lens mapping, causes changes in both shape and size of the image. Points in the lens plane where

$$\det \mathcal{A} = 0, \tag{3.22}$$

form closed curves, the *critical curves*. Their corresponding image curves residing in the source plane are called *caustics*. Because of Eq. (3.22), sources on caustics should be magnified by an infinitely large factor. Since every astrophysical source is extended, however, its magnification remains finite. An infinitely large magnification simply does not occur in reality. Nevertheless, images near critical curves can be significantly magnified and distorted, which, for instance, is indicated by the giant luminous arcs formed from source galaxies near caustics. Knowledge about the exact shape and location of these curves already allows one to make solid statements about

the system's matter distribution. In Fig. 3.2, the mapping of an extended source is demonstrated for a non-singular circularly symmetric lens. A source close to the point caustic at the lens center produces two tangentially oriented arcs close to the outer critical curve and a faint image at the lens center. A source on the outer caustic produces a radially elongated image on the inner critical curve and a tangentially oriented image outside the outer critical curve. Due to these image properties, the outer and inner critical curve are denoted as *tangential* and *radial*, respectively.

In addition to the lens mapping, the deflection by the gravitational potential also causes a time delay for light rays traveling from a source to an observer. This can be understood from the fact that the path of a photon traveling in a curved geometry is longer than in a flat one. Assuming an observer at redshift $z = 0$, the traveling time of light rays can be expressed as

$$t(\boldsymbol{\theta}) = \frac{1+z_l}{D}\left[\frac{1}{2}(\boldsymbol{\theta}-\boldsymbol{\beta})^2 - \Psi(\boldsymbol{\theta})\right], \tag{3.23}$$

where z_l is the redshift of the lens and $D \equiv D_{ds}/(D_s D_d)$. If the deflection potential is known, Eq. (3.23) allows to calculate the relative time delay between different images.

Considering lensing in the framework of TeVeS, we also need to specify the form of the free function μ_B. Unless we use the simplistic form of the free function introduced at the end of Sec. 2.2.2 B, this also includes a choice for the constant k_B (or equivalently l_B) after rewriting the equations in terms of the MOND acceleration constant a_0 using Eq. (2.57) (Remember that we work with K_B, $\phi_C \approx 0$). If not specified in any other way, we shall set $k_B = 0.01$ in these cases. This is justified following the analysis of Ref. [50] where the TeVeS lensing maps have been shown to be generally insensitive to variations of the parameter k_B as long as it is small, $k_B \lesssim 0.01$. Also, we will assume $a_0 = 1.2 \times 10^{-10}\mathrm{m\ s^{-2}}$ in accordance with Sec. 2.2.1 and particular constructions of the free function will be given when needed.

3.1.3 Background cosmology

To calculate angular diameter distances in the context of gravitational lensing, we still need to choose a cosmological model in TeVeS. Throughout this thesis, we will assume that the cosmological branch of μ_B (or equivalently F) is chosen in such a way that the basic result ϕ, $\rho_\phi \ll 1$ presented in Sec. 2.2.2 C remains valid. There we have already discussed the resulting background equations and found them to be structurally identical to those obtained in the framework of GR, but we are still left with the problem of specifying the energy-matter content in a TeVeS universe.

Since previous constraints on the baryonic contribution such as from BBN still apply in this case [98] and we assume that there is no CDM, finding a suitable background model poses a serious challenge to the theory. First attempts of reconciling TeVeS with observations on supernovae of type Ia [92] have led to the development of an open minimal-matter cosmology with (In the following, we will always refer to present-day values of the cosmological parameters and therefore skip the subscript "0")

$$\Omega_m \sim 0.04, \quad \Omega_\Lambda \sim 0.46, \quad h \sim 0.7 \tag{3.24}$$

and although it is able to fit the data up to a redshift of $z \sim 1-2$, it was quickly realized that such a model will not be able to explain observations of CMB anisotropies [3] and the present matter power spectrum [86]. Similarly, a flat minimal-matter cosmology with

$$\Omega_m \sim 0.05, \quad \Omega_\Lambda \sim 0.95, \quad h \sim 0.7 \tag{3.25}$$

suffers from the same issues while providing a worse fit to the supernovae data.

An interesting solution for this problem is to consider that neutrinos have masses. Assuming three species of left-handed ordinary neutrinos with a mass around 2eV and their antiparticles, it has been possible to obtain power spectra for both CMB anisotropies and matter which are able to describe the observational data in a qualitatively acceptable way [86] (although the corresponding fits do not match the excellent agreement of a ΛCDM model). Interestingly, the idea of massive neutrinos around 2eV has already been discussed to provide a solution to the lack of matter on cluster scales [78, 79, 81] and to explain the observed weak lensing map of the galaxy cluster 1E0657 – 558 ("bullet cluster") [93, 130]. It should be mentioned that the needed neutrino mass of 2eV is barely consistent with the current upper limit on the electron neutrino's mass (e.g., see Ref. [131]). Depending on how the current data sets are analyzed, on obtains an upper mass limit of 2.2eV or 2.8eV; future measurements such as the Karlsruhe Tritium Neutrino Mass Experiment (KATRIN) [132, 133] will be able to explore a mass range well below the 2eV threshold. While such neutrinos must have been relativistic in the early universe, they should behave like nonrelativistic matter today, with their density evolving as $\rho_\nu \propto a^{-3}$. If we assume that these neutrinos followed a thermal distribution at the time of decoupling, one may estimate their current total contribution to the energy budget of the universe as $\Omega_\nu \sim 0.032\, h^{-2} m_\nu/\mathrm{eV}$ (see, e.g., Ref. [20]). Here we have assumed three neutrino generations together with their antiparticles and m_ν denotes the

[3] Here the main difficulty is the resulting angular-distance relation which is not able to match the observed position of the peaks in the angular power spectrum of the CMB.

mass of a single neutrino in eV. From this, one obtains the so-called flat modified hot dark matter (μHDM) cosmology whose parameters read

$$\Omega_m = \Omega_b + \Omega_\nu \sim 0.05 + 0.17 = 0.22, \quad \Omega_\Lambda \sim 0.78, \quad h \sim 0.7, \tag{3.26}$$

where we have generously set $m_\nu = 2.6$eV, leading to $\Omega_\nu \sim 0.17$ in accordance with the analysis of Ref. [86]. In situations relevant for gravitational lensing, the background of the μHDM model is close to a standard ΛCDM cosmology parametrized by

$$\Omega_m \sim 0.3, \quad \Omega_\Lambda \sim 0.7, \quad h \sim 0.7, \tag{3.27}$$

and for several applications it will suffice to consider the latter. As we shall discuss in Sec. 3.4, one is not bound to use ordinary neutrinos and there is evidence that a massive sterile neutrino provides a much better candidate to account for the missing energy-density in TeVeS or related theories. Furthermore, it is also possible to construct covariant formulations of MOND [40, 115] which yield a background evolution indistinguishable from ΛCDM without the need for an additional matter fluid. In the present thesis, however, we will not consider such alternatives.

3.2 Analytic model for nonspherical lenses in TeVeS

Equipped with the covariant framework of TeVeS, it is now possible to investigate the consequences and viability of the MOND paradigm beyond "classical" domain of fitting observed rotation curves. Building on an earlier noncovariant approach [91], for instance, this allowed several authors to test MOND against multiple-image lens systems from the CfA-Arizona Space Telescope Lens Survey (CASTLES)[4] [134] (see, e.g., Refs. [92, 135–137]). Their analysis was nevertheless restricted to models of *spherical geometry*, and thus only able to account for the size of the Einstein ring of observed lenses, but not for the exact position of collinear images in double-image systems, and of course not for quadruple-image systems. This intrinsic limitation is due to the fact that the MONDian acceleration $\mathbf{g}_M$ is related to the Newtonian one according to Eq. (2.33).

In the following sections, we will demonstrate how to create simple analytic models of *nonspherical lenses* in TeVeS, corresponding to the situation of $\mathbf{S} = \mathbf{0}$ in MOND. Without resorting to a numerical Poisson solver, these analytic models can thus be used to fit image positions in double-image and quadrupled-image systems of the CASTLES data sample.

[4] cfa-www.harvard.edu/castles

3.2.1 The Hernquist-Kuzmin Model

3.2.1 A Potential-density pair

The Kuzmin disk [138], defined by a Newtonian gravitational potential of the form

$$\Phi_{N,K} = \frac{-GM}{\sqrt{x^2 + y^2 + (|z| + b)^2}}, \quad b > 0, \tag{3.28}$$

is a well-known and simple model for a nonspherical density configuration: For $z > 0$, Eq. (3.28) corresponds to the Newtonian potential generated by a point mass located at $(0, 0, -b)$, in case of $z < 0$ it turns into the Newtonian potential of a point mass located at $(0, 0, b)$. Thus, above and below the disk, we effectively have a spherical Newtonian potential, which implies that truly $\mathbf{S} = \mathbf{0}$ in Eq. (2.33).

Hereafter, the idea is simply to model lens galaxies by replacing the auxiliary point lens potential of the Kuzmin disk with an auxiliary Hernquist potential [139]; we shall refer to this model as the Hernquist-Kuzmin (HK) model. A similar approach, using Plummer's model and a smooth transition at $z = 0$ instead, leads to the Plummer-Kuzmin model derived in Ref. [140] which provides a qualitatively good fit to the mass profile of observed galaxies. Although our proposed model is not a very good description of real galaxies, it enables us to derive fully analytic lens models in the context of MOND (see Sec. 3.2.1 B) and to study the influence of nonsphericity on the ability to fit image positions.

The Newtonian potential of the HK model takes the form

$$\Phi_{N,HK} = \frac{-GM}{\sqrt{x^2 + y^2 + (|z| + b)^2} + h}, \tag{3.29}$$

with b being the Kuzmin parameter and h denoting the core radius of the Hernquist profile. Choosing different ratios h/b, this model will produce different Hubble type galaxies, going from a pure Kuzmin disk galaxy for $h/b \to 0$ to a pure Hernquist sphere for $h/b \to \infty$. To clarify this situation and to characterize the nonsphericity of the model, one may simply expand the right-hand side of Eq. (3.29) far away from the disk ($r^2 = x^2 + y^2 + z^2$):

$$\Phi_{N,HK} = \frac{-GM}{r + h}\left(1 - \frac{|z|\, b}{(r + h)r}\right) + O\left(b^2\right). \tag{3.30}$$

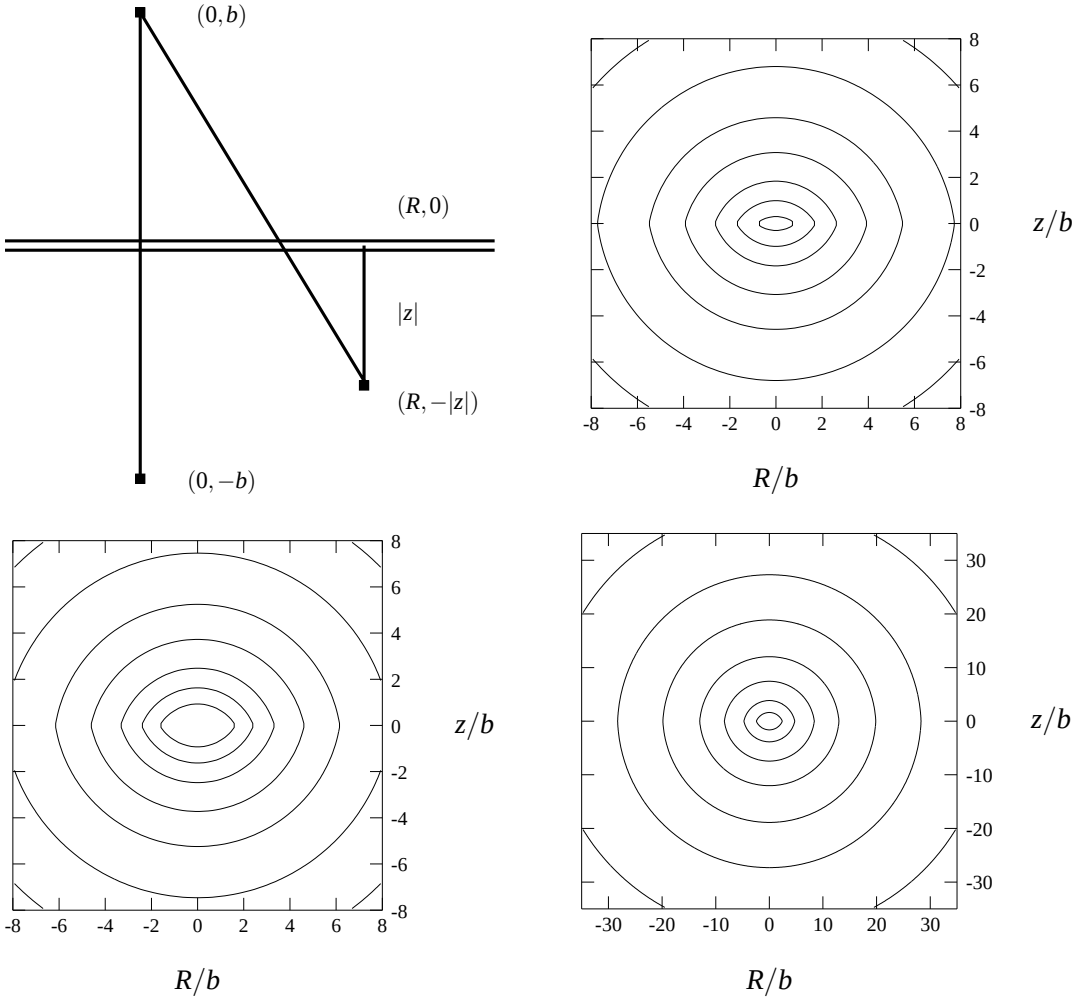

Figure 3.3: Contours of equal density in the (R, z) plane for the HK lens model (3.31) when $h/b = 0.1$ (*top right*), $h/b = 1$ (*bottom left*) and $h/b = 10$ (*bottom right*). Contour levels are $(0.01, 0.003, 0.001, ...)M/b^3$ (*top right*); $(0.001, ...)M/b^3$ (*bottom left*); $(0.0003, ...)M/b^3$ (*bottom right*). The *top left panel* illustrates the HK model: At the point $(R, -|z|)$ below the disk, the potential Eq. (3.29) is identical with that of a Hernquist distribution whose origin is located at a distance b above the disk's center.

Using Poisson's equation, we find that the underlying density distribution is given by

$$\rho_{HK} = \frac{Mh}{2\pi\sqrt{R^2 + (|z| + b)^2}\left(\sqrt{R^2 + (|z| + b)^2} + h\right)^3}, \tag{3.31}$$

where we have used the definition $R^2 = x^2 + y^2$. The corresponding density contours in the (R, z) plane are plotted in Fig. 3.3 for different values of h/b.

Considering the HK model for gravitational lensing, we choose the z-axis such that it is parallel to the line-of-sight and (x, y) are the Cartesian coordinates spanning the lens plane. Because we need to account for different possible orientations of galaxies, we additionally have to rotate the

disk. Defining $(r')^2 = (x')^2 + (y')^2 + (|z'| + b)^2$, where

$$\begin{aligned} x' &= (x\cos\phi - y\sin\phi)\cos\theta - z\sin\theta, \\ y' &= x\sin\phi + y\cos\phi, \\ z' &= (x\cos\phi - y\sin\phi)\sin\theta + z\cos\theta, \end{aligned} \tag{3.32}$$

the angle $(\pi/2) - \theta$ being the inclination of the galaxy's symmetry plane with respect to the line of sight and ϕ the galaxy's position angle (PA), Eq. (3.29) turns into

$$\Phi_{N,HK} = \frac{-GM}{r' + h}. \tag{3.33}$$

3.2.1 B Lensing Properties

Assuming spherical symmetric configurations and choosing the simplistic form of the free function μ_B introduced at the end of Sec. 2.2.2 B, we have the following relation for the total gravitational acceleration in TeVeS:

$$g_M(r) = g_N(r) + \sqrt{g_N(r)a_0}, \tag{3.34}$$

where $a_0 = 1.2 \times 10^{-10}\mathrm{ms}^{-2}$. Exploiting the above and introducing $z_0 = (x\cos\phi - y\sin\phi)\tan\theta$, the deflection angle's x-component yields

$$\begin{aligned} \alpha_x = {} & 2(x - b\cos\phi\cos\theta)\int_{-\infty}^{z_0} \frac{dz}{r'}\left(\frac{GM}{(r'+h)^2} + \frac{\sqrt{GMa_0}}{r'+h}\right) \\ & + 2(x + b\cos\phi\cos\theta)\int_{z_0}^{\infty} \frac{dz}{r'}\left(\frac{GM}{(r'+h)^2} + \frac{\sqrt{GMa_0}}{r'+h}\right). \end{aligned} \tag{3.35}$$

The integral (3.35) can be evaluated by means of elementary calculus, but as the resulting expression is quite lengthy, we shall skip its presentation at this point. Analogously, the closed analytic form for α_y can be derived, and as as a consequence, this is also true for the lensing quantities κ and γ.

Concerning the calculation of distances in gravitational lensing, we shall adopt a standard flat ΛCDM cosmology with $\Omega_m = 0.3$, $\Omega_\Lambda = 0.7$ and $h = 0.7$. This choice is justified by the fact that many covariant formulations of MOND mimic the behavior of a ΛCDM, accounting for marginal differences that will have no significant impact on our analysis. In particular, this is true

for the μHDM cosmology based on the assumption of massive neutrinos in TeVeS or for covariant approaches [40] yielding a Hubble expansion which is virtually indistinguishable from the ΛCDM model within the redshift range relevant for the lens systems we consider here (see Sec. 3.1.3).

3.2.2 Fitting procedure for CASTLE lenses

To model individual lens systems from the CASTLES sample, we will follow the approach presented in Ref. [141]: For each pair of images i and j, when tracing one light-ray back for each observed image to the source plane, the source position obtained from Eq. (3.14) should be the same for both images. We can thus simply compare the resulting source position for each image by computing their squared deviation,

$$\Delta_s^2 = \sum_{i \neq j} \left((x_{si} - x_{sj})^2 + (y_{si} - y_{sj})^2 \right), \tag{3.36}$$

where x_s and y_s denote the source position in Eq. (3.14). This is a measurement of how well the images retrace back to a single point in the source plane. Another quantity to minimize is the deviation of the lens center from the observed optical center, given by

$$\Delta_l^2 = x_l^2 + y_l^2, \tag{3.37}$$

However, our model has generally 9 fitting parameters (the lens mass M, the Kuzmin length b, the Hernquist length h, the PA angle, the inclination i, the source position (x_s, y_s) and the lens position (x_l, y_l)), while for a double-image system we have only four constraints from the two image positions, and another two constraints from the observed lens optical center. The problem is thus ill-posed.

To cure this and to ensure the uniqueness of the solution, we insert a regularization term in the minimization. This term is penalizing solutions deviating from the fundamental plane as well as face-on [5] and disky solutions, and solutions with an anomalous mass-to-light ratio or a large flux anomaly:

$$\mathcal{P} = \left[(\log FP)^2 + (\cos i)^2 + \left(\frac{b}{b+h} \right)^2 \right] + \left[\log \frac{f_{AB}}{f^{\rm obs}} \right]^2 + \left[\log \frac{M}{M_*} \right]^2 . \tag{3.38}$$

The deviation from the fundamental plane is measured by $\log FP = \log(h/h_1) - 1.26 \log(M/M_1)$,

[5] As there is strong observational evidence supporting that the system B0218+357 corresponds to a nearly face-on spiral galaxy [142, 143], we choose the regularization term for this particular lens such that edge-on solutions are penalized instead. Further relaxing the penalties with respect to both fundamental plane and observed flux ratio in Eq. (3.38), the fit substantially improves, corresponding to a factor of 20 in Δ_s.

where $h_1 = 0.72$kpc and $M_1 = 1.5 \times 10^{11} M_\odot$ [144].

Choosing a very small regularization parameter, $\lambda \sim (0.003'')^2$, we minimize the following regularized "χ^2-like" quantity,

$$\eta^2 = \Delta_s^2 + \Delta_l^2 + \lambda \mathcal{P}, \tag{3.39}$$

for 14 double-image systems and four quadruple-image systems of the CASTLES data sample. Note that we also check that our results are insensitive to the detailed choice of the regularization parameter [6] and that due to the sufficient number of constraints (position of lens and images), the fitting procedure for quadruple-image lenses is performed with $\lambda = 0$. The results are shown in Table 3.1 and Table 3.2, respectively. Finally, note that the observed mass of each lens was calculated according to Sec. 7.1 of Ref. [92].

3.2.3 Fitting results

3.2.3 A Double-image systems

Setting $\Delta_s < 0.01''$ as a reasonable threshold for acceptable fits of the HK lens, Table 3.1 shows that our model is able to describe the observed image positions of all double-image systems, with quite a number of these systems yielding plausible parameters within the context of MOND/TeVeS. For a better presentation, Figs. 3.4, 3.5 and 3.6 further illustrate this in terms of the found relations between modeled and observed lens masses and flux ratios, respectively. As can be seen from Fig. 3.5, for example, the HK model seems to be able to explain the flux ratios of these binaries in most cases.

However, there are a few outliers which we will discuss in the following. Since the model should be capable of reproducing all observational constraints and the lens mass should have a value close to the stellar mass ($M/M_* \simeq 1$) in TeVeS, these are characterized by very poor fitting parameters in terms of large differences between predicted and observed flux ratios or anomalous mass ratios M/M_* (deviation larger than a factor of 3).

RXJ0921+4529 The system RXJ0921+4529 contains two $z_s = 1.66$ quasar images and a $H = 18.2$ spiral galaxy located in between the quasar images. This galaxy lens is quite likely to be a member of a $z_l = 0.32$ x-ray cluster centered on the observed field [145]. Clearly, RXJ0921+4529

[6] In case of RXJ0921+4529, however, our choice of λ creates an over-regularization effect, which results in a best-fit lens mass that is roughly by a factor 10 smaller than estimated in Ref. [92] from fitting the system's Einstein ring size. Decreasing the regularization parameter to $\lambda \sim (3 \times 10^{-4}\,'')^2$ is able to resolve this issue, with Δ_s dropping by a factor 10 and the lens mass now being in accordance with the previous estimate of Ref. [92] (see Table 3.1).

Table 3.1: Fitting results for selected 2-image lens systems from the CASTLES sample: In the table, the observed lens mass M_* is calculated according to Sec. 7.1 of Ref. [92], the parameter r_h is the Hernquist length expected from half-light measurements (values are taken from Ref. [92]). We do not give η^2, but instead we list Δ_s and compare the inferred values of PA, the Hernquist length h, mass and flux ratio to observations. Additionally, we predict inclination and time delay for the particular lens models. Outliers are characterized by large differences between predicted and observed flux ratios and/or anomalous mass ratios M/M_* (deviation larger than a factor of 3) like, for instance, in case of RXJ0921+4529 which resides in a cluster. Note that the fitted lens position is given by $(x_l, y_l) \approx (0, 0)$ for all lenses.

Lens	z_l	b/h	h/r_h [kpc]	M (fit/obs) [$10^{11} M_\odot$]	PA [°]	incli.	Δ_s [″]	f_{AB} (fit/obs)	δt (fit/obs) [days]
Q0142-100	0.49	0.25	1.34/1.6	1.70/4.08	72.2	90.0	2.43×10^{-4}	8.06/8.22	151.5/-
B0218+357	0.68	1.0	2.19/1.8	2.69/2.67	-22.6	6.94	7.75×10^{-5}	0.759/0.587	7.52/10.5
HE0512-3329	0.93	0.24	1.45/1.8	1.49/2.91 [a]	28.2	90.0	3.90×10^{-6}	0.0013/1.175	19.6/-
SDSS0903+5028	0.39	0.76	1.83/1.8	2.77/3.80	-30.4	90.0	9.90×10^{-4}	2.29/2.17	135.2/-
RXJ0921+4529	0.31	0.037	7.59/1.8	20.0/0.34	60.2	90.0	5.85×10^{-4}	3.623/3.591	167.2/-
FBQ0951+2635	0.24	0.13	1.20/0.32	0.47/0.31	60.3	90.0	1.23×10^{-4}	2.74/3.53	13.2/-
BRI0952-0115	0.41	0.055	2.20/0.29	0.58/0.27	124.1	90.0	5.04×10^{-4}	3.52/3.52	8.11/-
Q0957+561	0.36	1.55	1.21/5.23	6.94/8.44	40.0	90.0	1.97×10^{-3}	14.3/1.08	752.4/417.0
Q1017-207	0.78	0.0092	2.39/1.19	0.83/0.74	88.8	89.9	2.16×10^{-4}	0.73/0.72	29.0/-
B1030+071	0.60	0.10	0.84/1.50	1.85/1.66	29.3	90.0	8.04×10^{-5}	36.6/36.6	346.8/-
HE1104-1805	0.73	0.33	0.58/2.48	4.91/3.32	61.9	90.0	1.96×10^{-3}	0.35/3.85	321.2/-
B1600+434	0.41	0.18	1.64/1.8	1.01/0.40	36.8	90.0	2.09×10^{-4}	0.83/0.84	32.2/51.0
PKS1830-211	0.89	0.48	2.75/1.8	1.33/1.48	62.3	90.0	4.14×10^{-4}	157.3/157.3	32.7/26.0
HE2149-2745	0.50	0.026	0.94/11.4	1.04/2.00	-30.0	90.0	2.30×10^{-4}	6.53/4.19	90.7/103.0
SBS0909+523	0.83	0.19	3.02/1.8	2.92/13.5 [a]	49.2	90.0	1.84×10^{-3}	1.42/1.42	65.9/-

[a] Note that the analysis of Ref. [92] assumed a different value for M_* based on a wrong magnitude in an older version of the CASTLES data set.

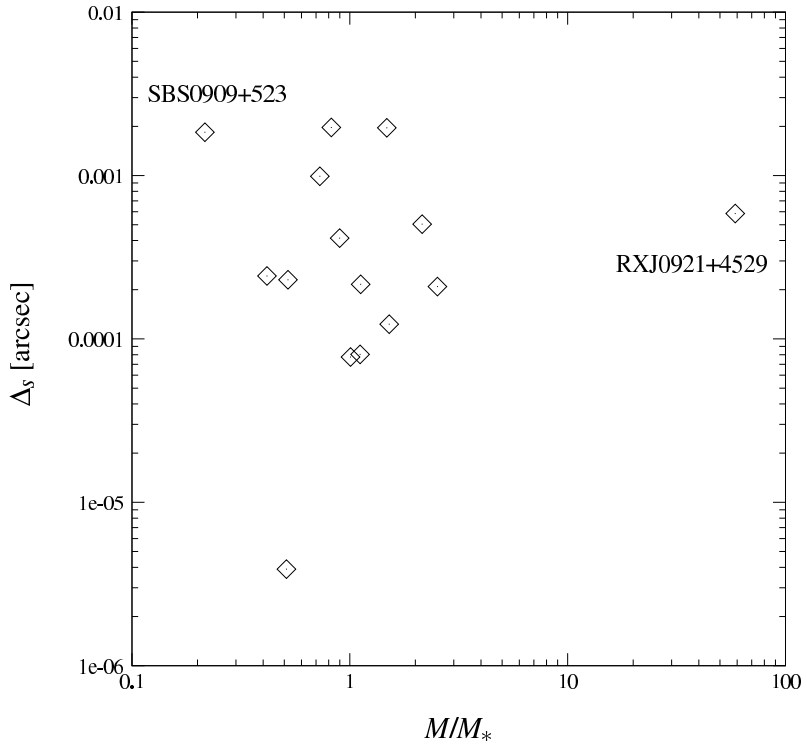

Figure 3.4: Illustration of the resulting ratios between modeled lens mass M and the corresponding stellar mass M_* for double-image systems in the CASTLES data set: Shown is the ratio M/M_* plotted against Δ_s. Since there is no additional DM on galactic scales, acceptable lens models in TeVeS should cluster around $M/M_* \simeq 1$; outliers are labeled with their names.

does not correspond to an isolated system, which complicates the situation in TeVeS and provides a possible explanation for the extremely poor fit/mass ratio ($M/M_* \approx 59$). The presence of a cluster could have caused difficulties in fitting the lens as the impact of an external field or other nonlinear effects may be important. In addition, remember that there are still unresolved issues in MOND and its extensions concerning clusters [50, 78, 79, 81, 93].

Q0957+561 The gravitational lens Q0957+561 is the most thoroughly studied one in literature. The system involves a radio-loud quasar at redshift $z_s = 1.41$ which is mapped into two images by a brightest cluster galaxy (BCG) and its parent cluster at redshift $z_l = 0.36$ [146, 147]. It is also known that the lens galaxy has a small ellipticity gradient and isophote twist which are properties the simple HK model cannot account for. Together with the fact that the lens is embedded into a cluster, this might be a reason for the huge discrepancy between observed and predicted flux ratio in the context of modified gravity.

HE1104-1805 The lens galaxy's colors are in agreement with a high-redshift early-type galaxy, and its redshift is roughly estimated as $z_l = 0.77$ [148]. Concerning its lensing properties, the system HE1104-1805 is quite uncommon in a the sense that the lens is closer to the bright image,

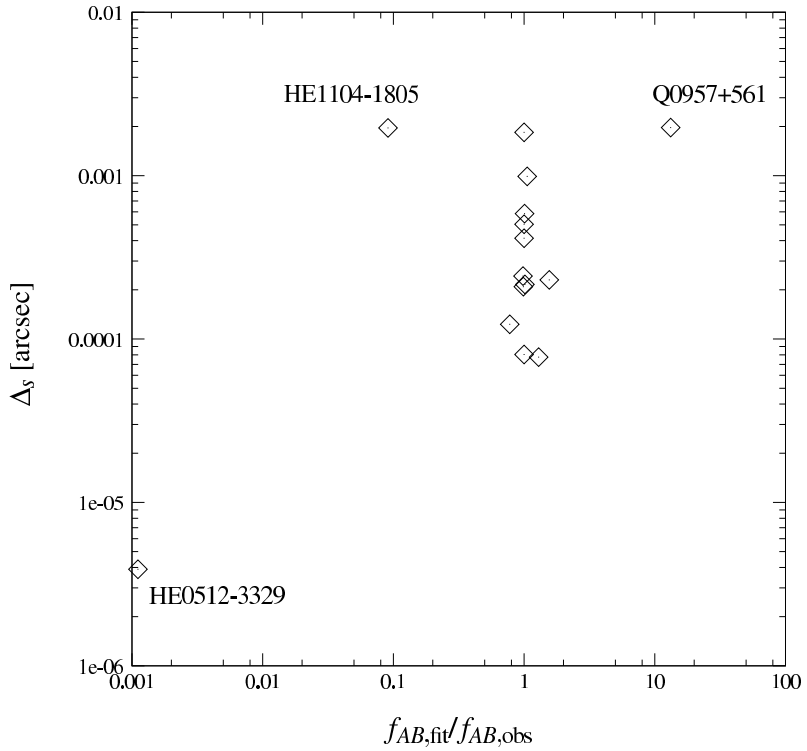

Figure 3.5: Illustration of the resulting relation between modeled and observed flux ratios for double-image systems in the CASTLES data set: Shown is the ratio $f_{AB,\mathrm{fit}}/f_{AB,\mathrm{obs}}$ plotted against Δ_s. As is obvious, acceptable lens models in TeVeS should cluster around $f_{AB,\mathrm{fit}}/f_{AB,\mathrm{obs}} \simeq 1$; outliers are labeled with their names.

rather than the faint one. As is known from lensing within the standard GR + CDM paradigm, simple models can create such configurations only for a narrow range of parameters due to the peculiar flux ratio. Assuming simple ellipsoidal lens models, however, these parameters imply a large misalignment between the light and the projected density. The only possibility to align the mass with the light, is to have a shear field being approximately twice as strong as estimated from the particular lens model.

Furthermore, the observed image separation is by a factor $2-3$ larger than that of a typical lens, strongly suggesting that the separation is enhanced by the presence of a group or a cluster. So far, however, there has been no direct observational evidence for such a structure in the lens' surrounding area. Analog to the aforementioned lens systems, the unsatisfying fit and the correspondingly inferred flux ratio might be a result of both lens environment and model limitations (see also Sec. 3.2.3 C and 3.2.3 D).

SBS0909+523 SBS0909+532 shows two images of a background quasar source at $z_s = 1.377$ separated by $1.11''$ [148]. Optical and infrared HST images indicate that the lensing galaxy has a large effective radius and a correspondingly low surface brightness. Additionally, the lens galaxy's

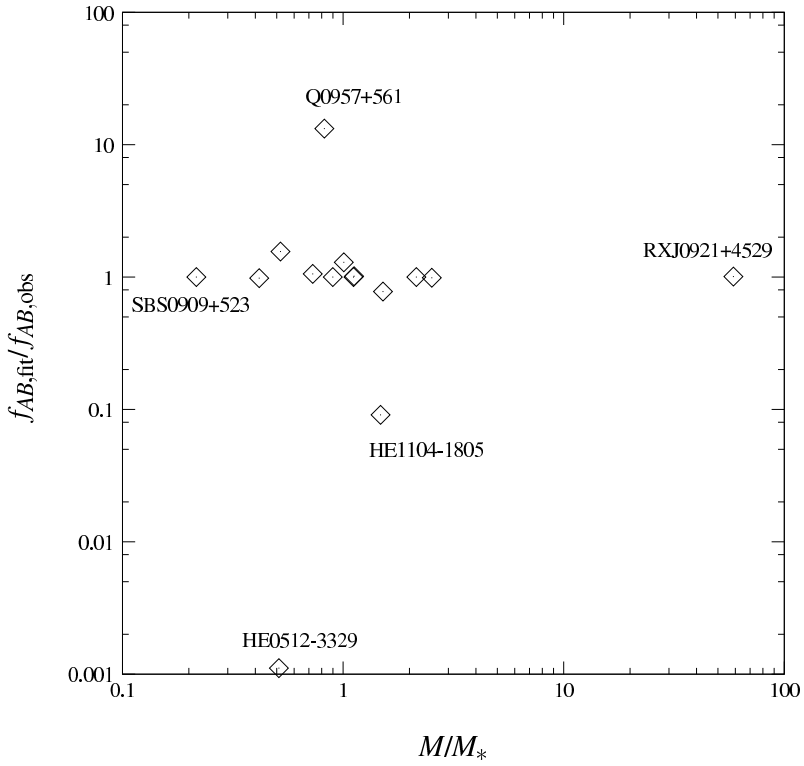

Figure 3.6: Mass ratio M/M_* plotted against the ratio of modeled and observed flux ratio for double-image systems in the CASTLES data set: Note that acceptable lens models in TeVeS should cluster close to the point (1, 1); outliers are labeled with their names.

redshift is estimated as $z_l = 0.83$ [149], and its total magnitude in the H-band has been measured as $H = 16.75 \pm 0.74$. Although the lens galaxy's colors are poorly measured, they seem consistent with those of an early-type galaxy at the observed redshift.

The large uncertainties are a result of the difficulty in subtracting the close pair of quasar images [148]. For instance, the uncertainty in the I-band magnitude, $I = 18.85 \pm 0.45$, allows a deviation of the mass estimate M_* by a factor of roughly 2.3 at the 2σ level, where we have used Eqs. (73) and (74) of [92]. Thus we argue that the low mass ratio (listed in Table 3.1) may be entirely due to these uncertainties in observed magnitudes, with better constrained observations possibly softening the found problem in TeVeS.

HE0512-3329 The system HE0512-3329 was discovered as a gravitational lens candidate in the course of a snapshot survey with the Space Telescope Imaging Spectrograph (STIS), with the images of the lensed quasar source being separated by $0.644''$ [150]. Although the lens galaxy has not been detected yet, measurements of strong metal absorption lines at redshift $z = 0.93$, identified in the integrated spectrum, hint towards a damped Lyα system intervening at this redshift.

Analyzing separate spectra of both image components, it has been pointed out that both dif-

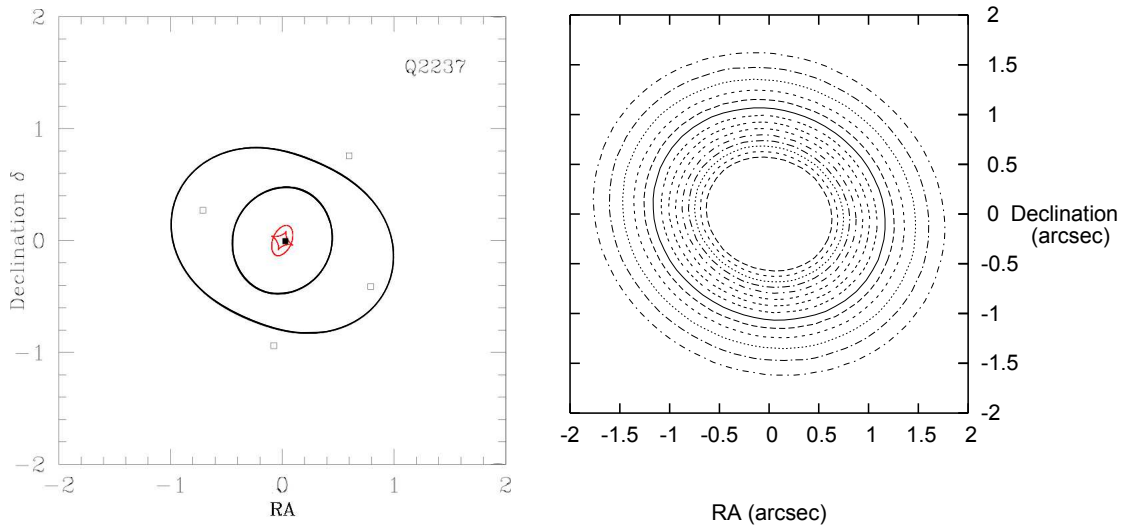

Figure 3.7: *Left panel*: Shown are the critical curves (black lines) and caustics (red lines) of the best-fit Hernquist-Kuzmin model for Q2237+030. The empty and filled squares denote the observed positions of images and source, respectively. *Right panel*: Convergence map κ of the best-fit Hernquist-Kuzmin model for Q2237+030, with the outer contour level starting at $\kappa = 0.7$ and increasing in steps of 0.1 up to a level of $\kappa = 2.0$.

ferential extinction and microlensing effects significantly contribute to the spectral differences and that one cannot be analyzed without taking into account the other [150]. For lens modeling purposes, the observed flux ratio can therefore only be used after correcting for both effects. Thus the large discrepancy between predicted and observed flux ratio might be a consequence of neglecting the above mentioned effects, rather than being intrinsic to TeVeS.

3.2.3 B Quadruple-image systems

As we can see from Table 3.2, most of the quadruple-image systems are very poorly fitted by the analytic HK model. In accordance with our goodness-of-fit criterion ($\Delta_s < 0.01''$) introduced in Sec. 3.2.3 A, there is just one system where the model is able to predict the image positions in a satisfying manner. Additionally, none of the observed flux ratios can be explained.

The only acceptable fit is given for Q2237+030, the nearby Einstein cross ($z_l = 0.04$ [151]), which is the only true bulge-disk system in our set. Also, its physical Einstein ring size in the lens plane is very small, $R_E \approx 0.7$kpc (in B1422+231, for instance, it is already by a factor of roughly 10 larger [152]). Nevertheless, it is not possible to give a reasonable explanation for the flux ratios using the smooth HK model. Taking effects due to microlensing into account, which are not considered in the present analysis, could be able to relax the situation. Note that the lens galaxy actually contains a bar feature [153] which is ignored in our analysis.

Table 3.2: Fitting results for selected 4-image lens systems from the CASTLES sample: Note that all positions (RA and declination) are given in units of ″. The observed position angle and inclination of Q2237+030 (major-axis) are PA= 77.2° and $i = 64.5°$, respectively, assuming a circular face-on disk. Replacing the auxiliary Hernquist with a Jaffe profile barely changes the numbers: inclination and PA change by about 5°, the predicted mass by roughly 10% .

	PG1115+080	Q2237+030	B1422+231	SDSS0924+0219
z_l	0.31	0.04	0.34	0.39
z_s	1.72	1.69	3.62	1.52
D_l [kpc]	957.2	163.6	1020.2	1116.6
D_s [kpc]	1874.2	1874.0	1637.6	1867.0
D_{ls} [kpc]	1413.2	1810.8	1341.7	1252.1
Image A	$(-0.947, -0.690) \pm 0.003$	$(-0.075, -0.939) \pm 0.003$	$(0.375, 0.973) \pm 0.003$	$(-0.162, 0.847) \pm 0.003$
Image B	$(-1.096, -0.232) \pm 0.003$	$(0.598, 0.758) \pm 0.003$	$(0.760, 0.656) \pm 0.003$	$(-0.213, -0.944) \pm 0.003$
Image C	$(0.722, -0.617) \pm 0.003$	$(-0.710, 0.271) \pm 0.003$	$(1.097, -0.095) \pm 0.003$	$(0.823, 0.182) \pm 0.003$
Image D	$(0.381, 1.344) \pm 0.003$	$(0.791, -0.411) \pm 0.003$	$(-1.087, -0.047) \pm 0.003$	$(-0.701, 0.388) \pm 0.003$
Source	$(-0.011, 0.091)$	$(0.027, -0.0051)$	$(0.089, 0.030)$	$(-0.024, -0.047)$
Lens	$(-0.0011, -0.0041)$	$(0.00066, 0.00096)$	$(-0.00093, 0.0065)$	$(0.019, -0.0051)$
M ($M_{\rm fit}/M_*$) [$10^{11} M_\odot$]	7.80/1.23	0.78/1.19	4.83/0.77	2.80/0.32
h [kpc]	2.25	0.44	8.42	1.57
b/h	0.56	1.85	0.29	2.17
PA angle [°]	244.8	246.6	117.9	266.4
Inclination [°]	44.5	30.6	48.6	40.5
Δ_s [″]	0.0402	0.0026	0.0593	0.0612
Flux ratio (obs)	4.03:2.53:0.65:1	2.62:1.64:1.30:1	31.1:34.6:18.4:1	12.5:5.68:4.81:1
Flux ratio (fit)	3.98:4.15:1.40:1	0.81:0.66:0.68:1	8.56:6.53:7.51:1	1.66:0.69:0.86:1

PG1115+080 The lens galaxy in PG1115+080 and its three neighbors belong to a single group at $z_l = 0.311$, with the group being centered southwest of the lens galaxy's position [154, 155]. Reasonable fits of this lens typically involve a significant amount of external shear in the context of GR + CDM. Moreover, the observed anomaly of the flux ratio (~ 0.9) between two of the images strongly hints towards an additional perturbation of the system caused by a satellite galaxy or a globular cluster. Similar to Sec. 3.2.3 A, we have a gravitationally bound system which will likely involve a different approach than provided by the isolated HK model.

B1422+231 The system B1422+231 shows almost the same characteristics as PG1115+080 [156]. Again, the lens belongs to a galaxy group which is centered south of the lens galaxy ($z_l = 3.62$). In Ref. [157], the lensing system was fit using a very flat singular isothermal ellipsoid (SIE) [158, 159] plus an external shear field. However, HST observations revealed that the lens galaxy's optical axis ratio is much closer to unity than assumed for the flat SIE, favoring rounder lens models with larger external shear.

SDSS0924+0219 Estimated colors and magnitudes of the lens galaxy are consistent with those of a typical elliptical galaxy at $z_l = 0.4$ [160]. Although the lens environment does not show any nearby objects perturbing the system, quite an amount of external shear is needed to obtain a satisfying fit to observations, with the lens being typically modeled by a (flattened) singular isothermal sphere (SIS). Additionally, microlensing plays an important role in explaining the observed flux ratios within GR + CDM, which is likely to be true in TeVeS as well.

3.2.3 C Maximum nonspherical shear of a Kuzmin lens

As we have seen, the outliers in our selection of quadruple-image lenses correspond to systems with a large external shear. In PG1115+080, for example, this is due to a neighboring galaxy group. However, the same situation also appears in uncrowded environments, usually constraining the lensing potential to require a substantial ellipticity. From Sec. 3.2.3 B, it seems that our present analytic model is not able to generate such a potential in most cases. As is known, almost all quadruple-image systems show evidence for the need of an external shear field [158, 161, 162] by violating a certain inequality of the image positions. It is perhaps not surprising that the current isolated HK model fails to fit these lenses [7]. To gain a better understanding about this issue, we consider a pure edge-on Kuzmin lens ($h = 0$) and derive the maximum variation of the shear at

[7] Note that our analysis does not take into account external shear effects, which would complicate the relation between lens mapping and associated density distribution due to nonlinearity in modified gravity. While our main task is to explore the capability of the HK model, such contributions should certainly be addressed in future work.

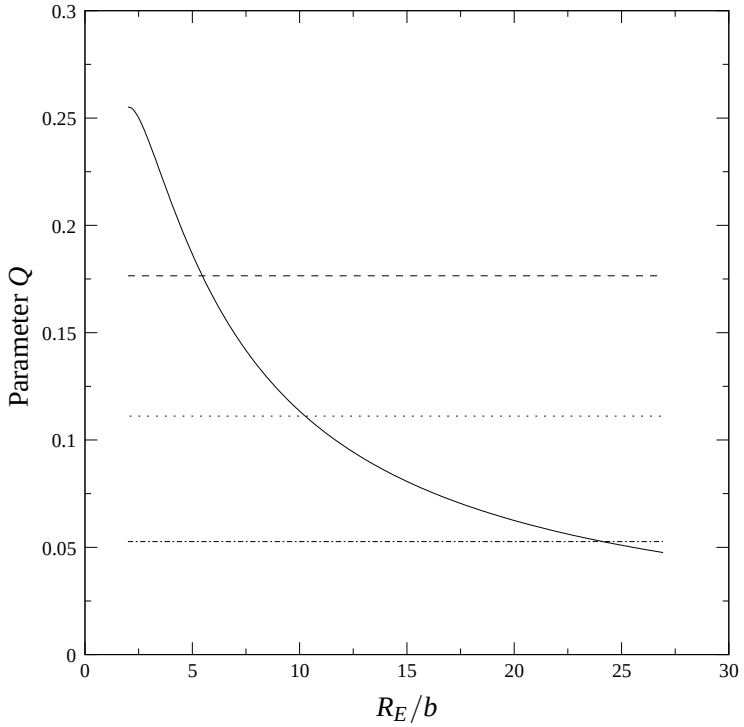

Figure 3.8: Nonspherical shear parameter Q for a simple TeVeS Kuzmin lens (solid line), assuming $a_0 D/c^2 = 0.03$: Additionally, we show the results for a SIE model with a potential axis ratio of 0.9 (dotted-dashed line), 0.8 (dotted line) and 0.7 (dashed line), respectively.

the Einstein radius R_E by comparing its values on the major and minor axis. For this reason, let us introduce a quantity Q which is given as follows:

$$Q \equiv \frac{\gamma(R_E, 0) - \gamma(0, R_E)}{\gamma(R_E, 0) + \gamma(0, R_E)}. \tag{3.40}$$

The parameter defined above will indicate the level of the shear field's nonsphericity at the Einstein radius and is a function of the dimensionless radius R_E/b. Note that in case of the Kuzmin lens, the quantity Q depends on redshift.

Figure 3.8 shows Q as function of R_E/b for the pure Kuzmin model (solid line), assuming $a_0 D = 0.03$. This value has been chosen in accordance with the majority of lens redshifts in the CASTLES sample, and changing it does have no significant qualitative impact on the basic outcome. Additionally, we also present the result for the singular isothermal ellipsoid (SIE) model [159], with the potential axis ratio varying from 0.7 to 0.9 (shown by horizontal lines). As we can see, the Kuzmin model becomes comparable to a very round SIE if $R_E/b \gtrsim 10$.

To obtain a sufficiently strong quadruple moment, i.e. nonspherical shear, at the Einstein radius ($Q > 0.2$), these disk-only models must satisfy the condition $b > 0.2R_E$. In case of PG1115, the

observed ring size can be estimated as $R_E \approx 5$kpc, so to fit four images, one might actually expect that $b \gtrapprox 1$kpc. However, trying to fit the above mentioned Einstein ring size using the stellar mass only, we also find that this would need a Kuzmin parameter close to zero ($b \approx 0$), corresponding to a very concentrated point-like lens. Although we have only given a plausibility argument, rather than a rigorous proof, this could explain why we cannot find a value of b that meets both requirements and why the HK model mostly fails to fit quadruple-image systems.

3.2.3 D Experimenting with hypothetical lenses

Another possibility of investigating the fitting capability of our model is to generally explore its parameter space and to study the structure of critical curves and caustics. To avoid any limitations that might be due to the particularly chosen radial profile, we furthermore replace the auxiliary Hernquist profile with the more general Dehnen profile [163]. Its Newtonian potential and the corresponding density profile read as

$$\Phi_{N,D}(r) = \frac{GM}{\alpha}\left[-1 + \left(\frac{r}{r+h}\right)^{\alpha}\right], \quad \rho_D(r) = \frac{Mh(1+\alpha)}{4\pi r^{2-\alpha}(r+h)^{2+\alpha}}, \tag{3.41}$$

where h is a characteristic length of the model. Depending on the value of α, the Dehnen model represents different density distributions, ranging from quite cuspy to more broadened profiles. For $\alpha = 0$ and $\alpha = 1$, Eq. (3.41) reduces to the models of Jaffe [164] and Hernquist, respectively. Allowing different values for α, we repeat the fitting procedure for the quadruple-image systems discussed in Sec. 3.2.3 B. The result is basically the same as for the HK model, with the parameters listed in Table 3.2 not significantly changing. In case of the Jaffe profile ($\alpha = 0$), for instance, inclination and PA are altered by about 5° and the predicted mass by approximately 10%.

To further illuminate the insufficiency of our model, let us have a more detailed look at the caustic structure, taking the system PG1115+080 as an example: Choosing a plausible setting for the lens system in MOND, we fix its size to $h = 0.72$kpc and the PA to 77.2° (observed value). In accordance with the best-fit results, we additionally assume a lens mass of $M = 8 \times 10^{11} M_\odot$ and vary the Dehnen index α, the model's "diskyness" $b/(h+b)$ as well as the inclination on a range from -1 to 1, 0.1 to 0.9 and 10° to 90°, respectively. For a selection of such lenses, the corresponding critical curves and caustics are shown in Fig. 3.9. Then, among all resulting lens models, we select those which exhibit the strongest (nonspherical) shear, corresponding to a large astroid caustic size. Since the lens mass should be close to the stellar mass ($M/M_* \simeq 1$)

in MOND/TeVeS, the idea is now to stepwise decrease the mass of these models. In all cases, we find that, due to the caustics' contraction, the source crosses the astroid caustic way before M/M_* reaches unity, thus not corresponding to a quadruple-image system anymore. Typically, the crossing seems to take place when the lens model's mass is roughly around $4 - 6 \times 10^{11} M_\odot$. For $\alpha = 1$, $b/(h + b) = 0.38$ and an inclination of 44.5°, this situation is illustrated in the left and middle panel of Fig. 3.10. Note that we have kept the source position fixed at $(-0.011, 0.091)''$ for our analysis, with the lens being centered on the origin.

Again, this provides a possible explanation why the Dehnen-Kuzmin model (including the HK model) mostly fails to fit quadruple-image systems, supporting our earlier conclusion from Sec. 3.2.3 C. Given that $M/M_* \simeq 1$ in TeVeS, our model is obviously not able to generate sufficiently strong shear (hence large caustics) and a large Einstein ring at the same time. For comparison, we also present the resulting caustics and critical curves of a best-fit SIS + γ_{ext} model in the right panel of Fig. 3.10. As is known, its deflection potential can be expressed as

$$\Psi(\xi, \theta) = c\xi + \frac{\gamma}{2}\xi^2 \cos\Big(2(\theta - \theta_\gamma)\Big). \tag{3.42}$$

Choosing the lens' position $(x_l, y_l) = (0.0028, 0.0048)''$, $c = 1.14''$, $\gamma = 0.07$ and $\theta_\gamma = 88.7°$, the above model is able to fit the observations of PG1115+080 satisfyingly.

3.2.4 Discussion

We have found that the HK model is able to describe the observed image positions of all analyzed double-image systems, with 10 of these systems yielding plausible parameters within the context of TeVeS. Additionally, our model is mostly able to explain the flux ratios of these binaries. Note that the implied masses for most of these lenses are quite similar to those derived from the spherically symmetric models applied in Ref. [92], but that the big advantage of our nonspherical model is its ability to fit the precise image-positions rather than just the size of the Einstein ring.

On the other hand, 5 double-image systems do not provide a reasonable fit: While for two of these systems, the found problems are likely to be solved by considering observational uncertainties, a more accurate model or additional effects such as extinction and microlensing, the other three lenses appear to be lacking an obvious explanation [8]. It is however quite striking that all

[8] Note, however, that the stellar mass estimates depend on the adopted initial mass function and star formation rate, and can vary by a factor of 4 in the R-band, which could partly solve the problem of the mass-ratio discrepancy, but not the flux ratio anomalies.

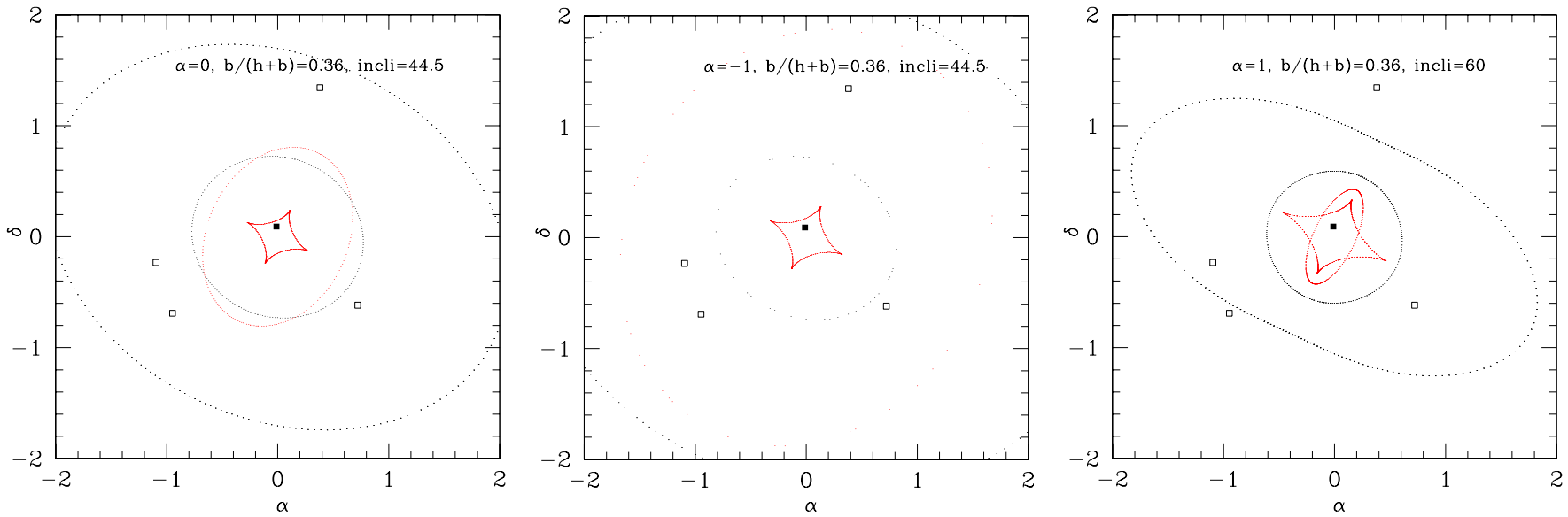

Figure 3.9: Experimenting with hypothetical lenses: Shown are the critical curves (black lines) and caustics (red lines) of different Dehnen-Kuzmin models characterized by the parameters α, $b/(h+b)$ and inclination ("core" radius and PA are fixed to $h = 0.72$kpc and 77.2°, respectively). All models assume a lens mass of $M = 8 \times 10^{11} M_{\odot}$ which is approximately 8 times the stellar mass of the lens galaxy in PG1115+080. The empty and filled squares denote the observed image and source positions of PG1115+080.

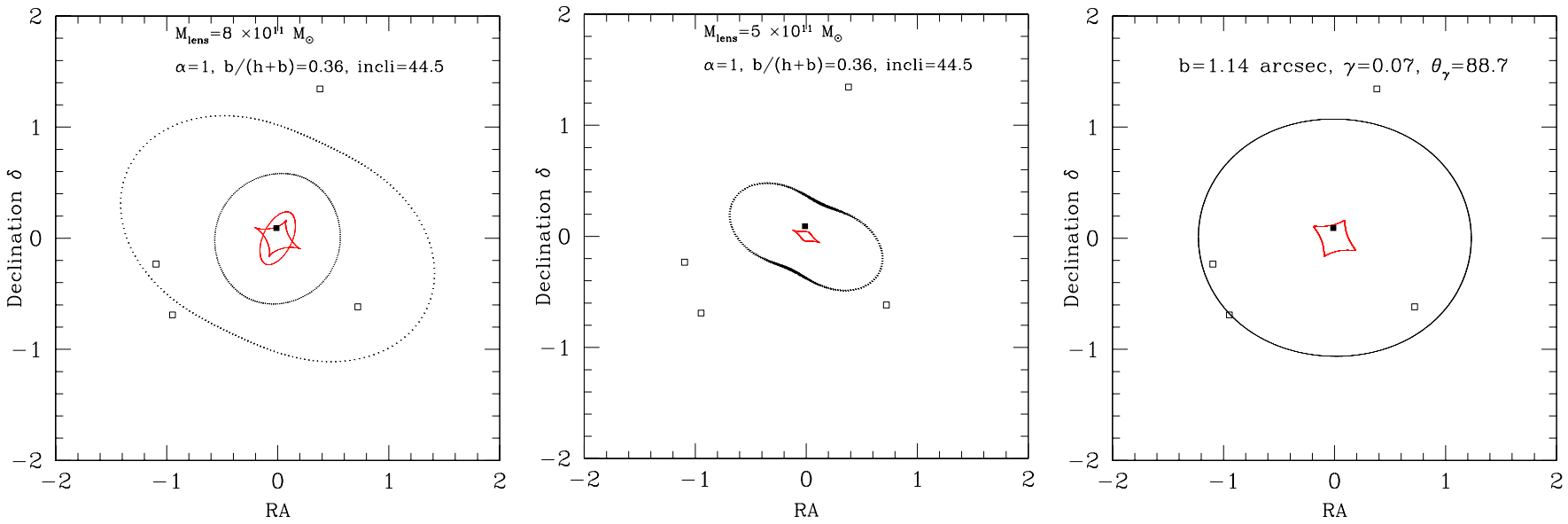

Figure 3.10: Effects of reducing the lens mass: Shown are the critical curves (black lines) and caustics (red lines) of a Dehnen-Kuzmin model ($\alpha = 1$, $b/(h+b) = 0.38$, $h = 0.72$kpc, PA$= 77.2°$ and $i = 44.5°$), assuming $M = 8 \times 10^{11} M_\odot$ (*left panel*) and $M = 5 \times 10^{11} M_\odot$ (*middle panel*), respectively. The empty and filled squares denote the observed image and source positions of PG1115+080, the stellar mass of the lens is estimated as $M_* \approx 10^{11} M_\odot$. *Right panel*: Critical curves (black lines) and caustics (red lines) of the best-fit SIS+γ_{ext} model given by Eq. (3.42).

these remaining outliers are actually residing in (or close to) *groups or clusters* of galaxies. Since TeVeS lensing is much more sensitive to the underlying three-dimensional distribution of the lens than in GR [50], this means that effects due to environment or nonlinearity could have an important incidence. Moreover, it is known for a while that additional dark matter is needed for galaxy clusters in MOND and it has recently been shown that this is the case for groups, too [80]. Possible explanations for this "cluster dark matter" range from the presence of numerous clouds of cold gas [165] through the existence of neutrinos with a mass around several eV [166] to the nontrivial effects of the vector field (or of an additional scalar field) in TeVeS or other covariant formulations of MOND [34, 84, 167]. Several studies (including the recent analysis of the velocity dispersions of globular clusters in the halo of NGC 1399 [168]) have also provided first evidence for such dark matter on *galaxy scales* in MOND, which is typical for galaxies residing at the center of clusters only. This may be interpreted as a small-scale variant of the aforementioned cluster problem (although the two are not necessarily related to each other) and could thus provide an additional reason for the poor fits obtained for the two-image lenses residing in groups or clusters.

For the four quadruple-image systems, it is a different story: the only acceptable fit is obtained for the Einstein cross Q2237+030, but even in this case, the observed flux ratios cannot be reproduced. However, the anomalous flux ratios here are most likely due to microlensing effects which have not been considered in our analysis. We can thus conclude that MOND does not provide a solution to the flux anomaly issue, mainly because smooth MOND models naturally predict smooth magnification patterns. Among the 3 very poorly fitted lenses, only PG1115+080 and B1422+231 appear in a crowded environment, which could cause the same perturbing effects as for non-isolated double-image systems; the remaining lens, SDSS0924+0219, appears relatively isolated. We argue that, especially in this particular case, the poor fits are due to the intrinsic limitation of the HK model: Indeed, we have shown that the model is unable to produce a large Einstein ring and a large nonspherical shear at the same time. Although we have not presented a rigorous proof, we have tried to make this limitation plausible by analyzing the maximum nonspherical shear of a TeVeS Kuzmin lens as well as the caustic structure of different HK models. We have also tried models based on the more general Dehnen profile [163], but this has not led to a satisfactory solution either. Again, note that our analysis did not consider any contribution due to external shear effects.

In summary, we conclude that our analytic models generally provide good fits to the image positions of isolated two-image lenses, but that some problems are encountered for non-isolated

lens systems. On the other hand, we have shown that our models are barely able to fit quadruple-image systems, which is essentially traced back to the intrinsic limitations of our model. The present study has thus pinpointed some lenses for which more detailed approaches such as a full three-dimensional numerical model should be devised. While our analytic models do obviously not yet represent a definitive test of MOND/TeVeS with gravitational lensing, they have nevertheless provided a new step toward understanding this quite unexplored research area and isolating the possibly challenging lens systems for the future.

3.3 Gravitational lensing by intercluster filaments

3.3.1 Weak lensing anomalies and filamentary structures

Recently, strange and hard-to-explain features have been discovered in galaxy clusters, such as the "dark matter core" devoid of galaxies at the center of the "cosmic train wreck" cluster Abell 520 [169] or the "dark clusters" discussed in Ref. [170]. In what follows, we shall consider the possibility that this kind of features could be due to the gravitational lensing effects generated by intercluster filaments in a TeVeS universe. However, we are not performing a detailed lensing analysis of any particular cluster in the presence of filaments, but rather provide a proof of concept that the influence of filaments could be much less negligible than within the framework of GR + CDM.

Filaments are among the most prominent large-scale structure of the universe. From simulations in ΛCDM cosmologies, we know that almost every two neighboring clusters are connected by a straight filament with a length of approximately $20 - 30$Mpc [171]. For instance, the dynamics of field galaxies, which are generally embedded in such filaments, as well as their weak lensing properties are persistently influenced by this kind of structure, generally encountering accelerations of about $0.01 - 0.1 \times 10^{-10}\mathrm{m\ s}^{-2}$. Filaments also cover a fair fraction of the sky, much larger than the covering factor of galaxy clusters. Thus, there is a good chance that filaments might be superimposed with other objects on a given line of sight, hence affecting the analysis of observational data like, for example, weak lensing shear measurements.

Short straight filaments are structures which, at the best, are partially virialized in two directions perpendicular to their axis. According to Ref. [171], a filament generally corresponds to an overdensity of about $10 - 30$, having a cigar-like shape. Furthermore, filamentary structures tend to have a low density gradient along their axis and, in the perpendicular directions, they have a

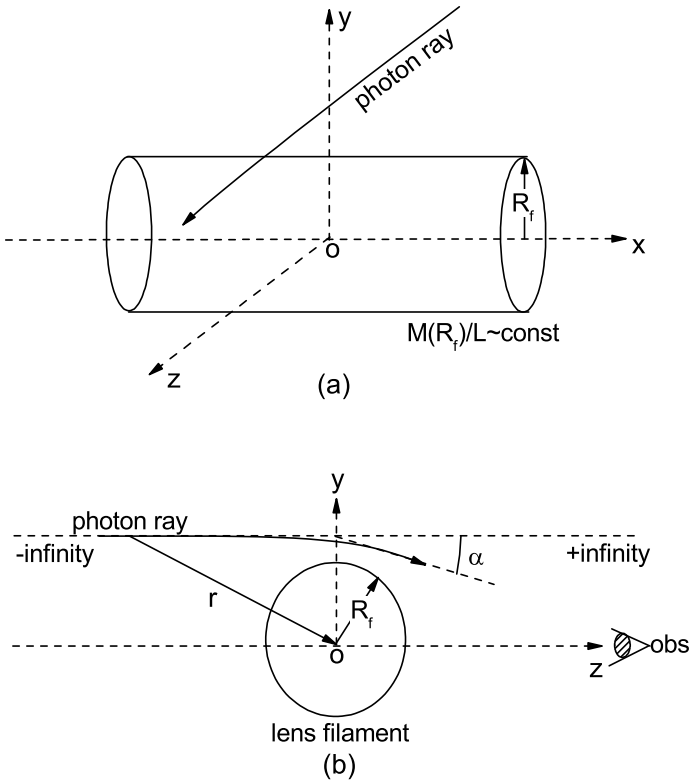

Figure 3.11: Light deflection by an infinitely elongated cylinder of constant mass density: The unperturbed photon traveling along the *z*-direction passes the filament at the distance y (impact parameter) from the filament's axis and is deflected by the angle $\hat{\alpha}$. The line density of the filament is assumed to be constant, $\lambda = M/L = \rho\pi R_f^2$, where ρ is the volume density and R_f is the cylinder's radius.

nearly uniform core which tapers to zero at larger radii (usually about $2-5$ times their core radius). Since filaments are typically much longer than their diameter, we shall approximately treat them as infinite uniform cylinders of radius $R_f = 2.5h^{-1}$Mpc. Lacking a structure formation N-body simulation in the framework of TeVeS, we shall adopt the naive assumption that filamentary structures have roughly the same properties as in a ΛCDM model and we will justify this approach in Sec. 3.3.3.

3.3.2 Modeling a filamentary lens

We investigate the effect of gravitational lensing caused by a straight filament connecting two galaxy clusters in both GR and TeVeS gravity. As a first simple approach, we shall take the filament's matter density profile to equal an infinitely elongated and uniform cylinder which is

illustrated in Fig. 3.11. The cylinder's line density,

$$\lambda = M/L = \rho\pi R_f^2, \tag{3.43}$$

is taken to be constant, where M is the total mass, L denotes the length along the symmetry axis, R_f is the cylinder's radius, and ρ is the volume density. A photon traveling perpendicular to the filament's axis will change its propagation direction when passing by the cylinder due to the local gravitational field which is assumed to be a weak perturbation to flat spacetime, i.e. all further calculations may be carried out within the nonrelativistic approximation discussed in Sec. 3.1.

In our example (see Fig. 3.11), the filament's axis is aligned with the x-axis, and light rays propagating along the z-direction are dragged into the $\pm y$-directions due to the symmetry of the resulting gravitational field. Keeping this configuration and introducing cylindrical coordinates, we may rewrite Eq. (3.13) as

$$\hat{\alpha}(y) = 4y \int_y^\infty \frac{\Phi'_{\mathrm{tot}}}{\sqrt{r^2 - y^2}} dr, \tag{3.44}$$

where the prime denotes the derivative with respect to the cylindrical radial coordinate r, i.e. $\Phi'_{\mathrm{tot}} = d\Phi_{\mathrm{tot}}/dr$. Considering the symmetry properties of our cylindrical lens model and the configuration in Fig. 3.11, Eq. (3.18) further simplifies to

$$\kappa(y) = \frac{1}{2} \frac{D_l D_{ls}}{D_s} \frac{\partial \hat{\alpha}(y)}{\partial y}, \tag{3.45}$$

with the convergence κ being related to the quantities γ ($\gamma^2 = \gamma_1^2$, $\gamma_2 = 0$) and $A \equiv \det \mathcal{A}$ as follows:

$$\kappa = \gamma = \frac{1 - A^{-1}}{2}. \tag{3.46}$$

Furthermore, let us introduce the complex reduced shear g given by

$$g = \frac{\gamma_1 + i\gamma_2}{1 - \kappa}. \tag{3.47}$$

To lowest order, this quantity is the expectation value of the ellipticity χ of galaxies weakly distorted by the lensing effect, thus corresponding to the signal which can actually be observed. The absolute value of the reduced shear is $|g| = \gamma/(1 - \kappa)$, and since we have $\kappa = \gamma \ll 1$ in our case, we obtain $|g| \sim \kappa = \gamma$. Note that the above result is independent of the particular law of gravity.

3.3.2 A The uniform filament in Newtonian gravity

The Newtonian gravitational field of our filament model is given by

$$g_N(r) = |\nabla\Phi_N(r)| = \begin{cases} \dfrac{G\lambda}{2\pi}\dfrac{r}{R_f^2}, & r < R_f \\ \\ \dfrac{G\lambda}{2\pi}\dfrac{1}{r}, & r \geq R_f \end{cases}, \tag{3.48}$$

with λ being the previously defined line density given by Eq. (3.43). For $R_f \leq y$, evaluating the integral (3.44) yields

$$\hat{\alpha}_N(y) = G\lambda = \text{const.} \tag{3.49}$$

Inserting the above into Eq. (3.45), we may obtain the corresponding convergence field. As expected, κ_N equals to zero outside the cylinder's projected matter density. For $y < R_f$, the deflection angle has to be calculated from

$$\hat{\alpha}_N(y) = \frac{2G\lambda y}{\pi}\left(\int_y^{R_f} \frac{rdr}{R_f^2\sqrt{r^2-y^2}} + \int_{R_f}^{\infty} \frac{dr}{r\sqrt{r^2-y^2}}\right). \tag{3.50}$$

Carrying out the integrations in (3.50), we finally end up with the following expression:

$$\hat{\alpha}_N(y) = \frac{2G\lambda}{\pi}\left(\frac{y\sqrt{R_f^2-y^2}}{R_f^2} + \arcsin\left(\frac{y}{R_f}\right)\right). \tag{3.51}$$

Using Eq. (3.45), the convergence in this case turns out to be

$$\kappa_N(y) = 2\frac{D_l D_{ls}}{D_s}\frac{G\lambda}{\pi R_f^2}\sqrt{R_f^2-y^2}. \tag{3.52}$$

3.3.2 B The uniform filament in TeVeS

Now we shall consider light deflection within the framework of TeVeS gravity, again using the simplistic form of the free interpolating function μ_B introduced at the end of Sec. 2.2.2 B. Assuming a cylindrically symmetric configuration, the total gravitational acceleration may be written in the following way:

$$g_M(r) = |\nabla\Phi_M(r)| = g_N(r) + \sqrt{g_N(r)a_0}, \tag{3.53}$$

where r denotes the cylindrical radial coordinate and $\Phi_M(r)$ is the total nonrelativistic gravitational potential in TeVeS. The constant $a_0 = 1.2 \times 10^{-10}\text{m s}^{-2}$ characterizes the acceleration scale at which MONDian effects start to become important compared to Newtonian contributions. Since filaments are the most low-density structures within the universe, their internal (Newtonian) gravity is very small. Therefore, the MONDian influence yields an enhancement of the gravitational field which is on the order of a_0/g_N, being extremely large in such objects. For this reason, we may expect a substantial difference concerning the lensing signal caused by filamentary structures in TeVeS. Equipped with Eqs. (3.44), (3.48) and (3.53) we are ready to proceed with the analysis of our cylindrical filament model: For $R_f \leq y$, the deflection angle is given by

$$\hat{\alpha}_M(y) = \hat{\alpha}_N(y) + \sqrt{\frac{8G\lambda a_0}{\pi}} y \int_y^\infty \frac{dr}{\sqrt{r}\sqrt{r^2 - y^2}} = G\lambda + \frac{\Gamma(1/4)}{\Gamma(3/4)}\sqrt{2G\lambda a_0 y}. \tag{3.54}$$

In this case, the convergence reads as follows:

$$\kappa_M(y) = \frac{D_l D_{ls}}{D_s}\frac{\Gamma(1/4)}{\Gamma(3/4)}\sqrt{\frac{G\lambda a_0}{8y}}. \tag{3.55}$$

For $y < R_f$, the integral (3.44) has to be split in several parts, similarly to Eq. (3.50). Using elementary calculus, we finally arrive at

$$\begin{aligned}\hat{\alpha}_M(y) =& \hat{\alpha}_N(y) + \sqrt{\frac{2G\lambda a_0}{\pi}}\frac{y^{3/2}}{R_f}\left(4\sqrt{\frac{R_f^2 - y^2}{R_f y}} - \mathcal{B}_{\left(y^2/R_f^2,1\right)}(3/4, 1/2)\right) \\ &+ \sqrt{\frac{2G\lambda a_0 y}{\pi}}\mathcal{B}_{\left(0,y^2/R_f^2\right)}(1/4, 1/2)\,,\end{aligned} \tag{3.56}$$

where $\hat{\alpha}_N(y)$ is given by (3.51) and $\mathcal{B}_{(p,q)}(a, b)$ is the generalized incomplete Beta function defined by

$$\mathcal{B}_{(p,q)}(a, b) = \int_p^q t^{a-1}(1 - t)^{b-1}dt, \quad Re(a), Re(b) > 0. \tag{3.57}$$

As the expression for the convergence κ_M turns out to be quite lengthy, we will drop it at this point.

From Eqs. (3.54) and (3.55), we find that α_M outside the cylinder's projection increases with the square root of the impact parameter y ($\alpha_N = \text{const}$) while κ_M decreases with the inverse square root of y ($\kappa_N = 0$). This reveals a fundamental difference between MOND/TeVeS and GR: Since $\kappa_N = 0$, we also have $\gamma_N = 0$ and $A_N = 1$ according to Eq. (3.46), meaning that there will be no

distortion effects as well as no change in the total flux between source and image, i.e. wherever the projected matter density is zero, the lens mapping will turn into identity. However, this is no longer true in the context of TeVeS as the convergence and the shear field do not vanish (cf. Fig. 3.12). Obviously, the MONDian influence does not only enhance effects that are already present in GR, but rather creates something new, which, in principle, could be used to distinguish between laws of gravity (see Sec. 3.3.6). Since α_M continues to increase with the square root of the impact parameter far away from the filament, one might wonder how this affects very distant systems and whether such a model leads to inconsistencies. As will become clear in a moment, there is, in fact, no real problem. The found growth of α_M is a direct consequence of modeling the filament as an infinite cylinder. Clearly, this approximation will break down once the impact parameter gets sufficiently large, at which point we expect the deflection angle to start decreasing. However, even if the approximation held at arbitrarily large values of y, one would not necessarily be in trouble. The reason is that one can only measure relative deflection angles: As α_M grows sublinearly, the relative deflection (caused by the filament) between light rays passing through some distant system will become very small, eventually turning toward zero if the system is located sufficiently far away from the filament. Finally, note that if one considers varying the inclination angle θ of the filament's axis to the line of sight, the lensing properties derived in this section have to be rescaled by a factor of $\sin^{-1}\theta$ in both GR and TeVeS.

3.3.3 Model application

From ΛCDM large-scale structure simulations, it has been shown that there are close cluster pairs with a separation of $5h^{-1}$Mpc or less which are always connected by a filament [171]. At separations between 15 and $20h^{-1}$Mpc, still about a third of cluster pairs is connected by a filament. On average, more massive clusters are connected to a larger number of filaments than less massive ones. Additionally, these simulations indicate that the most massive clusters form at the intersections of the filamentary backbone of large-scale structure. For straight filaments, the radial profiles show a fairly well-defined radius R_f beyond which the profiles closely follow an r^{-2} power law, with R_f being around $2.0h^{-1}$Mpc for the majority of filaments. The enclosed overdensity within R_f varies from a few times up to 25 times the mean density, independent of the filament's length. Along the filaments' axes, material is not distributed uniformly. Towards the clusters, the density rises, indicating the presence of cluster infall regions.

As previously stated, we will assume that filamentary structures in TeVeS have similar prop-

erties as in a CDM dominated universe based on GR. To justify this assumption, one may, for example, resort to the μHDM cosmology (see Sec. 3.1.3) and on the fact that filaments are generic [9] and have similar characteristics in hot dark matter (HDM) and CDM scenarios [172–174]. For instance, neutrino dark matter is known to collapse into sheets and filaments in HDM simulations. Concerning the uniform model introduced in Sec. 3.3.2, we thus take the filament's radius as $R_f = 2.5h^{-1}$Mpc, and set its overdensity to $\delta = 20$, where δ denotes the density contrast defined by

$$\delta = \frac{\rho - \rho_0}{\rho_0} \tag{3.58}$$

and ρ_0 is the intergalactic mean density.

On the other hand, analyzing the Perseus-Pisces segment, [175] concluded that a MONDian description of filaments would not need any additional nonbaryonic mass component. Due to rather large systematic uncertainties, however, this result remains highly speculative and does not rule out our approach where filamentary structures have higher densities. Nevertheless, we will also include this case, where filaments consist of baryonic matter only, into our analysis. Since the absolute density of a filament in this situation is approximately by a factor $10 - 100$ smaller than in μHDM, we do expect the MONDian influence to become even more important (compared to a GR scenario with the same background cosmology). Encouraged by the MOND simulations discussed in Ref. [176], we shall stick to the assumption that both shapes and relative densities of filaments are similar to the ΛCDM case when considering a universe made out of baryonic matter only, thus keeping the choice $\delta = 20$.

In order to calculate the intergalactic mean density and the necessary angular diameter distances for lensing, we shall use the flat μHDM cosmology in Eq. (3.26) introduced in Sec. 3.1.3. To investigate whether the such derived results are sensitive to the background assumption, we will also consider the less realistic flat minimal-matter cosmology given by Eq. (3.25). Furthermore, the model-dependent intergalactic mean density ρ_0 is calculated according to

$$\rho_0 = \Omega_m \rho_c (1 + z_l)^3, \tag{3.59}$$

where $\rho_c = 3H_0^2/8\pi G$ is the critical density and z_l is the lens redshift, i.e. the filament's redshift. Concerning the framework of GR, we shall use a flat ΛCDM cosmology with $\Omega_m = 0.3$ and

[9] Note that the occurrence of filamentary structures is a generic feature of gravitational collapse from a Gaussian random field which does not depend on the specific form of the law of gravity.

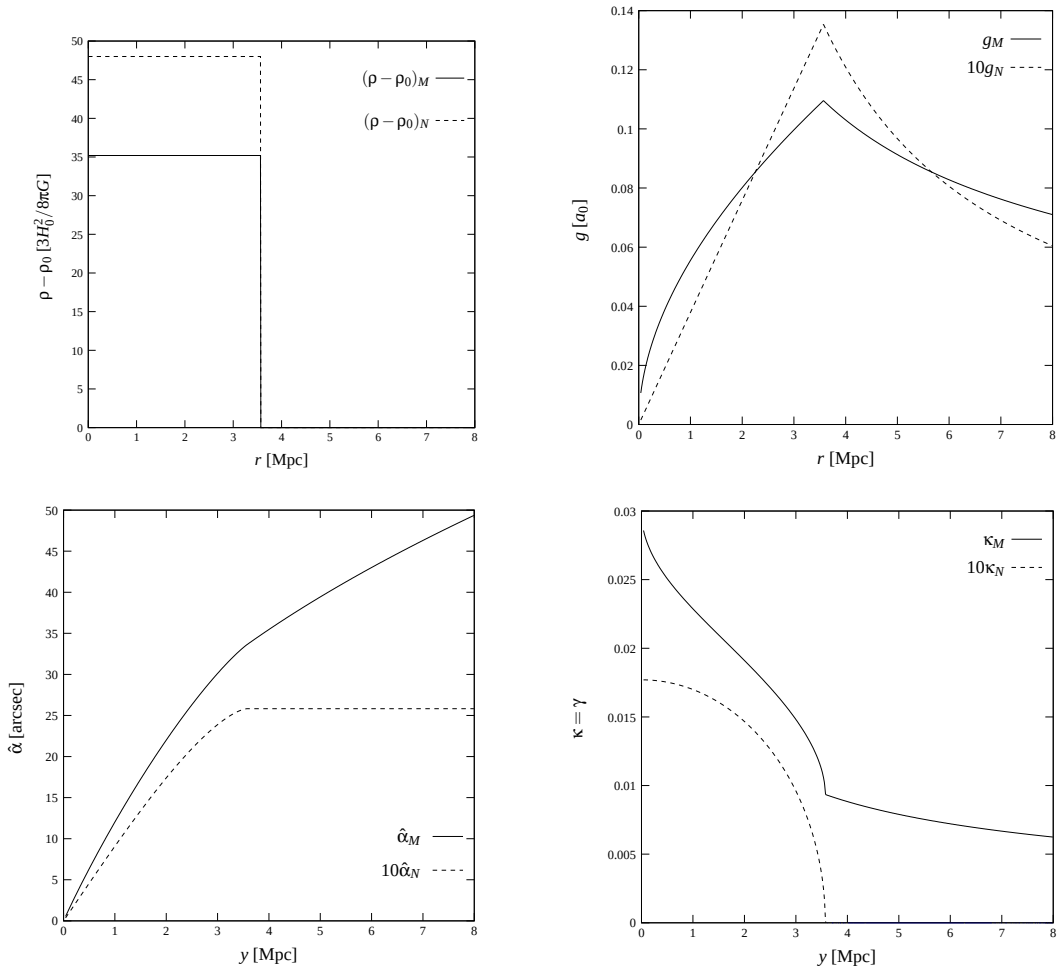

Figure 3.12: Density profile $\rho(r)$ (*top left*), radial evolution $g(r)$ of the total gravitational acceleration (*top right*), deflection angle $\hat{\alpha}(y)$ (*bottom left*) and convergence $\kappa(y)$ (*bottom right*; $\kappa = \gamma = (1 - A^{-1})/2$) in GR (dashed) and TeVeS (solid) gravity for the uniform filament cylinder model whose axis is inclined by an angle $\theta = 90°$ to the line of sight, assuming $z_l = 1$, $z_s = 3$ and the flat μHDM cosmology (3.26) in TeVeS. The radius of the filament is $R_f = 2.5\,h^{-1}$Mpc and the overdensity within the filament is taken as 20 times the mean density ρ_0. Note that, for consistency, the Newtonian results are based on a flat ΛCDM cosmology with $\Omega_m = 0.3$ and $\Omega_\Lambda = 0.7$.

$\Omega_\Lambda = 0.7$, which allows one to consistently compare the corresponding results to those obtained in TeVeS.

3.3.3 A The μHDM scenario

Using the TeVeS cosmology specified in (3.26) and considering a filament which is inclined by an angle $\theta = 90°$ to the line of sight, both the Newtonian and the MONDian deflection angle as well as the corresponding convergence are plotted in the bottom left and bottom right panel of Fig. 3.12, with the filament placed at redshift $z_l = 1$ and background sources at $z_s = 3$. Whereas the Newtonian signal is rather small, $\kappa_N \lesssim 10^{-3}$, the filament can create a convergence on the

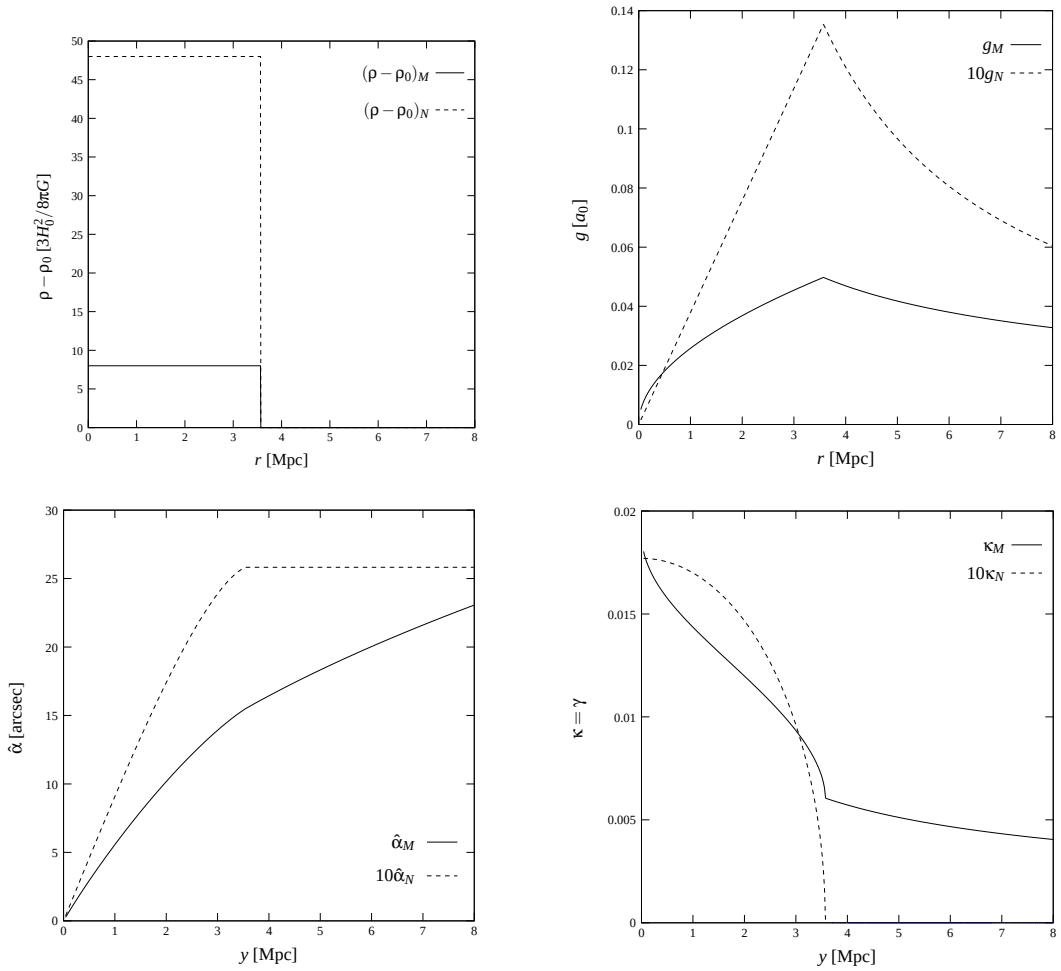

Figure 3.13: Same as Fig. 3.12, but now assuming the flat minimal-matter cosmology Eq. (3.25) in TeVeS.

order of $\kappa \sim 0.01$ in TeVeS. This even remains true in the outer regions, where $\kappa_N = 0$, if we take into account that it can have other orientations, i.e. a different inclination angle θ. For example, a nearly end-on filament with $\theta = 10°$ has a lensing power 6 times larger than that of a face-on filament, i.e. $\theta = 90°$.

Using Eq. (3.46), we therefore infer that a single TeVeS filament may generate a shear signal which is on the same order as the convergence, $\gamma \sim 0.01$, as well as a magnification bias at a 2% level, $A^{-1} \sim 1.02$. Additionally, we present the density $\rho(r)$ and the radial evolution of the total gravitational acceleration $g(r)$ in the top left and top right panel of Fig. 3.12, respectively. Note again that the GR results are based on a flat ΛCDM cosmology with $\Omega_m = 0.3$ and $\Omega_\Lambda = 0.7$ for consistency.

3.3.3 B The baryons-only scenario

Now let us switch to the minimal-matter background given by (3.25). Keeping all remaining parameters exactly the same as in the last section, the corresponding results are presented in Fig. 3.13. Although the convergence is slightly smaller than in the μHDM case (roughly by a factor of $1.5 - 2$), we find that also in this case, single filamentary structures are capable of producing a lensing signal which is of the same order, $\kappa \sim \gamma \sim 0.01$. Again, this is even true outside the "edges" of the filament's projected matter density, accounting for the fact that the inclination angle θ may vary, $0° \leq \theta \leq 90°$.

3.3.4 Oscillating density model

Matter density fluctuations are steadily present throughout the universe. Thus, as a more realistic approach, we shall use a fluctuating density profile to describe a filament and its surrounding area including voids, i.e. regions in the universe where the local matter density is below the intergalactic mean density. To keep our analysis on a simple level, let us write the density fluctuation as (r still denotes radial coordinate in cylindrical coordinates)

$$\delta(r) = \begin{cases} \delta_0 \left(\frac{\pi r}{R_f}\right)^{-1} \sin\left(\frac{\pi r}{R_f}\right), & r < 2R_f \\ \\ 0, & r \geq 2R_f \end{cases}, \tag{3.60}$$

where $\delta(r)$ denotes the density contrast defined in (3.58), $\delta_0 = 4$ is the density fluctuation amplitude (this value ensures a positive overall matter density) and $R_f = 2.5h^{-1}$Mpc again the filament's characteristic radius. Multiplying with the mean density ρ_0 and integrating along the radial direction, we find that the mass per unit length enclosed by an infinite cylinder of radius r reads as (Note that we neglect the contribution due to the mean density background)

$$\frac{M(r)}{L} = \begin{cases} \frac{2\rho_0\delta_0 R_f^2}{\pi}\left(1 - \cos\left(\frac{\pi r}{R_f}\right)\right), & r < 2R_f \\ \\ 0, & r \geq 2R_f \end{cases}, \tag{3.61}$$

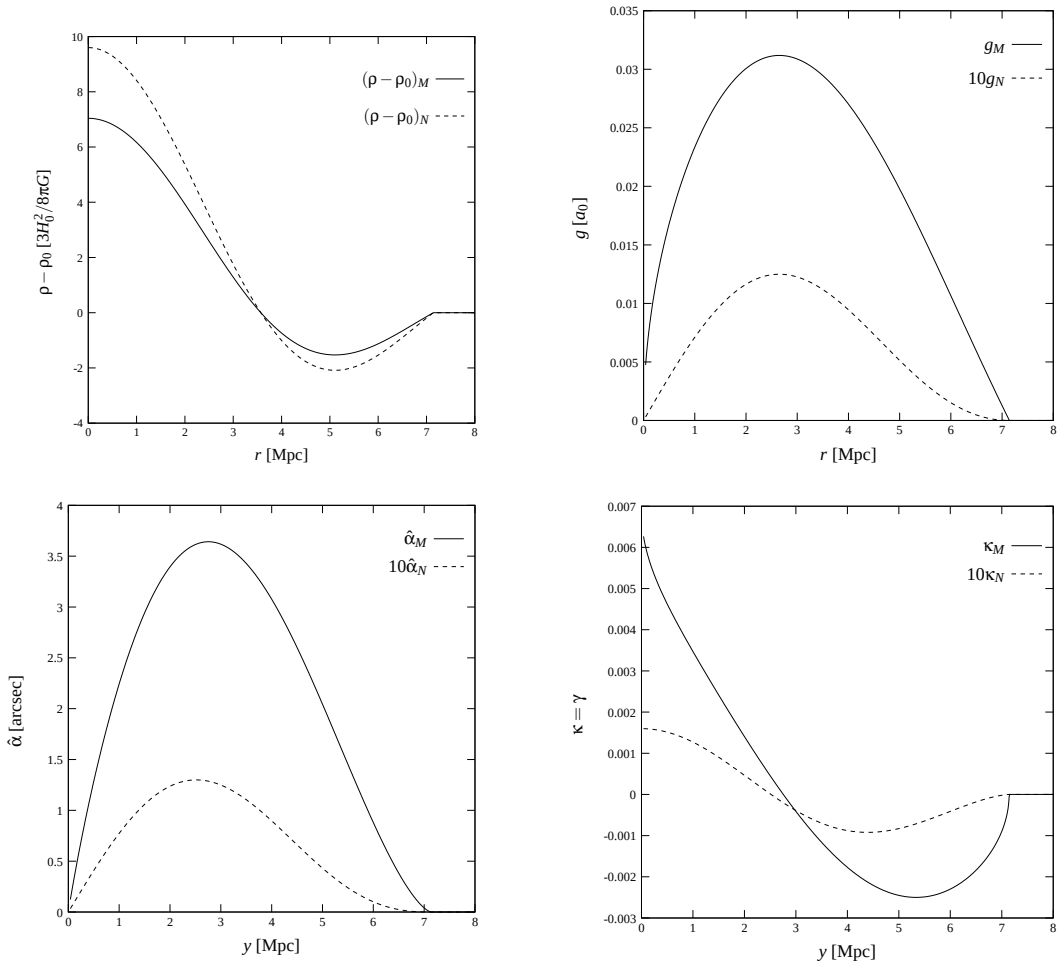

Figure 3.14: Density profile $\rho(r)$ (top left), radial evolution $g(r)$ of the total gravitational acceleration (top right), deflection angle $\hat{\alpha}(y)$ (bottom left) and convergence $\kappa(y)$ (bottom right; $\kappa = \gamma = (1 - A^{-1})/2$) in GR (dashed) and TeVeS (solid) gravity for the oscillating density model given by Eq. (3.60) ($\theta = 90°$), assuming $\delta_0 = 4$, $R_f = 2.5\,h^{-1}$Mpc, $z_l = 1$, $z_s = 3$ and the flat μHDM cosmology (3.26) in TeVeS. Note that, for consistency, the Newtonian results are based on a flat ΛCDM cosmology with $\Omega_m = 0.3$ and $\Omega_\Lambda = 0.7$.

where ρ_0 is the mean intergalactic matter density given by Eq. (3.59). From Eq. (3.61), we directly see that the Newtonian gravitational acceleration in this case is

$$g_N(r) = \frac{GM(r)}{2\pi L}\frac{1}{r}. \tag{3.62}$$

Using Eqs. (3.44), (3.53) and (3.62), we are now able to numerically calculate the lensing properties of this configuration. Choosing lens and source redshift again as $z_l = 1$ and $z_s = 3$, respectively, and assuming the previously used cosmological background models (see Sec. 3.3.3), the resulting deflection angle as well as the convergence are shown in bottom panel of Fig. 3.14 (flat μHDM cosmology) and 3.15 (flat minimal-matter cosmology), assuming $\theta = 90°$. Here the occurrence of negative κ-values simply reflects the fact that our model (3.60) generates a local

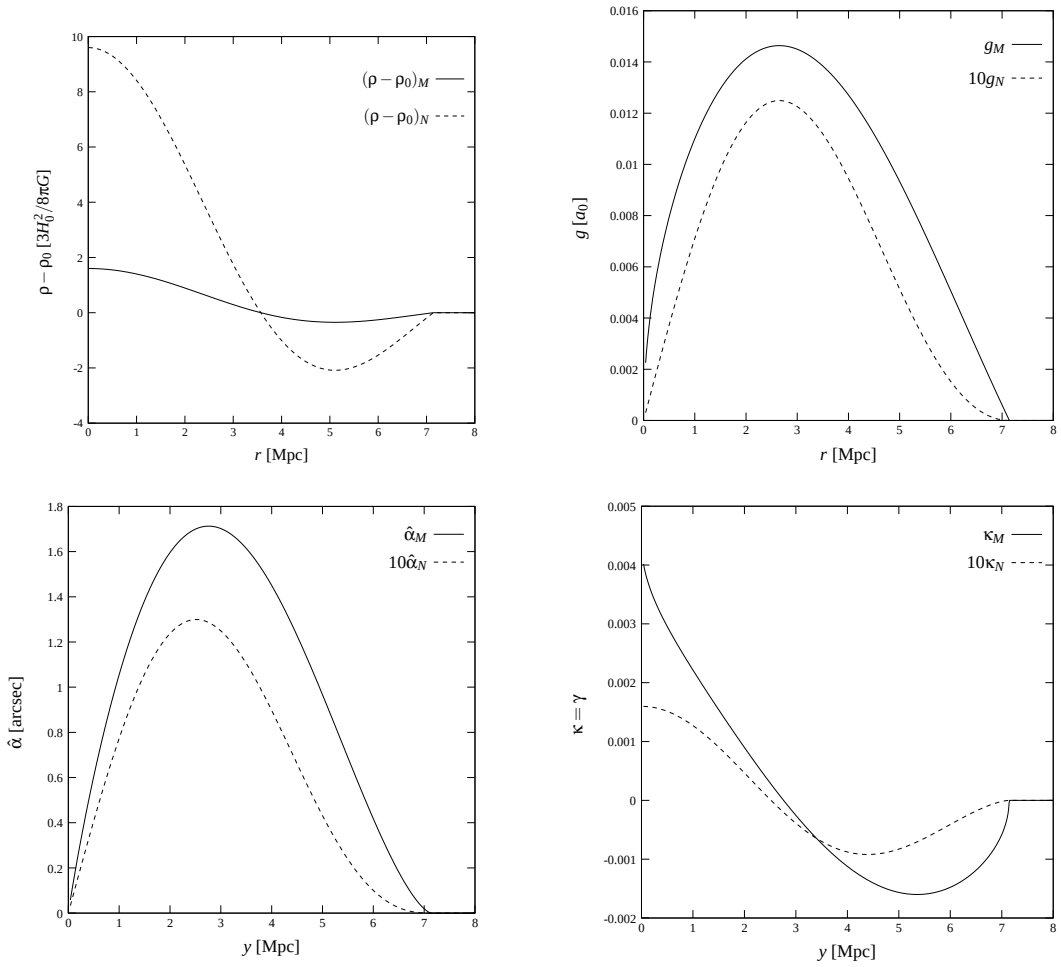

Figure 3.15: Same as Fig. 3.14, but now assuming the flat minimal-matter cosmology Eq. (3.25) in TeVeS.

underdensity, $1+\delta(r)<1$, with the overall matter density ρ being strictly non-negative at any radius. Compared to the Newtonian case where $\kappa_N \lesssim 10^{-4}$, we again find that a face-on TeVeS filament may cause a significantly larger lensing signal, which is now on the order of $\kappa\sim\gamma\sim 10^{-3}$ within both TeVeS cosmologies. As the results of the μHDM and the minimal-matter cosmology approximately differ by a factor $1.5-2$ just as in Sec. 3.3.3, the order-of-magnitude lensing effects caused by TeVeS filaments are also in this case more or less cosmologically model-independent.

Close to the filament's axis, where $\kappa\sim 4\times 10^{-3}$, one can actually have a lensing signal $\kappa=\gamma=0.01$ assuming that the inclination angle is small, $\theta\lesssim 20^\circ$. Although such angles correspond to rather special configurations, we may conclude that also for our simple oscillation model, single TeVeS filaments potentially generate a lensing signal ~ 0.01, which is similar to our result in Sec. 3.3.3. However, note that the above discussion is based upon the choice of (3.60) and $\delta_0=4$. Considering a higher overdensity along its axis, even a face-on filament described by a similar fluctuating profile could easily create a shear field $\gamma\sim 0.01$ for $y\lesssim R_f$.

Table 3.3: Parameters of the superimposed filaments in Sec. 3.3.5

Plane	PA [°]	incl. [°] [b]	Shift from origin [kpc] [c]	Redshift z
2	90	12	$(0, -150)$	0.25
3	45	45	$(600, 0)$	0.30

[b] Inclination of the filament's axis to the line of sight.
[c] Shift of the filament's projection in the corresponding redshift plane.

3.3.5 Superimposing filaments with other objects

To demonstrate the contribution of filamentary structures to the lensing map of other objects, e.g. galaxy clusters, we superimpose two differently orientated filaments with a toy cluster along the line of sight, assuming the previously introduced μHDM cosmology and different redshifts for each component. If all objects are sufficiently far away from each other ($\gtrsim$ 100Mpc), we may approximately treat them as isolated lenses at a certain redshift slice, i.e. the corresponding deflection angles can be calculated separately [10]. Thus, we may resort to the well-known multiplane lens equation [129, 177]:

$$\boldsymbol{\eta} = \frac{D_s}{D_1}\boldsymbol{\xi}_1 - \sum_{i=1}^{n} D_{is}\hat{\boldsymbol{\alpha}}_i(\boldsymbol{\xi}_i), \tag{3.63}$$

where n is the number of lens planes, D_{ij} corresponds to the angular diameter distance between the i-th and the j-th plane and $\boldsymbol{\xi}_i$ is recursively given by

$$\boldsymbol{\xi}_i = \frac{D_i}{D_1}\boldsymbol{\xi}_1 - \sum_{j=1}^{i-1} D_{ji}\hat{\boldsymbol{\alpha}}_j(\boldsymbol{\xi}_j), \quad 2 \le i \le n. \tag{3.64}$$

Comparing Eq. (3.63) to the lens equation for a single lens plane, we identify the total deflection angle as

$$\hat{\boldsymbol{\alpha}}_{\rm tot}(\boldsymbol{\xi}_1) = \hat{\boldsymbol{\alpha}}_1(\boldsymbol{\xi}_1) + \sum_{i=2}^{n} \frac{D_{is}}{D_{1s}}\hat{\boldsymbol{\alpha}}_i(\boldsymbol{\xi}_i) = \hat{\boldsymbol{\alpha}}_c + \hat{\boldsymbol{\alpha}}_f. \tag{3.65}$$

Here $\hat{\boldsymbol{\alpha}}_c$ and $\hat{\boldsymbol{\alpha}}_f$ are the deflection angle of an isolated cluster at z_1 and an additional contribution due to the superimposed filaments, respectively. Analog to the case of a single plane, further lensing quantities such as the total convergence and the total shear can be calculated from Eq. (3.65), using the general relations introduced in Sec. 3.1. For simplicity, we shall assume that the

[10] Note that in general, one would have to solve the full nonlinear TeVeS scalar field equation, which is beyond the scope of the present analysis.

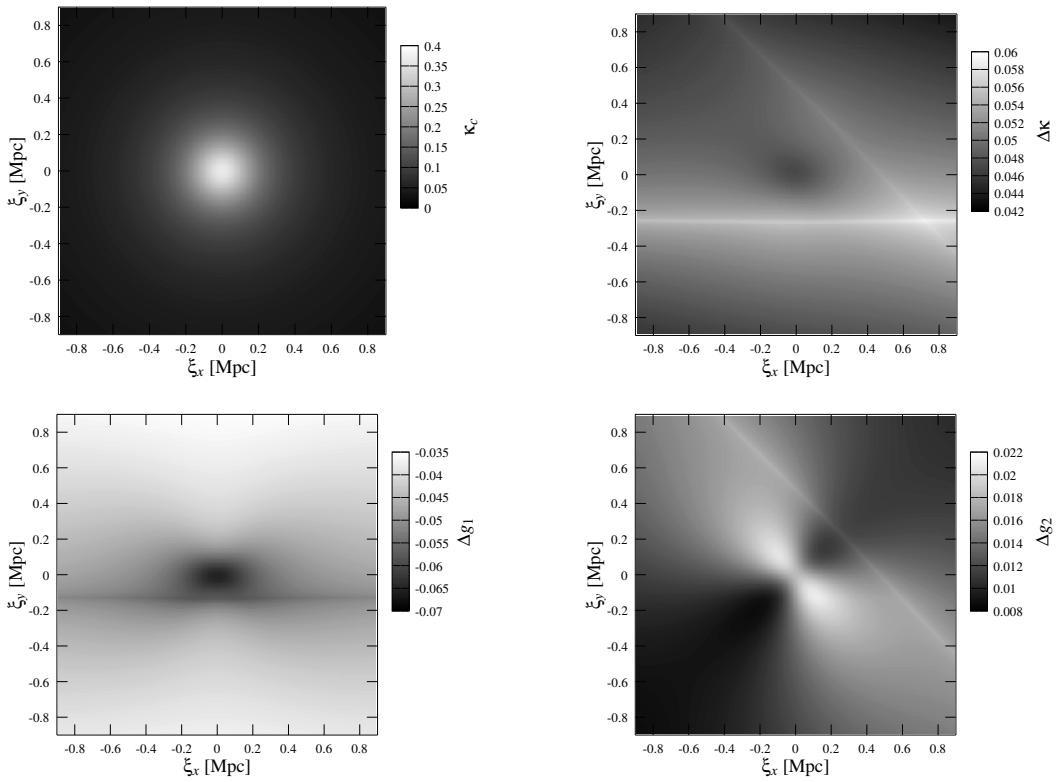

Figure 3.16: Superposition of two filaments with a toy cluster along the line of sight: Shown are the cluster's convergence map κ_c in absence of any filamentary structures along the line of sight (*top left*) and the filaments' contribution $\Delta\kappa = \kappa_{tot} - \kappa_c$ to the total convergence (*top right*) and as well as to the components of the reduced shear, $\Delta g_1 = \gamma_{tot,1}/(1-\kappa_{tot}) - \gamma_{c,1}/(1-\kappa_c)$ and $\Delta g_2 = \gamma_{tot,2}/(1-\kappa_{tot}) - \gamma_{c,2}/(1-\kappa_c)$, respectively (*bottom panel*).

cluster's TeVeS potential follows the "quasi-isothermal" profile given in Ref. [93]:

$$\Phi(\mathbf{r}) = v^2 \log \sqrt{1 + \frac{|\mathbf{r} - \mathbf{r}_0|^2}{p^2}}, \tag{3.66}$$

with v being the asymptotic circular velocity, p a scale length and $\mathbf{r}_0$ the center's position.

Concerning the numerical setup, we set $v^2 = 2 \times 10^6 \mathrm{km}^2\ \mathrm{s}^{-2}$ and $p = 200\mathrm{kpc}$, fixing the cluster's redshift to $z_1 = 0.2$. Furthermore, we choose the uniform filament model discussed in Sec. 3.3.2 and assume that filaments have a constant overdensity of $\delta = 20$ as well as the same characteristic radius $R_f = 2.5h^{-1}\mathrm{Mpc}$. While the cluster is centered at the origin ($\xi_x = \xi_y = 0$), the two filaments are set up according to the parameters given in Table 3.3. Finally, we place the source plane at a redshift of $z_s = 1$. Note that this specific setting corresponds to a more realistic lensing configuration compared to our order-of-magnitude analysis in the previous sections, where our choice is again motivated by results based on a ΛCDM universe.

From the top right panel of Fig. 3.16, we see that the filaments' contribution to the total

convergence map, $\Delta\kappa = \kappa_{tot} - \kappa_c$ (κ_c is the cluster's convergence map in absence of any filamentary structures along the line of sight) is comparable to our previous findings, with the signal again being on the order of 0.01. Also, note the distortion effects caused by the cluster and the peak close to the region where the two filaments overlap. Obviously, the contribution pattern depends on the actual configuration as well as on the type and amount of the considered objects along the line of sight and can generally be quite complex. Additionally, we present the changes in the reduced shear components, $\Delta g_1 = \gamma_{tot,1}/(1-\kappa_{tot}) - \gamma_{c,1}/(1-\kappa_c)$ and $\Delta g_2 = \gamma_{tot,2}/(1-\kappa_{tot}) - \gamma_{c,2}/(1-\kappa_c)$, due to the filaments' presence in the bottom panel of Fig. 3.16.

At this point, we should emphasize that we have considered the impact of filamentary structures alone. Depending on their particular position along the line of sight, additional (foreground) objects such as galaxies, galaxy clusters or voids might locally contribute on a comparable level or even exceed the signal caused by filaments. Of course, this further complicates the interpretation of the corresponding lens mapping and we conclude that extracting the filaments' contribution can generally pose quite a challenge.

3.3.6 Discussion

Regardless of the actual used cosmological background, we have shown that TeVeS filaments can account for quite a substantial contribution to the weak lensing convergence and shear field, $\kappa \sim \gamma \sim 0.01$, as well as to the amplification bias, $A^{-1} \sim 1.02$. This is even true outside, but close ($y \sim 2R_f$) to the projected "edges" of the filament's matter density, taking into account that the filamentary structures may be inclined to the line of sight by rather small angles ($\theta \lesssim 20°$). Additionally, we have demonstrated the impact of filaments onto the convergence map of other objects by considering superposition with a toy cluster along the line of sight. Again, our results have shown an additional contribution comparable to that of a single isolated filament and that the contribution pattern of filaments can be generally quite complex [11].

Although our analysis is mainly of theoretical interest, the above result points to an interesting possibility concerning recent measurements of weak lensing shear maps. For instance, the weak shear signal in the "dark matter peak" of Abell 520 [169] is roughly at a level of 0.02, which is comparable to what filaments could produce in TeVeS, but not in GR (also cf. [179]). Therefore,

[11] Here we have considered the lensing signal generated by single filaments alone. Simulating the cosmic web in a standard ΛCDM cosmology, [178] have found a shear signal $\gamma \sim 0.01 - 0.02$ along filamentary structures, which seems quite similar to what TeVeS can do. Note, however, that this signal is entirely dominated by the simulation's galaxy clusters, with the filament's signal being much smaller, approximately on the order of $10^{-4} - 10^{3}$.

we conclude that filamentary structures might actually be able to cause such anomalous lensing signals within the modified framework.

In principle, the predicted difference in the weak lensing signal could also be used to test the viability of modified gravity. As several attempts to detect filaments by means of weak lensing methods have failed so far, e.g. the analysis of Abell 220 and 223 [180], this might already be a first hint to possible problems for such modifications. On the other hand, shear signals around $\gamma \sim 0.01$ are still rather small to be certainly detected by today's weak lensing observations, and lacking N-body structure formation simulations in TeVeS, we cannot even be sure about how filaments form and how they look like in a MONDian universe compared to the CDM case. Another point of concern is whether the treatment within the nonrelativistic limit of TeVeS provides a good description at the scales we have considered here. Previous work has shown that TeVeS vector perturbations have a significant impact on the evolution of large-scale structure [86, 87], which could also be important for a discussion of filaments. Clearly, more investigation is needed to gain a better understanding about the impact of filamentary structures.

3.4 Constraining neutrino dark matter with cluster lenses

3.4.1 Massive sterile neutrinos: A possible remedy for TeVeS

As we have discussed in Sec. 3.1.3, massive ordinary neutrinos with a mass around 2eV provide an interesting candidate for the missing energy-density in TeVeS and the question of the viability of the assumed neutrino mass is soon expected to be answered by the upcoming results of the KATRIN experiment. Nevertheless, the rather unsatisfactory results of this solution on large scales, especially for the CMB anisotropy power spectrum (a ΛCDM model provides a better fit to the data), and problems within galaxy groups [80] have led to deem the hypothesis of very massive ordinary neutrinos unattractive. Alternatively, the required additional matter could be provided in the form of (right-handed) sterile neutrinos (SNs) which are motivated by theoretical considerations in particle physics (e.g., see Refs. [181–183] and references therein) and offer an elegant way to explain the small masses of active neutrinos via the *seesaw mechanism* [12] [184–186]. The main motivation for considering the existence of one or possibly more generations of SNs comes

[12]The seesaw mechanism is a possibility to generate neutrino masses. In its simplest form, the standard model Lagrangian is extended by a combination of Dirac and Majorana mass terms, with the left-handed Majorana mass set to zero and the right-handed Majorana mass to a large value which is typically associated with some grand unification scale. As a consequence of this construction, the mass matrix, whose eigenvalues describe the physical neutrino masses, gives rise to a very light left-handed neutrino and a very heavy right-handed one.

from the combined data of different neutrino oscillation experiments: Since the flavor eigenstates of neutrinos are different from their corresponding mass eigenstates, the principles of quantum mechanics dictate that there is a probability of finding a neutrino with an initially given flavor in another flavor state at a later time, i.e. neutrinos may oscillate into a different flavor state. This behavior has been observed in several experiments based on the detection of solar and atmospheric neutrinos, and provides firm evidence for the fact that neutrinos are not massless particles. Furthermore, these experiments allow one to determine the squared mass differences Δm^2 between distinct mass eigenstates. If there were only three generations of ordinary neutrinos, then there should only exist two independent Δm^2's. However, results of more recent laboratory-based experiments such as the Liquid Scintillator Neutrino Detector seem to disagree with this picture as their interpretation requires at least three independent Δm^2's. The problem can be alleviated by adding SNs to the standard model which may oscillate into ordinary neutrinos and vice versa. As experimental effort into this direction has just begun and stringent constraints on the properties of SNs do not yet exist, there is currently great freedom in their theoretical description.

Returning to the field of gravitation and cosmology, the conceptual advantage of such an approach lies in combining the success of modified gravity on small scales with new physics in a sector of the standard model which is known to be incomplete [187] and in need of revision [13]. Motivated by a possible interpretation of the MiniBooNE experiment [188], Angus [189] has suggested to use a single light species of SNs with a mass of approximately 11eV and investigated its consequences. If such SNs decouple while they are relativistic and in thermal equilibrium, one should obtain both a background evolution and a CMB anisotropy power spectrum which are basically indistinguishable from a standard ΛCDM cosmology [14], while at the same time, this additional hot dark matter (HDM) component may give rise to a correct prediction of the linear matter power spectrum and represents a suitable candidate for the missing mass in galaxy clusters without spoiling MONDian dynamics on galactic scales [190]. As for the nonlinear regime of structure formation, the situation is still unclear. Because of the more sophisticated mathematical structure of the nonlinear TeVeS field equations (or that of related theories) as opposed to those

[13] Without resorting to a modification of gravity, SNs in the keV mass range still provide a viable candidate for all the dark matter in the universe [183]. In this case, however, one may expect similar fine-tuning issues on small scales as in current CDM models.

[14] Although this has not been explicitly calculated, one can use the following argument: For common choices of the TeVeS parameters, the impact of perturbations due to the extra fields is small at early times, i.e. those relevant for the CMB. Thus the theory exhibits a GR-like behavior, which allows to directly adopt the results of Angus for TeVeS. This is further supported by the nearly identical results for the CMB power spectrum in TeVeS [86] and GR [189], assuming three active neutrinos with a mass around 2eV. However, it is still an open question whether secondary anisotropies such as the thermal or kinetic Sunyaev-Zel'dovich effects leave a different signature than in ΛCDM.

of GR, there seems currently no way to gain reliable information about the nonlinear evolution. This difficulty is somewhat reflected by the fact that the resulting field equations in the quasistatic, nonrelativistic limit typically remain highly nonlinear. Assuming an *ad hoc* modification of the original MOND formula Eq. (2.33), however, a first simplified attempt into this direction is discussed in Ref. [191].

It is noteworthy that TeVeS or TeVeS-like theories in combination with sufficiently abundant massive neutrinos provide the most consistent relativistic MOND framework presented in the literature so far [15]; nevertheless, there are still innumerable aspects which need to be tested further. As we have discussed in Sec. 3.2.1, one possibility to employ the tool of gravitational lensing is to test the theory with the help of multiple-image galaxy lens systems. Another way of challenging the theory is offered by weak galaxy-galaxy lensing. Using data from the Red-Sequence Cluster Survey and the Sloan Digital Sky Survey (SDSS), it has been found that the most luminous galaxies ($\gtrsim 10^{11} L_{\odot}$) would require a substantial fraction of nonbaryonic matter [192]. Although this result needs to be confirmed by larger data sets before a firm conclusion can be drawn, it might hint towards a problem with the original MOND idea on galactic scales. Again, SNs with a mass around 11eV could provide a remedy as they should be able to cluster densely enough in such massive systems [190]. However, it remains to be seen in detail whether such an approach can explain observations. Summarizing the above, we note that the assumption of 11eV SNs has the potential to remedy the problems of TeVeS-like theories on many different scales and therefore merits further investigation.

In the following, we suggest to test TeVeS and the massive SN hypothesis in the context of complex lens systems which are typically present in the central regions of galaxy clusters. A previous analysis [193] already revealed that such an environment can put stringent constraints on the distribution and plausibility of the needed dark neutrino component, thus providing an excellent testbed for our purposes. Generally, the advantage of galaxy clusters lies in the independent estimates of baryonic matter, inferred from observed x-ray and stellar luminosities, and of the system's total mass distribution based on a combination of weak and strong gravitational lensing. Being insensitive to the dynamical state of the deflecting mass, the latter techniques are particularly suited to constrain the properties of the dark component. In contrast to weak lensing estimates, strong lensing is basically free of statistical uncertainties and offers a unique and robust probe of the mat-

[15] Note that there are certain theories which aim at reproducing MOND and large-scale observations without any additional dark matter [40], but it is currently unknown whether such models naturally give rise to the observed properties of galaxy clusters.

ter distribution on scales $\lesssim$ 100kpc. Here we shall use strong lensing to further test the viability of 11eV SNs. Unlike conventional CDM, light SNs are subject to strong phase-space bounds set by the Tremaine-Gunn limit [194], which allows one to check cluster lens models inferred within the modified framework for consistency. Since this limit prevents SNs from clustering into dense clumps, galaxy cluster lenses with a considerable amount of dark substructure provide an ideal target for our intentions. As a first example, we shall study the galaxy cluster Abell 2390 (A2390) with its notorious straight arc, and investigate whether it is possible to reproduce this particular lens feature in TeVeS. Again, we shall restrict ourselves to weak fields and quasistatic systems [16], which allows one to make use of the relations presented in Sec. 3.1. Based on the assumption of a single species of 11eV SNs [189, 190], we shall further use a flat cosmological model with

$$\Omega_m = \Omega_b + \Omega_\nu = 0.29, \quad \Omega_\Lambda = 0.71, \quad h = 0.7 \tag{3.67}$$

to calculate angular diameter distances in the context of gravitational lensing. Note that this gives a background which is virtually indistinguishable from a standard ΛCDM model. A particular choice for the free function $\mu_B(y)$, suitable for the gravitational lensing analysis of A2390, will be given and discussed in Sec. 3.4.4.

The following sections are structured as follows: Starting with an observational summary of the galaxy cluster A2390 and its pronounced straight arc in Sec. 3.4.3, we highlight why this system provides an excellent candidate for our intentions. Continuing with the setup for a simplified density model of A2390 in Sec. 3.4.4, we discuss results for quasiequilibrium configurations in Sec. 3.4.5. Based on the latter, we outline a systematic approach to cluster lenses in TeVeS, and describe a lens model for the straight arc in Sec. 3.4.6. Finally, we conclude in Sec. 3.4.7. For clarity, several technical and numerical details are given in the appendix.

3.4.2 The Tremaine-Gunn bound

In the following, we shall discuss why light (ordinary or sterile) neutrinos cannot cluster into arbitrarily dense clumps. If one assumes that such neutrinos were thermally produced in the early universe and account for the missing mass in galaxy clusters, this fact can then be used to place a lower bound on the neutrino mass, which is known as the Tremaine-Gunn bound [194]. At early times, when temperatures are sufficiently large such that one may neglect the particles' rest mass,

[16] Note a caveat here: The present approximation ignores possible contributions arising from perturbations of the vector field A_μ which could have a significant impact on cluster scales. This issue is further discussed in Sec. 3.4.7.

the neutrinos are in thermal equilibrium and their distribution is basically given by the Fermi-Dirac distribution of a massless particle (here we consider a single neutrino species and ignore perturbations),

$$f(\mathbf{p})d^3p = \frac{g_\nu}{(2\pi)^3}\left(e^{p/T}+1\right)^{-1} d^3p, \tag{3.68}$$

where we have used natural units with $\hbar = c = 1 = \kappa_B$ (κ_B is the Boltzmann constant), T denotes the temperature and g_ν is the degeneracy factor. As the universe cools down, the neutrinos eventually decouple from the rest of the cosmic inventory (at around $T \sim 1$MeV) and their Fermi-Dirac distribution freezes in. Since both their momenta and temperature scale as a^{-1} thereafter, their distribution today is still given by Eq. (3.68) - not by the equilibrium distribution of nonrelativistic particles - because the phase space distribution was preserved after decoupling. Furthermore, their present temperature reads

$$T_\nu = \left(\frac{4}{11}\right)^{1/3} T_\gamma \approx 1.95K, \tag{3.69}$$

where T_γ is the observed temperature of the CMB today and the prefactor results from the fact that the additional heating due to electron-positron annihilation occurred after neutrino decoupling. The argument presented in Ref. [194] is now the following: Because the neutrinos are noninteracting, the density of a fluid element in phase space is conserved due to Liouville's theorem. Therefore, the maximum fine-grained phase-space density is conserved. As a consequence, the maximum coarse-grained phase-space density must not exceed that of the fine-grained one. From Eq. (3.68), we find that the maximum fine-grained phase-space density is $g_\nu/2(2\pi)^3$ which provides a limit for any bound neutrino system found today. Not that this phase-space bound corresponds to half of the Pauli limit. If these systems resemble isothermal gas spheres, their velocity distribution is Maxwellian and the maximum coarse-grained phase-space density is $\rho_0 m_\nu^{-4}(2\pi)^{-3/2}\sigma^{-3}$, where ρ_0 is the central density, m_ν denotes the neutrino mass and σ is the one-dimensional velocity dispersion. Thus we end up with

$$m_\nu^4 > 2\frac{(2\pi)^{3/2}\rho_0}{g_\nu\sigma^3}. \tag{3.70}$$

Alternatively, if one assumes a given value for m_ν, Eq. (3.70) can be used to constrain the maximally allowed density or the velocity dispersion. Finally, note that the argument we have presented here would also work for any hypothetical Maxwell-Boltzmann particles. It does not work for bosons because their equilibrium phase-space density does not have a maximum.

3.4.3 Observations of the galaxy cluster A2390

3.4.3 A X-ray gas and member galaxies of A2390

The galaxy cluster A2390 at redshift $z = 0.23$ [195, 196] is one of the richest and most luminous clusters known in the literature. Several interesting properties, e.g. the large abundance of lensing arcs and arclets [197], an elongated galaxy distribution [198] and its large velocity dispersion [199], have made the analysis of this system particularly attractive. In the context of GR, A2390 has been subject to extensive study by means of different techniques including virial (e.g., Ref. [200]), x-ray [201–204], redshift-space caustic [205] and both weak [206–210] and strong [211–214] lensing studies.

Observations with CHANDRA exhibit a very concentrated and highly peaked x-ray emission, indicating a strong cooling flow which is centered on cluster's central cD galaxy [202]. On large scales, the x-ray morphology has been found to be strongly elliptical with an overall position angle (PA) comparable to the main cluster direction in the optical (PA = 133°) [197]. Here and below, the PA is defined as the angular offset of the major axis with respect to the north-south direction, being measured counterclockwise. The data provide evidence for an elongated x-ray morphology in the very central part, and suggest the existence of a substructure in the cluster gas located roughly 40″ ($\sim$ 147kpc) from the cluster center. The CHANDRA image further reveals large-scale cavities in the x-ray surface brightness extending approximately 400kpc from the center, where a sharp break in the surface brightness profile is visible. As observed in several other clusters [215], such cavities are likely produced by bubbles of radio plasma emitted by the central active galactic nucleus. Despite these irregularities and the appearance of a secondary gas peak, however, the x-ray observations indicate that the system as a whole is relatively regular and, to good approximation, dynamically relaxed. Thus, if one excludes the cluster's central part, the overall assumption of hydrostatic equilibrium appears as a reasonable one.

There are also several studies of individual galaxies within the cluster. For instance, the properties of the central cD galaxy have been examined using optical [216], infrared and radio observations [217]. A large sample of 216 confirmed cluster members based on photometric and spectroscopic information is presented in Ref. [218]. More recent observations include a selection of 48 early-type member galaxies which has been used to investigate their evolutionary status [219]. We note that the available observational data will be important for building a realistic cluster model in TeVeS.

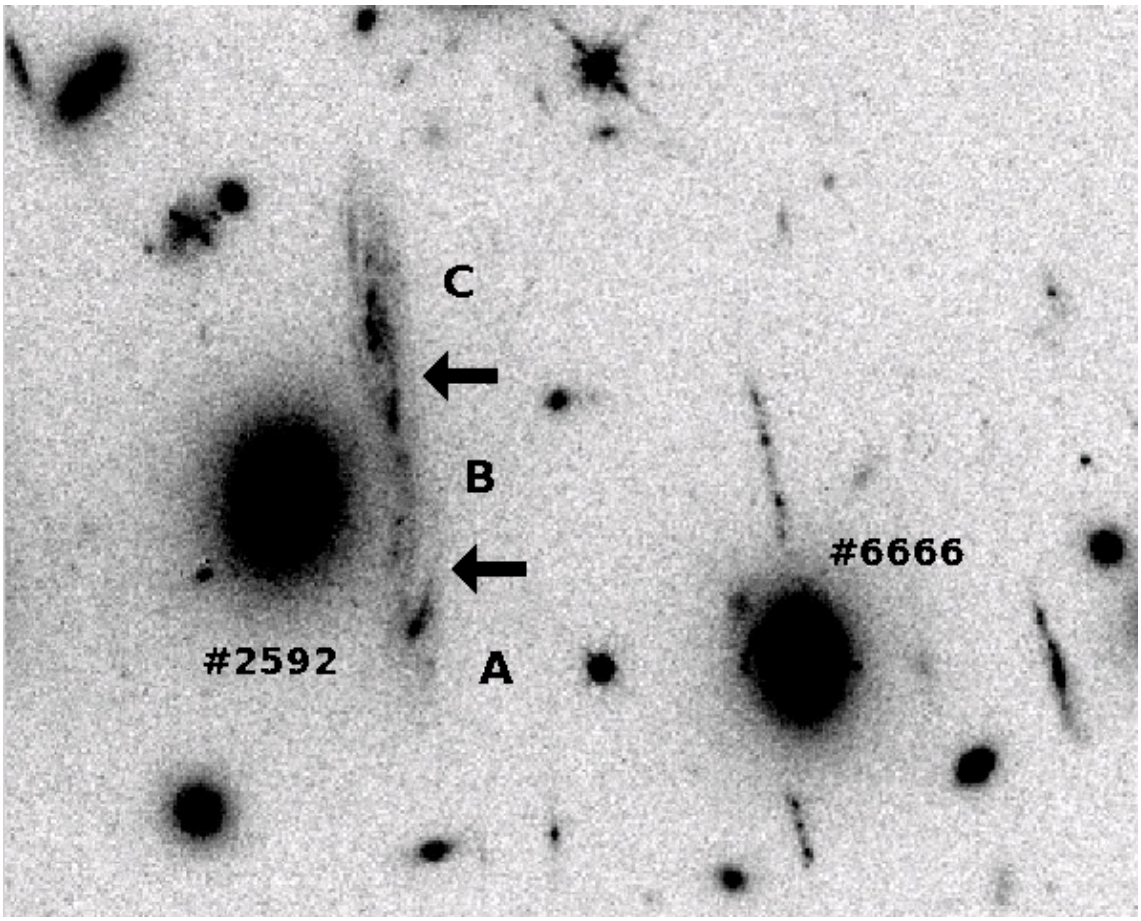

Figure 3.17: A small section of an HST/WFPC2 observation of A2390 shows the impressive straight arc on the left side. Characterized by two breaks along its light profile (present in other observed bands as well), the arc can be decomposed into three segments labeled *A*, *B* and *C*, respectively [197]. Also visible are the galaxy 2592, which is located adjacent to the arc, as well as the galaxy 6666 (see Table 3.4).

3.4.3 B The straight arc of A2390

Among several arcs and arclets, the cluster A2390 exhibits an unusual, strongly lensed straight arc (see Fig. 3.17) which is located approximately 38″ (∼ 140kpc) from the central cD galaxy [197]. This particular arc is unusual in the sense that, as it is both located in the outer core region and adjacent to a lens galaxy lying in between arc and cD galaxy, it would be expected to appear curved with respect to the massive cluster center or the closest galaxy. Along its light profile, the arc further exhibits two breaks in surface brightness, symmetrically located relative to the closest galaxy's center. Spectroscopic analysis of the arc revealed that it is actually the joint image of two different sources, one at redshift $z = 0.913$ (corresponding to $B - C$ in Fig. 3.17) [197] and the other at $z = 1.033$ (corresponding to A) [220]. In addition, ISOCAM observations of the image segment $B - C$ indicate the presence of an active star forming region and support the scenario of

two interacting source galaxies at $z = 0.913$ [221]. Nevertheless, the found straightness requires a rather special lens configuration (also see Sec. 3.4.5 A).

Apart from the system A2390, there also exist other detections of (relatively) straight images which are typically well modeled from the visible distribution of bright galaxies helped by the central cluster potential [222–224]. As already pointed out in the literature [211], a similar approach for A2390 within the usual framework of CDM would require extremely high mass-to-light ratios for individual galaxies, and thus yields a rather unrealistic scenario. In recent years, several authors have considered possible lens models which aim at reproducing such a straight image, and a first attempt was performed in Ref. [197]. For instance, the fold caustic of a single, highly elliptical cluster lens can be used to create a straight image [212]. Such a model gives a result comparable with the arc's morphology, but fails to explain infrared observations. Adopting a very large ellipticity of the central cluster profile, it was demonstrated how a cusp model may produce the desired elongated image morphology [214]; however, this solution seems incompatible with other lensing constraints of the system. Building on the existence of x-ray substructure in the arc's vicinity, the authors of Ref. [213] employed a two-component model using an elliptical cluster center with axis ratio $b/a = 0.7$ to explain the arc. Despite a slight deviation at $\sim 1\sigma$ significance, the obtained x-ray temperature profile and the projected mass within $38''$ ($\sim$ 140kpc) appear consistent with those derived from the observed x-ray luminosity [202].

It seems obvious that any suitable model needs substantial fine-tuning to form the necessary lens configuration for straight images. As a consequence, all of these models are extremely sensitive and unstable with respect to perturbations due to the closest galaxy or additional substructure in the intracluster medium (ICM). While this does not pose a problem *per se*, it is nevertheless interesting to look for models with improved stability. From a general analysis on how to form straight images [211], it has been concluded that the most likely configuration involves a dark mirror component of the nearest galaxy located on the opposite side of the arc, counterbalancing the effect of the visible galaxy. With the help of the central cluster profile, this yields a so-called *beak-to-beak model* which explains the observed straight arc and, if realized with such a "dark galaxy," is sufficiently stable against local perturbations. Alternatively, there is also the possibility of a *lips catastrophe* [211], i.e. a lips caustic just emerged or just about to emerge in three-dimensional caustic space (for a demonstration of a lips catastrophe in A370 see Ref. [225]). Since such a model requires the lensing convergence - equal to the projected matter density in GR only - to peak at the arc's position, however, it is not supported by observations.

3.4.3 C A challenge for TeVeS and hot dark matter

Concerning the situation in TeVeS, we may already state that the "dark galaxy" approach, i.e. a nonluminous matter distribution of galactic size, cannot be achieved with our choice of 11eV SN HDM. Assuming that these particles are relativistic and thermalized at the time of decoupling (just like for active neutrinos around a temperature of several MeV which is much larger than the considered mass) [17], their Fermi-Dirac distribution freezes in, and their phase-space density is constrained by the Tremaine-Gunn (TG) limit [194]. For instance, a HDM galaxy in TeVeS would have a typical phase-space occupation number (we neglect factors of π and order unity)

$$\begin{aligned}\frac{\hbar^3 dN}{d^3x d^3p} &\sim \frac{M}{m_\nu}\left(\frac{\hbar}{m_\nu \sigma r_C}\right)^3 \sim \frac{a_0^2\hbar^3}{G m_\nu^4 \sigma^5} \\ &\sim 10^3\left(\frac{m_\nu}{11\mathrm{eV}}\right)^{-4}\left(\frac{\sigma}{100\mathrm{km\ s^{-1}}}\right)^{-5},\end{aligned} \tag{3.71}$$

which exceeds unity, and thus the TG limit for thermal relics, unless the HDM mass m_ν is much larger than 11eV (e.g., $\sim$ 1keV warm dark matter) and/or the structure's velocity dispersion $\sigma \gg$ 100km s^{-1}, hence above the galactic scale. The estimate given in Eq. (3.71) assumes that the structure's dense core is subject to the Newtonian regime ($\mu_B \sim 1$), which gives a core size $r_C \sim GM/\sigma^2$, and the total mass $M \sim \sigma^4/Ga_0$ can be well approximated within the "deep-MOND" limit ($\mu_B \sim \sqrt{y}$). Also note that moving to masses significantly larger than $m_\nu = 11$eV would spoil the dynamics of MOND in galaxies and thus eliminate the use of such HDM in the first place [190].

Therefore, a combination of HDM and modified gravity may, in principle, face a challenge in order to create observed effects of dark substructure. The TG phase-space bound not only applies to HDM substructure, but also to its global distribution within the cluster, which presents a well-posed and constraining general test of TeVeS or similar theories supplemented by an additional HDM component. As other realistic lens models for the straight arc [213] also suggest a substantial amount of dark substructure, a basic question is whether there are TeVeS lens models which are compatible with the TG bound for 11eV SNs. Before we can address this point, however, we need a reliable way of modeling the straight arc in TeVeS. An approach into this direction will be discussed below.

[17] Note that whether or not SNs decouple whilst in thermal equilibrium depends on the assumed model, production mechanism and parameters, e.g. the mixing to active neutrinos. Since the physical processes in the early universe are yet unknown, the relic distribution of SNs is quite uncertain. Here we choose a thermal distribution to obtain the desired cosmological properties as discussed in Refs. [189, 190].

In preparation for the following sections, we introduce the terminology and procedure used for two different kinds of lens configurations in our analysis:

Quasiequilibrium configurations Here we consider configurations which are based on the assumption of hydrostatic equilibrium. Both the cluster gas and the (SN) HDM component are modeled by symmetric, central density distributions, the latter having a maximum phase-space density set by the TG limit which is inferred in a self-consistent way by considering the equation of state for a partially degenerate neutrino gas [81, 190] (see App. A). In addition, we include substructure in the form of visible galaxies and further allow for perturbations of the central distribution (gas + HDM) which are modeled by the same density profile as the central one (corresponding to structure of equal scale). We then check whether such configurations can produce the observed straight image in TeVeS.

Nonequilibrium configurations In this case, we allow for any HDM distribution which is capable of explaining the straight arc. This includes complex distributions with multipeaked mass densities and concentrations of different scale. Although we outline a general approach to lens models in TeVeS, we restrict our analysis to a bimodal configuration based on a model in GR (cf. Table 3.5 below) whose components exhibit dispersions $\sigma \gtrsim 500\text{km s}^{-1}$ and appear consistent with the crude estimate of Eq. (3.71), i.e. $\sigma \gtrsim 400\text{km s}^{-1}(m_\nu/11\text{eV})^{4/5}$. Approximately treating each density peak as a symmetric equilibrium distribution of SNs, we investigate whether they satisfy the TG phase-space limit for $m_\nu = 11\text{eV}$. For simplicity, we do not account for baryonic substructure (galaxies) in this context.

3.4.4 Quasiequilibrium model of A2390

Because of the nonlinear relation of the TeVeS scalar field to the underlying matter distribution, we cannot work with projected quantities, but need to perform our calculations in three dimensions. This significantly complicates the lensing analysis of A2390 and requires knowledge about the cluster's three-dimensional matter density. A first approach to our problem is to consider cluster configurations which are based on the assumption of hydrostatic equilibrium.

3.4.4 A Distribution of baryonic material

Using available data of x-ray gas [202, 204] and individual galaxies [219], we have modeled the distribution of baryons in A2390. Here we shall briefly present the results which are relevant for the analysis in Sec. 3.4.5. A detailed description of our procedure can be found in App. B.

Table 3.4: Positions, line-of-sight configurations and masses of individual galaxy components for the density model of A2390: At the cluster's redshift ($z = 0.23$), an angular scale of $1''$ corresponds to approximately 3.7kpc.

Galaxy ID [d]	θ_x	θ_y	ξ_x	ξ_y	Line-of-sight configuration		Projected stellar mass $M(< 1.5'')$	
		$['']$		[kpc]	A	B [kpc]	M_1	M_2 $[10^{11} M_\odot]$
#2180	−48.21	−16.98	−178.04	−62.71	0	+850	2.02	1.60
#2592	−34.29	13.32	−126.63	49.19	0	+850	3.51	4.66
#2619	−13.04	28.80	−48.16	106.36	0	+850	1.09	0.49
#2626	−34.62	29.86	−127.85	110.27	0	−850	1.40	0.79
#6666	−50.25	14.03	−185.57	51.81	0	−850	2.89	3.21
Substructure [e]	−37	25	−137	92	-	-	-	-
Center	0	0	0	0	-	-	-	-

[d] Identifiers for galaxies are taken from Ref. [219].
[e] The given values roughly indicate the position of the x-ray substructure presented in Ref. [213].

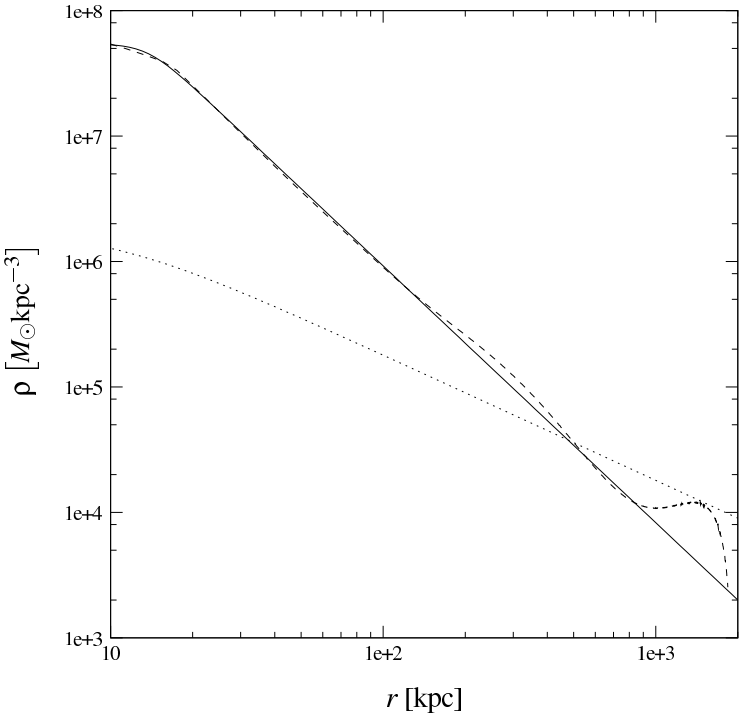

Figure 3.18: TeVeS equilibrium configuration of 11eV sterile neutrinos in A2390: The figure shows the calculated density distribution of neutrinos (dashed line), the analytic fit to this density using the profile specified in Eq. (3.78) (solid line) and the central baryonic matter distribution derived from x-ray observations (dotted line).

Figure 3.18 shows the density distribution inferred from x-ray observations with CHANDRA (dotted line). In addition to this central profile, we consider the contribution of five massive early-type galaxies which are located close to the straight arc. The masses of these galaxies are derived following a twofold approach: The first estimate (denoted as M_1) is based on a direct conversion of observed luminosity to stellar mass while the second one (M_2) uses a dynamical method. In what follows, we shall consider both prescriptions and present results for the two different mass estimates below. We further assume that all galaxies can be described by a spherical density profile which is closely related to the Hernquist profile [139] for elliptical galaxies (see App. B.2). Using the notation of Ref. [219], the basic properties of our models for the galactic components are illustrated in Table 3.4.

3.4.4 B Adding massive neutrinos

As previously mentioned, TeVeS requires an additional matter component to consistently describe observations of galaxy clusters. Assuming 11eV SNs within the original formulation of MOND, the authors of Ref. [190] derived their corresponding equilibrium density and (radial) velocity dispersion distributions for a sample of 30 galaxy groups and clusters, including the system A2390.

Starting from the observed density and temperature of the ICM [204], $\rho_x(r)$ and $T_x(r)$, respectively, the assumption of hydrostatic equilibrium immediately allows one to determine the gravitational field as a function of radius:

$$g(r) = \frac{-\kappa_B T_x(r)}{w m_p r}\left(\frac{d\log\rho_x(r)}{d\log r} + \frac{d\log\ \kappa_B T_x(r)}{d\log r}\right), \tag{3.72}$$

where κ_B is the Boltzmann constant, $w \approx 0.6$ is the mean molecular weight and m_p the mass of the proton. The such derived result is typically accurate to $\sim 10\%$ if equilibrium is realized [204]. Using the above, one directly obtains the total enclosed MOND mass which is given by

$$M(r) = \frac{r^2 g(r)\tilde{\mu}(x)}{G}, \quad x = \frac{g}{a_0}. \tag{3.73}$$

Here $\tilde{\mu}$ corresponds to the MOND interpolating function defined in Eqs. (2.33) and (2.34). Note that this is the only stage where the modification of gravity is involved. Once this function is specified, Eq. (3.73) can be used to obtain the cluster's total density distribution, which then allows one to determine the contribution due to SNs by subtracting the known density of the ICM. Considering the equation of state for a partially degenerate neutrino gas, the resulting SN density ρ_ν is then used to infer the associated radial velocity dispersion σ_ν needed for equilibrium. A detailed description of the actual calculation can be found in App. A. To check whether the results for ρ_ν and σ_ν are compatible with each other, one can exploit the TG phase-space constraint [194]. Assuming a Maxwellian velocity distribution, the maximally allowed density $\rho_{\nu,\mathrm{max}}$ for a given value of σ_ν reads

$$\rho_{\nu,\mathrm{max}} = \frac{g_\nu}{2}\frac{m_\nu^4}{(2\pi)^{3/2}\hbar^3}\sigma_\nu^3, \tag{3.74}$$

where the number of allowed helicity states is assumed as $g_\nu = 2$ [190, 226] and $m_\nu = 11\mathrm{eV}$. For the "simple" MOND interpolating function which is defined as

$$\tilde{\mu}(x) = \frac{x}{1+x}, \tag{3.75}$$

it has been found that the calculated SN phase-space density of all considered systems reaches the TG limit in the central part ($r \lesssim 20\mathrm{kpc}$ for A2390) [190], meaning that the SNs acquire their densest possible configuration in that region. If the equilibrium assumption is valid, this result further implies that a small portion of the dynamical mass must be covered by the brightest cluster galaxy. As for the cD galaxy of A2390 and its contribution in this context, we refer the reader to

App. B.3.

In principle, we could directly adopt the SN density of A2390 calculated in Ref. [190] for our simple cluster model if we specified a TeVeS free function μ_B which corresponds to the choice Eq. (3.75) in MOND. For numerical reasons discussed in Ref. [50] and to maximize possible MONDian effects, however, we assume a TeVeS free function of the following form:

$$\mu_B(y) = \frac{\sqrt{y}}{1+\sqrt{y}}, \tag{3.76}$$

where y is defined according to Eqs. (2.48) and (2.49). Apart from its simplicity, Eq. (3.76) is close to Bekenstein's original choice of the free function [50], and thus allows one to derive the TeVeS lens properties in a fully analytic way for certain configurations like, for example, spherically symmetric lens models [92]. In the intermediate and low acceleration regime, which is typically realized in galaxy clusters, the MONDian counterpart of Eq. (3.76) can be expressed as [43]

$$\tilde{\mu}(x) = \frac{\sqrt{1+4x}-1}{\sqrt{1+4x}+1}, \tag{3.77}$$

which is known to yield a less favorable description for the rotation curves of spiral galaxies than Eq. (3.75) as it enhances gravity too efficiently [227]. Inserting the above into Eq. (3.73), we have repeated the analysis of Ref. [190] for A2390, and calculated the equilibrium SN density distribution suitable for our cluster model in TeVeS. The resulting density profile is shown as a dashed line in Fig. 3.18. Note that the apparent waviness is not a numerical artifact, but rather emerges from using the data of Ref. [204] in Eq. (3.72). As the free function Eq. (3.77) enhances gravity more efficiently than Eq. (3.75), the SN density is notably decreased (cf. Fig. 2 of Ref. [190]), with the effect becoming stronger for larger radii. In the center, however, there is basically no change, indicating that the previous constraints due to the TG limit remain the same. To simplify the input into a numerical solver, the obtained SN density can be well fit by a profile of the following form:

$$\rho(r) = \frac{\rho_0}{(1+(r/r_0)^\gamma)^{1/4}}, \tag{3.78}$$

where $\rho_0 \sim 5.5\times10^7 M_\odot\mathrm{kpc}^{-3}$, $r_0 \sim 14\mathrm{kpc}$ and $\gamma \sim 8.2$. For comparison to the numerical result (dashed line), the analytic fit (solid line) is also illustrated in Fig. 3.18.

Note that the actual choice of the free function, which fixes the equilibrium distribution of SNs, will have no significant impact on the results for quasiequilibrium configurations presented

in Sec. 3.4.5. While the main cluster potential will almost be the same - it is exactly the same in case of spherical symmetry - for different μ_B, only the effects of substructure, e.g. the contribution of individual galaxies in A2390, should be affected by the particular form of the function μ_B. Therefore, our decision to use Eq. (3.76) will result in optimistic estimates of effects intrinsic to the framework of TeVeS. Since we are interested in the regime of strong lensing, however, we expect these differences to be rather mild.

3.4.5 Quasiequilibrium lens configurations

As a first approach, we shall investigate the strong lensing properties of quasiequilibrium configurations based upon several variations of the cluster model presented in Sec. 3.4.4. Although these models do not provide a realistic description of the cluster's core region, their study will be extremely useful to explore intrinsic TeVeS effects and to see whether TeVeS offers alternative mechanisms - different from those in GR - which can produce straight images. For the sake of clarity, we discuss details on the used numerical tools and the basic simulation setup in App. C.

3.4.5 A Analysis of the TeVeS lensing maps

Considering the previously introduced equilibrium model of the cluster, we are still left with substantial freedom regarding the galaxies' line-of-sight positions which are not constrained by observations and may vary over the cluster's extent which we define by the model's cutoff radius $R = 1\text{Mpc}$ introduced in App. B.1. Also, to account for nonsphericity of the cluster, we shall allow an additional ellipticity for the central density distribution (x-ray and SNs) which is solely modeled within the observed plane. Together with a respective PA, this gives a total of 7 free parameters for our simple model if we fix the galaxies' M/L ratios. As for the range of ellipticities, we choose a maximum corresponding to an axis ratio of $b/a \sim 0.7$. Moving significantly beyond this threshold would cause a severe mismatch to x-ray observations [202, 213], thus yielding a rather unrealistic cluster description.

Modifications of the overall density profile along the line of sight have already been studied in Ref. [50]: Varying the lens' extent between two extreme configurations, a disklike and a strongly "cigar-shaped" lens, can cause changes of up to $10-20\%$ in the lensing maps as well as the critical curves. For realistic cluster models lying in a range between these extrema, however, this effect is expected to be less pronounced, typically accounting for deviations on the order of a few percent. Therefore, we shall ignore such modifications in this work. Also, since the straight arc's sources

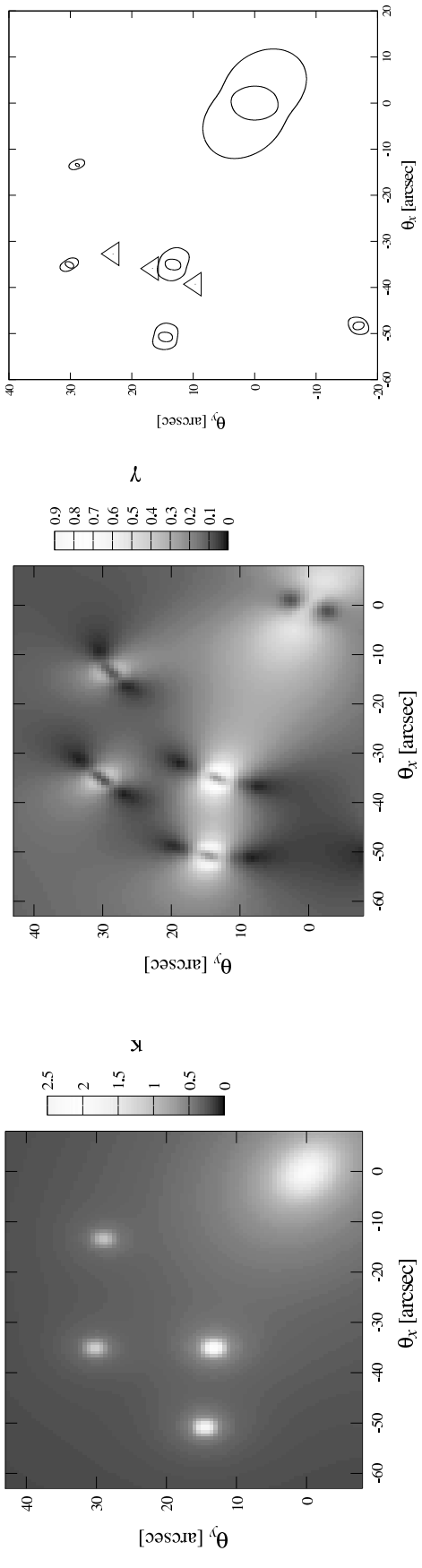

Figure 3.19: TeVeS lensing maps for a quasiequilibrium configuration: Shown are the resulting convergence κ (*left panel*), shear modulus γ (*middle panel*), and critical curves (*right panel*) for a cluster model with $e = 0.7$, PA = 115°, mass model M_1 and line-of-sight configuration B. The triangles indicate the observed position of the straight arc.

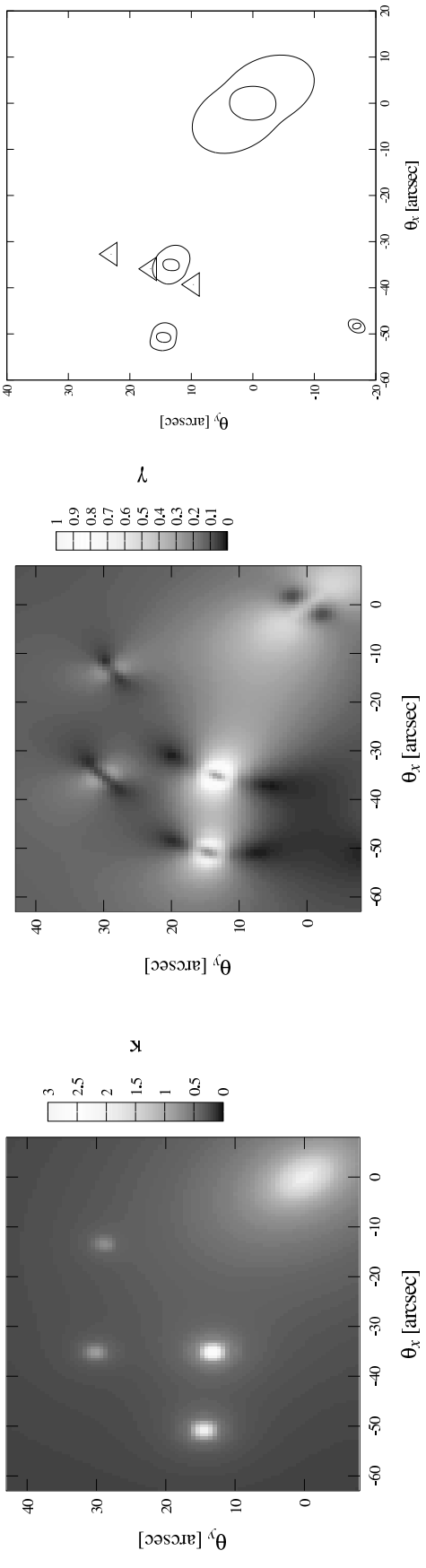

Figure 3.20: Same as Fig. 3.19, but assuming PA = 133° and mass model M_2.

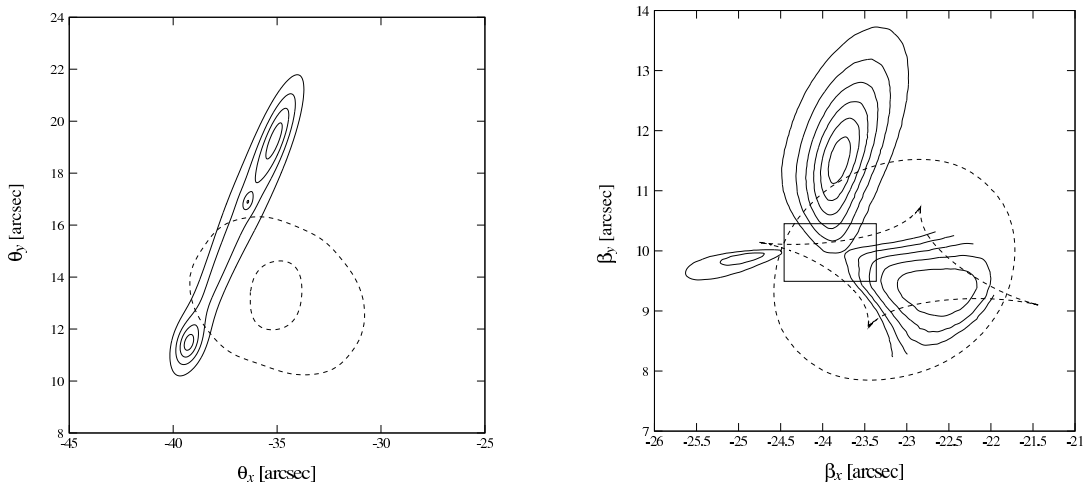

Figure 3.21: *Left panel*: The generated image contours (solid lines), resembling the observed luminosity distribution of the straight arc, and the critical curves (dashed lines) for an equilibrium cluster model with $e = 0.7$, PA = 133°, mass model M_2 and line-of-sight configuration *B*. *Right panel*: The resulting source distribution (solid lines) and lens caustics (dashed lines), where contours have been determined by averaging the calculated source points onto a regular grid. The open contour lines are due to a cutoff of the mapped image. In both panels, contours are in arbitrary units and chosen at equidistant levels.

are located close in redshift space (the corresponding distances D_s and $D = D_d D_{ds}/D_s$ only differ by roughly 3%), we restrict ourselves to a single source plane for our analysis. Unless otherwise stated, we will always work with a lens and source redshift of $z_l = 0.23$ and $z_s = 1$, respectively.

For different plausible cluster configurations, we have found no quasiequilibrium model that is capable of producing (nearly) straight images at the observed arc's position. As all of our results are qualitatively very similar, we only present a selection of simulation runs in the following. For example, Fig. 3.19 shows the calculated TeVeS lensing maps assuming an axis ratio $b/a \approx 0.7$ corresponding to an ellipticity of $e = 0.7$, PA = 115°, mass model M_1 and line-of-sight configuration *B* (see Table 3.4). A similar case is illustrated in Fig. 3.20, assuming PA = 133° and mass model M_2 while keeping all other parameters the same. We note that the lensing properties in the arc's vicinity are almost entirely dominated by the closest galaxy. The structure of the critical curves (right panel) already reveals that such models will produce strongly bent images with respect to the galaxy 2592 at the position of interest. To elucidate this point and to demonstrate the problems of such configurations, we have constructed a luminosity distribution, which roughly resembles the observed image morphology. This distribution has then been mapped back into the source plane, assuming the "second" cluster model presented in Fig. 3.20. The generated image and its associated source distribution are shown in the left and right panels of Fig. 3.21, respectively. Our particular example exhibits several features indicating that the model is not compatible with the observed straight image. These features can be summarized as follows:

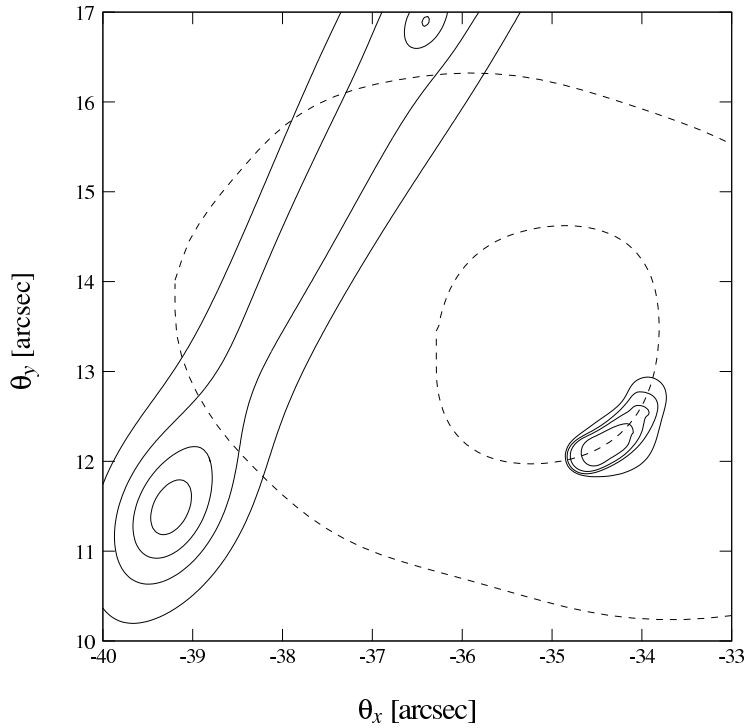

Figure 3.22: Occurrence of a new image for quasiequilibrium configurations: Shown is the observed straight arc and an additional, strongly magnified image which forms around the radial critical curve (dashed line), assuming the upper patch of the source distribution illustrated in the right panel of Fig. 3.21. The resulting image has been smoothed using a top-hat function with a diameter of roughly $0.4''$. Contours are still equidistant, but different for each image; the outermost contour of the two images is identical and the increase between the contours of the new image is four times larger than between those of the straight arc.

(a) Around the area where the three source patches visible in the right panel of Fig. 3.21 appear to intersect (marked with a rectangle), the inferred source distribution becomes multivalued. This remains true even after taking into account that the image is due to two distinct sources (see Sec. 3.4.3 B), and thus the lens model turns out to be ambiguous and inconsistent.

(b) Apart from the tangential caustic, i.e. the inner dashed line shown in the figure's right panel, the found source distribution also crosses the radial (outer) caustic, implying the existence of further images different from the straight arc. Assuming the upper patch of the source distribution illustrated in the right panel of Fig. 3.21, the occurrence of a new image is demonstrated in Fig. 3.22. However, there is no evidence for such additional images as they are not observed in the system.

(c) Assuming an average size of roughly $1''$ ($\sim$ 10kpc) for galaxies at $z = 1$, the source's constituents appear too big in angular size (up to $4''$), yielding a rather unlikely scenario. This problem further deteriorates if one tries to avoid the issues related to (a) and (b) by lowering the total mass of the nearby (lens) galaxy 2592.

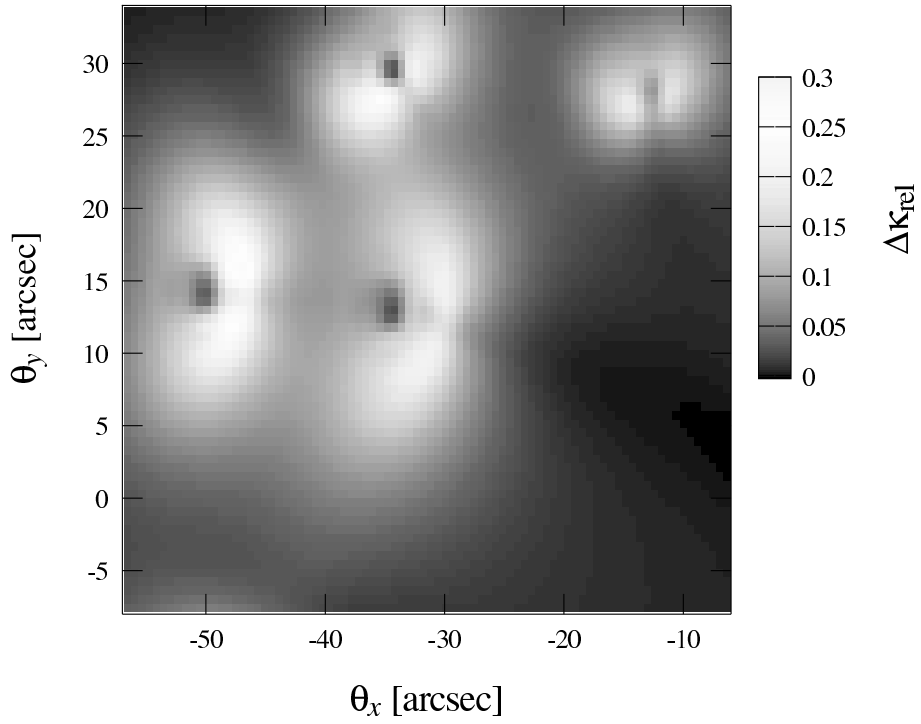

Figure 3.23: Relative difference of the convergence maps calculated for the two line-of-sight configurations *A* and *B*: The here presented result assumes $e = 0.7$, PA = 133°, and mass model M_1.

Observations further indicate the presence of several faint elongated objects whose orientation is approximately the same as that of the arc, with a scatter of only a few degrees [197]. Together with the above, these arclets strongly support the requirement for a special lens composition rather than the necessity for unusual source properties, suggesting that the lens configurations considered here are inappropriate to explain the straight image.

This is the basic result of all simulated cluster models, which seems to be insensitive to the used mass model (M_1 or M_2) or the actual line-of-sight alignment of galactic components. To quantify the effect of the latter, we compared the lensing maps of individual models for two extreme line-of-sight configurations, *A* and *B*. Adopting the parameters of the realization presented in Fig. 3.19, Fig. 3.23 displays the obtained relative difference between the corresponding convergence maps. As we can see, the deviation can reach values up to $\sim$ 30% in regions of low (effective) surface density, but remains smaller ($\lesssim$ 15%) in regions where $\kappa \gtrsim 1$. A comparison of the corresponding critical curves and caustics of galaxies reveals that this line-of-sight effect typically affects their position on the order of $\sim$ 10%, which has no qualitative impact on our results. As for the dependence on the actually used mass models (galaxies), we will investigate the influence of varying M/L ratios in the next section.

3.4.5 B Variation of mass-to-light ratios

So far, we have restricted our analysis to two sets of M/L ratios for the cluster's galaxies (see Table 3.4). How robust are our results with respect to variations of these ratios? Here we take a simplified approach to obtain reasonable estimates of the effect on the strong lensing properties, in particular, the critical curves. In what follows, we use a Hernquist profile [139] with fixed core radius $r_H = 3\text{kpc}$ for the density distribution of galaxies [corresponding to the limit $\epsilon = 0$ in Eq. (B.2)]. In the isolated case and for our choice of the free function μ_B, this allows one to express the lensing properties fully analytically [50], and the deflection angle is given by

$$\hat{\alpha}(\xi) = \frac{r_H A(\xi)}{\sqrt{|\xi^2 - r_H^2|}} \left(\frac{4\xi\sqrt{GMa_0}}{r_H} + \frac{4GM\xi}{\xi^2 - r_H^2} \right) - \frac{4GM\xi}{\xi^2 - r_H^2}, \tag{3.79}$$

where

$$A(\xi) = \begin{cases} \operatorname{arsinh} \sqrt{\left|1 - (r_H/\xi)^2\right|} & \xi < r_H \\ \arcsin \sqrt{1 - (r_H/\xi)^2} & \xi > r_H \end{cases}. \tag{3.80}$$

Furthermore, we will assume that

(a) the superposition principle remains valid; i.e. the lensing maps of isolated galaxies and the cluster background can just be added, which is rigorously true if the components are infinitely separated from each other and leads to an optimistic estimate otherwise, and that

(b) the cluster background at each galaxy's position can be modeled as an external contribution with locally constant convergence κ_C and shear modulus γ_C.

Choosing polar coordinates, the latter yields an effective cluster deflection potential of the following form:

$$\Psi(\theta, \varphi) = \frac{\kappa_C}{2}\theta^2 + \frac{\gamma_C}{2}\theta^2 \cos(2(\varphi - \varphi_0)), \tag{3.81}$$

where the external shear's principle axes system is defined by φ_0. Locally, the system's total shear modulus, relevant for the determination of critical curves and caustics, depends nonlinearly on the contribution due to the Hernquist lens and the cluster,

$$\gamma_{\text{tot}}^2 = (\gamma_{1,H} + \gamma_{1,C})^2 + (\gamma_{2,H} + \gamma_{2,C})^2. \tag{3.82}$$

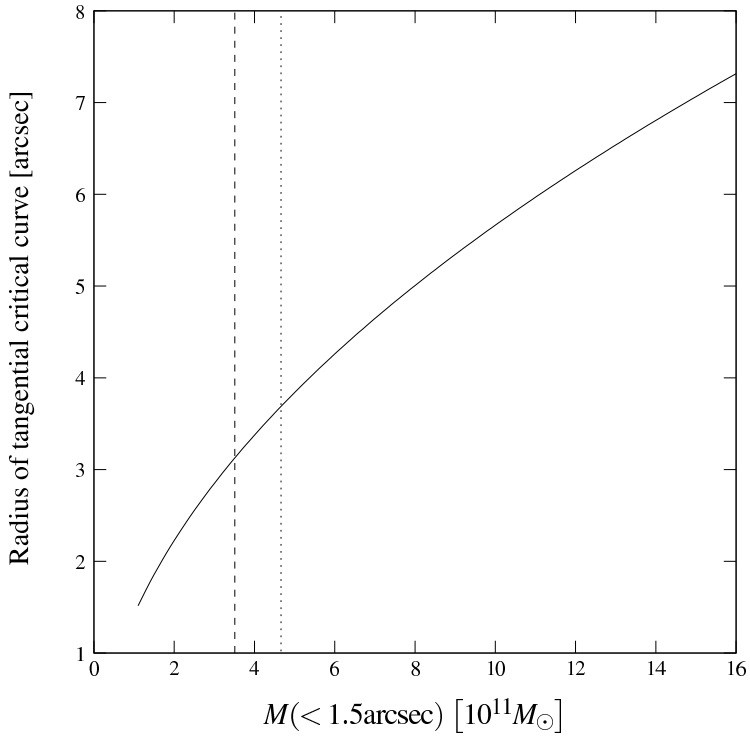

Figure 3.24: Predicted mean radius of tangential critical curves of a Hernquist lens embedded into the external cluster field: The mean radius is plotted as a function of the projected enclosed mass within an aperture of 3″ diameter (∼ 11kpc). The vertical lines indicate the values of the galaxy 2592 for mass model M_1 (dashed line) and M_2 (dotted line), respectively.

Because of the shear's tensor property, the above is anisotropic, which directly affects the resulting position of critical curves given by Eq. (3.22),

$$(1-\kappa)^2 - \gamma^2 = 0. \tag{3.83}$$

To obtain the mean effect due to the cluster background, we perform an average over φ and all possible orientations of the external shear field, which leads to

$$\overline{\gamma^2} = \gamma_H^2 + \gamma_C^2. \tag{3.84}$$

We use the simulation result for an equilibrium cluster model with $e = 0.7$, PA $= 115°$ and no galaxies to estimate the parameters of the background model. Around the arc's position, this roughly fixes $\kappa_C \approx 0.29$ and $\gamma_C \approx 0.17$. For this case, Fig. 3.24 shows the resulting mean radius of the tangential critical curve as a function of the enclosed galactic mass within an aperture of 3″ diameter. While this should give a reasonable picture for the galaxy 2592, which resides close to the arc, the such estimated radii will be too large for the other galaxies. These are located in regions

where the background has a weaker impact (κ_C and γ_C take lesser values), leading to an optimistic prediction of their mean critical-curve size. Assuming small variations in M/L, the figure suggests no qualitative changes of our previous results. Even if we consider that M/L ratios may change up to a factor of 4 in the infrared, we find a maximum increase of the mean critical-curve radius corresponding to a factor of approximately 2. At most, such an extreme scenario could come close to a merged-cusp model for the galaxies 2592 and 6666, but this configuration cannot explain the arc due to its inappropriate orientation and position of critical curves and caustics in the lens and source plane, respectively. We therefore infer that the basic result of Sec. 3.4.5 A does not depend on the particularly assumed M/L ratios of individual galaxies - unless the background potential is substantially modified.

We have also explored the influence of perturbations to the central cluster profile. For this reason, we have assumed a secondary spherical clump made out of gas and SNs which follows the same profile as the central distribution and accounts for $10-15\%$ of the system's total mass. The clump's position has been chosen from a narrow range roughly centered on the detected substructure in the x-ray map [202, 213] (see Table 3.4). Again, we have found no qualitative difference compared to previous simulations. The calculated deviations in the lensing maps are on the order of a few percent, leaving a basically negligible impact on the critical curves and caustics. Similar statements apply to an overall increase of the central density profile by $10-20\%$.

Together with the results presented in Sec. 3.4.5 A, we thus conclude that TeVeS quasiequilibrium configurations with 11eV SNs are not capable of explaining the observed arc. In particular, we find no evidence for the formation of beak-to-beak or lips catastrophes [211] due to intrinsic TeVeS effects, which could give rise to straight images. Therefore - just as in GR - a suitable TeVeS lens model needs substantially more mass as well as a special density distribution in the cluster's core region. A general procedure on how to obtain such models will be discussed in the next section.

3.4.6 Nonequilibrium lens configurations

In the following, we shall outline a general approach for modeling cluster lenses in TeVeS which allows one to use existing GR lens models to estimate the needed TeVeS lens properties. Adopting a bimodal lens model for the straight arc, we will present an example of such a lens and discuss implications for the modified framework.

3.4.6 A Systematic approach to cluster lenses

Taking a naive point of view, one might expect that strong lensing is subject to the strong acceleration regime, and therefore it should be enough to consider the limit $\mu_B \to 1$. In this case, all relevant equations would reduce to their GR counterparts, allowing a conventional lensing analysis. Previous calculations [50] have shown that such an approximation is not justified. In particular, the scalar field can have a significant impact on the second derivatives of the lensing potential. For instance, this can increase the radii of critical curves by up to a factor of 2, depending on the assumed mass distribution of the lens (cf. Figure 7 of Ref. [50]). As we shall see below, however, there is another way of simplifying the lensing problem in TeVeS.

Let us return to the scalar field given by Eq. (2.55). Integrating once, we may recast this equation as

$$\mu_B \boldsymbol{\nabla}\phi = \frac{k_B}{4\pi}\left(\boldsymbol{\nabla}\Phi_N + \boldsymbol{\nabla}\times\mathbf{h}\right), \tag{3.85}$$

where $\mathbf{h}$ is a regular vector field determined up to a gradient by the condition that the curl of the right-hand side of Eq. (3.85) must vanish. We note that the main difficulty associated with solving the scalar equation are the generally nonvanishing components of $\mathbf{h}$. If for any reason $\mathbf{h} \approx \mathbf{0}$, Eq. (3.85) reduces to a relatively simple algebraic relation between the gradients of the scalar and the Newtonian potential,

$$\mu_B \boldsymbol{\nabla}\phi \approx \frac{k_B}{4\pi}\boldsymbol{\nabla}\Phi_N, \tag{3.86}$$

which can easily be inverted by numerical means to give $\boldsymbol{\nabla}\phi$, assuming that the Newtonian potential (or only its gradient) are known. Therefore, we want to address the question of how the field $\mathbf{h}$ is affecting the corresponding lensing maps in the strong lensing regime. We already expect $\mathbf{h}$ to be important around local extrema of the Newtonian potential, but it is difficult to make any intuitive guesses about its quantitative impact in stronger gravity regions as well as on the final projected result. The most straightforward approach to this problem is a direct comparison of simulations treating the full scalar equation to those where $\mathbf{h} = \mathbf{0}$. To this end, we have taken our previous quasiequilibrium models and fed them into a modified version of our solver, now assuming Eq. (3.86) to determine the scalar gradient. Since our choice of μ_B is very close to that presented in Ref. [92] (see, e.g., Ref. [50]), our code assumes

$$|\boldsymbol{\nabla}\phi| = \sqrt{a_0\,|\boldsymbol{\nabla}\Phi_N|} \tag{3.87}$$

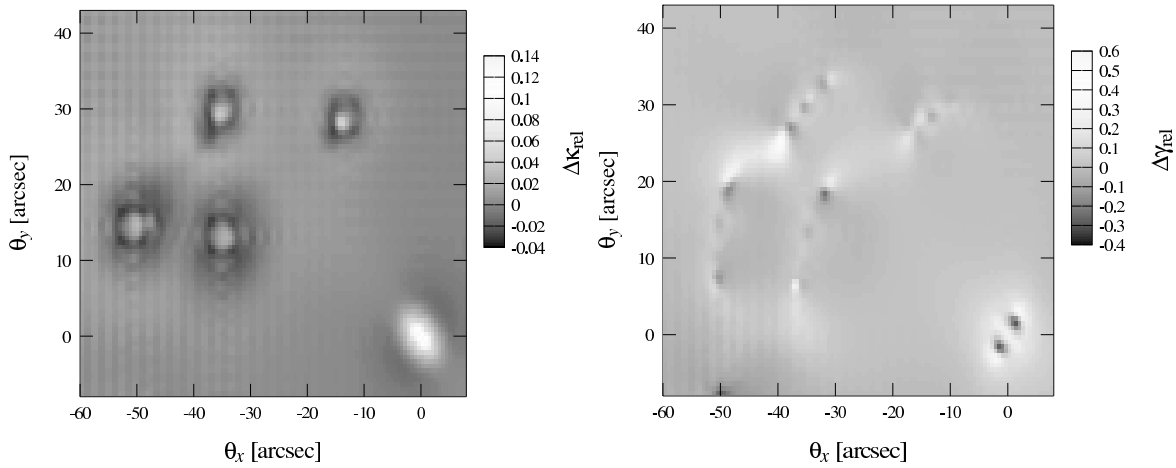

Figure 3.25: Simulation results with proper treatment of the scalar field equation compared to those where the curl field **h** has been set to zero: The figure illustrates the relative deviation in the corresponding lensing maps, the convergence κ (*left panel*) and the shear modulus γ (*right panel*), assuming an equilibrium model with $e = 0.7$, PA = 133°, mass model M_1, and line-of-sight configuration *B*. The visible gridlike structure is a combined effect of Fourier fluctuations, interpolation, and the division by values close to zero.

to calculate $\boldsymbol{\nabla}\phi$. For instance, adopting an equilibrium model with $e = 0.7$, PA = 133°, mass model M_1 and line-of-sight configuration *B*, the relative deviation of the lensing maps from the proper solution is presented in Fig. 3.25. While the convergence varies by $5 - 15\%$, differences in the shear map can be as high as $\sim 50\%$. As expected, the largest deviations occur in regions where the Newtonian gradient approaches the null vector, which, for example, can be seen in the very core of the central elliptic profile for both the convergence and shear maps.

Clearly, the impact of the curl field **h** is not negligible in regions of low gravity. Concerning the domain of strong lensing, however, we find the following: Comparing the corresponding critical curves and caustics, the curl field turns out to be much less important. Interestingly, the obtained deviation with respect to their position in the lens and source plane, respectively, is only about $\lesssim 2 - 3\%$. Within a sufficiently large environment around these curves accounting for all strong lensing features, the accuracy of the approximated (**h** = **0**) lensing maps is typically of the same order, meaning that the curl field negligibly contributes to the strong lensing properties of a given matter distribution. Our result appears to generally hold for strong cluster lenses and indicates that it is enough to consider Eq. (3.86) in the context of TeVeS lens models. Therefore, if one specifies the line-of-sight extent of the total system as well as individual matter components, this offers a direct systematic way of modeling strong lenses in TeVeS.

3.4.6 B Modeling the straight arc in TeVeS

Based on the result of Sec. 3.4.6 A, one could, in principle, take an available GR lens fitting routine, modify it to include the TeVeS scalar field according to Eq. (3.86), and use it to obtain a lens model for the straight arc. It is obvious that such an approach will be computationally more demanding because the scalar's contribution has to be evaluated in three dimensions, and one also needs to invoke numerical integration to derive the desired projected quantities. In the following, however, let us consider an alternative way to estimate the necessary deflection mass and its distribution in TeVeS. For this reason, we start from the bimodal GR model derived in Ref. [213] which, in addition to the central matter clump, assumes a smaller subcomponent at approximately 45″ ($\sim$ 166kpc) from the cluster center. The second clump is motivated by the existence of substructure in the cluster's x-ray map which is used to infer its position in the lens plane. Both clumps are chosen to follow a pseudoisothermal elliptic mass distribution (PIEMD) [228], but the subcomponent's profile is assumed to be spherically symmetric. Correcting for the here used cosmological background, the model gives an enclosed projected mass of $M_a \sim 1.2 \times 10^{14} M_\odot$ within a circular aperture of 38″ ($\sim$ 140kpc) radius from the cluster center. As typical for strong lensing mass models, this estimate should lie within $\sim$ 30% of the true value [229].

Using the arguments presented in Sec. 3.4.6 A, it is obvious that there exists an analogous bimodal lens model in TeVeS. To obtain a spherically averaged density estimate in TeVeS, we ignore the secondary clump, which negligibly contributes to the enclosed mass within the given aperture, and also assume that the main component can be described by a spherically symmetric density profile. Thus, its three-dimensional matter distribution can be written as

$$\rho(r) = \rho_0 \frac{r_C^2}{r_C^2 + r^2}, \tag{3.88}$$

where ρ_0 is the central density and r_C the core radius. Alternatively, Eq. (3.88) may be written in terms of its asymptotic velocity dispersion σ_∞ associated with the density profile of a singular isothermal sphere:

$$\rho(r) = \frac{1}{2\pi G} \frac{\sigma_\infty^2}{r_C^2 + r^2}. \tag{3.89}$$

Table 3.5: Fiducial parameters of the bimodal lens configuration presented in Ref. [213]: Here the subclump is offset by approximately 45″ (∼ 166kpc) from the main component.

	b/a	PA [°]	r_C [″]	σ_∞ [km s^{-1}]
Central main clump	0.71	49.2	12 ± 5	950 ± 100
Subclump	1	–	$7 - 12$	$420 - 500$

The corresponding enclosed mass of this density distribution at radius r reads

$$M(r) = 4\pi r_C^2 \rho_0 \left(r - r_C \arctan\left(\frac{r}{r_C}\right)\right). \tag{3.90}$$

Since our choice of the free function allows us to make use of Eq. (3.87), it is possible to express the enclosed mass in TeVeS, which effectively generates the same dynamical mass as Eq. (3.88), as

$$M_{\rm eff}(r) = M(r) + \frac{a_0 r^2}{2G}\left(1 - \sqrt{1 + \frac{4GM(r)}{a_0 r^2}}\right) = M(r)\frac{4s}{\left(1 + \sqrt{1+4s}\right)^2}, \tag{3.91}$$

where $s = GM(r)/a_0 r^2$. As previously noted, however, the choice of Eq. (3.76) does not yield a good description of galaxy rotation curves. Adopting a TeVeS free function corresponding to Eq. (3.75), a similar calculation leads to

$$M_{\rm eff}(r) = \frac{[M(r)]^2}{M(r) + a_0 r^2/G} = M(r)\frac{s}{1+s}. \tag{3.92}$$

Setting $r_C \approx 13''$ (48kpc) [213] and requiring that the enclosed projected dynamical mass within 38″ is still given by M_a, the above expressions can be used to derive the underlying density distributions which, together with the resulting surface density profiles, are illustrated in Fig. 3.26. The visible density drop-off within $r \lesssim 20$kpc is a consequence of the assumed PIEMD and probably unphysical, but can easily be avoided by changing the central profile in favor of a peaked and finite core, fixing the enclosed mass around $r = 140$kpc (and thus keeping the lens properties needed for the arc). Of course, our results depend on the assumed line-of-sight extent specified by Eq. (3.88), but the derived surface densities should vary by only a few percent for different models (see Sec. 3.4.5 A). We also note that the "modified" density profiles yield a finite mass; for both Eqs. (3.91) and (3.92), the total mass is given by (taking the limit $s \to 0$)

$$\lim_{r\to\infty} M_{\rm eff}(r) = \frac{16\pi^2 G r_C^4 \rho_0^2}{a_0}. \tag{3.93}$$

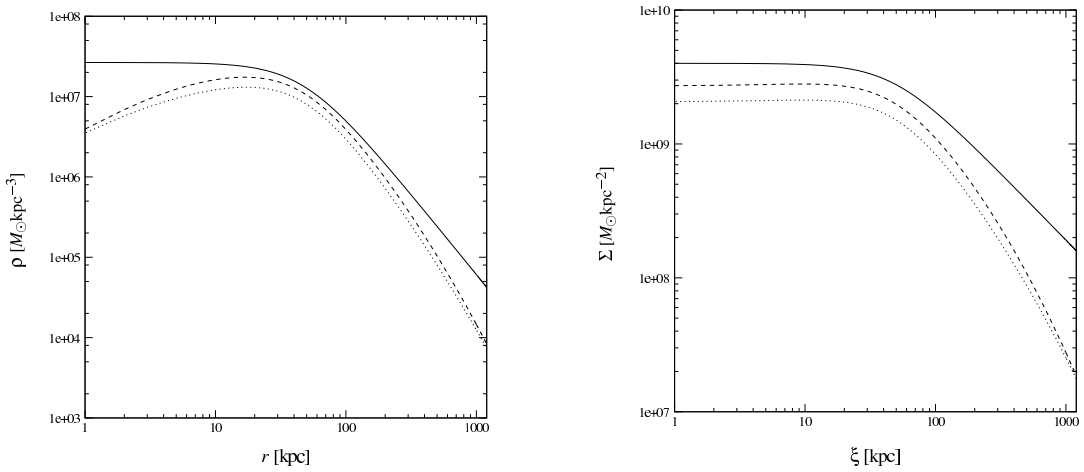

Figure 3.26: Spherically averaged density (*left panel*) and corresponding projected surface density (*right panel*) profiles for the bimodal lens model in TeVeS: Shown are the results for the Newtonian dynamical mass (solid line) and the two TeVeS free interpolating functions corresponding to Eq. (3.91) (dotted line) and Eq. (3.92) (dashed line), respectively. Note that the three-dimensional mass density profiles are entirely dominated by the contribution of SNs within a radius of a few hundred kpc. For $r \lesssim 25-30$kpc, the derived densities are well below the TG-limit-saturating equilibrium distribution of 11eV SNs in Fig. 3.18, and they are also much broader. This already indicates that the main component's phase-space limit is not violated here.

Although the profiles are not diverging, the relevant mass typically extends to large radii. Therefore, the use of such profiles within the full TeVeS solver is very inefficient because very large box sizes would be necessary to perform the calculations, which underlines the advantage of neglecting the curl field for strong lensing models (see Sec. 3.4.6 A). The resulting total lensing mass is entirely dominated by SNs within a radius of a few hundred kpc, which allows one to ignore the contribution of gas and stellar material to excellent approximation. We have checked that the three-dimensional density distributions in Fig. 3.26, basically representing the lens model's main component, are consistent with the TG limit estimated for hydrostatic equilibrium and a Maxwellian velocity distribution, following the approach of Ref. [190]. This is already indicated by the fact that the derived densities are much broader and well below the TG-limit-saturating 11eV SN equilibrium distribution (shown in Fig. 3.18) for $r \lesssim 25-30$kpc. At the arc's position ($\theta = 38''$), the actual enclosed projected mass of the TeVeS lens models is given by $6.1 \times 10^{13} M_\odot$ or $8.0 \times 10^{13} M_\odot$, assuming Eq. (3.91) or (3.92), respectively. Here the model's subcomponent deserves special attention: Naively treating the problem, the smaller clump's presence acts as a perturbation to the total system's phase-space density, and thus it is trivially in accordance with the estimated TG limit since the main clump is. However, this approach typically leads to overestimating the TG limit, considering that the secondary clump should be regarded as a bound object by itself. Taking the view that A2390 has undergone recent merger activity, it seems reasonable to

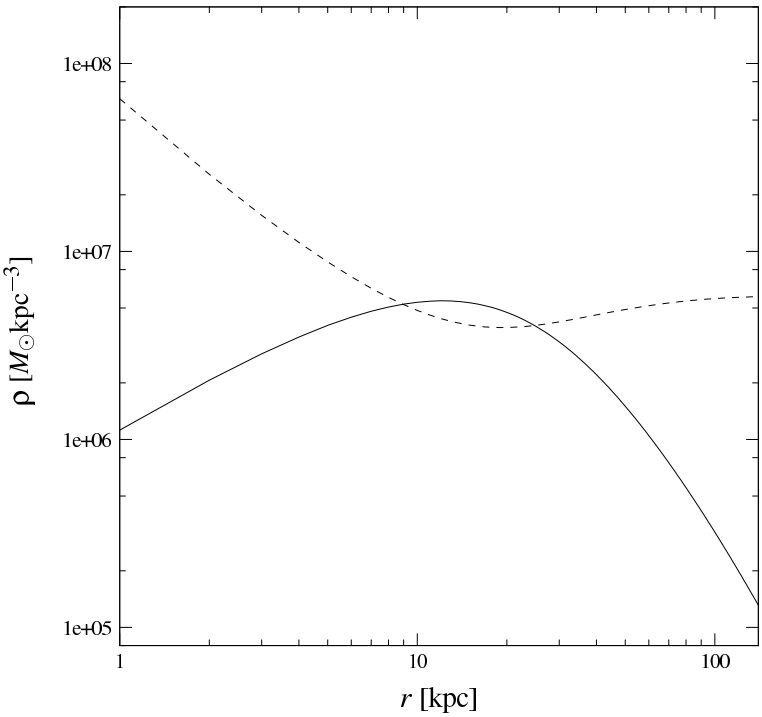

Figure 3.27: Estimated 11eV SN density distribution (solid line) and corresponding TG limit (dashed line) for a subclump model with $r_C \approx 7''$ (26kpc) and $\sigma_\infty \approx 500$km s^{-1}: The origin is centered on the subcomponent, and the TG limit has been calculated according to Eq. (3.74), following the prescription of Ref. [190]. Note that the slight "wiggly" feature of the dashed line is due to a nonuniform dispersion $\sigma(r)$ which is computed in a self-consistent way [190].

assume that the subcomponent has formed at a sufficiently earlier time, and therefore it should be subject to its own phase-space distribution. This suggests that one should examine the secondary clump separately. Considering the subclump as an isolated object entirely dominated by 11eV SNs, we have repeated the above TG analysis for the range of parameters listed in Ref. [213] (see Table 3.5). It is important to note that the bimodal lens model requires the secondary deflector to be an extended object with $r_C \sim 7 - 12''$. Moving to smaller core radii, the lensing potential would start to resemble that of a point lens and the model would fail to reproduce the observed arc. Moreover, it is likely that one would also violate constraints due to other observed images in this system. A very massive and compact deflector such as a supermassive black hole is therefore not a viable possibility, which is further supported by the lack of evidence for a very strong and point-like x-ray or radio source at the subclump's position. To achieve a rather realistic TeVeS mass estimate, we have adopted a free interpolating function corresponding to Eq. (3.75) for our calculations. The obtained SN density profile and the TG limit according to Eq. (3.74) are illustrated for two cases in Figs. 3.27 and 3.28. Assuming $r_C \approx 7''$ (26kpc) and $\sigma_\infty \approx 500$km s^{-1}, the subcomponent's density slightly exceeds the TG limit (up to 30%) within a range of approximately

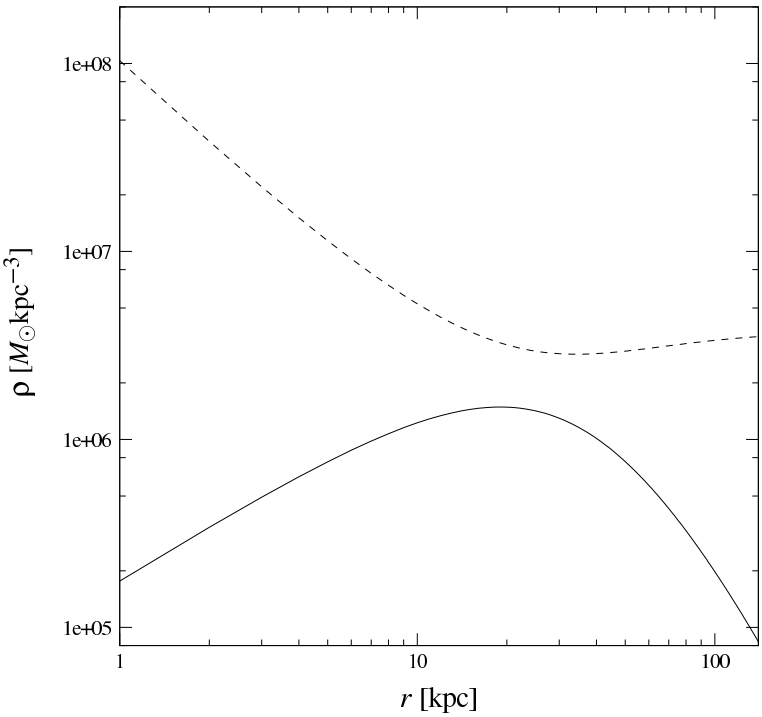

Figure 3.28: Same as Fig. 3.27, but assuming $r_C \approx 10''$ (37kpc) and $\sigma_\infty \approx 440$km s^{-1}.

$10 - 25$kpc. Moving toward larger radii ($r \gtrsim 50$kpc), the SN density consistently stays below this limit. For a less compact model with $r_C \approx 10''$ (37kpc) and $\sigma_\infty \approx 440$km s^{-1}, the TG bound is never exceeded. Generally, our results seem to rule out configurations where the subclump is modeled with small values of r_C ($\lesssim 8 - 9''$) whereas the bimodal TeVeS lens appears consistent with 11eV SN HDM for larger choices of the core radius. Before drawing such a conclusion, however, we need to consider how strong the implication of the present analysis really is.

First of all, we note that the lens model is based on the PIEMD model given by Eq. (3.88). This clearly introduces a bias on our estimates; other assumptions about the components' density distributions might yield a different result. In particular, the PIEMD model leads to an unphysical drop of the central density which could affect our estimate of the TG bound. To check this, we have modified the central SN density profile of the subclump model presented in Fig. 3.27 in favor of a uniform core, but without changing its properties beyond $r \approx 15$kpc (the arc appears at $r \approx 26$kpc from the subcomponent's center). The resulting density profile and the corresponding TG limit are shown in Fig. 3.29. While the TG bound is still violated within $\sim 10 - 25$kpc, we see that the density limit is notably decreased in the center, almost matching the assumed SN distribution. Therefore, it is unlikely that shifting matter to the central region can help to avoid an excess of the TG bound. Next, our estimates assume that the subclump can be treated as an

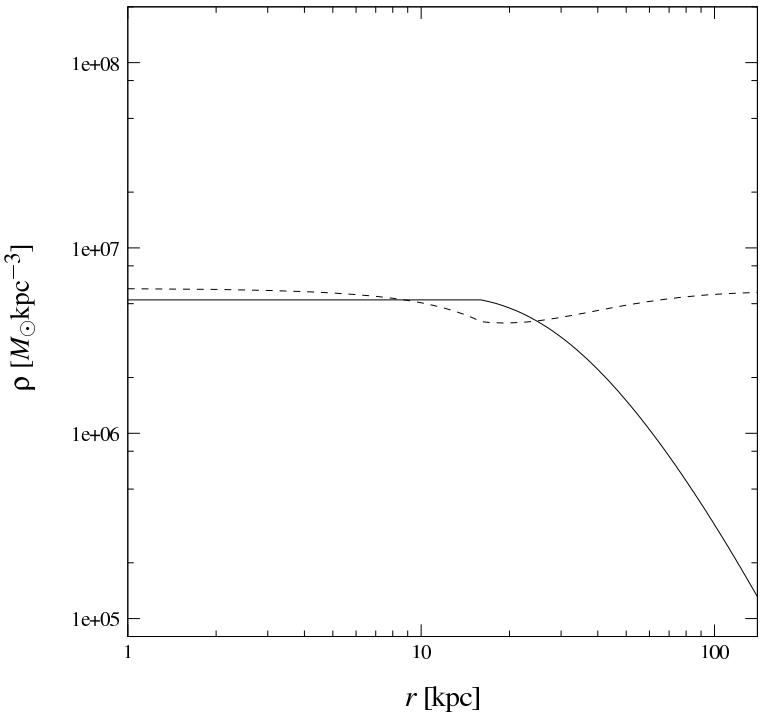

Figure 3.29: Same as Fig. 3.27, but now assuming a uniform core of the SN distribution. Note that the radius at which the density becomes constant ($r \approx 15$kpc) is fixed by requiring a continuous distribution of SNs.

isolated object. Since the clump resides within the background field of the main component, this is not rigorously true. Using Eq. (3.92), we find that the main component provides an external Newtonian gravitational field of around a_0 at the subclump's position. As for the subcomponent, this modifies the relation between gravitational field and underlying density distribution, and gives rise to an increase of the central SN density on the order of unity. Such a density boost could push seemingly consistent subclump models with $r_C \gtrsim 10''$ toward or even beyond the TG limit, but detailed statements about this issue are very sensitive to the actual model parameters.

Another point is related to the fact that our calculations rely on completely SN dominated lens components within $\sim$ 100kpc. If placed at or close to the subclump's center, already a relatively small, concentrated baryonic mass, e.g. a galaxy, on the order $10^8 - 10^9 M_\odot$ could help to relax the density constraint due to the TG limit [18]. Whether such an approach can be reconciled with observations of this region, however, remains to be seen. Last but not least, we also need to check the viability of the current estimate of the TG limit which has been derived under simplified conditions. In what follows, we shall discuss in more detail how these simplifications affect our analysis.

[18] From private communication with G. W. Angus.

As previously mentioned, the strong lensing domain in the center of A2390 is not in equilibrium and has a rather complicated nonsymmetric density distribution. This will obviously have an influence on the estimates for the TG limit. Considering nonequilibrium configurations in general, the velocity dispersion σ is expected to increase for a given matter distribution when moving away from equilibrium. Since the value of σ increases in this case, one would also obtain a higher density limit for SNs according to Eq. (3.74). Taking the additional asymmetry into account, however, the situation becomes less clear. Depending on the system's actual properties, the TG limit could increase or decrease, and there seems to be no universal rule allowing one to make solid statements for anisotropic systems. Finally, one should also adhere to deviations from a Maxwellian velocity distribution. This issue has been addressed in Ref. [230]. There it has been shown that the actual physical density limit becomes larger than the previous estimates of the TG limit which can be exceeded by up to a factor of 2. Again, this would imply that SNs could account for more mass in the cluster. Combining the three aspects from above, it seems reasonable to assume that the true density limit will be on average higher than our previous estimates, meaning that density models with SNs become more flexible. Note, however, that such an argument generally does not replace the need for a rigorous treatment of particular systems.

Given the accuracy of our present analysis and accounting for all of the above, we conclude that the bimodal TeVeS lens model for the arc is in accordance with the assumption of 11eV SNs. Nevertheless, it seems intriguing that the needed amount and distribution of 11eV SNs lies so close to what they can maximally contribute to the system. It should be obvious that all of our statements depend on the assumed lens configuration and are valid only for the bimodal model we have considered here. In particular, the bimodal lens model ignores the contribution of galaxies. These can have a significant impact on the lensing maps (see Sec. 3.4.5 A), which is especially true for the galaxy 2592 adjacent to the straight arc. A more realistic approach including all visible components would be useful to further constrain the properties of additional substructure and check whether such configurations remain consistent with respect to the TG limit. While our analysis is concerned only with the straight arc, the cluster A2390 actually exhibits a number of lensing features which should all be taken into account for a complete cluster model. Extending the investigation also to other massive galaxy clusters, future work should address such complex lens models and their implications for TeVeS or related theories and 11eV SNs; a systematic way for approaching this problem has been outlined above.

3.4.7 Concluding remarks

Here we have suggested the use of strong gravitational lensing by galaxy clusters as a test of the combined framework of TeVeS and massive SNs. Originally motivated by theoretical and recently also experimental particle physics [188, 231, 232], the idea of SNs with a mass around 11eV has gained further interest as it provides a possible remedy for the problems of TeVeS and related theories ranging from large cosmological scales down to galaxy clusters. Unlike conventional CDM, such a fermionic HDM component is subject to strong phase-space constraints imposed by the TG limit. This allows one to check cluster lens models inferred within the above framework (or related ones) for consistency.

As an example, we have studied the cluster lens A2390 with its notorious straight arc. Because of its elongation and orientation, the straight image appears to be quite unusual and indicates the need for a rather special lens configuration. Adopting the approximation for weak fields and quasistatic systems, one of the main problems associated with the lensing analysis is the nonlinear relation between the TeVeS metric potential and the underlying matter density distribution. This nonlinearity prevents one from working with projected quantities and requires one to perform all calculations in three dimensions. In addition, one is left with a nontrivial, Poisson-type partial differential equation for the TeVeS scalar field.

To make some progress, we have considered a class of cluster models, based on the assumption of hydrostatic equilibrium, and investigated their lensing properties. This has been achieved by employing a MPI parallel solver for the TeVeS scalar field equation and simulating the corresponding lensing maps on the HUYGENS supercomputer which is located in Amsterdam. Our results imply that such quasiequilibrium configurations are not capable of explaining the observed straight arc. In particular, we have found no evidence for the formation of beak-to-beak or lips catastrophes [211] due to intrinsic TeVeS effects, which could give rise to straight images. Line-of-sight effects and the impact of perturbations are typically small, changing the quantities of interest only on the order of a few percent. Similar to the situation in GR, a suitable TeVeS lens model therefore needs substantially more mass as well as a special density distribution in the cluster's core region.

Based on the above results, we have further outlined a general and systematic approach to cluster lenses which significantly reduces the problem's complexity by avoiding the need of solving the TeVeS scalar field equation. Combined with conventional lensing tools, this opens a new win-

dow to strong gravitational lensing in TeVeS-like modified gravity theories. As a first application, we have explored the TeVeS analog of the bimodal lens configuration discussed in Ref. [213]. For this model, we have derived the SN distribution necessary to produce the desired image, using a simplified approach. The obtained SN density profile has then been compared to the maximally allowed contribution set by the TG phase-space constraint. To this end, we have estimated the maximal density due to the TG limit following the prescription of Ref. [190] and found a slight excess of this limit for the model's secondary component if its core radius is small ($r_C \lesssim 8'' - 9''$). For less compact models, however, the TG bound is not violated. Given the accuracy of our current analysis, we therefore conclude that the bimodal TeVeS lens model appears consistent with the hypothesis of 11eV SNs.

Note that the bimodal lens model ignores the contribution of galaxies. As has been shown, these can have a significant impact on the lensing maps. A more realistic approach, including all visible components and other lensing constraints, should be taken into account to obtain better bounds on the required SN distribution and to check whether such configurations remain consistent with respect to the TG limit. Future work should address more accurate ways of estimating the TG limit in this context, and we suggest extending the investigation to other massive galaxy clusters which indicate the need for dark substructure. Unless one considers different solutions to the missing mass problem inherent to this particular kind of modifications (see, e.g., Ref. [40]), the basic approach presented here should apply to any class of tensor-vector or tensor-vector-scalar theory which recovers the dynamics of MOND in the nonrelativistic limit. Lensing by galaxy clusters could therefore provide an interesting discriminator between CDM and such modified gravity scenarios supplemented by SNs. In addition to the above, we note that next-generation neutrino experiments [233–235] will further constrain the plausibility of 11eV SNs. Even if they remain viable candidates, it still needs to be seen whether such SNs do actually cluster in the desired way [190].

Finally, we advert to the fact that our analysis neglects possible contributions due to perturbations of the TeVeS vector field A_μ. Such contributions are known to be crucial for the formation of large-scale structure [86, 87], where they provide the key to enhanced growth while perturbations of the scalar ϕ only play a subordinate role. As already pointed out in the literature [103], this typically affects scales $\gtrsim 0.1 - 1$Mpc and could be important for galaxy clusters. Owing to the more sophisticated structure of the field equations, however, even a rough magnitude of the vector's impact on these scales has not been estimated yet. Thus our work emphasizes the need for a quan-

titative description of these vector instabilities on small to intermediate scales, i.e. $\sim 0.01 - 1$Mpc. We also note that the result of such an analysis could strongly depend on the particularly assumed theory.

Despite the previously mentioned limitations of the present work, our numerical simulations are probably by far the most detailed in the context of TeVeS and certainly provide the first extensive study of strong lensing features within this modified gravity framework. Applications of our grid-based lensing code (e.g. with respect to offsets between visible matter and weak or strong lensing features [193, 236]) hold the promise of very constraining limits on TeVeS-like theories combined with HDM and other unified recipes for the dynamics of MOND and DM [40, 115, 237, 238].

Chapter 4

Structure formation in modified gravity theories

In the following sections, we shall investigate how modified gravity models influence the process of structure formation. Assuming a particular realization of a chameleon field (see Sec. 2.3.2), we discuss the nonlinear clustering of matter density perturbations in this context and point toward potentially observable signatures which may hold the key to distinguish such frameworks from the ΛCDM model. We will then proceed to TeVeS and focus on the question whether similar approaches are also possible in this specific class of theories.

4.1 General remarks

It is now commonly believed that the cosmological structure as seen today evolved from tiny perturbations around an isotropic and homogeneous spacetime in the very early universe. According to the standard picture, these perturbations originated from random quantum fluctuations within the universe's energy density at that time (typically associated with the Planck scale), but the exact physical processes occurring in this context are still unknown. A popular and remarkably successful approach is the inflationary model [239, 240] which not only provides a setting for generating the spectrum of initial perturbations, but also a suitable explanation for the observed flatness, isotropy and homogeneity of today's universe on large scales. Once inflation sets in, the vacuum fluctuations (in this case those of the inflaton field) are quickly driven outside of the horizon, where they freeze in due to the lack causal contact and effectively become classical. While this fixes the initial conditions for perturbations right after inflation, the further evolution is governed by grav-

itational attraction. As matter collapses into denser regions, it eventually form smaller structures such as galaxies and then clusters of galaxies, with large regions of empty space, the so-called voids, appearing in between.

Typically, these perturbations remain small until deep into the matter dominated era, which allows one to study their evolution with the help of cosmological perturbation theory (applicable to both GR and modified theories of gravity) by linearizing the gravitational field equations around the FRW solution. Due to the statistical nature of primordial fluctuations, however, one cannot make any specific statements about the their actual realization in the universe, but only infer information about the distribution they were drawn from. In the simplest inflationary scenarios, which are usually implemented with a single scalar field, it follows that the underlying distribution is Gaussian [1] and thus the perturbations are expected to be Gaussian random fields. In accordance with the fundamental cosmological assumptions, the statistical properties of these random fields, e.g. their mean or variance, do not change under rotations and translations . Taking the density contrast defined as $\delta = (\rho - \bar{\rho})/\bar{\rho}$ where $\bar{\rho}$ is the mean density, for example, the entire statistical information is encoded into the correlation function $\xi(y)$,

$$\xi(\mathbf{y}) \equiv \langle \delta(\mathbf{x})\delta(\mathbf{x}+\mathbf{y})\rangle \tag{4.1}$$

where the average extends over all positions $\mathbf{x}$ and orientations of $\mathbf{y}$. As dictated by isotropy, the correlation function cannot depend on the direction of $\mathbf{y}$, i.e. $\xi = \xi(y)$. More conveniently, the above is expressed in terms of the power spectrum $P(k)$ which is defined by the variance of δ in Fourier space,

$$\langle \delta(\mathbf{k})\delta^*(\mathbf{k}')\rangle = (2\pi)^3 P(k)\delta_D(\mathbf{k}-\mathbf{k}'), \tag{4.2}$$

where δ_D is the Dirac delta distribution which ensures that modes of different wave vector $\mathbf{k}$ are uncorrelated in Fourier space to guarantee homogeneity. Note that the variance on a scale of $8h^{-1}$Mpc, usually denoted as σ_8, is often used for characterizing the amplitude of the power spectrum.

As soon as δ or other perturbation variables approach values on the order of unity, any perturbative approach breaks down and nonlinear effects become important. Since this breakdown

[1] This property follows from the quantized harmonic oscillator in the vacuum state which predicts a Gaussian probability distribution for each wave vector $\mathbf{k}$. Since the density fluctuations arise from superpositions of enormous numbers of statistically independent vacuum fluctuations of the inflaton field, however, Gaussianity appears more generally as a consequence of the central limit theorem - independent of the underlying probability distributions of the individual Fourier coefficients [240].

occurs at times where basically all modes of interest are well within the horizon, i.e. $aH/k \ll 1$, one usually makes the assumption that time derivatives can safely be neglected compared to spatial ones and tackles the problem using the corresponding nonrelativistic equations (while taking into account the background evolution) since the involved gravitational fields remain small enough to be considered as perturbations to spacetime [2]. In GR, for instance, this is supported by the fact that the linearized Einstein equation for scales much smaller than the horizon becomes structurally identical with the Poisson equation obtained in the nonrelativistic limit. Most notably, this has led to the use of cosmological N-body simulations as a tool for studying the density evolution in the nonlinear regime. In the next section, we shall see how this idea may be applied to the framework of coupled scalar field models. Finally, note that even if the original density perturbation field is Gaussian, it must develop non-Gaussianities during the nonlinear evolution. This is evident because $\delta \geq -1$ by definition, but may grow to arbitrarily large values. Therefore, an originally Gaussian distribution of δ becomes increasingly skewed as it develops a tail toward infinite δ.

4.2 Nonlinear structure growth in chameleon models

In this section, we shall investigate the the nonlinear clustering of density perturbations in the context of coupled scalar field models. Introducing a suitable model which recovers the properties of a chameleon scalar (see Sec. 2.3.2), we give the relevant field equations for weak fields and quasi-static systems and outline a general N-body scheme applicable to this particular class of models. Accounting for spatial variations of the scalar field, we then present the first complete N-body simulations in this framework followed by a discussion of the obtained results and their implications.

4.2.1 Scalar field model with coupling to CDM

In the following, let us consider the specific coupled scalar field model introduced in Ref. [127] which is described by an action of the form (In accordance with most of the literature on this subject, we temporarily switch to a negative metric signature)

$$\mathcal{L}_s = \frac{1}{8\pi G}\int d^4x\,\sqrt{-g}\left[\frac{R}{2} - \frac{1}{2}g^{\mu\nu}\nabla_\mu\phi\nabla_\nu\phi + V_{\rm eff}(\phi)\right], \tag{4.3}$$

[2] Note that there is still no mathematically rigorous proof justifying such an approach.

where $G = G_N$, R denotes the Ricci scalar, ϕ is a dimensionless scalar field with canonical kinetic term and $V_{\text{eff}}(\phi)$ is an effective potential assumed as

$$V_{\text{eff}}(\phi) = V(\phi) - 8\pi G C(\phi)\mathcal{L}_{\text{CDM}}. \tag{4.4}$$

While $\mathcal{L}_{\text{CDM}}$ denotes the Lagrangian of CDM particles [3], the potential $V(\phi)$ and the coupling function $C(\phi)$ are given by

$$V(\phi) \equiv \Lambda_0\left(1 - e^{-\phi}\right)^{-\mu} \tag{4.5}$$

and

$$C(\phi) \equiv e^{\gamma\phi}, \tag{4.6}$$

respectively, where μ and γ are two dimensionless parameters and Λ_0 is a constant on the order of the cosmological constant. Considering the nonrelativistic, weak field limit of Eq. (4.4) ($\phi \ll 1$),

$$V_{\text{eff}}(\phi) \approx \Lambda_0\phi^{-\mu} + 8\pi G(1 + \gamma\phi)\rho_{\text{CDM}}, \tag{4.7}$$

the meaning of this particular parameterization can be understood as follows: As the scalar field ϕ tends to minimize the effective potential, the potential term $\Lambda_0\phi^{-\mu}$ and the coupling $(1 + \gamma\phi)$ to the CDM density lead to competing effects, favoring smaller and larger values of ϕ, respectively. The balance of these two effects is controlled by the parameters μ and γ. The parameter μ is assumed to be very small and controls the time when the effect of the scalar field (mainly exerting a finite-ranged scalar force on CDM particles on galaxy cluster scales) becomes important for cosmology while the parameter γ determines how large it will ultimately be [127].

From variation of the action defined in Eq. (4.3), one finds that the scalar field's equation of motion (EOM) is

$$\nabla^\mu\nabla_\nu\phi + V'(\phi) + 8\pi G\gamma e^{\gamma\phi}\rho_{\text{CDM}} = 0, \tag{4.8}$$

where the prime denotes the derivative with respect to ϕ, i.e. $V' \equiv dV/d\phi$. Furthermore, Einstein's equations can be expressed as

$$G_{\mu\nu} = 8\pi G\left(e^{\gamma\phi}\rho_{\text{CDM}}u_\mu u_\nu + T^{(\phi)}_{\mu\nu}\right), \tag{4.9}$$

[3]The CDM Lagrangian $\mathcal{L}_{\text{CDM}}$ specifies the geodesic flow for many point-like particles of four-velocity u_μ and density ρ_{CDM}

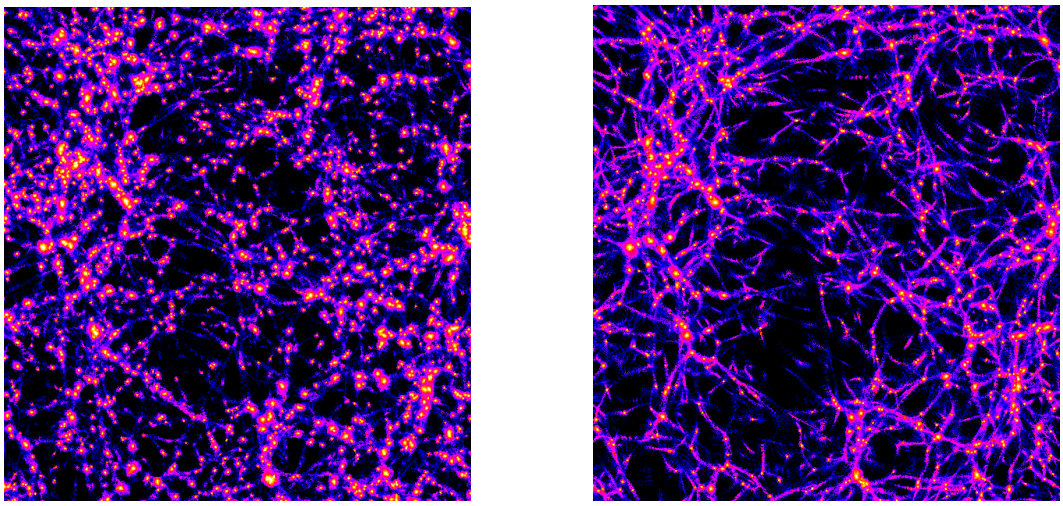

Figure 4.1: Overdensity fields at $z = 0$ for the ϕCDM model with $\gamma = 1$, $\mu = 10^{-5}$ (*left*) and the ΛCDM model (*right*). As can be seen, the former has developed more small-scale structure within the void.

where $G_{\mu\nu}$ is the Einstein tensor and the right-hand side corresponds the energy-momentum tensors of CDM particles with four-velocity $u_\mu$and the scalar field, with the latter given by

$$8\pi G T^{(\phi)}_{\mu\nu} = \nabla_\mu\phi\nabla_\nu\phi - g_{\mu\nu}\left(\frac{1}{2}\nabla_\kappa\phi\nabla^\kappa\phi - V(\phi)\right). \tag{4.10}$$

Note that because of their coupling, the energy-momentum tensors for the scalar field ϕ and CDM particles are not individually conserved whereas their sum is.

The above equations summarize all the physics that will be used in our analysis. An immediate application is the prediction of a uniform Hubble expansion [127]. For values of $\gamma \sim O(1)$ and $\mu \ll 1$, the model's background expansion is completely indistinguishable from ΛCDM, with an actual difference on the order of $O(\mu)$. Basically, this is due to the large enough effective mass of the scalar which forces the field near the potential minimum and is almost time-independent for $\mu \ll 1$ (for a more quantitative explanation, see Ref. [127])

4.2.2 Nonrelativistic approximations

The first step towards a numerical simulation is to obtain the relevant equations of motion in the nonrelativistic and quasistatic limit (in the sense that the time derivatives can be safely neglected compared with the spatial derivatives). This task has already been performed in Ref. [127] where it was shown that the scalar field's EOM in Eq. (4.8) and the modified Poisson equation can be simplified to

$$\partial^2_{\mathbf{x}}\phi = 8\pi G a^2\left[\rho_{\rm CDM}C'(\phi) - \bar{\rho}_{\rm CDM}C'\left(\bar{\phi}\right)\right] + a^2\left[V'(\phi) - V'\left(\bar{\phi}\right)\right] \tag{4.11}$$

and

$$\partial^2_{\mathbf{x}}\Phi = 4\pi G a^3 \left[\rho_{\rm CDM} C(\phi) - \bar{\rho}_{\rm CDM} C\left(\bar{\phi}\right)\right] - a^3 \left[V(\phi) - V\left(\bar{\phi}\right)\right], \tag{4.12}$$

respectively, where the bar denotes background quantities, $\partial^2_{\mathbf{x}} \equiv -\boldsymbol{\nabla}^2_{\mathbf{x}}$ and $\boldsymbol{\nabla}_{\mathbf{x}}$ is the covariant spatial derivative with respect to the conformal coordinate $\mathbf{x}$. Note that the auxiliary dimensionless potential Φ is related to the usual nonrelativistic metric potential W through

$$\Phi \equiv aW + \frac{1}{2}\ddot{a}\mathbf{x}^2, \tag{4.13}$$

where the dot denotes the derivative with respect to conformal time. Finally, introducing the canonical momentum conjugate to $\mathbf{x}$, $\mathbf{p} = a\dot{\mathbf{x}}$, the EOM for CDM particles reads

$$\begin{aligned} \dot{\mathbf{x}} &= \frac{\mathbf{p}}{a}, \\ \dot{\mathbf{p}} &= -\boldsymbol{\nabla}_{\mathbf{x}}\Phi - \gamma a \boldsymbol{\nabla}_{\mathbf{x}}\phi. \end{aligned} \tag{4.14}$$

Note that the two terms on the right hand side appearing in the second relation of Eq. (4.14) correspond to gravity and scalar force, respectively [127]. Assuming that both ϕ and Φ are known from solving Eqs (4.11) and (4.12), the above may be used to evaluate the forces on CDM particles and to evolve their positions and momenta in time.

The validity and limitation of the approximation present in the above equations, in particular neglecting the time derivatives, have been extensively discussed in Ref. [127]. We emphasize that these approximations do not hold in linear regime where the scalar field's time dependence is essential for structure growth. However such terms have indeed been shown to be negligible on scales much smaller than the horizon scale [241]. In the following, we will analyze the first complete N-body simulations in the above framework. Compared to previous work [242, 243], our analysis does not involve any additional assumptions for solving the field equations and thus takes the spatial variation of ϕ into full account, leading to more quantitative and rigorous predictions. Considering the linear regime, it has already been possible to constrain the parameters μ and γ to a fairly narrow range. Here we set γ on the order of unity to force a significant ratio of the scalar force to gravity ($\sim 2\gamma$) and explore the range $10^{-7} \leq \mu \leq 10^{-5}$, covering three orders of magnitude. Restricting ourselves to the above should suffice as the model is either essentially indistinguishable from ΛCDM or deviates too much from it (already at the linear level) beyond this parameter space, thus being of no further interest [127].

4.2.3 A modified N-body code for coupled scalar field models

For the purposes of this work, we have adapted the Multi-Level Adaptive Particle Mesh (MLAPM) code [244] to include the scalar field and its coupling to the CDM N-body particles. One benefit of the adaptive scheme is that the majority of computing resources is dedicated to few high density regions to ensure higher resolution, which is desirable since we expect the behavior of the scalar field to be more complex there. The main modifications to the MLAPM code for our model can be summarized as:

(a) We have added a parallel solver for the scalar field based on Eq. (4.11). The solver uses a similar nonlinear Gauss-Seidel method [245] and the same criterion for convergence as the Poisson solver.

(b) The resulting value for ϕ after the first simulation step is used to calculate the local mass density of the scalar field and thus the source term for the modified Poisson equation which is solved using a fast Fourier transform to obtain the local gravitational potential Φ given by Eq. (4.12).

(c) The scalar force is obtained by differentiating ϕ, and the gravitational force is calculated by differentiating Φ, as required from Eq. (4.14).

(d) The momenta and positions of the CDM particles are then updated, taking into account both gravity and the scalar force, just as in normal N-body codes.

More technical details on the code as well as on how the field equations are implemented into MLAPM using its own internal units have been given in Ref. [127] and will not be presented here.

4.2.4 Matter power spectra from N-body simulations

Using the modified N-body code introduced in the last section, we have performed 6 simulation runs with parameters $\gamma = 0.5, 1$ and $\mu = 10^{-5}, 10^{-6}, 10^{-7}$, respectively. For all these runs, we consider 128^3 CDM particles, 128 domain grid cells in each direction, and the simulation box size is chosen as $B = 64h^{-1}$ Mpc. We further assume a ΛCDM background cosmology which provides a very good approximation for $\mu \ll 1$ [127], adopting present values for the fractional energy densities of CDM and dark energy, $\Omega_{\rm CDM} = 0.28$ and $\Omega_\Lambda = 0.72$. In addition, the normalization of the power spectrum is chosen as $\sigma_8 = 0.88$. Note that the current simulations only take CDM

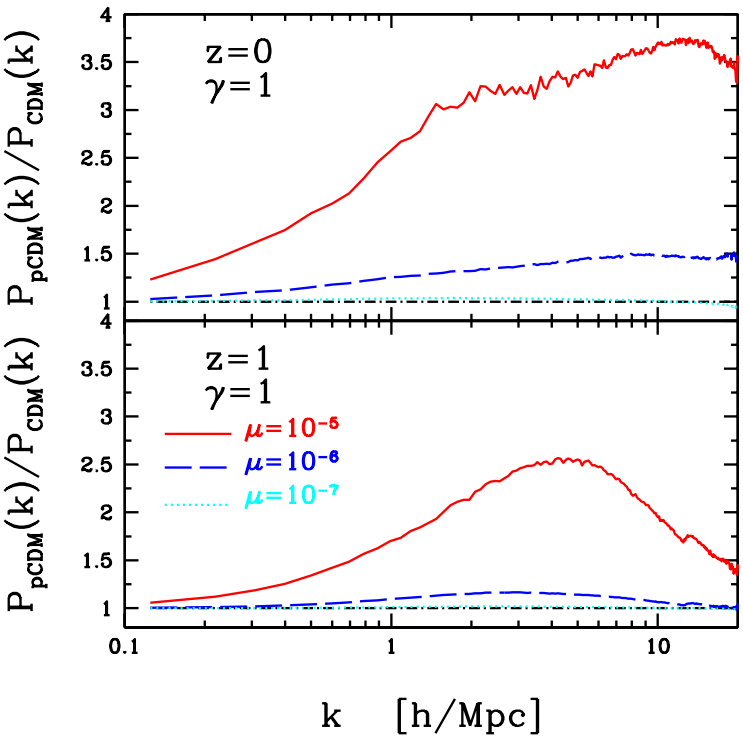

Figure 4.2: Ratios of calculated nonlinear matter power spectra for $\gamma = 1$ and $\mu = 10^{-5}$ (red line), 10^{-6} (blue line) and 10^{-7} (green line) as well as for ΛCDM (black dotted line): Shown are the results for two redshifts, $z = 1$ and $z = 0$. At large scales (small k) the curves converge toward the ΛCDM result (identical to 1). Note that the difference decreases at higher redshift and is expected to be small on both large and very small scales. Error bars of future lensing observations are likely small enough to detect any deviation from ΛCDM on intermediate scales ($k = 0.1 - 10h\mathrm{Mpc}^{-1}$) at a 30% level.

into account and that baryons will be added in a forthcoming study to investigate the bias effect caused by the coupling to dark matter. Given the above parameters, the mass and spatial resolution of the simulation are $9.71 \times 10^9 M_\odot$ and $23.44h^{-1}$kpc (for the most refined regions), respectively. This spatial resolution in high density regions is necessary and sufficient to precisely probe the scalar field in regions where the scalar force is considerably short-ranged.

All simulations started at redshift $z = 49$. In principle, one would need to generate modified initial conditions for the coupled scalar field model, i.e. the initial displacements and velocities of particles which are obtained from a given linear matter power spectrum, because the scalar field coupling also has an impact on the Zel'dovich approximation [246]. In practice, however, we find that the effect on the linear matter power spectrum at this high redshift is negligible, with a relative deviation $\lesssim 10^{-4}$ for our choice of the parameters γ and μ. Concerning the CDM particles in our simulations, we thus simply use the initial conditions for a ΛCDM model which are generated with the help of the GRAFIC tool [247], where we again assume $\Omega_{\mathrm{CDM}} = 0.28$, $\Omega_\Lambda = 0.72$ and $\sigma_8 = 0.88$. An example of the final density field obtained at redshift $z = 0$ is illustrated in Fig. 4.1.

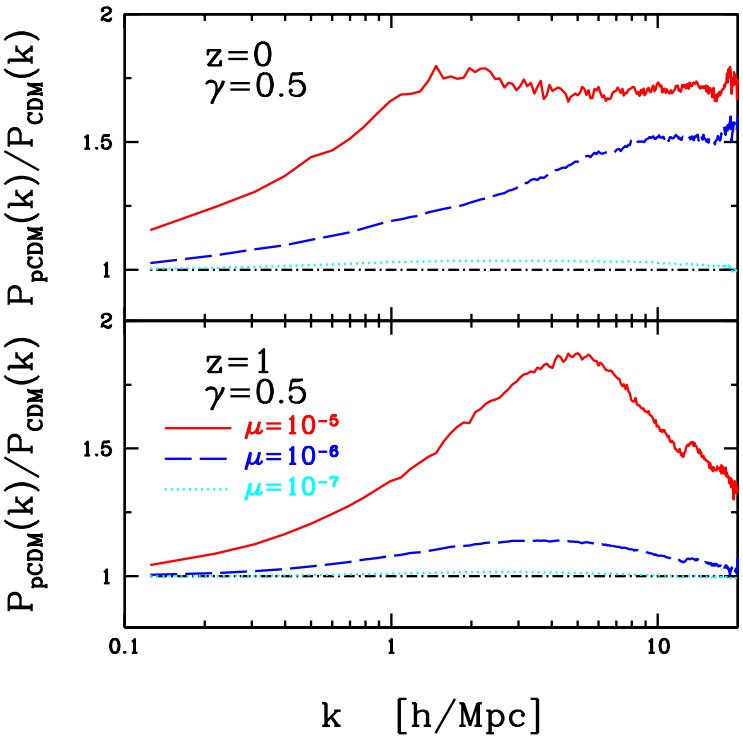

Figure 4.3: Same as Fig. 4.2, but now assuming $\gamma = 0.5$.

For comparison, the figure also shows the corresponding result of a standard ΛCDM simulation. The matter power spectra have been computed with the help of a (fast) Fourier transform of the matter density field, computed on a regular grid $N_G \times N_G \times N_G$ from the particle distribution via a Cloud-in-Cell algorithm (see, e.g. Ref. [248]). For the actual calculation, we set $N_G = 256$ which gives a maximum mode of $k \approx 20h\mathrm{Mpc}^{-1}$ well above the simulation resolution. The nonlinear matter power spectra of the models with $\gamma = 1$ and $\gamma = 0.5$ are displayed in Figs. 4.2 and 4.3, respectively.

As can be seen from the figures, the nonlinear power spectra can be substantially modified compared to a ΛCDM model. Qualitatively, the basic features of the results may be understood from our previous discussion of the chameleon effect in Sec. 2.3.2: For smaller values of μ and larger ρ_{CDM} (higher redshift), the scalar force is significantly suppressed and thus one obtains smaller deviations from ΛCDM. On the other hand, increasing the value of γ strengthens the scalar force and causes larger deviations from the ΛCDM model. Since large scales are beyond the probe of the scalar force [127], the power spectrum for small k is not significantly affected. Similarly, when moving to very large k, the chameleon effect suppresses the scalar force because the density on small scales is high, therefore softening the deviation from ΛCDM. Interestingly, the difference between the models becomes largest on intermediate scales which are relevant for galaxy clusters

($\sim 10^2 - 10^3$kpc). Observationally, this would most likely appear as a change of σ_8 on the order of 15-20% for models with $\gamma \sim 0.5 - 1$ and $\mu = 10^{-6}$ (see Figs. 4.2 and 4.3). For current lensing measurements such as the CFHT Legacy Survey (see, e.g., Ref. [249] or Fig. 11 of Ref. [250]) over a rather limited range, one cannot constrain these models since any variation of σ_8 appears to be lower than 30%. Future surveys such as the Kilo-Degree Survey (KIDS), however, will be able to measure the scale dependence within the range $k = 0.1 - 10h\text{Mpc}^{-1}$ where the deviation of the models from ΛCDM is maximal, and therefore open a new window to test these models and to constrain the interesting part of their parameter space. Finally, note that although we have restricted our analysis to the models introduced in Ref. [127], the general framework introduced here is also applicable to other possible constructions of coupled scalar fields.

4.3 Metric perturbations in TeVeS

As we have seen in the last section, it is generally possible to study modified frameworks with the help of conventional methods and tools. Now we shall investigate whether similar approaches may, in principal, be achieved in the context of TeVeS. In this case, one may not simply start with the nonrelativistic field equations because these do not include contributions of the vector field which are known to be crucial for the formation of structure on large scales [87]. Introducing a more general class of potential functions, we revisit the cosmological background evolution before turning our attention to metric perturbations in the conformal Newtonian gauge. Making an ansatz for scalar field perturbations in the modified Einstein-de Sitter cosmology, we demonstrate how the field equations can be cast into convenient form and discuss the resulting TeVeS analog of the growth equation. Finally, we outline several possible applications of our results.

4.3.1 Choice of the scalar field potential

For the purposes of our analysis, it is convenient to work with the notation introduced in Eq. (2.45) (see Sec. 2.2.2 A). This allows one to rewrite Eq. (2.50) as

$$V(\mu) = \frac{3\mu_0^2}{128\pi l_B^2}\left[\hat{\mu}\left(4 + 2\hat{\mu} - 4\hat{\mu}^2 + \hat{\mu}^3\right) + 2\log\left(1 - \hat{\mu}\right)^2\right], \tag{4.15}$$

where we have defined $\hat{\mu} \equiv \mu/\mu_0$ and μ_0 is a dimensionless constant related to k_B through $\mu_0 = 8\pi/k_B$. Again, note that the choice of $V = \mu^2 F/16\pi l_B^2$ fixes the theory's behavior in the nonrelativistic limit as well as the dynamics on cosmological scales. In order to avoid ambiguities in the

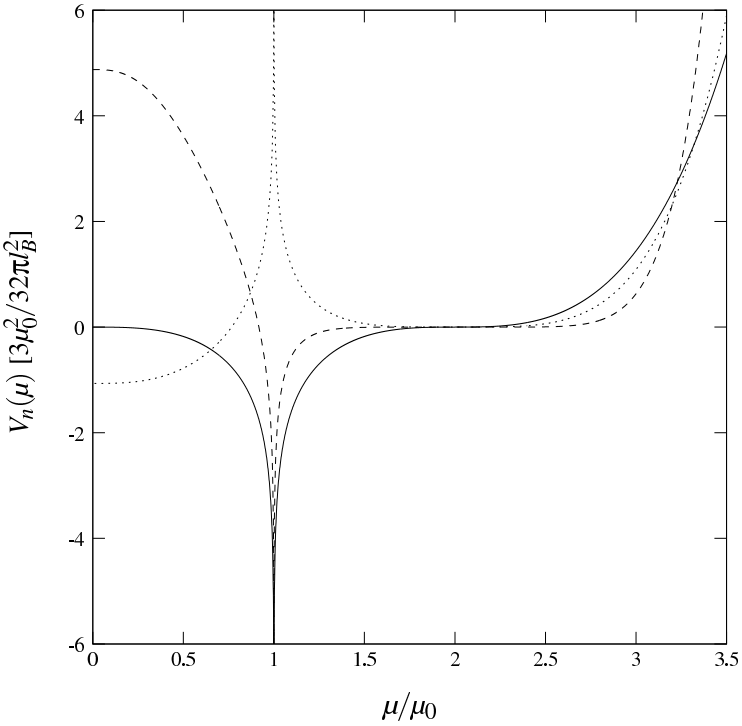

Figure 4.4: Illustration of the generalized potential $V_n(\mu)$ given by Eq. (4.16) for $n = 2$ (solid line), 3 (dotted line), and 6 (dashed line).

theory, one needs to specify the physically relevant branches of V. Translating the results from Sec. 2.2.2 B, one finds that quasistatic systems are characterized by the condition $V' \equiv dV/d\mu < 0$. If we want TeVeS to reproduce the dynamics of MOND in the nonrelativistic approximation, we have to choose the branch covering the range $0 < \mu < \mu_0$ since it is the singularity at $\mu = \mu_0$ which ensures the existence of a Newtonian limit. Similarly, cosmological models satisfy the condition $V' \geq 0$. To guarantee that the cosmological scalar field yields a strictly positive contribution to the energy density, one has to assume the monotonically increasing branch as the physical one (see Sec. 2.2.2 B). Since cosmological models require $V' \geq 0$, one obtains $\mu > \mu_0$ and thus cannot use the same potential branch as for quasistatic systems ($\mu < \mu_0$). Because V turns singular at $\mu = \mu_0$, potentials like the one specified in Eq. (4.15) therefore exhibit a disconnection between the regimes relevant for cosmology and quasistatic systems, respectively. Lacking a smooth transition between these two regimes, however, it is unclear how bound systems such as galaxies would decouple from the Hubble flow or if such a decoupling results in the quasistatic limit discussed above [4]. To resolve this issue, an interesting alternative has been proposed in Ref. [227], with its cosmology studied in Ref. [98]. In the following, however, we will not take this approach.

[4]There is *a priori* no guarantee for reaching the domain of quasistatic systems if one considers the growth of initial perturbations around a FRW background.

Instead - for reasons that will become clear below - we shall assume the following general class of potentials [96]:

$$V_n(\mu) = \frac{3\mu_0^2}{32\pi l_B^2}\left[\frac{n+4+(n+1)\hat{\mu}}{(n+1)(n+2)}(\hat{\mu}-2)^{n+1} + \frac{(-1)^n}{2}\log(1-\hat{\mu})^2 + \sum_{m=1}^{n}\frac{(-1)^{n-m}}{m}(\hat{\mu}-2)^m\right], \tag{4.16}$$

where $n \geq 2$ [5]. Adopting different values of n, Fig. 4.4 illustrates the resulting potential shape as a function of $\hat{\mu}$. Note that the such generalized potential reduces to Bekenstein's toy model in Eq. (4.15) if $n = 2$. The derivative of $V_n(\mu)$ takes a simpler form and can be expressed as

$$V_n'(\mu) = \frac{3\mu_0}{32\pi l_B^2}\hat{\mu}^2\frac{(\hat{\mu}-2)^n}{\hat{\mu}-1}. \tag{4.17}$$

As already mentioned, cosmological models in TeVeS must satisfy the condition $V' \geq 0$. As we have already seen in Sec. 2.2.2 B, one is, in principal, always free to choose between two possible potential branches if one requires that V' is single-valued. In accordance with previous investigations and to ensure a positive contribution of the scalar field to the energy density for every choice of n, we will use the branch ranging from the extremum at $\bar{\mu} = 2\mu_0$ to infinity. Under these preliminaries, it was found that the potential in Eq. (4.16) gives rise to tracker solutions of the scalar field [96], with a background evolution similar to other general cosmological theories involving tracker fields [120, 251, 252]. We shall further elaborate on this behavior and an approximate analytic treatment in Sect. 4.3.2 B.

4.3.2 Revisiting the cosmological background in TeVeS

4.3.2 A Evolution equations

Imposing the usual assumptions of an isotropic and homogeneous spacetime, both $g_{\mu\nu}$ and $\tilde{g}_{\mu\nu}$ are given by FRW metrics with scale factors a and $b = ae^{\bar{\phi}}$, respectively, where $\bar{\phi}$ is the background value of the scalar field (see our previous discussion in Sec. 2.2.2 C). For a spatially flat universe, the modified Friedmann equation in the matter frame reads

$$3H^2 = 8\pi G_{\text{eff}}\left(\bar{\rho}_\phi + \bar{\rho}\right), \tag{4.18}$$

[5] As previously pointed out in Ref. [96], this class of potentials will modify the dynamics of quasistatic systems if $n \neq 2$.

where we have expressed Eq. (2.65) in a more convenient way (the physical Hubble parameter is still defined as $H = \dot{a}/a^2$ and the overdot denotes the derivative with respect to conformal time). Here $\bar{\rho}$ corresponds to the FRW background density of the fluid and the scalar field density takes the form

$$\bar{\rho}_\phi = \frac{e^{2\bar{\phi}}}{16\pi G}\left(\bar{\mu}V' + V\right). \tag{4.19}$$

The effective gravitational coupling strength is given by

$$G_{\rm eff} = Ge^{-4\bar{\phi}}\left(1 + \frac{d\bar{\phi}}{d\log a}\right)^{-2} \tag{4.20}$$

which is generally time-varying through its dependence on the scalar field $\bar{\phi}$. Just as in GR, the energy density $\bar{\rho}$ evolves according to

$$\dot{\bar{\rho}} = -3\frac{\dot{a}}{a}(1+w)\bar{\rho}, \tag{4.21}$$

where w is again the EoS parameter of the matter fluid. In case of multiple background fluids, i.e. $\bar{\rho} = \sum_i \bar{\rho}_i$, the relative densities Ω_i are defined as

$$\Omega_i = 8\pi G_{\rm eff}\frac{\bar{\rho}_i}{3H^2} = \frac{\bar{\rho}_i}{\bar{\rho} + \bar{\rho}_\phi}. \tag{4.22}$$

The evolution of the scalar field $\bar{\phi}$ is governed by

$$\dot{\bar{\phi}} = \dot{\bar{\phi}}\left(\frac{\dot{a}}{a} - \dot{\bar{\phi}}\right) - \frac{1}{U}\left[3\bar{\mu}\frac{\dot{b}}{b}\dot{\bar{\phi}} + 4\pi G a^2 e^{-4\bar{\phi}}\left(\bar{\rho} + 3\bar{P}\right)\right], \tag{4.23}$$

where $\bar{P}$ is the fluid's background pressure and the function U is related to the potential V,

$$U(\bar{\mu}) = \bar{\mu} + 2\frac{V'}{V''}. \tag{4.24}$$

In addition, the scalar field obeys the constraint equation

$$\dot{\bar{\phi}}^2 = \frac{1}{2}a^2 e^{-2\bar{\phi}}V' \tag{4.25}$$

which can be inverted to obtain $\bar{\mu}(a, \bar{\phi}, \dot{\bar{\phi}})$. For later use, we also introduce the relation

$$2\frac{\dot{a}}{a}\frac{\dot{b}}{b} - \frac{\ddot{b}}{b} - \bar{\mu}\dot{\bar{\phi}}^2 = 4\pi G a^2 e^{-4\bar{\phi}}\left(\bar{\rho} + \bar{P}\right) \tag{4.26}$$

which follows from combining Eq. (4.18) with Eq. (4.25) and the corresponding Raychaudhuri equation (see Ref. [101]).

As already mentioned in Sec. 2.2.2 C, previous investigations [43, 86, 96] have shown that a broad range of expressions for the potential V (including the choice in Eq. (4.16)) leads to $e^{\bar{\phi}} \approx 1$ and $\bar{\rho}_\phi \ll 1$ throughout cosmological history. Therefore, the background evolution is very similar to the standard case of GR, with only small corrections induced by the scalar field.

4.3.2 B Tracker solutions of the scalar field

For the class of potentials specified in Eq. (4.16), it has been found that the scalar field exhibits a (stable) tracking behavior and synchronizes its energy density with the dominant component of the universe [86, 96]. Tracking occurs as V' tends to its zero point where $\bar{\mu} = 2\mu_0$, and the evolution of the field $\bar{\phi}$ during tracking is approximately given by

$$\bar{\phi} = \bar{\phi}_0 + \frac{|1+3w|}{2\beta\mu_0|1-w|-|1+3w|}\log a, \tag{4.27}$$

where $\bar{\phi}_0$ is an integration constant and $\beta = \pm 1$, with the actual sign depending on the background fluid's EoS parameter w and Eq. (4.23). Its density $\bar{\rho}_\phi$ then exactly scales like that of the fluid, and the relative density parameter Ω_ϕ turns approximately into a constant,

$$\Omega_\phi = \frac{(1+3w)^2}{6\mu_0\,(1-w)^2}. \tag{4.28}$$

Note that the right-hand side of Eq. (4.27) slightly differs from the expression presented in Ref. [96]. In App. D.1, we discuss why this is the case and show that Eq. (4.27) is indeed the correct result.

Following the lines of Ref. [96], $\bar{\mu}$ may then be expressed as $\bar{\mu} = 2\mu_0(1+\epsilon)$ with $0 < \epsilon \ll 1$. Using $V'(2\mu_0) = 0$ and expanding V' to lowest order in ϵ, Eq. (4.25) leads to

$$\epsilon = \frac{1}{2}\left(\frac{16\pi l_B^2}{3\mu_0}\frac{e^{2\bar{\phi}}}{a^2}\dot{\bar{\phi}}^2\right)^{1/n}. \tag{4.29}$$

It turns out that this is the only stage at which the constant l_B enters the evolution equations. In preparation for Sect. 4.3.3, we further take the time derivative of the above, which yields the useful relation

$$\dot{\bar{\phi}}\dot{\epsilon} = \frac{2}{n}\left(\ddot{\bar{\phi}}^2 - \dot{\bar{\phi}}\frac{\dot{a}}{a} + \dddot{\bar{\phi}}\right)\epsilon. \tag{4.30}$$

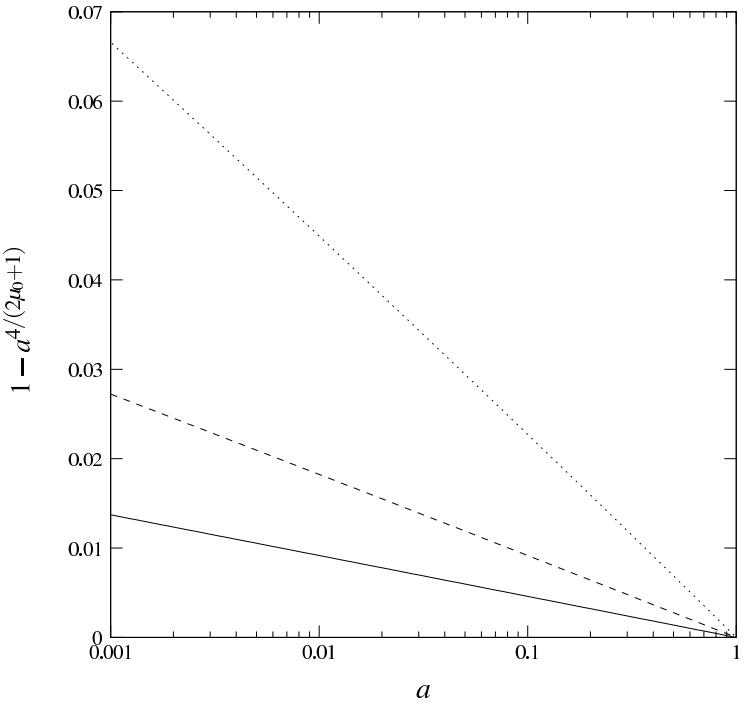

Figure 4.5: Relative deviation of the Hubble expansion in the modified Einstein-de Sitter cosmology from the ordinary GR case: Shown are the results for $\mu_0 = 200$ (dotted line), 500 (dashed line), and 1000 (solid line).

Note that stable tracking requires ϵ to asymptotically decrease to zero, i.e. $\epsilon \to 0$. Therefore one has the condition $\dot{\epsilon} < 0$ which may be used to infer the proper sign of the parameter β in Eq. (4.27) (see App. D.1).

4.3.2 C Modified Einstein-de Sitter cosmology

In what follows, we shall assume a universe entirely made of pressureless matter with perfect tracking of the scalar field, corresponding to the Einstein-de Sitter model in GR. Setting $\bar{P} = w = 0$ fixes $\beta = -1$, and thus the scalar field can be written as

$$\bar{\phi} = \bar{\phi}_0 - \frac{1}{2\mu_0 + 1} \log a. \tag{4.31}$$

To find the proper value of β, one may either insert Eq. (4.27) into Eq. (4.23), or use the argument presented in App. D.1. Since the fluid evolves according to Eq. (4.21), the density takes the form $\bar{\rho} = \bar{\rho}_0 a^{-3}$, with $\bar{\rho}_0$ being the background density's value today. Thus exploiting Eq. (4.28) allows one to rewrite the modified Friedmann equation in the matter frame as

$$H^2 = H_0^2 a^{-3+4/(2\mu_0+1)}, \tag{4.32}$$

where we have used the definition

$$H_0^2 = e^{-4\bar{\phi}_0}\frac{8\pi G\bar{\rho}_0}{3}\left(1+\frac{1}{6\mu_0-1}\right)\left(1-\frac{1}{2\mu_0+1}\right)^{-2}. \tag{4.33}$$

From Eq. (4.32), it is evident that the deviation of the Hubble expansion from the ordinary Einstein-de Sitter case is entirely characterized by the parameter μ_0. For several reasons [43], μ_0 should take a rather large value on the order of $100-1000$, and thus this deviation will be small. Assuming different choices of μ_0, Fig. 4.4 shows the relative difference between the models as a function of the scale factor a, indicating that the change of the expansion is only at the percent level.

4.3.3 Perturbations in conformal Newtonian gauge

4.3.3 A Preliminaries

Now we will turn to metric perturbations around a spatially flat FRW spacetime in TeVeS. Starting point is the set of linear perturbation equations for TeVeS which have been derived in fully covariant form in Ref. [101]. For simplicity, we shall restrict the analysis to scalar modes only and work within the conformal Newtonian gauge. In this case, metric perturbations are characterized by two scalar potentials Ψ and Φ, and the line element in the matter frame is given by

$$ds^2 = a^2\left[-(1+2\Psi)d\tau^2 + (1-2\Phi)\delta_{ij}dx^i dx^j\right]. \tag{4.34}$$

Similarly, one needs to consider perturbations of the other fields: While the fluid perturbation variables are defined in the usual way, i.e. the density perturbation, for instance, is expressed in terms of the density contrast δ,

$$\rho = \bar{\rho} + \delta\rho = \bar{\rho}\,(1+\delta)\,, \tag{4.35}$$

the scalar field is perturbed as

$$\phi = \bar{\phi} + \varphi, \tag{4.36}$$

where φ is the scalar field perturbation. Finally, the perturbed vector field is written as

$$A_\mu = ae^{-\bar{\phi}}\left(\bar{A}_\mu + \alpha_\mu\right), \tag{4.37}$$

where $\bar{A}_\mu = (1, 0, 0, 0)$ and

$$\alpha_\mu = (\Psi - \varphi, \boldsymbol{\nabla}\alpha)\,. \tag{4.38}$$

Note that the time component of the vector field perturbation is constrained to be a combination of metric and scalar field perturbations, which is a consequence of the unit-norm condition given by Eq. (2.40). Therefore, one needs to consider only the longitudinal perturbation component α. The full set of perturbation equations is given in App. D.2.

4.3.3 B A closer look at scalar field perturbations

To begin with, we consider perturbations of the scalar field. From previous numerical analysis, these have been found to play only a negligible role for structure formation [86, 89]. Since the perturbed scalar field equation is of second order, it is helpful to introduce an auxiliary perturbation field γ which allows one to split the scalar field equation into a system of two first-order equations. Performing this split, the two resulting equations (expressed in Fourier space) are given by

$$\begin{aligned}\dot{\gamma} =& \frac{\bar{\mu}}{a} e^{-3\bar{\phi}} k^2 \left(\varphi + \dot{\bar{\phi}}\alpha\right) - 2\frac{\bar{\mu}}{a} e^{\bar{\phi}} \dot{\bar{\phi}} \left(3\dot{\tilde{\Phi}} + k^2 \tilde{\zeta}\right) \\ & - 3\frac{\dot{b}}{b}\gamma + 8\pi G a e^{-3\bar{\phi}} \bar{\rho} \left[\left(1 + 3C_s^2\right)\delta + (1 + 3w)\left(\tilde{\Psi} - 2\varphi\right)\right]\end{aligned} \tag{4.39}$$

and

$$\dot{\varphi} = -\frac{1}{2U} a e^{-\bar{\phi}} \gamma + \dot{\bar{\phi}}\tilde{\Psi}. \tag{4.40}$$

Here $\tilde{\Psi} = \Psi - \varphi$ and $\tilde{\Phi} = \Phi - \varphi$ are the metric potentials expressed in the Einstein frame, $k = |\mathbf{k}|$ is the modulus of the comoving wave vector $\mathbf{k}$, and C_s denotes the matter fluid's sound speed which is defined as the ratio between the fluid's pressure perturbation δP and the corresponding density perturbation $\delta\rho$, i.e. $C_s^2 = \delta P/\delta\rho$. The perturbation $\tilde{\zeta}$ is related to α through

$$\tilde{\zeta} = \left(e^{-4\bar{\phi}} - 1\right)\alpha. \tag{4.41}$$

Assuming a general matter fluid whose background evolution is given by Eq. (4.21) together with a cosmological constant, we take the time derivative of Eq. (D.21) and eliminate $\dot{\theta}$ with the help of Eq. (D.15) from the resulting expression. The next step is to get rid of the time derivatives of $\tilde{\Phi}$. This can be achieved by exploiting an algebraic relation which is obtained from combining Eqs.

(D.22) and (D.23). Finally, using Eqs. (D.11) and (4.39), one arrives at

$$\begin{aligned}&\left[2\frac{\dot{a}}{a}\frac{\dot{b}}{b}-\frac{\ddot{b}}{b}-\bar{\mu}\dot{\bar{\phi}}^2-4\pi G a^2 e^{-4\bar{\phi}}\bar{\rho}(1+w)\right]\tilde{\Psi}\\&=\left[\bar{\mu}\left(4\dot{\bar{\phi}}^2+2\dot{\bar{\phi}}\frac{\dot{a}}{a}+\ddot{\bar{\phi}}\right)+\dot{\bar{\mu}}\dot{\bar{\phi}}+4\pi G a^2 e^{-4\bar{\phi}}\bar{\rho}(1+3w)\right]\varphi.\end{aligned}\tag{4.42}$$

From Eq. (4.26), one immediately sees that the coefficient in front of $\tilde{\Psi}$ vanishes. Thus the above gives a trivial identity and we cannot infer any information on the relation between the scalar field perturbation φ and the metric potential $\tilde{\Psi}$. This somewhat reflects the fact that φ corresponds to a full degree of freedom in the theory and the occurrence of trivial relations like in Eq. (4.42) is indeed a generic feature of modified gravity theories of this kind [6]. For purposes that will become clear below, however, let us introduce a function B_φ such that

$$\tilde{\Psi}=B_\varphi\varphi.\tag{4.43}$$

In general, B_φ will be a function of time and perhaps even depend on scale. Moreover, it is likely that its particular form will also depend on the used cosmological model and the choice of the scalar potential V.

As for the auxiliary perturbation γ, it is possible to arrive at a similar relation as given in Eq. (4.42). To see this, we multiply Eq. (D.20) with the scale factor b and take the time derivative. Combining the result with Eqs. (D.18) and (D.23), we eliminate $\dot{E}$ and the time derivative of $\tilde{\zeta}$, respectively. Substituting $\dot{\varphi}$ and $\dot{\gamma}$ with the help of Eqs. (4.39) and (4.40), respectively, one eventually ends up with

$$\begin{aligned}&ae^{-\bar{\phi}}\left[3\frac{\dot{b}}{b}\frac{\bar{\mu}}{U}\dot{\bar{\phi}}-\frac{\dot{a}}{a}\dot{\bar{\phi}}+\dot{\bar{\phi}}^2+\ddot{\bar{\phi}}+\frac{1}{U}4\pi G a^2 e^{-4\bar{\phi}}\bar{\rho}(1+3w)\right]\gamma\\&-6\frac{\dot{b}}{b}\left[\dot{\bar{\mu}}\dot{\bar{\phi}}+\bar{\mu}\ddot{\bar{\phi}}+2\left(\dot{\bar{\phi}}+\frac{\dot{b}}{b}\right)\bar{\mu}\dot{\bar{\phi}}+4\pi G a^2 e^{-4\bar{\phi}}\bar{\rho}(1+3w)\right]\varphi\\&-2\left[2\frac{\dot{b}}{b}\left(\dot{\bar{\phi}}-\frac{\dot{b}}{b}\right)+\frac{\ddot{b}}{b}+\bar{\mu}\dot{\bar{\phi}}^2+4\pi G a^2 e^{-4\bar{\phi}}\bar{\rho}(1+w)\right]\left(3\dot{\tilde{\Phi}}+k^2\tilde{\zeta}+3\frac{\dot{b}}{b}\tilde{\Psi}\right)=0.\end{aligned}\tag{4.44}$$

Using the background relations presented in Sec. 4.3.2 A, we find that Eq. (4.44) again yields a trivial identity, with a general structure very similar to that found before. A direct comparison

[6] From private communication with C. Skordis.

between Eqs. (4.42) and (4.44) suggests the definition of another function B_γ which is given by

$$\left(3\dot{\tilde{\Phi}} + k^2\tilde{\zeta}\right) + ae^{-\bar{\phi}}B_\gamma\gamma = 0. \tag{4.45}$$

Now assuming that the functions B_φ and B_γ (corresponding to the new degrees of freedom of scalar and vector field, respectively) are known, one can show from a suitable combination of the perturbation equations in App. D.2 that the metric potentials are solely expressible in terms of the matter fluid variables, putting the equations into a form more suitable for further investigations. Since γ corresponds to an auxiliary perturbation field related to φ, however, one might expect that these functions will not be fully independent from each other.

Taking the view that B_φ and B_γ emerge from a mathematically well-defined limiting process of the above equations, the algebraic structure of Eqs. (4.42) and (4.44) suggests that they may be related according to the corresponding coefficients of the scalar field perturbations φ and γ. In situations where $\bar{\mu}$ is close to its minimum (such as during tracking), i.e. $\bar{\mu} = 2\mu_0(1+\epsilon)$, we further have the two first-order expressions

$$\frac{\bar{\mu}}{U} = 1 - \frac{2}{n}\epsilon \tag{4.46}$$

and

$$\frac{2\mu_0}{U} = 1 - \frac{n+2}{n}\epsilon, \tag{4.47}$$

which can be exploited in Eq. (4.44), leading to the the ansatz

$$4\mu_0\left(3\dot{\tilde{\Phi}} + k^2\tilde{\zeta}\right) + ae^{-\bar{\phi}}\left(1 - \frac{n+2}{n}\epsilon\right)B_\varphi\gamma = 0 \tag{4.48}$$

to first order in ϵ. If indeed such a relation exists or at least provides a suitable approximation, it should be possible to verify this with the help of the field equations or directly by numerical analysis. Current work is investigating this issue in more detail. One obvious concern is that such an approach could introduce inconsistencies which would spoil any results obtained under the assumption of Eq. (4.48). As we shall see in the next section, however, this does not appear to be the case. The above relations may then be used to eliminate the scalar field variables φ and γ from the perturbation equations. As will become clear, this forms the key to deriving approximate expressions for the metric potentials in analogy to the framework of GR. In accordance with the findings of Ref. [87], B_φ should take values on the order of μ_0 and, for simplicity, we will further assume that B_φ may be treated as a constant.

4.3.4 Applications on subhorizon scales

4.3.4 A Modified Poisson equations

In the following, we shall assume the previously discussed modified Einstein-de Sitter cosmology with perfect tracking of the scalar field $\bar{\phi}$. This allows one to use the corresponding background expressions presented in Sec. 4.3.2 C and considerably simplifies the analysis of the modified equations. Adopting the relations for φ and γ presented in Sect. 4.3.3 B and assuming that $B_\varphi =$ const, one may now express metric perturbations solely in terms of the matter fluid variables and a detailed derivation of this result can be found in App. D. As a first application, we shall investigate the behavior of this model for scales much smaller than the horizon. In this case, one has $aH/k \ll 1$ and the metric potentials approximately take the form (again see App. D for details)

$$\tilde{\Psi}, \tilde{\Phi} \propto \frac{\delta}{k^2}. \tag{4.49}$$

Just as in GR, the potentials depend on the density contrast only and they also exhibit the same scale dependence (which is not too surprising as we are working within the linearized approximation). Unlike the ordinary Einstein-de Sitter case, however, the time dependence of the metric potentials is more complex and involves the field $\bar{\phi}$ which is therefore expected to have a significant impact on the growth of density perturbations.

4.3.4 B Growth of density perturbations

Equipped with an analytic expression for the the potential $\tilde{\Psi}$ (or equivalently Ψ), we now proceed with the analysis of structure growth in the context of TeVeS. As is well known, the ordinary Einstein-de Sitter model in GR gives rise to a growth equation of the form

$$\frac{d^2\delta}{da^2} + \frac{3}{2a}\frac{d\delta}{da} - \frac{3}{2a^2}\delta = 0, \tag{4.50}$$

with the two solutions $\delta \propto a^{-3/2}$ and $\delta \propto a$. Following the same derivation as in GR, the TeVeS analog of Eq. (4.50) for our present assumptions reads

$$\frac{d^2\delta}{da^2} + \frac{1}{2a}\left(3 + \frac{4}{2\mu_0 + 1}\right)\frac{d\delta}{da} - \frac{\tilde{A}}{a^2}\left(1 + B_\varphi^{-1}\right)\delta = 0, \tag{4.51}$$

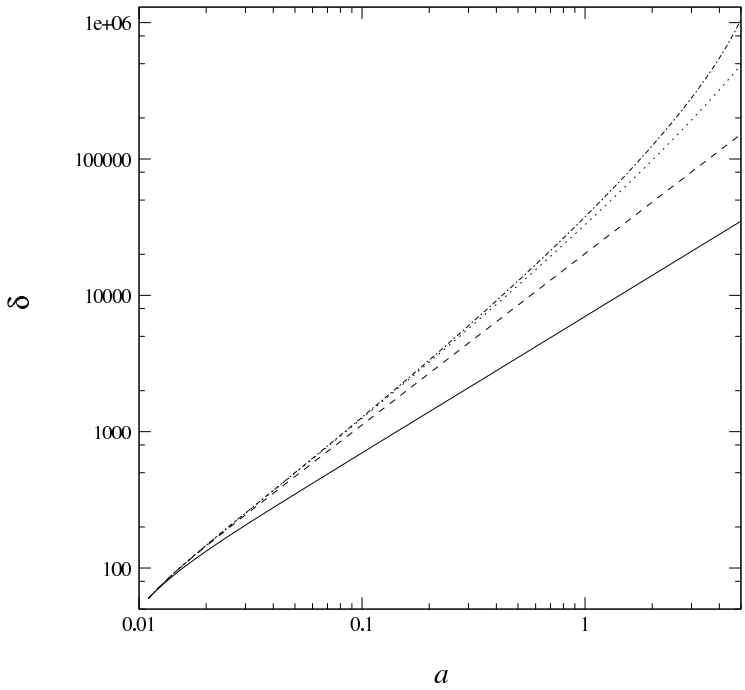

Figure 4.6: Evolution of subhorizon density perturbations in the modified Einstein-de Sitter cosmology: Assuming a potential with $n = 4$ and a scalar perturbation ratio $B_\varphi = 3\mu_0/2$, the figure illustrates results for $K_B = 1$ (dashed line), 0.1 (dotted line), and 0.09 (dashed-dotted line). For comparison, the corresponding evolution in the ordinary Einstein-de Sitter model is also shown (solid line).

where $\tilde{A}$ depends on $\bar{\phi}$ and is given by Eq. (D.30). Assuming $B_\varphi = 3\mu_0/2$ and setting $\mu_0 = 1000$, $l_B = 100$Mpc, $\bar{\phi}_0 = -0.003$ [7] and $n = 4$ for the scalar potential, Fig. 4.6 shows the numerically calculated evolution of δ for different values of K_B and an arbitrary, but fixed choice of initial conditions at $a = 0.01$. As can be seen from the figure, our simple model recovers the enhanced growth reported in Ref. [87] for small values of K_B (~ 0.1). For larger values of K_B ($\gtrsim 1$), however, this enhancement does not occur and the density contrast follows a power law with $\delta \propto a^{1.27}$, thus still growing faster than in the ordinary Einstein-de Sitter case. This behavior can be better understood by expanding the function $\tilde{A}$ in terms of the scalar field $\bar{\phi}$ which is much smaller than unity, i.e. $|\bar{\phi}| \ll 1$. This immediately yields

$$\tilde{A} \approx \frac{3B_\varphi}{2\mu_0} + 6\left[3\frac{B_\varphi}{\mu_0} + \frac{4}{K_B}\left(1 - \frac{B_\varphi}{\mu_0}\right)\right]\bar{\phi} + O\left(\bar{\phi}^2\right), \tag{4.52}$$

where we have additionally neglected terms proportional to ϵ and used that $\mu_0 \gg 1$. If K_B is sufficiently large compared to $\bar{\phi}$, the zeroth-order term in the above will dominate and thus $\tilde{A} \approx$

[7] Note that the choice of a small negative value for $\bar{\phi}$ does not automatically violate causality [43, 253] and is in accordance with the results of Ref. [87].

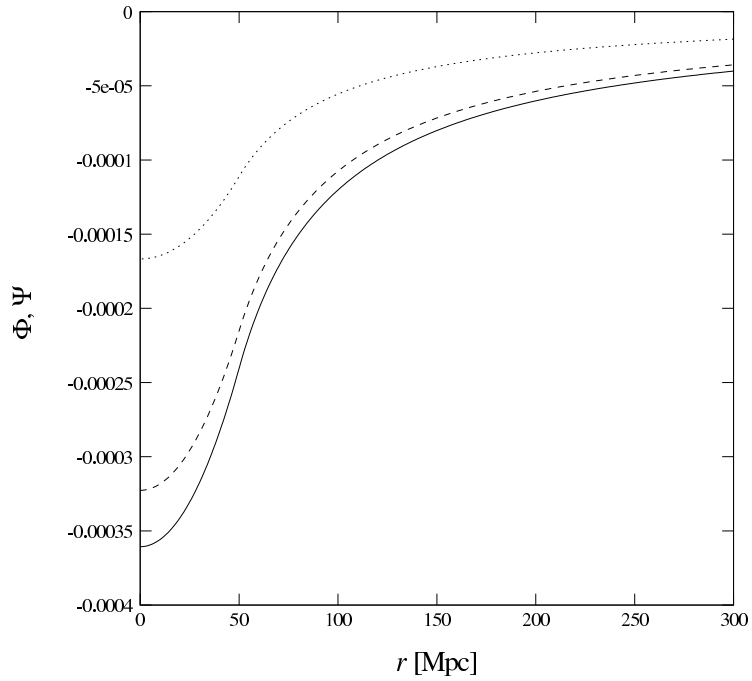

Figure 4.7: Metric perturbations Ψ and Φ for a top-hat overdensity at redshift $z = 1$ ($a = 0.5$): Assuming $K_B = 0.1$, the figure shows the resulting potentials Ψ (dashed line), Φ (solid line) and the corresponding GR result (dotted line; the potentials are the same) as a function of the physical radial coordinate r.

$3B_\varphi/2\mu_0$. In this case, one can solve Eq. (4.51) analytically and we find $\delta \propto a^p$ with

$$p = \frac{1}{4}\left(\sqrt{1 + 24\frac{B_\varphi}{\mu_0}} - 1\right) \tag{4.53}$$

for the growing solution. On the other hand, if K_B is chosen small enough, the term proportional to $\bar{\phi}$ in Eq. (4.52) will become important, leading to the enhanced growth observed in Fig. 4.6. Although likely related to our present approximations, Eq. (4.52) suggests that for $B_\varphi = \mu_0$, which would correspond to Eq. (4.50) in the limit of large K_B, additional growth should be suppressed since the term proportional to $\bar{\phi}/K_B$ vanishes; indeed, we have numerically verified that enhanced growth does not occur in this case. Whether such a feature remains for more realistic time-varying choices of B_φ (possibly motivated from numerical analysis) remains to be seen. Also note that all models which exhibit enhanced growth eventually run into a singularity which appears to be connected to the used logarithmic approximation for $\bar{\phi}$ in Eq. (4.31), but could also arise as a consequence of our assumption that $B_\varphi = \text{const}$. Clearly, this warrants further investigation and should ideally include cosmologies which also account for the effects of DE.

To conclude this section, we demonstrate how the mechanism responsible for enhanced growth generates differences between the matter frame potentials Ψ and Φ (Remember that in GR, such

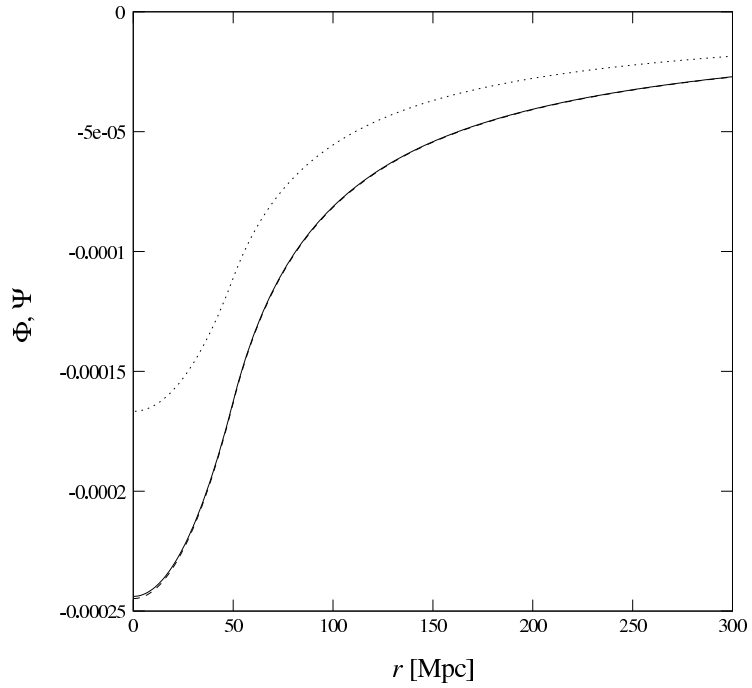

Figure 4.8: Same as Fig. 4.7, but now assuming $K_B = 1$.

a difference can only be caused by anisotropic stress). For this purpose, we switch to physical coordinates and use the two different Poisson equations specified by Eqs. (D.28) and (D.28) to calculate the potentials for a spherical top-hat distribution at redshift $z = 1$ with a radius $R = 50$Mpc and overdensity $\delta_0 = 0.1$, keeping the same parameters as before. The resulting potentials are illustrated in Figs. 4.7 and 4.8 for $K_B = 0.1$ and $K_B = 1$, respectively. A small value of K_B drives the potentials apart, corresponding to relative deviation of around 10% in Fig. 4.7, whereas the two potentials are basically identical for $K_B \gtrsim 1$.

4.3.5 Summary and further applications

Here we have considered the growth of perturbations in the context of TeVeS. The structure of the linearized perturbation equations suggests the introduction of two new functions, B_φ and B_γ, which fully characterize the new degrees of freedom arising from the scalar and vector field, respectively. Assuming these functions to be approximately constant and choosing a cosmological background corresponding to the Einstein-de Sitter model in GR, we have derived the TeVeS analog of the growth equation and discussed its dependence on the theory's parameters. In accordance with the findings of Ref. [87], enhanced growth only occurs for small values of the constant K_B, which also results in a difference between the matter frame potentials Ψ and Φ, the so-called gravitational slip. For larger values of K_B, the solution of the growth equation essentially follows a power law

whose exponent is determined by the assumed values of B_φ and B_γ and may differ from that of the ordinary Einstein-de Sitter model in GR.

If supplemented with numerical estimates for the functions B_φ and B_γ, the framework introduced in the last section appears as a particularly suitable parametrization for detailed studies of the growth factor in TeVeS. Such parameterizations have recently gained interest as a general way of investigating potentially observable signatures of modified gravity [254, 255] and open the possibility to adopt conventional methods and tests which are frequently applied in the context of GR. Taking weak gravitational lensing, for example, it would be interesting to see how the enhanced growth quantitatively affects estimates on different signals such as galaxy number counts and especially the associated noise which is expected to drop in a theory where structure grows faster than in GR. A first application into this direction regarding the detectability of large-scale voids in a TeVeS-like universe is currently in progress. Furthermore, one might consider our results as a first approach toward investigations of the nonlinear clustering of density perturbations in these theories. Although one expects the linearity in the gravitational sector to break down at some point, mainly because of nonlinearities arising from the potential terms which are responsible for the theory's MONDian limit, this approximation should hold long enough to investigate the influence of vector perturbations on cluster scales. For instance, a particular criterion for the validity of such an approach would be the requirement that the perturbed expression for the function μ derived in Ref. [101] is satisfied,

$$\delta\mu = 2\frac{V'}{V''}\tilde{\Psi} + 4\bar{\dot{\phi}}\frac{e^{2\bar{\phi}}}{a^2 V''}\dot{\varphi}. \tag{4.54}$$

The above prospects on new and potentially powerful ways of constraining the theory underline the importance of further research in this field which, regarding a systematic analysis of TeVeS-like models, is still at a very early stage. Future work should also extend investigations to more general tensor-vector theories and explore whether similar approaches are also applicable in these frameworks. Finally, note that even if the presently made assumptions turn out to be a bad description of the growth in TeVeS, our model provides an interesting tool for generically studying effects in modified gravity with enhanced growth.

Chapter 5

Summary

In this thesis, we have tried to address several possibilities on how to constrain hypothetical modifications to the gravitational sector, focusing on the subset of tensor-vector-scalar theory as an alternative to CDM on galactic scales and a particular class of chameleon models which aim at explaining the coincidences in the DE sector.

Beginning with the framework of TeVeS theory, we have developed analytic models for non-spherical lenses which allowed us to test the theory against observations of multiple-image systems. While isolated double-image lenses are generally well explained, the situation for quadruple-image systems and lenses in dense environments such as groups or clusters appears challenging. Nevertheless, we have argued that the found problems are mainly related to our simplistic lens model which does not account for any effects due to environment and may strictly be applied to isolated systems only. Despite being inconclusive, our analysis has pinpointed certain systems which call for a more detailed analysis in the future and could hold the key to make solid statements about theory's performance in the domain of galactic lenses.

As the next step, we have investigated the role of intercluster filaments in TeVeS. The typically very low density of these large-scale objects suggests that departures from GR are expected to be quite significant. Modeling filaments as infinitely long cylinders, we have analyzed their lensing properties and confirmed this expectation. Furthermore, we have shown that a single filament can contribute a shear signal on the order of 0.01 and considering multiple filaments along the line of sight, this can add up, leading to a significant and complex impact on the shear measurements of other objects. In principle, our findings also allow one to falsify TeVeS by excluding a large lensing signal through measurements around the position of a known filament. Given the current

observational uncertainties, however, this seems practically impossible.

We then moved to the missing mass problem in TeVeS and considered the possibility of massive sterile neutrinos with a mass of 11eV. To test this hypothesis, we have outlined how to use cluster lenses with a significant level of substructure to constrain the allowed neutrino density set by the Tremaine-Gunn bound. The key input here is that if one detects a sufficiently dense dark matter concentration within such a lens system, then neutrinos within a given mass range would be immediately ruled out. A preliminary analysis of the lensing cluster Abell 2390, however, appears to be consistent with a mass of 11eV. Nevertheless, we have suggested the search for other cluster lens candidates combined with a more detailed analysis which is likely to give tighter constraints than the analysis presented in this thesis.

Leaving the field of TeVeS for a little bit, we further considered coupled scalar field models and presented a general framework for exploring the nonlinear clustering of density perturbations by means of *N*-body simulations. Choosing a particular realization for a chameleon model where the scalar field only couples to CDM particles, we have performed the first complete simulations in the sense that the spatial variation of the scalar field on small scales has been fully taken into account. For a reasonable range of model parameters, our results predict that the best chance of discriminating such theories from the standard ΛCDM model might come from observations on intermediate scales which are relevant for galaxy clusters ($\sim 10^2 - 10^3$kpc) and there is a good chance that future surveys such as the Kilo-Degree Survey might be able to detect such a signal.

Finally, we have discussed the prospects of applying similar methods or techniques to study the linear and nonlinear evolution of density perturbations in TeVeS. The main obstacle arising for this class of theories is that one cannot start from the nonrelativistic field equations because these do not include contributions of the vector field which are known to be crucial for the formation of structure on large scales. To find a possible way around this problem, we have tried to motivate an ansatz for the perturbations of the scalar field, which allows one to cast the perturbation equations into a more convenient form. Although there are still several open questions regarding our approach, it allowed us obtain the TeVeS analog of the growth equation in the modified Einstein-de Sitter cosmology and appears as a useful framework for general studies of gravity theories with enhanced growth. On a more speculative level, we have further outlined the possibility of investigating the nonlinear regime of structure formation at least to some extent.

Appendix A

Partially degenerate neutrino gas in galaxy clusters

A.1 Nonrelativistic Fermi gas

For a system of identical fermionic particles in thermal equilibrium, the average number of states with energy ϵ_i is given by

$$\langle n_i \rangle = g_i \left(e^{(\epsilon_i - \mu)/\kappa_B T} + 1 \right)^{-1}, \tag{A.1}$$

where κ_B is the Boltzmann constant, μ is the chemical potential and g_i denotes the degeneracy factor. Using that $g_i = g$ and $\epsilon_i = p_i^2/2m$ for nonrelativistic particles, taking the continuum limit gives rise to the distribution function (m is the particle mass)

$$f(\epsilon)d\epsilon = g\frac{\sqrt{2}m^{3/2}}{2\pi^2\hbar^3}\sqrt{\epsilon}\left(e^{(\epsilon-\mu)/\kappa_B T} + 1 \right)^{-1} d\epsilon \tag{A.2}$$

which allows one to determine the corresponding thermodynamic properties of the gas. Considering spherically symmetric configurations and introducing the radial velocity dispersion σ, the corresponding equation of state is given parametrically as

$$\rho = g\frac{\sqrt{2}m^4}{2\pi^2\hbar^3}\sigma^3 F_{1/2}(\chi) \tag{A.3}$$

and

$$P = g\frac{\sqrt{2}m^4}{3\pi^2\hbar^3}\sigma^5 F_{3/2}(\chi), \tag{A.4}$$

where

$$F_p(\chi) = \int_0^\infty x^p \left(e^{x-\chi} + 1\right)^{-1} dx \tag{A.5}$$

and $\chi = \mu/\kappa_B T$ (for a derivation see, e.g., Ref. [256]). In the limit of full degeneracy (corresponding to very large positive values of χ), this yields $P \propto \rho^{5/3}$ while the non-degenerate limit (corresponding to very large negative values of χ) leads to the classical result $P \propto \rho\sigma^2$.

A.2 Massive neutrinos in hydrostatic equilibrium

In an expanding and cooling universe, neutrinos (ordinary or sterile) with a mass on the order of several eV or larger may be considered as nonrelativistic particles at the late stages of cosmological evolution (matter era and further stages). This applies in particular to galaxy clusters where such neutrinos should move with velocities much smaller than the speed of light [81, 190]. As these particles are fermions, we may treat them using the relations presented in the last section. The equation of state given by Eqs. (A.3) and (A.4) formally depends on the chemical potential, but there is no independent way of estimating χ apart from numerical simulations of a collapsing baryon-neutrino fluid. Lacking such simulations in the modified framework, however, we will start from the estimated density ρ_ν to obtain the chemical potential necessary for an equilibrium configuration. In the following, we will outline the procedure applied in Sec. 3.4 to calculate the TG bound.

Assuming that the neutrino gas is in hydrostatic equilibrium, the pressure obeys

$$\frac{d}{dr} P_\nu(r) = -\rho_\nu(r) g(r), \tag{A.6}$$

where $g(r)$ is the total gravitational force at radius r. Combining the above with Eqs. (A.3) and (A.4), we determine χ as a function of radius (one possibility of achieving this is described in e.g. Ref. [190]). This result is used to calculate the corresponding velocity dispersion σ_ν which will generally differ from that of the ICM. Inserting σ_ν into Eq. (3.74), we then find the maximally allowed neutrino density $\rho_{\nu,\mathrm{max}}$. Since σ_ν generally varies with the radius, this obviously yields the TG bound as a function of position. Finally, note that future simulations of galaxy clusters in this context will not only probe the estimated values of χ, but also tell us whether the such obtained differences between the velocity dispersions of neutrinos and ICM are actually realistic.

Appendix B

Modeling the baryonic content of A2390

B.1 X-ray gas and central mass distribution

To derive a reasonable model for the gas distribution in A2390, we use the results given in Ref. [202]. The intrinsic electron density derived from CHANDRA observations (shown in Fig. 10 of Ref. [202]) can be well described by a spherical profile of the following form:

$$n_e(r) = \frac{n_0}{\left(1 + (r/r_0)^2\right)^{1/2}}, \tag{B.1}$$

where $n_0 = 0.1\text{cm}^{-3}$ and $r_0 = 10\text{kpc}$. Assuming a mean molecular weight of $w = 0.6$ and an additional factor of 1.2 to account for the global effect of the cluster's stellar components, we thus obtain an expression for the effective central density profile with a central density of $\rho_0 = 1.8 \times 10^6 M_\odot\ \text{kpc}^{-3}$. Since the volume integral of Eq. (B.1) diverges, we smoothly cut the profile at radius R within a range of 200kpc. The cutoff scale is set to $R = 1\text{Mpc}$ which corresponds to $0.7r_{500}$ [1] as given in Ref. [204]. This yields a total integrated mass of $M \sim 1.3 \times 10^{14} M_\odot$ and a surface density profile which is in good agreement with a $10 - 20\%$ gas fraction of the enclosed projected lensing mass estimated in the framework of GR [206, 208]. The density distribution specified by Eq. (B.1) is illustrated in Fig. 3.18 (dotted line).

Although our choice for the density profile is less accurate and results in a slightly smaller mass than typical β models [202, 213] or more flexible ones [204], it will be sufficient for our analysis. As is shown in Sec. 3.4.4 B, the relevant lensing mass is mostly dominated by the contribution of

[1] Assuming the framework of GR with CDM, the overdensity radius r_{500} is the radius within which the mean matter density is 500 times the critical density of the universe at the cluster's redshift.

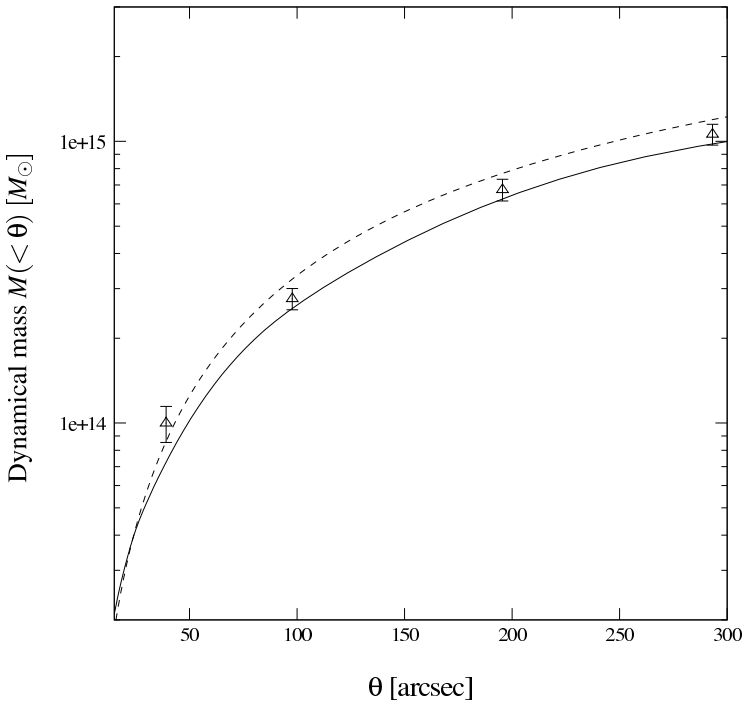

Figure B.1: Enclosed projected (Newtonian) dynamical mass profiles for our TeVeS equilibrium model (gas + SNs; solid line) and an NFW model (dashed line). The lower mass of the TeVeS model is mostly caused by the approximate description of the gas density given in Eq. (B.1); triangles indicate the estimates from weak lensing observations. At the arc's position ($\theta \approx 38''$), the relative difference between the models is about 10%.

SNs. Thus the strong lensing results, which we are primarily interested in here, will be relatively insensitive to the actual assumption of the central baryonic distribution. Adopting the more realistic density models above in a few selected simulation runs, otherwise identical to those presented in Sec. 3.4.5, we find only small differences on the order of a few percent in the corresponding results and confirm our argument. This is also indicated by comparing the enclosed projected dynamical mass profiles of our cluster model (gas + SNs) to the Navarro-Frenk-White (NFW) profile [257] estimated in Ref. [204] (see Fig. B.1). Although the TeVeS model underestimates the mass, the discrepancy from the NFW model is only about 10% at the arc's position ($\theta \approx 38''$). In addition, the figure shows the weak lensing results obtained from the Canada-France-Hawaii Telescope (CFHT) for a photometric redshift distribution based on the CFHT Legacy Survey data [208, 258]. The relative good agreement between dynamical and weak lensing mass estimates further implies that structure along the line of sight plays no significant role and does not affect our analysis. All presented quantities have been corrected for the cosmological model specified in Eq. 3.67. Note, however, that a rather accurate description of the gas density as well as its temperature profile is important to estimate the neutrino content necessary for hydrostatic equilibrium in TeVeS [190].

B.2 Galaxy morphology and masses

Since a rather detailed model of the cluster might be important in TeVeS, we also need to take the contribution of individual galaxies into account. For simplicity, we only consider the most massive member galaxies in the immediate vicinity of the straight arc's observed position; galaxies which are located farther away are unlikely to affect the TeVeS lensing maps in this region, which is confirmed by our results presented in Sec. 3.4.5. Although A2390 exhibits a rich class of galaxy morphologies, with many galaxies showing elliptical or lenticular shapes, the impact of individual morphologies on the arc's environment can safely be neglected due to the galaxies' sufficiently large distances. While this is not necessarily true for the galaxy 2592 (see Fig. 3.17) which resides directly adjacent to the arc, a spherical density model provides a good description, which is indicated by the rather mild ellipticity seen in the optical HST image. As can be seen in Sec. 3.4.5, this approximation does not affect the basic results of our analysis - at least in the case of quasiequilibrium configurations.

Furthermore, we assume that all considered galaxies can be modeled by a matter distribution of the form

$$\rho(r) = \frac{M r_H}{2\pi(r+\epsilon)(r+r_H)^3}, \tag{B.2}$$

where $\rho(0) = M/(2\pi\epsilon r_H^2)$ is the central matter density, and the profile's core radius is universally set to $r_H = 3\text{kpc}$. The length scale ϵ corresponds to a smoothing parameter becoming necessary due to the limited resolution of our simulations and is specified in App. C.2. For $\epsilon = 0$, Eq. (B.2) reduces to the well-known Hernquist profile [139] which closely approximates the de Vaucouleurs $R^{1/4}$ law for elliptical galaxies.

To infer the masses of individual galaxies, needed for our strong lensing analysis, we consider the data of the spectro-photometric catalog compiled in Ref. [219], which lists magnitudes for 48 galaxies inside the cluster A2390. All magnitudes are given in the Gunn r band [259], and a simple formula [260] to convert the R Johnson magnitude and the $B-V$ color index to the Gunn r band can be found in the literature [2]. Accordingly, we have computed $r_\odot$, the Gunn r magnitude of the sun, adopting $R_\odot = 4.42$ [261] and $(B-V)_\odot = 0.64$ [262]. We have found $r_\odot = 4.95$ which is rather close to the r value inferred from SDSS, the corresponding band being quite similar to the Gunn r band. Our result for $r_\odot$ has then been used to evaluate the absolute luminosities of the

[2]For further reference, an excellent description of the Gunn magnitude system is given on the website `http://ulisse.pd.astro.it/Astro/ADPS/`.

galaxies given in Ref. [219].

Next, we need a realistic mass-to-light ratio (M/L) in order to determine the galaxy masses. To this end, we have followed a twofold approach: First, we have adopted a constant M/L derived by combining the relation between M/L and the $g-r$ color index presented in Ref. [263] with the $g-r$ colors for massive ellipticals in the red sequence of the SDSS given in Ref. [264]. The corresponding masses are labeled as M_1. Second, we have also considered M/L as a function of M in agreement with the results for the galaxies of A2390 discussed in Ref. [219]. For this, a dynamical mass estimate based on measured velocity dispersions was used. As elliptical galaxies are mostly subject to the strong gravity regime within their half-light radius, however, estimates in both MOND/TeVeS and Newtonian dynamics should be roughly the same. This second mass estimate, denoted as M_2, is probably more reliable since it involves fewer assumptions. The properties of the such obtained galaxy models are listed in Table 3.4.

B.3 Role of the central cD galaxy

Assuming an equilibrium model for A2390, it has been found that 11eV SNs reach their densest possible configuration for $r \lesssim 20$kpc (see Sec. 3.4.4 B). Since Eq. (3.78) takes the TG bound into account, our cluster model misses some mass in the central part and does not correspond to a genuine equilibrium situation. A way of compensating for this is to consider an additional contribution due to the central cD galaxy. Following the lines of Ref. [190], one can estimate a total galaxy mass of approximately $M = 1.8 \times 10^{12} M_\odot$. As the central region of A2390 is neither spherically symmetric nor in equilibrium [202, 204], it is important to note that such an approach has no real physical meaning, but rather offers a convenient way to tweak our cluster model.

What does the above mean for our lensing analysis? Modeling the cD galaxy as a point mass, a straightforward calculation shows that its impact on the TeVeS lensing maps can be safely neglected. At the position of the straight arc (38″ or 140kpc from the cluster center), the additional matter gives rise to changes of $1-2\%$. Moving to smaller radii, the deviation grows, but we are not interested in this region anyway. Thus we consider the cluster model presented in Sec. 3.4.4 as sufficient for our investigation.

Appendix C

Numerical tools and setup for A2390

C.1 Solving the scalar field equation

Having set the framework of gravitational lensing and cosmology in Sec. 3.1, we may proceed with calculating the desired TeVeS lensing maps. The main problem associated with this task is to solve the scalar field equation specified in Eq. (2.55) which can be rewritten as

$$\Delta\phi = \bar{\rho}, \tag{C.1}$$

where the effective density $\bar{\rho}(\rho, \partial_i\phi, \partial_i\partial_j\phi)$ is

$$\bar{\rho} = \frac{k_B G}{\mu_B}\rho - 2\frac{k_B l_B^2}{\mu_B}\frac{\partial\mu_B}{\partial y}\left((\partial_i\phi)(\partial_j\phi)(\partial_i\partial_j\phi)\right), \tag{C.2}$$

and indices run from 1 to 3. Equation (C.1) corresponds to a nonlinear second order elliptic boundary value problem and can be tackled numerically. A Fourier-based solver operating on an equidistant grid has been presented in Ref. [50] where the basic algorithm and involved approximations are extensively discussed. The main idea is to employ an iterative relaxation scheme of the form ($\bar{\rho}^{(0)}$ is calculated from an appropriate initial guess $\phi^{(0)}$)

$$\Delta\tilde{\phi}^{(n)} = \bar{\rho}^{(n)}, \quad \phi^{(n+1)} = \omega\tilde{\phi}^{(n)} + (1-\omega)\phi^{(n)}, \tag{C.3}$$

where we have introduced the relaxation parameter $\omega \in \mathbb{R}$, an additional iteration field $\tilde{\phi}^{(n)}$ and

$$\begin{aligned} \bar{\rho}^{(n)} &= \frac{k_B G}{\mu_B^{(n)}}\rho - 2\left(\frac{\partial \mu_B}{\partial y}\right)^{(n)} \frac{k_B l_B^2}{\mu_B^{(n)}} \left(\left(\partial_i \phi^{(n)}\right)\left(\partial_j \phi^{(n)}\right)\left(\partial_i \partial_j \phi^{(n)}\right)\right), \\ \mu_B^{(n)} &= \mu_B\left(y^{(n)}\right), \quad \left(\frac{\partial \mu_B}{\partial y}\right)^{(n)} = \frac{\partial \mu_B}{\partial y}\left(y^{(n)}\right), \quad y^{(n)} = k_B l_B^2 |\boldsymbol{\nabla}\phi^{(n)}|. \end{aligned} \tag{C.4}$$

As the scalar field's gradient decreases much more slowly compared to the Newtonian gradient far away from the lens, one would actually be obliged to move to very large volumes to neglect contributions from outside the box and obtain correct results for the deflection angle. Assuming a fixed grid size, this would excessively degrade the resolution of the corresponding two-dimensional lensing maps. Fortunately, there is a way of avoiding this problem: Considering a finite grid with $N + 1$ points per dimension (N is chosen as an even number), we may rewrite the scalar part of the deflection angle as the sum of contributions coming from both inside and outside the grid's volume:

$$\hat{\boldsymbol{\alpha}}_s = 2 \int_{-\frac{N}{2}\Delta x}^{\frac{N}{2}\Delta x} \boldsymbol{\nabla}_\perp \phi^{(\mathrm{in})} dz + 2 \int_{-\infty}^{-\frac{N}{2}\Delta x} \boldsymbol{\nabla}_\perp \phi^{(\mathrm{out})} dz + 2 \int_{\frac{N}{2}\Delta x}^{\infty} \boldsymbol{\nabla}_\perp \phi^{(\mathrm{out})} dz, \tag{C.5}$$

where the quantity Δx denotes the distance between neighboring grid points. Assuming that the scalar field at the boundaries is approximately given by that of a point lens, i.e.

$$\phi^{(\mathrm{out})} \approx \sqrt{GMa_0}\log(r), \tag{C.6}$$

we obtain the following expression (M denotes the total mass inside the volume):

$$\hat{\boldsymbol{\alpha}}_s = 2 \int_{-\frac{N}{2}\Delta x}^{\frac{N}{2}\Delta x} \boldsymbol{\nabla}_\perp \phi^{(\mathrm{in})} dz + 4\mathbf{A}, \tag{C.7}$$

where

$$\mathbf{A} = \frac{\sqrt{GMa_0}}{q}\left[\frac{\pi}{2} - \arctan\left(\frac{N\Delta x}{2q}\right)\right]\begin{pmatrix} x \\ y \end{pmatrix} \tag{C.8}$$

and $q^2 = x^2 + y^2$. Thus, if the point lens approximation is applicable, we need to perform the integration only over our finite grid since all contributions from outside the box can be expressed analytically.

One of the numerical challenges of our analysis of A2390 is that we need to resolve galac-

tic scales in a cluster-wide box, which requires a relatively large number of grid points. Since all calculations have to be performed in three dimensions, this clearly exceeds the capacity of a single-processor machine, in terms of both needed time and memory, and therefore calls for a more powerful computer architecture. For this reason, we have implemented a parallel version of the original solver using the Message Passing Interface (MPI) standard. The parallelization as well as all calculations presented in Sec. 3.4 have been carried out on the HUYGENS supercomputer at SARA in Amsterdam within the HPC-EUROPA Transnational Access Programme. The HUYGENS system consists of 104 nodes, with 16 dual core processors (IBM Power6, 4.7 GHz) as well as either 128 GBytes or 256 GBytes of memory per node, thus providing an excellent environment for our needs.

The parallel solver has been tested with analytic TeVeS models such as the Hernquist lens (see, e.g., Ref. [50, 92]), and has also been compared to previous calculations for the "bullet cluster" [50], yielding exactly the same results - up to machine accuracy - as the serial version for identical input parameters. Considering the numerical setup for A2390, we choose a physical box size of $V = d^3 = (4\text{Mpc})^3$ in order to meet the requirements of the point lens approximation at the grid's boundaries. Performing a variety of test runs, we have found that the solver's convergence property quickly deteriorates if we increase the number of grid points per dimension N, meaning that the code takes many iteration steps or even fails to converge [1]. Typically, this problem already occurs at $N = 512$ and manifests itself through extreme fine-tuning of the constant relaxation parameter ω. Depending on the particularly used density model of the cluster, acceptable values for ω vary within a range of $0.7 - 0.9$, but allow them to be easily identified just after a few iterations. Compared to the analysis of Ref. [50], we thus obtain no universal value for the relaxation parameter. Similarly, we also note that the solver's behavior becomes more sensitive with respect to the scalar's initial guess. This is expected because the effective deviation from the desired solution increases with N and can usually be accounted for by slightly modifying the original point mass ansatz of Ref. [50] to achieve a finite core,

$$\phi^{(0)}(r) \propto \log(r + r_c), \tag{C.9}$$

where r_c is on the order of a few d/N. While more elaborated guesses are also possible, they typically do not yield a much better performance.

[1] It is quite likely that the problem is partly related to the destabilizing influence of high frequency modes. These modes are able to "see" and amplify numerical artifacts which are present both in regions around local extrema, where the derivative of scalar potential exhibits values close to zero, and at the grid's boundaries.

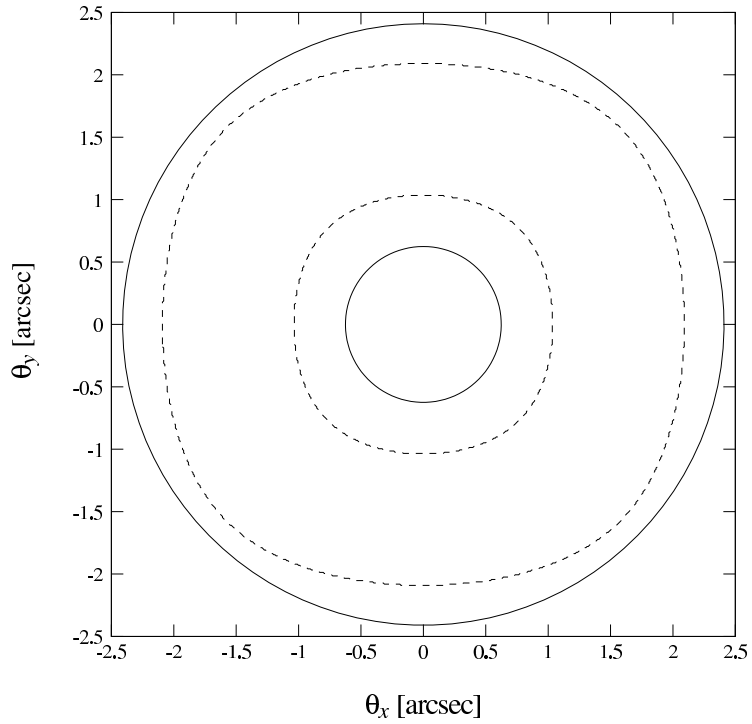

Figure C.1: Predicted critical curves for an isolated galaxy given by Eq. (B.2): Assuming an aperture mass of $3.5\times10^{11}M_{\odot}$ within a $3''$ ($\sim$ 11kpc) diameter as well as a lens and source redshift of $z_l = 0.23$ and $z_s = 1$, respectively, we present results for both a high resolution ($\sim 0.05''$, solid line) and a low resolution setting ($\sim 1.2''$, dashed line) with subsequent interpolation.

C.2 Numerical setup for A2390

In all simulation runs, we set the number of grid points per dimension to $N = 896$. This yields a resolution of approximately $1.2''$ ($\sim$ 4.5kpc) for our choice of $d = 4$Mpc. To improve the numerical stability of our Fourier solver, we further require all density components to be centered within their respective subcube, which can lead to a maximal deviation of $0.6''$ from the positions listed in Table 3.4. In addition, we assume a smoothing parameter $\epsilon = 1$kpc for the galaxy profile given by Eq. (B.2). Once the desired fields and derivatives are calculated, we use a cubic spline to interpolate our results and determine the relevant lensing quantities. For the given specifications, individual simulation runs typically require $30 - 50$ iteration steps to converge, and can last up to 24 hours using 32 processors.

The interpolation approach is justified because the exact result is expected to be relatively smooth. To support this argument, we performed a small numerical experiment: Assuming an aperture mass of $3.5 \times 10^{11} M_{\odot}$ within a $3''$ ($\sim$ 11kpc) diameter and the parameters from above, we compared the predicted critical curves of an isolated galaxy given by Eq. (B.2) for low res-

olution ($\sim 1.2''$) with subsequent interpolation to those calculated for a higher resolution setting ($\sim 0.05''$). Choosing a lens and source redshift of $z_l = 0.23$ and $z_s = 1$, respectively, the results are shown in Fig. C.1. While the radial critical curve is not very well recovered, the radius of the tangential critical curve, which is relevant for our considerations on the straight arc [2], is only underestimated by roughly 10% on average. Considering the full cluster model of A2390, however, galaxies are not isolated, but reside within the cluster's background field, which leads to a boost of their corresponding Einstein radii. Therefore, we expect the accuracy of the calculated lensing properties, including critical curves and caustics, to be significantly improved and sufficient for our analysis in this case.

[2] Although radial caustics can produce straight images, the resulting orientation (pointing towards the center of the corresponding lens) is not compatible with the observed arc.

Appendix D

Perturbation equations in TeVeS

D.1 Scalar field evolution during tracking

In the following, we will assume the potential defined in Eq. (4.16) and use the notation and definitions of Ref. [96]. There it has been found that the scalar field evolves during tracking as

$$\bar{\phi} = \bar{\phi}_0 + \phi_1 \log a, \tag{D.1}$$

where

$$\phi_1 \equiv \frac{d\bar{\phi}}{d \log a} \tag{D.2}$$

is approximately constant. Indeed, following the derivation presented in Ref. [96], one can show that

$$\frac{\phi_1}{1+\phi_1} = \frac{\beta}{2\mu_0} \sqrt{\left(\frac{1+3w}{1-w}\right)^2}, \tag{D.3}$$

where $\beta = \pm 1$ denotes the sign of the scalar field's time derivative, i.e.

$$\beta \equiv \operatorname{sgn} \dot{\bar{\phi}}. \tag{D.4}$$

To see that the sign in Eq. (D.3) is chosen appropriately, one uses Eq. (D.1) and finds that

$$\beta = \operatorname{sgn}\left(\phi_1 \frac{\dot{a}}{a}\right) = \operatorname{sgn} \phi_1 = \operatorname{sgn} \beta, \tag{D.5}$$

where we have assumed that $|\phi_1| \ll 1$ for the last equality. Note that this is justified because of the requirement $\mu_0 \gg 1$ for viable cosmological models.

Here the right-hand side of Eq. (D.3) deserves special attention: Naively evaluating the square root, one obtains the result of Ref. [96]. As the argument's sign does depend on the actual choice of w, however, one has

$$\sqrt{\left(\frac{1+3w}{1-w}\right)^2} = \frac{|1+3w|}{|1-w|}, \tag{D.6}$$

which eventually gives the result in Eq. (4.27). During tracking, the field $\bar{\mu}$ (see Sec. 4.3.2 B) evolves as $\bar{\mu} = 2\mu_0(1+\epsilon)$, where

$$\log\epsilon \propto -\frac{2\phi_1 + 3(1+w)}{n}\log a, \tag{D.7}$$

and thus $2\phi_1 + 3(1+w) > 0$ emerges as a condition for stable tracking. For a universe dominated by a cosmological constant Λ, one has $w = -1$ and therefore $\beta = 1$. Since the time derivative of $\bar{\phi}$ changes its sign when passing from the matter to the Λ era (resulting in $\bar{\rho}_\phi$ momentarily going to zero) [86], it follows that $\beta = -1$ during matter domination. This result is in accordance with previous work [43, 87] where it has been shown that $\bar{\phi}$ decreases with time during the matter era.

D.2 Perturbation equations in conformal Newtonian gauge

The fully covariant form of the linear perturbation equations in TeVeS has been derived in Ref. [101]. Here we will summarize the resulting perturbation equations for scalar modes in conformal Newtonian gauge. Furthermore, we shall assume a spatially flat spacetime geometry and introduce the fluid's sound speed C_s which is defined as the ratio between the fluid's pressure perturbation δP and the corresponding density perturbation $\delta\rho$, i.e. $C_s^2 = \delta P/\delta\rho$. As usual, we express the equations in Fourier space using the comoving wave vector $\mathbf{k}$ in accordance with the coordinate system specified in Sec. 4.3.

Einstein frame perturbations Instead of using Eq. (4.34), one may also express perturbations in the Einstein frame [86, 101]. In this case, the perturbed Einstein frame metric $\tilde{g}_{\mu\nu}$ may be written as

$$\tilde{g}_{00} = -b^2 e^{-4\bar{\phi}}\left(1 + 2\tilde{\Psi}\right), \tag{D.8}$$

$$\tilde{g}_{0i} = -b^2\partial_i\tilde{\zeta}, \tag{D.9}$$

$$\tilde{g}_{ij} = b^2\left(1 - 2\tilde{\Phi}\right)\delta_{ij}. \tag{D.10}$$

In terms of matter frame variables, the Einstein frame perturbations are given by the following relations:

$$\tilde{\Psi} = \Psi - \varphi, \tag{D.11}$$

$$\tilde{\Phi} = \Phi - \varphi, \tag{D.12}$$

$$\tilde{\zeta} = \left(e^{-4\bar{\phi}} - 1\right)\alpha. \tag{D.13}$$

To avoid lengthy expressions in the perturbed field equations, it is convenient to make use of variables from both frames.

Matter fluid equations The density contrast for scalar modes in conformal Newtonian gauge evolves as

$$\dot{\delta} = -(1+w)\left(k^2\theta + 3\dot{\Phi}\right) - 3\frac{\dot{a}}{a}\left(C_s^2 - w\right)\delta, \tag{D.14}$$

where the velocity potential θ obeys

$$\dot{\theta} = -\frac{\dot{a}}{a}(1-3w)\theta + \frac{C_s^2}{1+w}\delta - \frac{\dot{w}}{1+w}\theta - k^2\frac{2}{3}\Sigma + \Psi, \tag{D.15}$$

the quantity Σ denotes the shear of the matter fluid and $k = |\mathbf{k}|$. Note that the equations for perturbations of the matter fluid remain unaltered compared to the standard case of GR.

Scalar field equation The perturbed scalar field equation yields

$$\begin{aligned}\dot{\gamma} =& \frac{\bar{\mu}}{a}e^{-3\bar{\phi}}k^2\left(\varphi + \overleftarrow{\phi}\alpha\right) - 2\frac{\bar{\mu}}{a}e^{\bar{\phi}}\overleftarrow{\phi}\left(3\dot{\tilde{\Phi}} + k^2\tilde{\zeta}\right) \\ & - 3\frac{\dot{b}}{b}\gamma + 8\pi G a e^{-3\bar{\phi}}\bar{\rho}\left[\left(1+3C_s^2\right)\delta + (1+3w)\left(\tilde{\Psi} - 2\varphi\right)\right]\end{aligned} \tag{D.16}$$

and

$$\dot{\varphi} = -\frac{1}{2U}ae^{-\bar{\phi}}\gamma + \overleftarrow{\phi}\tilde{\Psi}. \tag{D.17}$$

Here γ denotes the perturbation of an auxiliary field introduced to split the scalar field equation into two first-order equations [101].

Vector field equation The two first-order equations coming from the perturbed vector equation are

$$K_B\left(\dot{E} + \frac{\dot{b}}{b}E\right) = 8\pi G a^2\bar{\rho}(1+w)\left(1 - e^{-4\bar{\phi}}\right)(\theta - \alpha) - \bar{\mu}\overleftarrow{\phi}\left(\varphi - \overleftarrow{\phi}\alpha\right) \tag{D.18}$$

and

$$\dot{\alpha} = E + \tilde{\Psi} + \left(\overleftarrow{\phi} - \frac{\dot{a}}{a}\right)\alpha, \tag{D.19}$$

where the auxiliary scalar mode E is gauge-invariant and related to $F_{\mu\nu}$, the field strength tensor of A_μ which appears in Eq. (2.43) [101].

Generalized Einstein equations From the scalar modes of the perturbed generalized Einstein equations, one obtains the Hamiltonian constraint

$$-2k^2\tilde{\Phi} - 2e^{4\bar{\phi}}\frac{\dot{b}}{b}\left(3\dot{\tilde{\Phi}} + k^2\tilde{\zeta} + 3\frac{\dot{b}}{b}\tilde{\Psi}\right) + ae^{3\bar{\phi}}\overleftarrow{\phi}\gamma - K_B k^2 E = 8\pi G a^2\bar{\rho}(\delta - 2\varphi) \tag{D.20}$$

and the momentum constraint equation

$$\dot{\tilde{\Phi}} + \frac{\dot{b}}{b}\tilde{\Psi} - \bar{\mu}\overleftarrow{\phi}\varphi = 4\pi G a^2 e^{-4\bar{\phi}}\bar{\rho}(1+w)\theta. \tag{D.21}$$

Finally, the two propagation equations read

$$\begin{aligned} &6\ddot{\tilde{\Phi}} + 2k^2\left(\dot{\tilde{\zeta}} - e^{-4\bar{\phi}}\tilde{\Psi}\right) + 2e^{-4\bar{\phi}}k^2\tilde{\Phi} + 2\frac{\dot{b}}{b}\left(6\dot{\tilde{\Phi}} + 3\dot{\tilde{\Psi}} + 2k^2\tilde{\zeta}\right) + 4\overleftarrow{\phi}\left(3\dot{\tilde{\Phi}} + k^2\tilde{\zeta}\right) \\ &+3\frac{\bar{\mu}}{U}ae^{-\bar{\phi}}\overleftarrow{\phi}\gamma - 6\left(-2\frac{\ddot{b}}{b} + \frac{\dot{b}^2}{b^2} - 4\overleftarrow{\phi}\frac{\dot{b}}{b}\right)\tilde{\Psi} = 24\pi G a^2 e^{-4\bar{\phi}}\bar{\rho}\left(C_s^2\delta - 2w\varphi\right) \end{aligned} \tag{D.22}$$

and

$$\tilde{\Phi} - \tilde{\Psi} + e^{4\bar{\phi}}\left[\dot{\tilde{\zeta}} + 2\left(\frac{\dot{b}}{b} + \overleftarrow{\phi}\right)\tilde{\zeta}\right] = 8\pi G a^2\bar{\rho}(1+w)\Sigma. \tag{D.23}$$

D.3 Approximation for subhorizon scales

In what follows, we will assume the modified Einstein-de Sitter cosmology introduced in Sec. (4.3.2 C). The first step is to express the metric potentials in terms of matter fluid variables only, using Eqs. (4.42) and (4.48) together with the perturbation equations. Starting from Eq. (4.48), we take its time derivative and after a bit of algebra, we finally arrive at (B_φ = const)

$$\begin{aligned} &\frac{e^{-4\bar{\phi}}}{2}\left(3k^2\tilde{\Psi} - 2k^2\tilde{\Phi} + k^2 B_\varphi\overleftarrow{\phi}\alpha + \frac{4B_\varphi}{\mu_0}\pi G a^2\bar{\rho}\delta\right) \\ &+\left[9\left(\frac{2\mu_0}{B_\varphi}\overleftarrow{\phi} - \frac{\dot{b}}{b}\right)^2 + (1-6\mu_0)\,\overleftarrow{\phi}^2 + \frac{2B_\varphi}{\mu_0}\pi G a^2 e^{-4\bar{\phi}}\bar{\rho}\right]\tilde{\Psi} \\ &+\left[3\left(\frac{2\mu_0}{B_\varphi}\overleftarrow{\phi} - \frac{\dot{b}}{b}\right) - B_\varphi\overleftarrow{\phi}\right]\left(k^2\tilde{\zeta} + 12\pi G a^2 e^{-4\bar{\phi}}\bar{\rho}\theta\right) = O(\epsilon). \end{aligned} \tag{D.24}$$

As can be seen from above, Eq. (D.24) relates the three (gravitational) fields Ψ, Φ and α, where α is related to $\tilde{\zeta}$ through Eq. (D.13), to the matter perturbation variables δ and θ. For the next equation, we eliminate the time derivative of $\tilde{\zeta}$ between Eqs. (D.19) and (D.23), which leads to

$$\tilde{\Phi} + \left(1 - e^{4\bar{\phi}}\right) E - e^{4\bar{\phi}}\tilde{\Psi} - 4\dot{\bar{\phi}}\alpha + e^{4\bar{\phi}}\left(\frac{\dot{a}}{a} + 5\dot{\bar{\phi}}\right)\tilde{\zeta} = 0. \tag{D.25}$$

Differentiating the above and eliminating all remaining time derivatives by suitable combination of the perturbation equations, one finds

$$\begin{aligned}
&- e^{4\bar{\phi}} k^2 \tilde{\zeta} + \left[2\mu_0 \frac{1 - e^{4\bar{\phi}}}{K_B} \dot{\bar{\phi}}^2 - 16 \frac{1 + e^{4\bar{\phi}}}{1 - e^{4\bar{\phi}}} \dot{\bar{\phi}}^2 - 8\dot{\bar{\phi}}^2 \right. \\
&\left. - 4\ddot{\bar{\phi}} + \left(1 - e^{4\bar{\phi}}\right)\left(\frac{\ddot{a}}{a} - 2\frac{\dot{a}^2}{a^2} - 4\dot{\bar{\phi}}\frac{\dot{a}}{a} + 5\ddot{\bar{\phi}} + 5\dot{\bar{\phi}}^2 \right) \right] \alpha \\
&+ \left[4e^{4\bar{\phi}} \frac{1 + e^{4\bar{\phi}}}{1 - e^{4\bar{\phi}}} \dot{\bar{\phi}} \left(\frac{\dot{a}}{a} + 5\dot{\bar{\phi}} \right) + \frac{1 - e^{4\bar{\phi}}}{K_B} 8\pi G a^2 \bar{\rho} \right] \tilde{\zeta} \\
&+ \left[\left(1 - \frac{1 - e^{4\bar{\phi}}}{K_B} \right) \frac{2\mu_0}{B_\varphi} \dot{\bar{\phi}} - e^{4\bar{\phi}} \left(4 \frac{1 + e^{4\bar{\phi}}}{1 - e^{4\bar{\phi}}} \dot{\bar{\phi}} + \frac{\dot{a}}{a} + 5\dot{\bar{\phi}} \right) \right. \\
&\left. - e^{4\bar{\phi}} \left(B_\varphi \dot{\bar{\phi}} + \frac{6\mu_0}{B_\varphi} \dot{\bar{\phi}} - 3\frac{\dot{b}}{b} \right) \right] \tilde{\Psi} + 4\dot{\bar{\phi}} \left(\frac{1 + e^{4\bar{\phi}}}{1 - e^{4\bar{\phi}}} - 1 \right) \tilde{\Phi} \\
&+ \left[1 - 3e^{4\bar{\phi}} - 2\frac{\left(1 - e^{4\bar{\phi}}\right)^2}{K_B} \right] 4\pi G a^2 e^{-4\bar{\phi}} \bar{\rho} \theta = O(\epsilon).
\end{aligned} \tag{D.26}$$

Finally, the last equation is obtained from eliminating E between Eqs. (D.25) and (D.20). Together with the relations presented in Sec. 4.3.3 B, one eventually ends up with

$$\begin{aligned}
&- k^2 \left(2 - \frac{K_B}{1 - e^{4\bar{\phi}}} \right) \tilde{\Phi} - k^2 \frac{K_B e^{4\bar{\phi}}}{1 - e^{4\bar{\phi}}} \tilde{\Psi} - k^2 \frac{4K_B}{1 - e^{4\bar{\phi}}} \dot{\bar{\phi}} \alpha \\
&- e^{4\bar{\phi}} \left[2\left(\frac{\dot{b}}{b} + \frac{2\mu_0}{B_\varphi} \dot{\bar{\phi}} \right) - \frac{K_B}{1 - e^{4\bar{\phi}}} \left(\frac{\dot{a}}{a} + 5\dot{\bar{\phi}} \right) \right] k^2 \tilde{\zeta} \\
&+ \frac{4e^{4\bar{\phi}}}{B_\varphi} \left(4\pi G a^2 e^{-4\bar{\phi}} \bar{\rho} - \frac{6\mu_0^2}{B_\varphi} \dot{\bar{\phi}}^2 \right) \tilde{\Psi} - \left(\frac{\dot{b}}{b} + \frac{2\mu_0}{B_\varphi} \dot{\bar{\phi}} \right) \\
&\times 24\pi G a^2 \bar{\rho} \theta - 8\pi G a^2 \bar{\rho} \delta = O(\epsilon).
\end{aligned} \tag{D.27}$$

Since Eqs. (D.24), (D.26) and (D.27) form a closed system for the fields Ψ, Φ and α, the corresponding solution of this system will give the fields as expressions of the matter fluid variables only. Inserting the logarithmic approximation for the evolution of $\bar{\phi}$ specified in Eq. (4.31) and using that for subhorizon scales $aH/k \ll 1$, we expand the corresponding equations for the matter

frame potentials Ψ and Φ in powers of aH/k and find to lowest order:

$$\tilde{\Psi} = -\tilde{A}\frac{a^2H^2}{k^2}\delta, \tag{D.28}$$

$$\tilde{\Phi} = -\tilde{B}\frac{a^2H^2}{k^2}\delta, \tag{D.29}$$

where

$$\tilde{A} = \frac{6\mu_0 - 1}{(2\mu_0+1)^2}\frac{\left(4\mu_0 + 2B_\varphi\right)\left(2e^{4\bar{\phi}} - e^{8\bar{\phi}} - 1\right) + K_B B_\varphi\left(1 - e^{4\bar{\phi}}\right)}{6\left(2 - e^{4\bar{\phi}} - e^{-4\bar{\phi}}\right) + K_B\left(2e^{4\bar{\phi}} + 3e^{-4\bar{\phi}} - 5\right)} + O(\epsilon) \tag{D.30}$$

and

$$\tilde{B} = \frac{6\mu_0 - 1}{(2\mu_0+1)^2}\frac{6\mu_0\left(2e^{4\bar{\phi}} - e^{8\bar{\phi}} - 1\right) + K_B B_\varphi\left(e^{4\bar{\phi}} - e^{8\bar{\phi}}\right)}{6\left(2 - e^{4\bar{\phi}} - e^{-4\bar{\phi}}\right) + K_B\left(2e^{4\bar{\phi}} + 3e^{-4\bar{\phi}} - 5\right)} + O(\epsilon). \tag{D.31}$$

Note that although we have not presented the resulting expressions to first order in ϵ for clarity, their contribution is fully taken into account for all calculations conducted in Sec. 4.3.4.

Bibliography

[1] S. Weinberg, *The First Three Minutes: A Modern View of the Origin of the Universe*, edited by Weinberg, S. (New York: Basic Books, Updated ed., 1993)

[2] F. Zwicky, ApJ, **86**, 217 (1937)

[3] V. C. Rubin and W. K. Ford, Jr., ApJ, **159**, 379 (1970)

[4] V. C. Rubin, W. K. J. Ford, and N. . Thonnard, ApJ, **238**, 471 (1980)

[5] A. Bosma, in *Dark Matter in Galaxies*, IAU Symposium, Vol. 220, edited by S. Ryder, D. Pisano, M. Walker, & K. Freeman (2004) pp. 39–+, arXiv:astro-ph/0312154

[6] A. Diaferio, S. Schindler, and K. Dolag, Space Sci. Rev., **134**, 7 (2008), arXiv:0801.0968

[7] R. Massey, T. Kitching, and J. Richard, Reports on Progress in Physics, **73**, 086901 (2010), arXiv:1001.1739 [astro-ph.CO]

[8] G. R. Blumenthal, S. M. Faber, J. R. Primack, and M. J. Rees, Nature, **311**, 517 (1984)

[9] S. Perlmutter, G. Aldering, G. Goldhaber, R. A. Knop, P. Nugent, P. G. Castro, S. Deustua, S. Fabbro, A. Goobar, D. E. Groom, I. M. Hook, A. G. Kim, M. Y. Kim, J. C. Lee, N. J. Nunes, and The Supernova Cosmology Project, ApJ, **517**, 565 (1999), arXiv:astro-ph/9812133

[10] D. J. Eisenstein, I. Zehavi, D. W. Hogg, R. Scoccimarro, M. R. Blanton, R. C. Nichol, R. Scranton, H. Seo, M. Tegmark, Z. Zheng, S. F. Anderson, J. Annis, N. Bahcall, J. Brinkmann, S. Burles, *et al.*, ApJ, **633**, 560 (2005), arXiv:astro-ph/0501171

[11] A. D. Chernin, I. D. Karachentsev, O. G. Kashibadze, D. I. Makarov, P. Teerikorpi, M. J. Valtonen, V. P. Dolgachev, and L. M. Domozhilova, Astrophysics, **50**, 405 (2007), arXiv:0706.4171

[12] T. Schrabback, J. Hartlap, B. Joachimi, M. Kilbinger, P. Simon, K. Benabed, M. Bradač, T. Eifler, T. Erben, C. D. Fassnacht, F. W. High, S. Hilbert, H. Hildebrandt, H. Hoekstra, K. Kuijken, P. J. Marshall, Y. Mellier, E. Morganson, P. Schneider, E. Semboloni, L. van Waerbeke, and M. Velander, A&A, **516**, A63+ (2010), arXiv:0911.0053 [astro-ph.CO]

[13] B. R. Granett, M. C. Neyrinck, and I. Szapudi, ApJ, **683**, L99 (2008), arXiv:0805.3695

[14] P. Astier, J. Guy, N. Regnault, R. Pain, E. Aubourg, D. Balam, S. Basa, R. G. Carlberg, S. Fabbro, D. Fouchez, I. M. Hook, D. A. Howell, H. Lafoux, J. D. Neill, N. Palanque-Delabrouille, *et al.*, A&A, **447**, 31 (2006), arXiv:astro-ph/0510447

[15] M. Tegmark, M. R. Blanton, M. A. Strauss, F. Hoyle, D. Schlegel, R. Scoccimarro, M. S. Vogeley, D. H. Weinberg, I. Zehavi, A. Berlind, T. Budavari, A. Connolly, D. J. Eisenstein, D. Finkbeiner, J. A. Frieman, *et al.*, ApJ, **606**, 702 (2004), arXiv:astro-ph/0310725

[16] S. Cole, W. J. Percival, J. A. Peacock, P. Norberg, C. M. Baugh, C. S. Frenk, I. Baldry, J. Bland-Hawthorn, T. Bridges, R. Cannon, M. Colless, C. Collins, W. Couch, N. J. G. Cross, G. Dalton, *et al.*, MNRAS, **362**, 505 (2005), arXiv:astro-ph/0501174

[17] J. Benjamin, C. Heymans, E. Semboloni, L. van Waerbeke, H. Hoekstra, T. Erben, M. D. Gladders, M. Hetterscheidt, Y. Mellier, and H. K. C. Yee, MNRAS, **381**, 702 (2007), arXiv:astro-ph/0703570

[18] D. N. Spergel, R. Bean, O. Doré, M. R. Nolta, C. L. Bennett, J. Dunkley, G. Hinshaw, N. Jarosik, E. Komatsu, L. Page, H. V. Peiris, L. Verde, M. Halpern, R. S. Hill, A. Kogut, *et al.*, ApJS, **170**, 377 (2007), arXiv:astro-ph/0603449

[19] G. Hinshaw, J. L. Weiland, R. S. Hill, N. Odegard, D. Larson, C. L. Bennett, J. Dunkley, B. Gold, M. R. Greason, N. Jarosik, E. Komatsu, M. R. Nolta, L. Page, D. N. Spergel, E. Wollack, *et al.*, ApJS, **180**, 225 (2009), arXiv:0803.0732

[20] S. Dodelson, *Modern Cosmology*, edited by Dodelson, S. (Amsterdam, The Netherlands: Academic Press. ISBN 0-12-219141-2, XIII + 440 p., 2003)

[21] G. Bertone, D. Hooper, and J. Silk, Phys. Rep., **405**, 279 (2005), arXiv:hep-ph/0404175

[22] G. Bertone, D. G. Cerdeno, M. Fornasa, R. Ruiz de Austri, and R. Trotta, ArXiv e-prints (2010), arXiv:1005.4280

[23] A. Klypin, A. V. Kravtsov, O. Valenzuela, and F. Prada, ApJ, **522**, 82 (1999), arXiv:astro-ph/9901240

[24] B. Moore, S. Ghigna, F. Governato, G. Lake, T. Quinn, J. Stadel, and P. Tozzi, ApJ, **524**, L19 (1999), arXiv:astro-ph/9907411

[25] J. A. Sellwood and A. Kosowsky, in *Gas and Galaxy Evolution*, Astronomical Society of the Pacific Conference Series, Vol. 240, edited by J. E. Hibbard, M. Rupen, & J. H. van Gorkom (2001) pp. 311–+, arXiv:astro-ph/0009074

[26] W. J. G. de Blok, Advances in Astronomy, **2010** (2010), doi:10.1155/2010/789293, arXiv:0910.3538

[27] G. Gilmore, M. Wilkinson, J. Kleyna, A. Koch, W. Evans, R. F. G. Wyse, and E. K. Grebel, Nuclear Physics B Proceedings Supplements, **173**, 15 (2007), arXiv:astro-ph/0608528

[28] G. Gentile, P. Salucci, U. Klein, D. Vergani, and P. Kalberla, MNRAS, **351**, 903 (2004), arXiv:astro-ph/0403154

[29] O. Y. Gnedin and H. Zhao, MNRAS, **333**, 299 (2002), arXiv:astro-ph/0108108

[30] E. J. Copeland, M. Sami, and S. Tsujikawa, International Journal of Modern Physics D, **15**, 1753 (2006), arXiv:hep-th/0603057

[31] S. Chongchitnan and G. Efstathiou, Phys. Rev. D, **76**, 043508 (2007), arXiv:0705.1955

[32] M. E. Peskin and D. V. Schroeder, *An Introduction to Quantum Field Theory*, edited by Peskin, M. E. & Schroeder, D. V. (Westview Press, Perseus Books Group, ISBN 978-0-201-50397-5, 1995)

[33] P. West, *Introduction to Supersymmetry and Supergravity* (World Scientific, Singapore, 1990)

[34] H. Zhao, ApJ, **671**, L1 (2007), arXiv:0710.3616

[35] A. A. Starobinskij, Physics Letters B, **91**, 99 (1980)

[36] S. Capozziello, V. F. Cardone, S. Carloni, and A. Troisi, International Journal of Modern Physics D, **12**, 1969 (2003), arXiv:astro-ph/0307018

[37] S. M. Carroll, V. Duvvuri, M. Trodden, and M. S. Turner, Phys. Rev. D, **70**, 043528 (2004), arXiv:astro-ph/0306438

[38] G. Dvali, G. Gabadadze, and M. Porrati, Physics Letters B, **485**, 208 (2000), arXiv:hep-th/0005016

[39] G. Dvali, G. Gabadadze, M. Kolanović, and F. Nitti, Phys. Rev. D, **64**, 084004 (2001), arXiv:hep-ph/0102216

[40] B. Li and H. Zhao, Phys. Rev. D, **80**, 064007 (2009), arXiv:0904.2935

[41] C. W. Misner, K. S. Thorne, and J. A. Wheeler, *Gravitation*, edited by Misner, C. W., Thorne, K. S., & Wheeler, J. A. (San Francisco: W.H. Freeman and Co., 1973)

[42] R. M. Wald, *General Relativity* (Chicago: University of Chicago Press, 1984)

[43] J. D. Bekenstein, Phys. Rev. D, **70**, 083509 (2004), astro-ph/0403694

[44] M. Milgrom, ApJ, **270**, 371 (1983)

[45] M. Milgrom, ApJ, **270**, 384 (1983)

[46] M. Milgrom, ApJ, **270**, 365 (1983)

[47] J. Bekenstein and M. Milgrom, ApJ, **286**, 7 (1984)

[48] L. Ciotti, P. Londrillo, and C. Nipoti, ApJ, **640**, 741 (2006), astro-ph/0512056

[49] O. Tiret and F. Combes, A&A, **464**, 517 (2007), arXiv:astro-ph/0701011

[50] M. Feix, C. Fedeli, and M. Bartelmann, A&A, **480**, 313 (2008), arXiv:0707.0790

[51] A. H. Broeils, A&A, **256**, 19 (1992)

[52] R. H. Sanders and M. A. W. Verheijen, ApJ, **503**, 97 (1998), astro-ph/9802240

[53] R. B. Tully and J. R. Fisher, A&A, **54**, 661 (1977)

[54] S. S. McGaugh, W. J. G. de Blok, J. M. Schombert, R. Kuzio de Naray, and J. H. Kim, ApJ, **659**, 149 (2007), arXiv:astro-ph/0612410

[55] B. Famaey, G. Gentile, J.-P. Bruneton, and H. Zhao, Phys. Rev. D, **75**, 063002 (2007), arXiv:astro-ph/0611132

[56] R. H. Sanders and E. Noordermeer, MNRAS, **379**, 702 (2007), arXiv:astro-ph/0703352

[57] M. Milgrom and R. H. Sanders, ApJ, **658**, L17 (2007), arXiv:astro-ph/0611494

[58] R. H. Sanders and S. S. McGaugh, ARA&A, **40**, 263 (2002), arXiv:astro-ph/0204521

[59] J. D. Bekenstein, Contemp. Phys., **47**, 387 (2006), astro-ph/0701848

[60] B. Famaey and J. Binney, MNRAS, **363**, 603 (2005), astro-ph/0506723

[61] B. Famaey, J.-P. Bruneton, and H. Zhao, MNRAS, **377**, L79 (2007), arXiv:astro-ph/0702275

[62] S. S. McGaugh, ApJ, **683**, 137 (2008), arXiv:0804.1314

[63] M. Milgrom, ApJ, **455**, 439 (1995), arXiv:astro-ph/9503056

[64] F. J. Sánchez-Salcedo and X. Hernandez, ApJ, **667**, 878 (2007), arXiv:astro-ph/0702443

[65] G. W. Angus, MNRAS, **387**, 1481 (2008), arXiv:0804.3812

[66] M. Milgrom and R. H. Sanders, ApJ, **599**, L25 (2003), arXiv:astro-ph/0309617

[67] G. W. Angus, B. Famaey, O. Tiret, F. Combes, and H. S. Zhao, MNRAS, **383**, L1 (2008), arXiv:0709.1966

[68] F. Bournaud, P.-A. Duc, E. Brinks, M. Boquien, P. Amram, U. Lisenfeld, B. S. Koribalski, F. Walter, and V. Charmandaris, Science, **316**, 1166 (2007), arXiv:0705.1356

[69] G. Gentile, B. Famaey, F. Combes, P. Kroupa, H. S. Zhao, and O. Tiret, A&A, **472**, L25 (2007), arXiv:0706.1976

[70] M. Milgrom, ApJ, **667**, L45 (2007), arXiv:0706.0875

[71] S. S. McGaugh, J. M. Schombert, G. D. Bothun, and W. J. G. de Blok, ApJ, **533**, L99 (2000), arXiv:astro-ph/0003001

[72] S. S. McGaugh, ApJ, **632**, 859 (2005), arXiv:astro-ph/0506750

[73] S. M. Faber and R. E. Jackson, ApJ, **204**, 668 (1976)

[74] R. H. Sanders, MNRAS, **407**, 1128 (2010), arXiv:1002.2765 [astro-ph.CO]

[75] G. Gentile, B. Famaey, H. Zhao, and P. Salucci, Nature, **461**, 627 (2009), arXiv:0909.5203

[76] M. Milgrom, MNRAS, **398**, 1023 (2009), arXiv:0909.5184

[77] F. Donato, G. Gentile, P. Salucci, C. Frigerio Martins, M. I. Wilkinson, G. Gilmore, E. K. Grebel, A. Koch, and R. Wyse, MNRAS, **397**, 1169 (2009), arXiv:0904.4054

[78] R. H. Sanders, ApJ, **512**, L23 (1999), arXiv:astro-ph/9807023

[79] R. H. Sanders, MNRAS, **342**, 901 (2003), arXiv:astro-ph/0212293

[80] G. W. Angus, B. Famaey, and D. A. Buote, MNRAS, **387**, 1470 (2008), arXiv:0709.0108

[81] R. H. Sanders, MNRAS, **380**, 331 (2007), arXiv:astro-ph/0703590

[82] T. G. Zlosnik, P. G. Ferreira, and G. D. Starkman, Phys. Rev. D, **75**, 044017 (2007), arXiv:astro-ph/0607411

[83] J. Bruneton and G. Esposito-Farèse, Phys. Rev. D, **76**, 124012 (2007), arXiv:0705.4043

[84] R. H. Sanders, MNRAS, **363**, 459 (2005), arXiv:astro-ph/0502222

[85] C. Skordis, Phys. Rev. D, **77**, 123502 (2008), arXiv:0801.1985

[86] C. Skordis, D. F. Mota, P. G. Ferreira, and C. Bœhm, Physical Review Letters, **96**, 011301 (2006), arXiv:astro-ph/0505519

[87] S. Dodelson and M. Liguori, Physical Review Letters, **97**, 231301 (2006), arXiv:astro-ph/0608602

[88] F. Schmidt, M. Liguori, and S. Dodelson, Phys. Rev. D, **76**, 083518 (2007), arXiv:0706.1775

[89] P. Zhang, M. Liguori, R. Bean, and S. Dodelson, Physical Review Letters, **99**, 141302 (2007), arXiv:0704.1932

[90] M.-C. Chiu, C.-M. Ko, and Y. Tian, ApJ, **636**, 565 (2006), arXiv:astro-ph/0507332

[91] B. Qin, X. P. Wu, and Z. L. Zou, A&A, **296**, 264 (1995)

[92] H. Zhao, D. J. Bacon, A. N. Taylor, and K. Horne, MNRAS, **368**, 171 (2006), astro-ph/0509590

[93] G. W. Angus, H. Y. Shan, H. S. Zhao, and B. Famaey, ApJ, **654**, L13 (2007), astro-ph/0609125

[94] R. Takahashi and T. Chiba, ApJ, **671**, 45 (2007)

[95] J. G. Hao and R. Akhoury, Int. J. Mod. Phys., **D18**, 1039 (2009), arXiv:astro-ph/0504130

[96] F. Bourliot, P. G. Ferreira, D. F. Mota, and C. Skordis, Phys. Rev. D, **75**, 063508 (2007), arXiv:astro-ph/0611255

[97] L. M. Diaz-Rivera, L. Samushia, and B. Ratra, Phys. Rev. D, **73**, 083503 (2006), arXiv:astro-ph/0601153

[98] H. Zhao, International Journal of Modern Physics D, **16**, 2055 (2007), arXiv:astro-ph/0610056

[99] C. Armendariz-Picon and A. Diez-Tejedor, Journal of Cosmology and Astro-Particle Physics, **12**, 18 (2009), arXiv:0904.0809 [astro-ph.CO]

[100] V. F. Cardone and N. Radicella, Phys. Rev. D, **80**, 063515 (2009), arXiv:0908.0095 [astro-ph.CO]

[101] C. Skordis, Phys. Rev. D, **74**, 103513 (2006), arXiv:astro-ph/0511591

[102] C. Armendariz-Picon, V. Mukhanov, and P. J. Steinhardt, Phys. Rev. D, **63**, 103510 (2001), arXiv:astro-ph/0006373

[103] C. Skordis, Classical and Quantum Gravity, **26**, 143001 (2009), arXiv:0903.3602

[104] C. R. Contaldi, T. Wiseman, and B. Withers, Phys. Rev. D, **78**, 044034 (2008), arXiv:0802.1215

[105] E. Sagi, Phys. Rev. D, **80**, 044032 (2009), arXiv:0905.4001

[106] R. Reyes, R. Mandelbaum, U. Seljak, T. Baldauf, J. E. Gunn, L. Lombriser, and R. E. Smith, Nature, **464**, 256 (2010), arXiv:1003.2185

[107] J. D. Bekenstein and E. Sagi, Phys. Rev. D, **77**, 103512 (2008), arXiv:0802.1526

[108] T. G. Zlosnik, P. G. Ferreira, and G. D. Starkman, Phys. Rev. D, **74**, 044037 (2006), arXiv:gr-qc/0606039

[109] T. Jacobson and D. Mattingly, Phys. Rev. D, **64**, 024028 (2001), arXiv:gr-qc/0007031

[110] V. A. Kostelecký and S. Samuel, Phys. Rev. D, **39**, 683 (1989)

[111] V. A. Kostelecký, Phys. Rev. D, **69**, 105009 (2004), arXiv:hep-th/0312310

[112] C. M. Will, *Theory and Experiment in Gravitational Physics* (Theory and Experiment in Gravitational Physics, by Clifford M. Will, pp. 396. ISBN 0521439736. Cambridge, UK: Cambridge University Press, March 1993., 1993)

[113] C. Will, Living Reviews in Relativity, **4**, 4 (2001), arXiv:gr-qc/0103036

[114] S. Kanno and J. Soda, Phys. Rev. D, **74**, 063505 (2006), arXiv:hep-th/0604192

[115] H. Zhao and B. Li, ApJ, **712**, 130 (2010)

[116] A. Halle, H. Zhao, and B. Li, ApJS, **177**, 1 (2008)

[117] S. Hannestad and E. Mörtsell, J. Cosmology Astropart. Phys., **9**, 1 (2004), arXiv:astro-ph/0407259

[118] A. R. Liddle, P. Mukherjee, D. Parkinson, and Y. Wang, Phys. Rev. D, **74**, 123506 (2006), arXiv:astro-ph/0610126

[119] C. Wetterich, A&A, **301**, 321 (1995), arXiv:hep-th/9408025

[120] B. Ratra and P. J. E. Peebles, Phys. Rev. D, **37**, 3406 (1988)

[121] P. Brax, J. Martin, and A. Riazuelo, Phys. Rev. D, **64**, 083505 (2001), arXiv:hep-ph/0104240

[122] F. Perrotta, C. Baccigalupi, and S. Matarrese, Phys. Rev. D, **61**, 023507 (2000), arXiv:astro-ph/9906066

[123] J. Khoury and A. Weltman, Physical Review Letters, **93**, 171104 (2004), arXiv:astro-ph/0309300

[124] D. F. Mota and D. J. Shaw, Physical Review Letters, **97**, 151102 (2006), arXiv:hep-ph/0606204

[125] L. Amendola, Phys. Rev. D, **62**, 043511 (2000), arXiv:astro-ph/9908023

[126] T. Chiba, Phys. Rev. D, **64**, 103503 (2001), arXiv:astro-ph/0106550

[127] B. Li and H. Zhao, Phys. Rev. D, **80**, 044027 (2009), arXiv:0906.3880 [astro-ph.CO]

[128] M. Bartelmann and P. Schneider, Phys. Rep., **340**, 291 (2001), astro-ph/9912508

[129] P. Schneider, J. Ehlers, and E. E. Falco, *Gravitational Lenses* (Gravitational Lenses, XIV, 560 pp. 112 figs., Springer-Verlag Berlin Heidelberg New York, also Astronomy and Astrophysics Library, 1992)

[130] D. Clowe, M. Bradač, A. H. Gonzalez, M. Markevitch, S. W. Randall, C. Jones, and D. Zaritsky, ApJ, **648**, L109 (2006), astro-ph/0608407

[131] C. Kraus *et al.*, Eur. Phys. J., **C40**, 447 (2005), arXiv:hep-ex/0412056

[132] J. Bonn, in *Exotic Nuclei and Nuclear/Particle Astrophysics (II)*, American Institute of Physics Conference Series, Vol. 972 (2008) pp. 404–411

[133] J. Wolf, in *Proceedings of 34th International Conference on High Energy Physics (ICHEP 2008), Philadelphia, eConf C080730* (2008) arXiv:0810.3281

[134] E. E. Falco, C. S. Kochanek, J. Lehar, B. A. McLeod, J. A. Munoz, C. D. Impey, C. Keeton, C. Y. Peng, and H. . Rix, ArXiv Astrophysics e-prints (1999), astro-ph/9910025

[135] I. Ferreras, M. Sakellariadou, and M. F. Yusaf, Phys. Rev. Lett., **100**, 031302 (2008), arXiv:0709.3189 [astro-ph]

[136] I. Ferreras, N. E. Mavromatos, M. Sakellariadou, and M. F. Yusaf, Phys. Rev. D, **80**, 103506 (2009), arXiv:0907.1463

[137] M. Chiu, C. Ko, Y. Tian, and H. Zhao, ArXiv e-prints (2010), arXiv:1008.3114 [astro-ph.GA]

[138] G. Kuzmin, Astron. Zh., **33**, 27 (1956)

[139] L. Hernquist, ApJ, **356**, 359 (1990)

[140] M. Miyamoto and R. Nagai, PASJ, **27**, 533 (1975)

[141] R. Kayser, ApJ, **357**, 309 (1990)

[142] F. Grundahl and J. Hjorth, MNRAS, **275**, L67 (1995), arXiv:astro-ph/9506085

[143] T. York, N. Jackson, I. W. A. Browne, O. Wucknitz, and J. E. Skelton, MNRAS, **357**, 124 (2005), arXiv:astro-ph/0405115

[144] D.-M. Chen and H. Zhao, ApJ, **650**, L9 (2006), arXiv:astro-ph/0606506

[145] J. A. Muñoz, E. E. Falco, C. S. Kochanek, J. Lehár, B. A. McLeod, B. R. McNamara, A. A. Vikhlinin, C. D. Impey, H.-W. Rix, C. R. Keeton, C. Y. Peng, and C. R. Mullis, ApJ, **546**, 769 (2001), arXiv:astro-ph/0008124

[146] C. R. Keeton, E. E. Falco, C. D. Impey, C. S. Kochanek, J. Lehár, B. A. McLeod, H.-W. Rix, J. A. Muñoz, and C. Y. Peng, ApJ, **542**, 74 (2000), arXiv:astro-ph/0001500

[147] R. Barkana, J. Lehár, E. E. Falco, N. A. Grogin, C. R. Keeton, and I. I. Shapiro, ApJ, **520**, 479 (1999), arXiv:astro-ph/9808096

[148] J. Lehár, E. E. Falco, C. S. Kochanek, B. A. McLeod, J. A. Muñoz, C. D. Impey, H.-W. Rix, C. R. Keeton, and C. Y. Peng, ApJ, **536**, 584 (2000), arXiv:astro-ph/9909072

[149] L. M. Lubin, C. D. Fassnacht, A. C. S. Readhead, R. D. Blandford, and T. Kundić, AJ, **119**, 451 (2000), arXiv:astro-ph/9910523

[150] O. Wucknitz, L. Wisotzki, S. Lopez, and M. D. Gregg, A&A, **405**, 445 (2003), arXiv:astro-ph/0304435

[151] J. Huchra, M. Gorenstein, S. Kent, I. Shapiro, G. Smith, E. Horine, and R. Perley, AJ, **90**, 691 (1985)

[152] D. Rusin, C. S. Kochanek, and C. R. Keeton, ApJ, **595**, 29 (2003), arXiv:astro-ph/0306096

[153] H. K. C. Yee, AJ, **95**, 1331 (1988)

[154] T. Kundic, J. G. Cohen, R. D. Blandford, and L. M. Lubin, AJ, **114**, 507 (1997), arXiv:astro-ph/9704109

[155] C. D. Impey, E. E. Falco, C. S. Kochanek, J. Lehár, B. A. McLeod, H.-W. Rix, C. Y. Peng, and C. R. Keeton, ApJ, **509**, 551 (1998), arXiv:astro-ph/9803207

[156] T. Kundic, D. W. Hogg, R. D. Blandford, J. G. Cohen, L. M. Lubin, and J. E. Larkin, AJ, **114**, 2276 (1997), arXiv:astro-ph/9706169

[157] R. Kormann, P. Schneider, and M. Bartelmann, A&A, **286**, 357 (1994), arXiv:astro-ph/9311011

[158] A. Kassiola and I. Kovner, ApJ, **417**, 450 (1993)

[159] R. Kormann, P. Schneider, and M. Bartelmann, A&A, **284**, 285 (1994)

[160] N. Inada, R. H. Becker, S. Burles, F. J. Castander, D. Eisenstein, P. B. Hall, D. E. Johnston, B. Pindor, G. T. Richards, P. L. Schechter, M. Sekiguchi, R. L. White, J. Brinkmann, J. A. Frieman, and e. a. Kleinman, AJ, **126**, 666 (2003), arXiv:astro-ph/0304377

[161] H. J. Witt and S. Mao, MNRAS, **291**, 211 (1997), arXiv:astro-ph/9702021

[162] C. R. Keeton, C. S. Kochanek, and U. Seljak, ApJ, **482**, 604 (1997), arXiv:astro-ph/9610163

[163] W. Dehnen, MNRAS, **265**, 250 (1993)

[164] W. Jaffe, MNRAS, **202**, 995 (1983)

[165] M. Milgrom, ArXiv e-prints, **712** (2007), 0712.4203

[166] G. Gentile, H. S. Zhao, and B. Famaey, ArXiv e-prints, **712** (2007), 0712.1816

[167] D. Dai, R. Matsuo, and G. Starkman, Phys. Rev. D, **78**, 104004 (2008), arXiv:0806.4319 [gr-qc]

[168] T. Richtler, Y. Schuberth, M. Hilker, B. Dirsch, L. Bassino, and A. J. Romanowsky, A&A, **478**, L23 (2008), arXiv:0711.4077

[169] A. Mahdavi, H. Hoekstra, A. Babul, D. D. Balam, and P. L. Capak, ApJ, **668**, 806 (2007), arXiv:0706.3048

[170] T. Erben, L. van Waerbeke, Y. Mellier, P. Schneider, J.-C. Cuillandre, F. J. Castander, and M. Dantel-Fort, A&A, **355**, 23 (2000), arXiv:astro-ph/9907134

[171] J. M. Colberg, K. S. Krughoff, and A. J. Connolly, MNRAS, **359**, 272 (2005), arXiv:astro-ph/0406665

[172] A. Knebe, in *Revista Mexicana de Astronomia y Astrofisica Conference Series*, Revista Mexicana de Astronomia y Astrofisica Conference Series, Vol. 17, edited by V. Avila-Reese, C. Firmani, C. S. Frenk, and C. Allen (2003) pp. 41–41

[173] A. Knebe, J. E. G. Devriendt, A. Mahmood, and J. Silk, MNRAS, **329**, 813 (2002), arXiv:astro-ph/0105316

[174] P. Bode, J. P. Ostriker, and N. Turok, ApJ, **556**, 93 (2001), arXiv:astro-ph/0010389

[175] M. Milgrom, ApJ, **478**, 7 (1997), arXiv:astro-ph/9606148

[176] A. Knebe and B. K. Gibson, MNRAS, **347**, 1055 (2004), arXiv:astro-ph/0303222

[177] R. Blandford and R. Narayan, ApJ, **310**, 568 (1986)

[178] K. Dolag, M. Meneghetti, L. Moscardini, E. Rasia, and A. Bonaldi, MNRAS, **370**, 656 (2006), arXiv:astro-ph/0511357

[179] B. Famaey, G. W. Angus, G. Gentile, H. Y. Shan, and H. S. Zhao, in *Proceedings of the Sixth International Heidelberg Conference on Dark Matter in Astro- and Particle Physics (DARK 2007), Sydney, Eds. H. V. Klapdor-Kleingrothaus, G. Lewis, World Scientific, Singapore* (2008) pp. 393–401

[180] J. P. Dietrich, P. Schneider, D. Clowe, E. Romano-Díaz, and J. Kerp, A&A, **440**, 453 (2005), arXiv:astro-ph/0406541

[181] M. Marcolli and E. Pierpaoli, ArXiv e-prints (2009), arXiv:0908.3683

[182] A. Kusenko, Phys. Rep., **481**, 1 (2009), arXiv:0906.2968

[183] A. Boyarsky, J. Lesgourgues, O. Ruchayskiy, and M. Viel, Physical Review Letters, **102**, 201304 (2009), arXiv:0812.3256

[184] M. Gell-Mann, P. Ramond, and R. Slansky, in *Supergravity: Proceedings of the Supergravity Workshop at Stony Brook, North Holland (1979), p. 315* (1979)

[185] T. Yanagida, Progress of Theoretical Physics, **64**, 1103 (1980)

[186] M. Lindner, T. Ohlsson, and G. Seidl, Phys. Rev. D, **65**, 053014 (2002), arXiv:hep-ph/0109264

[187] M. C. Gonzalez-Garcia and Y. Nir, Reviews of Modern Physics, **75**, 345 (2003), arXiv:hep-ph/0202058

[188] C. Giunti and M. Laveder, Phys. Rev. D, **77**, 093002 (2008)

[189] G. W. Angus, MNRAS, **394**, 527 (2009), arXiv:0805.4014

[190] G. W. Angus, B. Famaey, and A. Diaferio, MNRAS, **402**, 395 (2010), arXiv:0906.3322

[191] C. Llinares, A. Knebe, and H. Zhao, MNRAS, **391**, 1778 (2008), arXiv:0809.2899

[192] L. Tian, H. Hoekstra, and H. Zhao, MNRAS, **393**, 885 (2009), arXiv:0810.2826

[193] P. Natarajan and H. Zhao, MNRAS, **389**, 250 (2008), arXiv:0806.3080

[194] S. Tremaine and J. E. Gunn, Physical Review Letters, **42**, 407 (1979)

[195] J. Le Borgne, G. Mathez, Y. Mellier, R. Pello, B. Sanahuja, and G. Soucail, A&AS, **88**, 133 (1991)

[196] H. K. C. Yee, E. Ellingson, R. G. Abraham, P. Gravel, R. G. Carlberg, T. A. Smecker-Hane, D. Schade, and M. Rigler, ApJS, **102**, 289 (1996)

[197] R. Pello, B. Sanahuja, J. Le Borgne, G. Soucail, and Y. Mellier, ApJ, **366**, 405 (1991)

[198] Y. Mellier, in *Clusters of Galaxies*, edited by M. J. Fitchett & W. R. Oegerle (1989) pp. 175–+

[199] R. G. Carlberg, H. K. C. Yee, E. Ellingson, R. Abraham, P. Gravel, S. Morris, and C. J. Pritchet, ApJ, **462**, 32 (1996), arXiv:astro-ph/9509034

[200] L. Benatov, K. Rines, P. Natarajan, A. Kravtsov, and D. Nagai, MNRAS, **370**, 427 (2006), arXiv:astro-ph/0605105

[201] H. Boehringer, Y. Tanaka, R. F. Mushotzky, Y. Ikebe, and M. Hattori, A&A, **334**, 789 (1998), arXiv:astro-ph/9803325

[202] S. W. Allen, S. Ettori, and A. C. Fabian, MNRAS, **324**, 877 (2001), arXiv:astro-ph/0008517

[203] A. K. Hicks, E. Ellingson, H. Hoekstra, and H. K. C. Yee, ApJ, **652**, 232 (2006), arXiv:astro-ph/0609334

[204] A. Vikhlinin, A. Kravtsov, W. Forman, C. Jones, M. Markevitch, S. S. Murray, and L. Van Speybroeck, ApJ, **640**, 691 (2006), arXiv:astro-ph/0507092

[205] A. Diaferio, M. J. Geller, and K. J. Rines, ApJ, **628**, L97 (2005), arXiv:astro-ph/0506560

[206] G. Squires, N. Kaiser, G. Fahlman, A. Babul, and D. Woods, ApJ, **469**, 73 (1996), arXiv:astro-ph/9602105

[207] H. Dahle, ApJ, **653**, 954 (2006), arXiv:astro-ph/0608480

[208] H. Hoekstra, MNRAS, **379**, 317 (2007), arXiv:0705.0358

[209] S. Bardeau, G. Soucail, J. Kneib, O. Czoske, H. Ebeling, P. Hudelot, I. Smail, and G. P. Smith, A&A, **470**, 449 (2007), arXiv:astro-ph/0703395

[210] K. Umetsu, M. Birkinshaw, G. Liu, J. Wu, E. Medezinski, T. Broadhurst, D. Lemze, A. Zitrin, P. T. P. Ho, C. Huang, P. M. Koch, Y. Liao, K. Lin, S. M. Molnar, H. Nishioka, *et al.*, ApJ, **694**, 1643 (2009), arXiv:0810.0969

[211] A. Kassiola, I. Kovner, and R. D. Blandford, ApJ, **396**, 10 (1992)

[212] D. Narasimha and S. M. Chitre, Journal of Astrophysics and Astronomy, **14**, 121 (1993)

[213] M. Pierre, J. F. Le Borgne, G. Soucail, and J. P. Kneib, A&A, **311**, 413 (1996), arXiv:astro-ph/9510128

[214] B. Frye and T. Broadhurst, ApJ, **499**, L115+ (1998), arXiv:astro-ph/9712111

[215] B. R. McNamara, P. E. J. Nulsen, M. W. Wise, D. A. Rafferty, C. Carilli, C. L. Sarazin, and E. L. Blanton, Nature, **433**, 45 (2005)

[216] I. Smail, A. C. Edge, R. S. Ellis, and R. D. Blandford, MNRAS, **293**, 124 (1998), arXiv:astro-ph/9707231

[217] A. C. Edge, R. J. Ivison, I. Smail, A. W. Blain, and J. Kneib, MNRAS, **306**, 599 (1999), arXiv:astro-ph/9902038

[218] R. G. Abraham, T. A. Smecker-Hane, J. B. Hutchings, R. G. Carlberg, H. K. C. Yee, E. Ellingson, S. Morris, J. B. Oke, and M. Rigler, ApJ, **471**, 694 (1996), arXiv:astro-ph/9605144

[219] A. Fritz, B. L. Ziegler, R. G. Bower, I. Smail, and R. L. Davies, MNRAS, **358**, 233 (2005), arXiv:astro-ph/0501379

[220] B. L. Frye, T. J. Broadhurst, H. Spinrad, and A. Bunker, in *The Young Universe: Galaxy Formation and Evolution at Intermediate and High Redshift*, Astronomical Society of the Pacific Conference Series, Vol. 146, edited by S. D'Odorico, A. Fontana, & E. Giallongo (1998) pp. 504–+

[221] L. Lemonon, M. Pierre, C. J. Cesarsky, D. Elbaz, R. Pello, G. Soucail, and L. Vigroux, A&A, **334**, L21 (1998), arXiv:astro-ph/9804088

[222] J. Wambsganss, P. Schneider, E. Giraud, and A. Weiss, ApJ, **337**, L73 (1989)

[223] G. Mathez, B. Fort, Y. Mellier, J. Picat, and G. Soucail, A&A, **256**, 343 (1992)

[224] M. Hattori, H. Matuzawa, K. Morikawa, J. Kneib, K. Yamashita, K. Watanabe, H. Boehringer, and T. G. Tsuru, ApJ, **503**, 593 (1998), arXiv:astro-ph/9803092

[225] H. M. Abdelsalam, P. Saha, and L. L. R. Williams, MNRAS, **294**, 734 (1998), arXiv:astro-ph/9707207

[226] D. Boyanovsky, Phys. Rev. D, **78**, 103505 (2008), arXiv:0807.0646

[227] H. S. Zhao and B. Famaey, ApJ, **638**, L9 (2006), astro-ph/0512425

[228] A. Kassiola and I. Kovner, ApJ, **417**, 450 (1993)

[229] P. Schneider, C. S. Kochanek, and J. Wambsganss, *Gravitational Lensing: Strong, Weak and Micro: , Saas-Fee Advanced Courses, Volume 33.* (Springer-Verlag Berlin Heidelberg, 2006)

[230] A. Kull, R. A. Treumann, and H. Boehringer, ApJ, **466**, L1+ (1996), arXiv:astro-ph/9606057

[231] M. H. Shaevitz and the Mini Boo NE Collaboration, Journal of Physics Conference Series, **120**, 052003 (2008)

[232] M. Maltoni and T. Schwetz, Phys. Rev. D, **76**, 093005 (2007), arXiv:0705.0107

[233] E. Calligarich, S. Centro, D. Gibin, A. Guglielmi, F. Pietropaolo, C. Rubbia, and P. R. Sala, Journal of Physics Conference Series, **203**, 012110 (2010)

[234] A. Suzuki, Progress in Particle and Nuclear Physics, **65**, 1 (2010)

[235] M. Zito, in *American Institute of Physics Conference Series*, American Institute of Physics Conference Series, Vol. 1222, edited by D. Kaplan, M. Goodman, & Z. Sullivan (2010) pp. 10–14

[236] H. Shan, B. Qin, B. Fort, C. Tao, X. Wu, and H. Zhao, MNRAS, **406**, 1134 (2010), arXiv:1004.1475 [astro-ph.CO]

[237] M. Milgrom, Phys. Rev. D, **80**, 123536 (2009), arXiv:0912.0790 [gr-qc]

[238] M. Milgrom, MNRAS, **405**, 1129 (2010), arXiv:1001.4444 [astro-ph.CO]

[239] A. H. Guth, Phys. Rev. D, **23**, 347 (1981)

[240] A. R. Liddle and D. H. Lyth, *Cosmological Inflation and Large-Scale Structure*, edited by Liddle, A. R. & Lyth, D. H. (Cambridge, UK: Cambridge University Press, ISBN 052166022X, pp. 414, 2000)

[241] H. Oyaizu, Phys. Rev. D, **78**, 123523 (2008), arXiv:0807.2449

[242] A. V. Macciò, C. Quercellini, R. Mainini, L. Amendola, and S. A. Bonometto, Phys. Rev. D, **69**, 123516 (2004), arXiv:astro-ph/0309671

[243] G. R. Farrar and R. A. Rosen, Physical Review Letters, **98**, 171302 (2007), arXiv:astro-ph/0610298

[244] A. Knebe, A. Green, and J. Binney, MNRAS, **325**, 845 (2001), arXiv:astro-ph/0103503

[245] W. H. Press, S. A. Teukolsky, W. T. Vetterling, and B. P. Flannery, *Numerical Recipes in C. The Art of Scientific Computing*, edited by Press, W. H., Teukolsky, S. A., Vetterling, W. T., & Flannery, B. P. (Cambridge, UK: Cambridge University Press, 2nd ed., 1992)

[246] G. Efstathiou, M. Davis, S. D. M. White, and C. S. Frenk, ApJS, **57**, 241 (1985)

[247] E. Bertschinger, ArXiv Astrophysics e-prints (1995), arXiv:astro-ph/9506070

[248] L. Casarini, A. V. Macciò, and S. A. Bonometto, J. Cosmology Astropart. Phys., **3**, 14 (2009), arXiv:0810.0190

[249] H. Hoekstra, Y. Mellier, L. van Waerbeke, E. Semboloni, L. Fu, M. J. Hudson, L. C. Parker, I. Tereno, and K. Benabed, ApJ, **647**, 116 (2006), arXiv:astro-ph/0511089

[250] L. Fu, E. Semboloni, H. Hoekstra, M. Kilbinger, L. van Waerbeke, I. Tereno, Y. Mellier, C. Heymans, J. Coupon, K. Benabed, J. Benjamin, E. Bertin, O. Doré, M. J. Hudson, O. Ilbert, R. Maoli, C. Marmo, H. J. McCracken, and B. Ménard, A&A, **479**, 9 (2008), arXiv:0712.0884

[251] P. G. Ferreira and M. Joyce, Physical Review Letters, **79**, 4740 (1997), arXiv:astro-ph/9707286

[252] C. Skordis and A. Albrecht, Phys. Rev. D, **66**, 043523 (2002), arXiv:astro-ph/0012195

[253] J. Bruneton, Phys. Rev. D, **75**, 085013 (2007), arXiv:gr-qc/0607055

[254] D. Huterer and E. V. Linder, Phys. Rev. D, **75**, 023519 (2007), arXiv:astro-ph/0608681

[255] E. V. Linder and R. N. Cahn, Astroparticle Physics, **28**, 481 (2007), arXiv:astro-ph/0701317

[256] L. D. Landau and E. M. Lifshitz, *Statistical Physics Part 1 & Part 2*, edited by Landau, L. D. & Lifshitz, E. M. (Course of theoretical physics, Pergamon International Library of Science, Technology, Engineering and Social Studies, Oxford: Pergamon Press, 3rd rev.and enlarg. ed., 1980)

[257] J. F. Navarro, C. S. Frenk, and S. D. M. White, ApJ, **462**, 563 (1996), arXiv:astro-ph/9508025

[258] A. Mahdavi, H. Hoekstra, A. Babul, and J. P. Henry, MNRAS, **384**, 1567 (2008), arXiv:0710.4132

[259] T. X. Thuan and J. E. Gunn, PASP, **88**, 543 (1976)

[260] D. Moro and U. Munari, A&AS, **147**, 361 (2000)

[261] J. Binney and M. Merrifield, *Galactic astronomy* (Princeton University Press, New York, Princeton series in astrophysics QB857.B522, 1998)

[262] J. Holmberg, C. Flynn, and L. Portinari, MNRAS, **367**, 449 (2006), arXiv:astro-ph/0511158

[263] E. F. Bell, D. H. McIntosh, N. Katz, and M. D. Weinberg, ApJS, **149**, 289 (2003), arXiv:astro-ph/0302543

[264] M. R. Blanton, D. Eisenstein, D. W. Hogg, D. J. Schlegel, and J. Brinkmann, ApJ, **629**, 143 (2005), arXiv:astro-ph/0310453